Room Temperature Ionic Liquids: Classical and *Ab initio* Molecular Dynamics Simulation Studies

A Thesis

Submitted For the Degree of

DOCTOR OF PHILOSOPHY

in the Faculty of Science

by

Bhargava B.L.

CHEMISTRY AND PHYSICS OF MATERIALS UNIT
JAWAHARLAL NEHRU CENTRE FOR ADVANCED SCIENTIFIC RESEARCH
(A DEEMED UNIVERSITY)
Bangalore – 560 064, India

OCTOBER 2007

DECLARATION

I hereby declare that the matter embodied in the thesis entitled "**Room Temperature Ionic Liquids: Classical and *Ab initio* Molecular Dynamics Simulation Studies**" is the result of investigations carried out by me at the Chemistry and Physics of Materials Unit, Jawaharlal Nehru Centre for Advanced Scientific Research, Bangalore, India under the supervision of Prof. S. Balasubramanian and that it has not been submitted elsewhere for the award of any degree or diploma.

In keeping with the general practice in reporting scientific observations, due acknowledgement has been made whenever the work described is based on the findings of other investigators. Any omission that might have occurred by oversight or error of judgement is regretted.

Bhargava B.L.

CERTIFICATE

I hereby certify that the matter embodied in this thesis entitled "**Room Temperature Ionic Liquids: Classical and *Ab initio* Molecular Dynamics Simulation Studies**" has been carried out by Mr. Bhargava B.L. at the Chemistry and Physics of Materials Unit, Jawaharlal Nehru Centre for Advanced Scientific Research, Bangalore, India under my supervision and that it has not been submitted elsewhere for the award of any degree or diploma.

Prof. S. Balasubramanian
(Research Supervisor)

Acknowledgements

It is my pleasure to thank my research supervisor Prof. S. Balasubramanian for giving me an opportunity to explore the interesting area of research on computational materials science. I am extremely thankful to him for teaching me the molecular dynamics simulations and for his guidance, support, and encouragement right from the beginning of this project. I sincerely acknowledge the academic freedom that I enjoyed in his group and the advices and the suggestions at various stages of the work. I also thank him for providing me excellent computing resources without which the project would not have been successful. The research training that I received from him will surely help me in approaching even more complex problems that I may pursue in the coming years.

I thank Prof. C.N.R. Rao, F.R.S, Chairman, CPMU, for research support and for being a source of inspiration for me. I am grateful to him for sharing his research experiences and for narrating us the motivating scientific anecdotes at various occasions in JNCASR.

I also would like to thank Jawaharlal Nehru Centre for providing me excellent research facilities, stimulating research ambience, and for the financial support.

I express my sincere thanks to all the faculty members of CPMU, TSU and EMU for the fruitful discussions I had with them and for the courses they offered. I am particularly thankful to Prof. Swapan K. Pati (TSU, JNCASR) for showing interest in my academic advancements and for his caring words.

I also thank Prof. Pati's group for the help in carrying out gas phase calculations and Prof. Ruth Lynden-Bell and Dr. M. Kanakubo for useful discussions.

I am thankful to the open source community for their service in providing the useful softwares and operating systems. I particularly acknowledge the developers of PINY_MD, CPMD, LAMMPS, VMD and xmovie softwares.

I have enjoyed the company and friendship of my present and past lab mates : M. Krishnan, Subrata Pal, Moumita Saharay, Sagar Sen, Saswati, Sunil Kumar, Manish C.M., Harshal Patel, Sheeba Jem, Lakshmi S., Ranjani, Sonu Swaika, V.V. Reddy, G. Srinivasa Raju, Chaitanya Krishna and Suman Mazumdar.

I thank all my friends for the moments I shared with them.

I am thankful to Deepa S. for sharing the joys and sorrows and being supportive.

I thank all the staff members of JNCASR for their constant help.

I acknowledge JNCASR, CCMS, CDAC, HPCF Hyderabad, Complab (JNCASR) for computational facilities and CSIR for Junior and Senior Research Fellowships.

Finally, I am thankful to my father and family members for their continued support and encouragement, and all those who have helped me directly or indirectly.

Preface

The thesis presents results of investigations on imidazolium cation based room temperature ionic liquids (RTILs), using *ab initio* molecular dynamics (AIMD) and classical molecular dynamics (MD) simulations. Chapter 1 introduces RTILs and provides comprehensive survey of earlier studies and a brief overview of the simulation methods and the analyses employed.

Chapter 2 presents the results of AIMD and MD simulations of 1,3-dimethylimidazolium chloride [mmim][Cl] at 425 K. The structure of the melt is characterized through radial (RDF) and spatial distribution functions (SDF). Transport properties such as diffusion coefficients of ions, shear viscosity and electrical conductivity of the liquid have been calculated. The dynamics of dipole and ion solvation in the liquid have been studied using solvation time correlation functions.

An atomistic MD simulation study of a planar vapor-liquid interface of 1,*n*-butyl-3-methylimidazolium hexafluorophosphate ([bmim][PF_6]) is presented in Chapter 3. Layering of the ions near the interface is observed as oscillations in the corresponding number density profiles. The amplitude of the oscillations in the electron density profile were found to be relatively diminished due to out-of-phase oscillations in the contributions from the anion and the cation. The butyl chains were found to be preferentially oriented along the interface normal, imparting a hydrophobic character to the surface.

Chapter 4 presents results of AIMD studies carried out on liquid [bmim][PF_6] and its mixture with CO_2. The simulations predict the formation of a weak cation-anion hydrogen bond. The anions were strongly polarized in the condensed phase. In the mixture, CO_2 molecules were found to interact better with the anion than with the cation. Such molecules present in the vicinity of the ions exhibit larger deviations from linearity in their instantaneous configurations. The backbone of the CO_2 molecules were aligned tangential to the PF_6 spheres and they were preferentially located in the octahedral voids of the anion.

Chapter 5 presents a refined atomistic potential for [bmim][PF_6] to overcome the drawbacks of the model used earlier. The refined model predicts the density of the liquid

at different temperatures between 300K and 500K within 1.4% of the experimental value. The calculated diffusion co-efficients of ions and the surface tension of the liquid agree well with experiment.

The development of a coarse grained model for the family of 1-*n*-alkylimidazolium hexafluorophosphate ILs is presented in Chapter 6. Good agreement with experiments is obtained for physical properties such as density and surface tension. The calculated neutron and X-ray weighted structure factors agree well with results from scattering experiments. Intermediate range ordering is observed for ILs containing cations with a longer alkyl chain, and its origin is discussed.

In an effort to identify the relationship between CO_2 solubility in ILs and the microscopic interactions between CO_2 and the anions present in a IL, gas phase DFT calculations were carried out. Chapter 7 presents structures, energies and vibrational features of several energy optimized anion-CO_2 complexes. The dominance of Lewis acid-base interactions was identified. In the optimized configurations, the CO_2 molecule was found to adopt a non-linear geometry. The calculated binding energy of the anion-CO_2 complexes were found to be inversely correlated with the experimentally measured solubility of CO_2 in ILs containing such anions.

Chapter 8 provides results from classical MD studies on [bmim][PF_6] - CO_2 mixtures studied at varying concentration of CO_2. The volume expansion of the mixture as computed from the simulations agree well with the experiments. The diffusion co-efficients of both the ions and that of CO_2 increases with increase in the CO_2 concentration.

The AIMD simulation of a RTIL electrolyte, [emim][F].2.3HF is presented in Chapter 9. The presence of a hydrogen bond between the acidic ring hydrogen of the cation and the fluoride anion is observed. The fluoride ions associate with HF molecules to form polyfluoride anions. The intermolecular structure of the solution is determined using RDF and SDFs. The distribution, geometry and vibrational characteristics of the polyfluoride anions have been characterized.

Nomenclature

- RTIL : Room Temperature Ionic Liquids
- VOC : Volatile Organic Compounds
- CFC : chlorofluoro carbons
- MD : Molecular Dynamics
- CPMD : Car Parrinello Molecular Dynamics
- NMR : Nuclear Magnetic Resonance
- DSC : Differential Scanning Calorimetry
- UAM : United Atom Model
- AAM : All Atom Model
- PME : Paticle Mesh Ewald
- TCF : Time Correlation Function
- RDF : Radial Distribution Function
- SDF : Spatial Distribution Function
- WAND : Wide Angle Neutron Diffraction
- WANS : Wide Angle X-ray Diffraction
- [mmim] : 1,3-dimethylimidazolium
- [emim] : 1-methyl,3-ethylimidazolium
- [bmim] : 1-n-butyl-3-methylimidazolium

- $\mathbf{r_i}$: Position vector of ith atom
- $\mathbf{p_i}$: Momentum of ith atom
- m_i : Mass of ith atom
- $\mathbf{F_i}$: Force acting on the ith atom
- H : Hamiltonian of a classical system
- N : Total number of particles present in a system
- V : Volume
- P : Pressure
- E : Total energy of a system
- T : Temperature
- μ : Chemical potential
- Γ : Phase space vector
- $f(\Gamma)$: Phase space distribution function
- $\Omega(N, V, E)$: Microcanonical partition function
- NPT-F : Isothermal-isobaric simulations with fully flexible cell
- NPT-I : Isothermal-isobaric simulations with isotropically flexible cell
- NVT : Isothermal simulations
- h : Planck's constant
- η_i : Thermostat 'position'
- p_{η_i} : Thermostat 'momentum'
- Q_i : Thermostat 'mass'
- N_f : Number of degrees of freedom
- $\tilde{\mathbf{P}}_{int}$: Pressure tensor of the system
- k_B : Boltzmann constant

Contents

Chapter 1

Introduction

1.1 Green Solvents

One of the greatest concern of 21st century is to control the ever increasing environmental pollution. Among the many contributors to the degradation of environment, are industrial solvents, that are considered the most damaging chemicals for two reasons. One is that they are used in huge amounts and the second is that they are usually volatile liquids. Solvents currently used in synthesis or catalysis are usually volatile organic compounds (VOC).

One can replace VOCs with solvents which do not affect on the environment. Water is one such solvent, however due to the low solubility of many organic compounds and the difficulty in recycling, its use is limited. Other solvents that are environmentally benign are supercritical fluids and room temperature ionic liquids (RTILs) called "Green Solvents" [1, 2].

1.1.1 Supercritical CO_2

The critical point of carbon dioxide is 72.8 atm and 31.1°C. Under thermodynamic conditions beyond these values, supercritical CO_2 possesses a unique property of liquid-like

density and gas-like transport [3]. It is non-toxic, recyclable, and its properties can be tuned. These characteristic features makes $scCO_2$ an environmentally benign solvent [4–7] for various solutes [8–10]. Unlike conventional liquids, the density of $scCO_2$ can even be doubled by doubling the pressure [11]. Tunability of the properties of supercritical fluids with temperature and pressure is one of the most attractive features for solvation. Supercritical CO_2 is becoming an important commercial and industrial solvent due to its role in compound extraction as well as its low toxicity and environmental impact. The relatively low temperature of the process and the stability of CO_2 also allows most compounds to be extracted with little damage or denaturing.

Among other applications, $scCO_2$ has also been used in the synthesis of nanomaterials [12–16]. It has been shown that the size of the nanocrystals can be changed by regulating solvent density, that in turn, tunes the steric repulsion between particle cores. $scCO_2$ is also used in asymmetric catalytic hydrogenation reactions in the manufacture of trimethyl cyclohexanone [17]. It has many more useful applications such as decaffeination of coffee, extracting volatile oils and fragrance compounds from various raw materials that are used in perfume industries and so on.

$scCO_2$ has been widely studied experimentally [18, 19] and simulations in the pure state [20–25] and as mixtures [26].

According to the principles of green chemistry [27], gaseous, liquid or solid wastes that are produced by industries should not be treated as inevitable byproducts of chemical manufacturing. Instead, new approaches must be considered to decrease or eliminate the waste before it is produced. Thus, RTILs have the potential to provide a nonvolatile solvent system [28–31] that can be used as a practical target for reducing waste and replacing VOCs. These low melting ionic salts with several interesting properties are discussed in detail in the following section.

1.2 Room Temperature Ionic Liquids

We come across several ionic salts in our daily lives. The most important being sodium chloride (NaCl) that is also called as common salt. Such ionic crystals are characterized by strong electrostatic interaction leading to large values of Madelung energy. These compounds are solids at room temperature and usually have very high melting points that greatly limits their use as solvents in most applications. For example, NaCl melts at 1074 K [32]. Some of the other conventional ionic salts such as $MgCl_2$ and $AlCl_3$ melts at temperatures 987K and 466K respectively.

Ionic liquids can be classified into three types: inorganic ionic liquids, protic ionic liquids and aprotic ionic liquids [33, 34]. Inorganic ionic liquids are the conventional high melting ionic salts that were discussed above. Protic and aprotic ionic liquids are low melting ionic compounds usually composed of mixture of organic and inorganic ions. For the protic ionic liquids there exists a dynamic equilibrium between the ionic and dissociated forms. In the case of aprotic ionic liquids, all the entities in the system exist as ions.

Polar solutes are easily solvated in an ionic environment. Although conventional ionic salts can be used for this purpose, the cost of melting these salts is uneconomical and hence these salts are not used.

On the other hand, a new class of ionic salts was discovered in the beginning of the 20th century, that possessed low melting points. The first ionic liquid $[EtNH_3][NO_3]$, that has a melting point of 12 °C was described as early as 1914 [35]. However, practical applications of these ILs were considered only in the last decade and since then they have been receiving an increasing attention of industry and academia.

Unlike the inorganic ionic salts, RTILs are composed of molecular ions. Under ambient conditions, they have negligible vapor pressure, are nontoxic, nonflammable and are very good solvents. They have been demonstrated to be good solvents for synthesis [2, 30, 31] and also can be used as catalysts. By combining different anions and cations, and by

varying the substituents on the cation, a large number of RTILs can be prepared. Trends in the variation of physical and chemical properties of RTILs upon changing the cation or the anion have been established. Knowing these trends, one can in principle have a tailor made RTIL for a particular application.

Some of the important properties of RTILs are discussed below.

1.2.1 Physical and chemical properties

RTILs possess a unique set of physico-chemical properties that make them suitable in numerous task-specific applications [36] in which conventional solvents are ineffective. Such properties include high thermal stability, high electrical conductivity, large electrochemical window, low nucleophilicity and capability to provide a weakly coordinating environment, and a good set of properties to solvate a wide variety of organic, inorganic and organometallic compounds. Physical properties of some of the RTILs have been provided in table 1.1.

Stability: The stability of ionic liquids is crucial for optimum process performance in most of the applications at least to a certain extent. Several studies have indicated that although not 100% inert, certain ionic liquids incorporating 1,3-dialkylimidazolium cations are generally better performing than traditional solvents under harsh process conditions such as those occurring in oxidation, photolysis and radiation processes [44].

Color: Ionic liquids of high quality, incorporating the 1-*n*-butyl,3-methylimidazolium ([bmim]) cation and a variety of anions such as hexafluorophosphate, tetrafluoroborate, trifluoromethylsulfonate and bis-trifluoromethylsulphonylimide have been reported to be colorless [45], although they are not 100% pure. The color of less pure ionic liquids generally ranges from yellowish to orange. Use of raw materials with color or excessive heating during the synthesis of imidazolium salt are reasons for the color of the IL. The color can be removed using activated charcoal.

Hygroscopicity: Water content influences the viscosity of ionic liquids. Ionic liquids

Table 1.1: Physical properties of some of the 1-alkyl,3-methylimidazolium ionic liquids [37–43]

R	X	T_g^a C	T_m^b C	T_d^c C	η^d cP	ρ^e g.cm^{-3}	σ^f mScm^{-1}
Et	BF_4	-92	13	447	37	1.28	14
^{n}Pr	BF_4	-88	-17	435	103	1.24	5.9
^{n}Bu	BF_4	-85	—	435	190(233)	1.21	3.5(8.6)
^{n}Bu	PF_6	-61	10	—	219(312)	1.37	1.6 (6.5)
^{n}Bu	$AlCl_4$	-88	—	—	(294)	1.23	(24.1)
^{n}Bu	CF_3SO_3	—	16	—	90	1.22	3.7
^{n}Bu	$N(Tf)_2$	—	-4	> 400	69	1.43	3.9
^{n}Bu	CF_3CO_2	-30	—	—	73	1.21	3.2
EtGly	none	-13	196[g]	21	1.11	—	

[a] Glass transition temperature, [b] Melting point, [c] Decomposition temperature, [d] Viscosity at 25 °C and in parenthesis at 30 °C, [e] Density at 25 °C, [f] Conductivity at 25 °C and in parenthesis at 60 °C, [g] boiling point. EtGly: Ethylene glycol.

become less viscous with increasing water content [46, 47]. Hydrolysis is also a possibility in the presence of water.

Hydrophobicity: The degree of polarity can be varied by adapting the length of 1-alkyl chain (in 1,3-substituted imidazolium cations), and the counter ion. Long chain IL salts have attracted some interest due to their liquid crystalline properties [48]. The anion chemistry too influences the properties of IL to a large extent.

Several interesting phenomena have been observed with ionic liquids, such as melting point depression when confined in nanospaces [49], transition from liquid to high-melting-point crystal when confined in multiwalled carbon nanotube [50], melting point depression

in the presence of compressed CO_2 [51].

1.2.2 Characteristics of RTILs

Vapor Pressure: Most RTILs have negligible vapor pressure [29]. A low vapor pressure is a direct indication of the high cohesive energy that is characteristic of ionic liquids. The strong electrostatic interaction between the ions is a major reason for the low vapor pressure. But recently it has been demonstrated that despite the low vapor pressure many ILs can be distilled at low pressures without decomposition [52]. This can extend the range of applications for the ILs where there is a need for distillation for their recovery. The vapor phase consists of ion pairs.

Liquid Range: RTILs have very wide liquid range. The low melting points of these compounds are a result of their chemical composition. RTILs contain large asymmetric organic cations (compared to their inorganic counterparts). The asymmetry lowers the lattice energy, and hence the melting point of the resulting ionic medium [53]. In some cases, even the anions are relatively large and play a role in lowering the melting point.

Solvent Properties: Ionic liquids are found to be good solvents for a wide range of both inorganic and organic compounds, and unusual combination of reagents can be brought into the same phase. Often composed of poorly coordinating ions, they have the potential to be highly polar yet non-coordinating solvents. Being immiscible with a number of organic solvents they provide a non-aqueous, polar alternative for two phase systems. Hydrophobic ionic liquids can also be used as immiscible polar phases with water. Due to their nonvolatility, they can be used in high-vacuum systems and eliminate many containment problems, since they do not evaporate. The major advantage of ILs is that they can be recycled and reused repeatedly. These compounds have been used as solvents in a number of chemical synthesis processes [30, 31] details of which will be discussed later.

1.2.3 Constituents of RTILs

RTILs are generally based on few cations such as imidazolium, pyridinium, pyrrolidinium, tetraalkylammonium and tetraalkylphosphonium. Some of these cations, such as imidazolium have a ring that is polar and nonpolar substituent side groups that can be alkyl chains or other groups. The chemical formulae of some of these cations are given in figure 1.1. Structures of some of the cations are provided in figure 1.2.

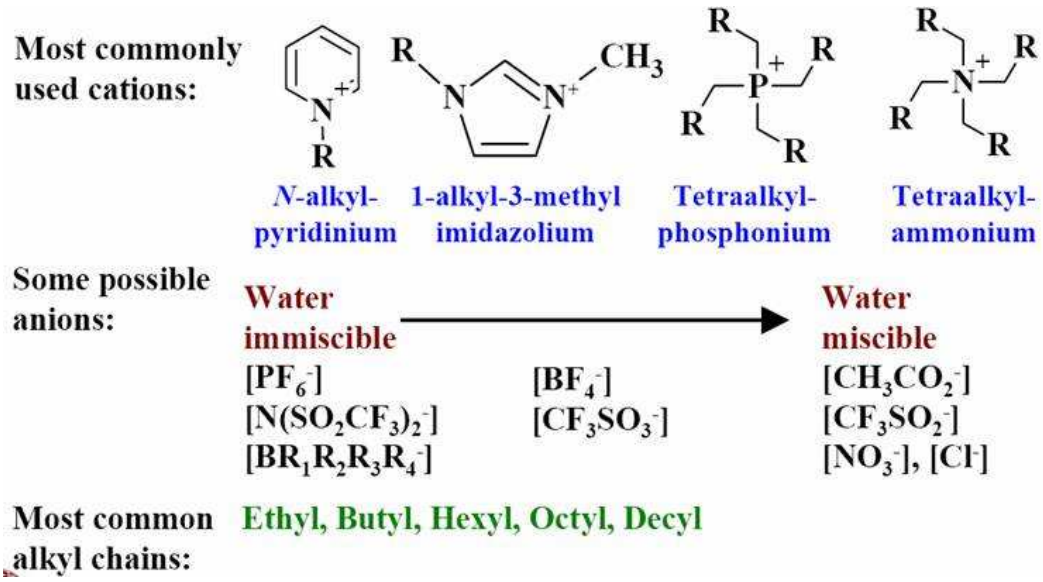

Figure 1.1: Constituents of room temperature ionic liquids.

Anions that constitute the RTILs are more in number compared to the cation bases. Generic anions include halides, nitrate, tetrafluoroborate, hexafluorophosphate, perchlorate, dicyanamide, bis-trifluoromethylsulphonylimide, methide etc, the structures of some of which are presented in figure 1.3. In general, the anions used in the ionic liquid can be broadly divided as fluorous and non-fluorous anions. Most prominent among the fluorous anions are the hexafluorophosphate (PF_6^-) and tetrafluoroborate (BF_4^-). The characteristics of an IL containing either of these salts can be dramatically different. For example, [bmim][PF_6] is immiscible [54] with water whereas [bmim][BF_4] is water soluble [55]. Similar large changes are observed when a fluorous anion is replaced with a non-fluorous one. For example, carbohydrates are sparingly soluble (< 0.5 g/L) in [bmim][BF_4], whereas

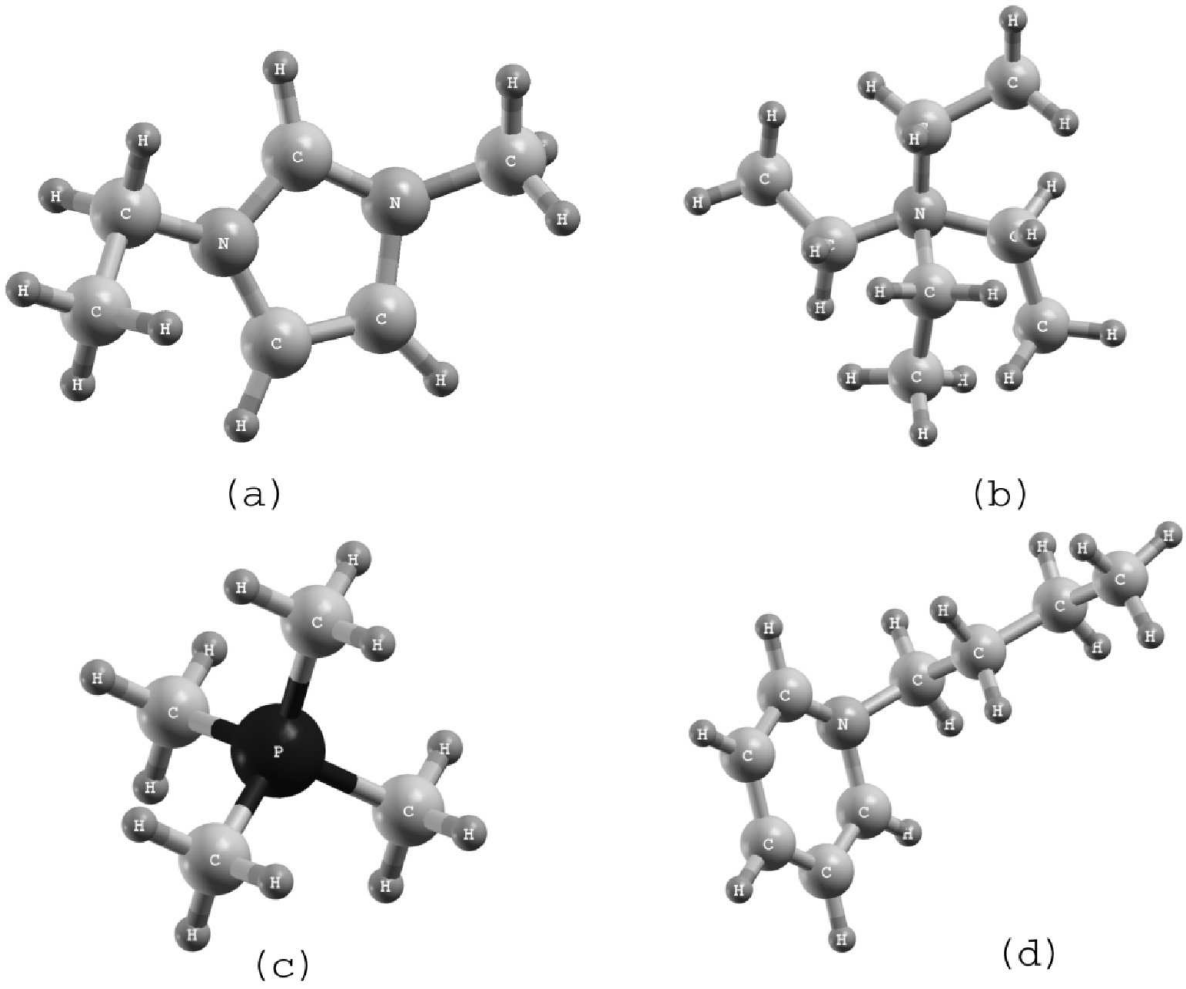

Figure 1.2: Some of the examples for cations of the room temperature ionic liquid (a) 1-ethyl,3-methylimidazolium (b) tetraethylammonium (c) tetramethylphosphonium (d) n-butylpyridinium

[bmim][dca] that is based on the dicyanamide anion dissolves large amount (around 200 g/L) of carbohydrates such as glucose and sucrose [56]. Despite their widespread use, ILs with PF_6^- and BF_4^- anion have been reported to sometimes decompose when heated in the presence of water, giving hydrogen fluoride (HF). This drawback has forced the introduction of alternate ions, many of which are still fluorous materials, but are bonded to carbon through the C-F bond that is inert to hydrolysis. These includes trifluoroacetate, $CF_3SO_3^-$, $(CF_3SO_3)_2N^-$ and methide.

Safety and cost concerns have lead to the introduction of new ILs with non-fluorous an-

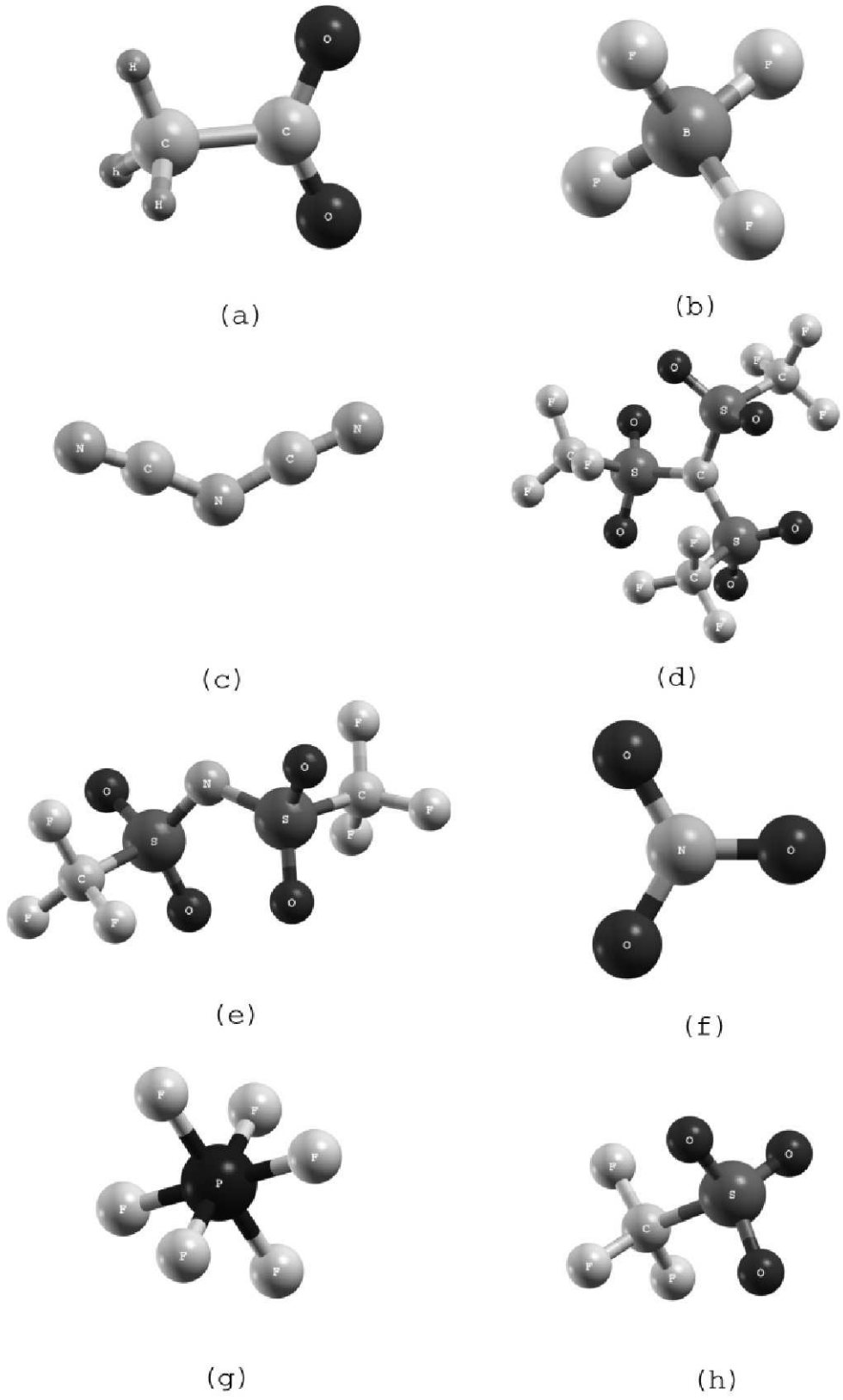

Figure 1.3: Some of the examples for anions of the RTILs (a) acetate (b) tetrafluoroborate (c) dicyanamide (d) methide (e) bis-trifluoromethylsulphonylimide (f) nitrate (g) hexafluorophosphate (h) trifluoromethylsulphate

ions, among which the salts derived from inexpensive bulk chemicals are most interesting. Alkylsulfate ions are a group of such anions that are likely to be reasonably non-toxic and biodegradable. A few other examples examples are n-octyl sulfate, dioctylsulfosuccinate etc.

1.2.4 Preparation

Ionic liquids can be prepared even in large quantities without any significant difficulties. Sufficiently pure ILs can be stored without decomposition for extended periods, although some are relatively hygroscopic.

There are two basic methods for the preparation of ionic liquids:

- Metathesis of a halide salt with, for instance, a silver, group 1 metal or ammonium salt of the desired anion
- Acid-base neutralization reactions
- The final method for the synthesis of ionic liquids is direct combination of a halide salt with a metal halide.

The first of the new ionic liquids, [emim][BF_4] was prepared in 1992, via metathesis of [emim] with Ag[BF_4] in methanol. This salt which melts at 12 °C may be prepared considerably more economically using [NH_4][BF_4] in acetone. The ease of preparation, combined with its immiscibility with a number of organic solvents and its relative moisture stability is leading to its increasing use in biphasic catalysis. Contamination such as small amount of halide ions will remain in the ionic liquids prepared using metathesis reaction. These halide ions may react with solute materials. Neutralization of aqueous solutions of amine with nitric acid is a popular method to prepare monoalkylammonium nitrate salts. The excess water is removed in the vacuum to isolate the ionic liquids. The purity of the ionic liquids can be ensured by dissolving them in either acetonitrile or tetrahydrofuran,

treating with activated charcoal for atleast 24 hours and finally removing the organic solvent in vacuo.

Although most of the RTILs used at present are non-toxic and non-flammable, it is not a universal fact. Some of them may be toxic or flammable. But the possibility of designing allows the preparation of ILs with desirable properties.

1.2.5 Applications of RTILs

Solvents: RTILs are main candidates for the replacement of volatile organic compounds used in the synthetic applications [2, 30, 31]. Diels-Alder reactions have been carried out in ionic liquids, that makes way for the replacement of lithium perchlorate-diethylether mixtures [57]. Alkylation of sodium β-napthoxide [58] using ionic liquids has been demonstrated. ILs are also used as solvents in hydrogenation reactions, hydroformylation, dimerization of butadiene, Heck reactions [30], Friedel-Crafts acylation [59] etc. Chloroaluminate ionic liquids are reported to be used to carry out electrophilic substitution reactions [60]. They have also been used in olefin dimerization, olefin polymerization and olefin hydrogenation.

Homogeneous and heterogeneous catalyst: Ionic liquids offer the advantage of both homogeneous and heterogeneous catalysts for some reactions. Selected ionic liquids can be immiscible with the reactants and products but can dissolve the catalysts. Chloroaluminate ILs are strong Lewis, Franklin and Bronsted acids. These liquids can be easily handled and can be non-volatile potential replacements for hazardous acids such as HF used in several acid-catalyzed reactions [61].

Biological reaction media: Enzymes being stable in ionic liquids open up the possibility for ILs to be used in biological reactions, such as the synthesis of pharmaceuticals. Most of the enzymes are catalytically active in ionic liquids or aqueous biphasic IL systems [62]. The selectivity and stability in these liquids is better than that in traditional media. Exploiting the unconventional solvent properties of ILs, biocatalyst recycling and product

recovery has been achieved that are not feasible with traditional solvents [62].

Electrochemical applications: Several ionic liquids have interesting electrochemical properties, making them useful for many electrochemical applications [63]. ILs can be used in the manufacturing of batteries, solar panel, polymer electrolytes, fuel cells etc. They also find applications in electro-optics.

Apart from these, RTILs have many diverse applications. One dimensional ion transport has been demonstrated in self-organized columnar ILs [64] that can be used in the transportation of ion, energy and information at nanometer level. These liquids offer thermodynamic stabilization for proteins [65]. They are used as plasticizers for poly(methylmethacrylate) [66]. ILs can also be used as liquid thermal storage media and heat transfer fluids in a solar thermal power plant [67]. Since the ionizing radiation does not affect ILs, they could be used to treat high level nuclear waste. ILs can selectively dissolve and remove gases, and thus finds application in the air purification on submarines and spaceships. They can also be used for refractive index matching, as lubricants, in dry cleaning, metal extraction, personal care, embalming, household products, coatings, in drug delivery, biomass processing and as biocides.

1.2.6 Liquid-crystalline properties

ILs containing long chain alkyl substituents have attracted some interest due to their liquid crystalline (LC) properties. Liquid crystalline property arise due to the formation of domains, "Coulombic" layers where the ionic head-groups interact with the counter-ions, and "van der Waals" layers built from (anti)parallel stacking of the alkyl chains. Hexafluorophosphate salts with cations up to C_{20}MIM have been investigated by differential thermal analysis (DTA) and show one or more LC transitions. Along with these several techniques such as differential scanning calorimetry, conductivity measurements, raman spectroscopy, small and wide-angle X-ray diffraction studies (S-WAXS), quasi-electron neutron scattering and single crystal X-ray diffraction have been applied to study the

phase behavior of low melting point liquid crystalline salts with hexafluorophosphate anion [68]. The low temperature phase transition found in the study is assigned to a crystal-crystal transition. In both the crystalline and the higher temperature mesophase, the structure remains as a monodispersed layer with interdigitated alkyl chains. This is a smectic-A confirmed by S-WAXS and Raman spectroscopy. Based on a detailed analysis, the complete conformational melting of alkyl chains has been reported [68].

1.3 Binary mixtures of room temperature ionic liquids

Along with pure RTILs, mixtures of RTIL with other compounds are also gaining attention. Several compounds are used with RTILs as binary mixtures for various applications. The recovery or extraction of the products of a chemical reaction that is conducted in an ionic liquid *via* distillation is difficult due to the low volatility of the solvent [69]. The possibility of redressing this limitation by using $scCO_2$ has attracted much recent attention [1, 51]. Furthermore, the interaction between the solute and the solvent in the mixture can impart new properties that the individual components may not possess. The current focus of research on these mixtures is on the need to understand the molecular level interactions between the RTIL and CO_2 [70–73].

The remarkable solubility of CO_2 in imidazolium based ILs [1,74], while the IL itself has immeasurably low solubility in CO_2 [1], opens up the possibility of extracting products of an organic reaction or contaminants from ionic liquids, using CO_2. Brennecke and coworkers [75] have demonstrated the separation of organic compounds and water from ILs using CO_2.

It has been observed that the viscosity of the ionic liquid decreases significantly with the addition of CO_2 or SO_2. Since ionic liquids usually have very high viscosity, the addition of these gases can increase the area of applications in which these mixtures can

be used. Along with these, some binary mixtures have been demonstrated to be having potential applications as electrolytes. Most important among them is the [emim][F].2.3HF mixture [63], where HF gas is saturated in the [emim][F] liquid. This mixture has very low viscosity, high electrical conductivity and a wide electrochemical window of over 3.0 V, that makes it suitable for various electrochemical applications.

The resulting binary mixture of RTIL may possess interesting properties that the pure RTIL may not be possessing, making it suitable to use it in altogether different application. The range of applications spanned by the RTILs can be expanded significantly using the binary mixtures.

1.4 Previous work

RTILs have been extensively studied using experimental [76–78] and theoretical methods [79–81]. The first RTIL $[EtNH_3][NO_3]$, that has a melting point of 12 °C was prepared as early as 1914 [35]. RTILs did not receive any attention for several decades, after this early work. An excellent review on the use of RTILs for synthesis and catalysis is published by Welton [30].

Characterization of ionic liquids has been carried out by several groups. Koel [82] has studied several imidazolium based ionic liquids using thermogravimetry, IR and UV-VIS spectroscopic methods [82] and has also determined the solubility of ionic liquids in several organic solvents. Huddleston *et al* [38] have carried out extensive studies on the characterization of hydrophilic and hydrophobic ionic liquids based on imidazolium cation. Their studies included the variation of the alkyl chain length and the anion to determine the effects on the water content, density, viscosity, surface tension, melting point and thermal stability. Similar studies have been carried out by Tokuda *et al* [83] and Jacquemin *et al* [84]. These studies characterize the effect of temperature on the transport properties of the ILs.

Numerous experimental studies have been reported on RTIL interfaces with gases

and liquids. Law *et al* [85–88] have used the direct recoil spectroscopy (DRS) to study the interfaces of *n*-alkylimidazolium ILs. They have also measured the surface tension of these liquids. Sum frequency vibrational spectroscopic studies [89, 90] have supplemented the DRS studies in determining the structure of the RTILs at the air-IL interface. Neutron reflectometry has indicated the surface ordering in the case of amphiphilic ionic liquids [91]. X-ray reflectivity studies have found an increase in the electron density at the surface [92]. Several computational studies have been reported on the interfaces of RTILs with the air and water. Lynden-Bell *et al* have studied the interfaces between RTILs and other liquids [93] as well as the RTIL-vapor interface [94, 95] using molecular dynamics (MD) simulations. Studies on aqueous interfaces with hydrophobic RTILs studied using MD have also been reported [96, 97].

Solvation dynamics in room temperature ionic liquids has been extensively studied using several experimental techniques by different groups such as Bart *et al* [98, 99], Karmakar *et al* [100,101], Maroncelli and coworkers [102–104] and others [105–108]. Solvation dynamics studies in ILs using computational methods have also been reported [109, 110].

The earliest computational study of an RTIL was the work of Lynden-Bell and coworkers on 1,3-dimethylimidazolium chloride [111]. This work was followed by several other studies using molecular dynamics method on various compounds based on the imidazolium cation [112–121]. Several force fields have been developed in an effort to provide better models for the simulations [111, 114, 122–126]. While most of these studies were aimed at obtaining the structure of the liquid, the efforts have also been made to determine the magnitude and directionality of interaction [127], spatial heterogeneity [128], single particle dynamics [129] etc. The simulations of these liquids has been reviewed by Hunt [130]. Computational studies have been applied for the investigation of interaction between the water and ILs [131], to determine the static dielectric properties [132], and to evaluate transport properties [133].

The crystal structure of a number of ILs has been determined [48, 134–139]. Crystal

polymorphism has been observed in several imidazolium based compounds. Neutron diffraction experiments have been carried out to study the liquid structure of ILs [140–143]. Inelastic neutron scattering studies have also been used to characterize the relaxation process of ILs [144].

Ionic liquids when used with other solvents like CO_2 are found to be useful for several applications. Use of CO_2 for the extraction of ILs back from the reaction mixture has been proposed. Brennecke and coworkers have studied the phase behavior and thermodynamic properties of different gases in ILs [74, 145] and CO_2 in particular [146]. Phase behavior of ILs with alcohols [147] has been reported. Attempts have been made to understand the interactions at the molecular level using ATR-IR spectroscopy [70] and X-ray diffraction [71]. Computational methods have also been applied to study the molecular level interactions in the binary systems containing CO_2 [72, 73, 148, 149].

1.5 Role of computer simulations

Computer simulations play a very important role in science today. They aid in the testing of theoretical models, and to understand and interpret experiments at the microscopic level.

Computer simulations also allow one to perform thought experiments - things that are just impossible to do in reality, but whose outcome greatly increases our understanding of phenomena - to be realized.

1.6 Molecular Dynamics

Molecular dynamics (MD) [150–152] is the study of molecules in motion. It has been widely applied in many branches of physics, chemistry, chemical engineering and biology [153] Studies of liquid systems, amorphous glass, crystals, biomolecular solutions, interfaces and various other systems have been carried out using MD. Classical molecular

dynamics assumes an empirical potential for the particle - particle interaction. The system of interest is modeled as N classical particles that interact via a predefined potential. Newton's equations of motion dictates the time evolution of this classical many body system.

1.6.1 Equations of motion

At any given time t for a system of N particles, the coordinates of the system denoted by $\mathbf{q}(\mathrm{t}) \equiv \mathbf{q}_1(t)$,$\mathbf{q}_2(t)$,...,$\mathbf{q}_N(t)$ and momenta denoted by $\mathbf{p}(\mathrm{t}) \equiv \mathbf{p}_1(t)$,$\mathbf{p}_2(t)$,...,$\mathbf{p}_N(t)$ defines the physical state of the system. The time evolution of coordinates and momenta is given by the Hamilton's equations of motion,

$$\dot{\mathbf{q}}_\mathbf{i} = \frac{\partial H}{\partial \mathbf{p}_\mathbf{i}} \tag{1.1}$$

$$\dot{\mathbf{p}}_\mathbf{i} = -\frac{\partial H}{\partial \mathbf{q}_\mathbf{i}} \tag{1.2}$$

where H($\mathbf{p}$,$\mathbf{q}$), the Hamiltonian of the system is a function of both coordinates and momenta. Assuming that the system is represented in Cartesian coordinates, if the potential of interaction is U($\mathbf{r}_1$,$\mathbf{r}_2$,...,$\mathbf{r}_N$). then the Hamiltonian is given by,

$$H(\mathbf{p},\mathbf{r}) = \sum_{i=1}^{N} \frac{{\mathbf{p}_\mathbf{i}}^2}{2m_i} + U(\mathbf{r_1}, \mathbf{r_2}, ..., \mathbf{r_N}) \tag{1.3}$$

The Hamilton's equations then becomes,

$$\begin{aligned} \dot{\mathbf{r}}_\mathbf{i} &= \frac{\partial H}{\partial \mathbf{p}_\mathbf{i}} = \frac{\mathbf{p}_\mathbf{i}}{m_i} \\ \dot{\mathbf{p}}_\mathbf{i} &= -\frac{\partial H}{\partial \mathbf{r}_\mathbf{i}} = \mathbf{F}_i \end{aligned}$$

where $\mathbf{F}_i$ denotes the force acting on the i^{th} atom and m_i is its mass. Combining the

above two equations we get

$$m_i \ddot{\mathbf{r}}_i = \mathbf{F}_i(\mathbf{r}) \tag{1.4}$$

where $\mathbf{F}_i(\mathbf{r})$ is the force felt by the ith particle due to all other particles of the system. Thus the Hamilton's equations of motion leads to Newton's equations of motion. The coupled Hamilton's equations of motion give the time evolution of the system when integrated with the set of initial conditions. A system with N particles, in three dimensions will have 6N degrees of freedom, i.e., 3N coordinates and 3N momenta. If all these elements are collected into a single vector $\mathbf{\Gamma}$(t)=($\mathbf{r}_1(t)$,$\mathbf{r}_2(t)$,...$\mathbf{r}_N(t)$,$\mathbf{p}_1(t)$,$\mathbf{p}_2(t)$,...$\mathbf{p}_N(t)$), a 6N dimensional vector, in 3 dimensions, results. This vector exists in the abstract 6N dimensional space called *phase space*. The evolution of $\mathbf{\Gamma}$(t) in time is governed by the Hamilton's equation.

The thermodynamic variables that describe a system are the total number of particles (N), the volume (V), pressure (P), energy (E), temperature (T) and chemical potential (μ). The different ensembles can be characterized by keeping some of these thermodynamic variables as constant.

1.6.2 Microcanonical Ensemble

The fixed values of thermodynamic variables, N, V and E characterize the microcanonical ensemble [151, 152, 154]. The equilibrium phase space distribution function corresponding to this ensemble is given as,

$$f(\mathbf{\Gamma}) = \frac{1}{N! h^{3N} \Omega(N, V, E)} \delta(H(\mathbf{\Gamma}) - E) \tag{1.5}$$

where h is a constant with the unit of action (energy $\times$ time), $\Omega(N, V, E)$ is the microcanonical partition function given by,

$$\Omega(N, V, E) = \frac{1}{N! h^{3N}} \int \delta(H(\mathbf{\Gamma}) - E) \, d\mathbf{\Gamma} \tag{1.6}$$

From the above equation, it can be seen that the microcanonical ensemble is the collection of those points in phase space belonging to the constant energy surface defined by the condition $H(\mathbf{\Gamma}) = E$. Microcanonical distribution can be generated in two ways. One is by the collection of large number of systems with initial conditions chosen from constant energy surface and the other is through the evolution of a dynamical system according to Hamilton's equations of motion. For an ergodic system, the microcanonical ensemble average of a physical observable A(Γ) can be written as,

$$\langle A \rangle = \frac{\int d\mathbf{\Gamma} A(\mathbf{\Gamma}) \delta(H(\mathbf{\Gamma}) - E)}{\int d\Gamma \delta(H(\mathbf{\Gamma}) - E)} \tag{1.7}$$

The time average from a single dynamical system, of the same physical observable is related to the ensemble average.

$$\overline{A} = \lim_{T \to \infty} \frac{1}{T} \int_0^T dt A(\mathbf{\Gamma}(t)) \to \langle A \rangle \tag{1.8}$$

The properties are averaged over ensemble in statistical mechanics, whereas in molecular dynamics, they are averaged over time. According to ergodic hypothesis, the ensemble average and time average are equivalent, provided the system is evolved for sufficiently long time such that it visits all the accessible points of the phase space. The possibility of generation of an equilibrium ensemble from a dynamical trajectory has several uses, including the calculation of structural properties, dynamical properties such as vibrational spectra, transport properties and also microscopic detailed motion of individual atoms. These features are general to any ensemble and not just restricted for the microcanonical ensemble. Experiments are usually performed at constant temperature or constant pressure conditions, that the MD in the microcanonical ensemble does not mimic. This demands the equations of motion that can generate the canonical ensemble, i.e., constant N, V, T ensemble or the isothermal-isobaric ensemble, i.e., constant N, P, T ensemble. Since the system in these cases cannot be assumed to be in isolation, there is a need to

include the presence of some external influence into the set of equations, that can thus be formulated in terms of non-Hamiltonian equations of motion. The external influence is accounted by coupling the system with a heat bath (thermostat) or a mechanical piston (barostat), thus extending the phase space variables with the additional dynamical variables for the description of time evolution of thermostat and/or barostat. The following sections provide brief overview of the canonical ensemble and the isobaric-isothermal ensemble MD.

1.6.3 Canonical Ensemble Molecular Dynamics: Nosé-Hoover Chains

Extended variable MD was first proposed by Andersen to perform constant temperature and/or constant pressure MD simulations [155]. The particles were allowed to change their velocities by stochastic collisions, whose new velocities were determined from the distribution chosen to reproduce canonical ensemble. Since this method results in discontinuous phase space trajectory, equations of motion obtained from an extended Hamiltonian were proposed by Nosé [156,157], that were constructed to generate deterministic and time-reversible phase space trajectories. These equations were later modified by Hoover, through a variable transformation resulting in Nosé-Hoover equations [158]. The realization that the Nosé-Hoover dynamics is not ergodic for small and stiff systems, lead to the proposal of Nosé-Hoover chains for the generation of canonical ensemble by Martyna *et al* [159–161]. Instead of single thermostat, the Nosé-Hoover chain (NHC) dynamics method consists of M coupled thermostats. The heat source/sink attached to the system is described by the thermostat variables η_1, η_2,..., η_M and their conjugate momenta p_{η_1},

p_{η_2},..., p_{η_M}. The equations of motion for the system with the thermostat chains are:

$$\begin{aligned}
\dot{\mathbf{r}}_i &= \frac{\mathbf{p}_i}{m_i} \\
\dot{\mathbf{p}}_i &= -\frac{\partial U}{\partial \mathbf{r}_i} - \frac{p_{\eta_1}}{Q_1}\mathbf{p}_i \\
\dot{\eta}_i &= \frac{p_{\eta_i}}{Q_i} \\
\dot{p}_{\eta_1} &= \sum_{i=1}^{N} \frac{\mathbf{p}_i}{m_i} \cdot \mathbf{p}_i - N_f k_B T - \frac{p_{\eta_2}}{Q_2} p_{\eta_1} \\
\dot{p}_{\eta_i} &= \frac{p_{\eta_{i-1}}^2}{Q_{i-1}} - k_B T - \frac{p_{\eta_{i+1}}}{Q_{i+1}} p_{\eta_i} \qquad i = 2, ..., M-1 \\
\dot{p}_{\eta_M} &= \frac{p_{\eta_{M-1}}^2}{Q_{M-1}} - k_B T
\end{aligned} \tag{1.9}$$

where $-\frac{\partial U(\mathbf{r}_i)}{\partial \mathbf{r}_i}$ represents the force on particle i due to all the other particles in the system and N_f is the number of degrees of freedom. These equations (1.10), known as the Nosé-Hoover chain (NHC) or Martyna-Tuckerman-Klein (MTK) equations, have the conserved energy:

$$H' = \sum_{i=1}^{N} \frac{\mathbf{p}_i^2}{2m_i} + U(\mathbf{r}) + \sum_{i=1}^{M} \frac{p_{\eta_i}^2}{2Q_i} + N_f k_B T \eta_1 + \sum_{i=2}^{M} k_B T \eta_i \tag{1.10}$$

1.6.4 Isothermal-Isobaric Molecular Dynamics

The isothermal-isobaric ensemble MD, requires the variation of the volume of the simulation cell to keep the average internal pressure equal to the external set pressure. The volume of the cell can change either isotropically without changing its shape [155] or anisotropically with change of shape [162–164].

The partition function for the NPT ensemble is

$$\Delta(N, P, T) = \int_0^\infty dV e^{-\beta PV} Q(N, V, T) \tag{1.11}$$

where P is the applied pressure. Following the seminal works of Andersen [155] and that of Parrinello and Rahman [162], Martyna *et al* [165] proposed the following equations of

motion for the generation of the distribution corresponding to the above equation.

$$\begin{aligned}
\dot{\mathbf{r}}_i &= \frac{\mathbf{p}_i}{m_i} + \frac{p_\epsilon}{W}\mathbf{r}_i \\
\dot{\mathbf{p}}_i &= \mathbf{F}_i - \left(1 + \frac{d}{N_f}\right)\frac{p_\epsilon}{W}\mathbf{p}_i - \frac{p_\eta}{Q}\mathbf{p}_i \\
\dot{V} &= \frac{dVp_\epsilon}{W} \\
\dot{p_\epsilon} &= dV(P_{int} - P) + \frac{d}{N_f}\sum_{i=1}^{N}\frac{\mathbf{p}_i^2}{m_i} - \frac{p_\eta}{Q}p_\epsilon \\
\dot{\eta} &= \frac{p_\eta}{Q} \\
\dot{p_\eta} &= \sum_{i=1}^{N}\frac{\mathbf{p}_i^2}{m_i} + \frac{p_\epsilon^2}{W} - (N_f+1)k_BT
\end{aligned} \tag{1.12}$$

where $\epsilon = \ln V$, p_ϵ is a momentum corresponding to ϵ, and P_{int} is the internal pressure given by

$$P_{int} = \frac{1}{dV}\left[\sum_{i=1}^{N}\left(\frac{\mathbf{p}_i^2}{m_i} + \mathbf{r}_i\mathbf{F}_i\right) - dV\frac{\partial U}{\partial V}\right] \tag{1.13}$$

The conserved energy is given by

$$H' = H(\mathbf{p}, \mathbf{r}, V) + \frac{p_\epsilon^2}{2W} + \frac{p_\eta^2}{2Q} + (N_f+1)k_BT\eta + PV \tag{1.14}$$

1.6.5 Interaction potential

The quality of the model used for the molecular structure and the potential of interaction determines the success of atomistic simulations. The interaction energies between the bonded atom and the non-bonded atom add up to give the total potential energy of the system of which the bonded interaction energy can be written as the sum of two, three and four body interactions. The interaction between the atoms connected by a bond is a two body interaction, the bending energy is due to three body interaction and the torsional energies are four body interactions. In our models, the bond between two atoms is treated as classical harmonic oscillator with a force constant K_b and equilibrium bond

length r_0. Similarly, the angle between bonds meeting at a given point is also allowed to vary harmonically around its equilibrium value with K_θ and θ_0 being the spring constant and the equilibrium bend angle respectively. A cosine power series of the dihedral angle is used to represent the torsional energy. The non-bonded interactions are modeled with the long range electrostatic forces that are handled through ewald summation and the van der Waals (dispersive) forces that are modeled as Lennard-Jones potential. In general, the total potential energy can be written as

$$\begin{aligned} U\left(\{\mathbf{r}\}\right) &= \frac{1}{2}\sum_{ij}^{bonds} K_r^{ij}\left(\mathbf{r}_{ij}-\mathbf{r}_{ij}^0\right)^2 + \frac{1}{2}\sum_{ijk}^{angles} K_\theta^{ijk}\left(\theta_{ijk}-\theta_{ijk}^0\right)^2 \\ &+ \sum_{ijkl}^{dihedrals}\sum_{n=0}^{6} a_n^{ijkl} cos^n\phi_{ijkl} + \frac{1}{4\pi\epsilon_0}\sum_{i}^{N}\sum_{j>i}^{N}\frac{q_i q_j}{r_{ij}} \\ &+ \sum_{i}^{N}\sum_{j>i}^{N} 4\epsilon_{ij}\left[\left(\frac{\sigma_{ij}}{r_{ij}}\right)^{12} - \left(\frac{\sigma_{ij}}{r_{ij}}\right)^{6}\right] \end{aligned} \tag{1.15}$$

where i, j, k, and l denote atom indices, q_i and q_j are the partial charges of i^{th} and j^{th} atom respectively, ϵ_0 is the permittivity of free space, K_r^{ij} and K_θ^{ijk} are the stretching and bending force constants respectively, ϕ_{ijkl} is the dihedral angle, and r_{ij} is the inter-atomic distance between atoms i and j. The non-bonded interaction comes into picture only for those atoms separated by more than three bond. Experimental studies and *ab initio* quantum chemical calculations are used to arrive at the potential parameters involved in Eq.1.15. For instance, the force constants can be obtained from spectroscopic studies, whereas X-ray diffraction studies provide the equilibrium bond lengths and angles. Vibrational spectroscopic techniques such as infra-red and Raman scattering, that are sensitive to conformational changes are of immense use in determining the torsional parameters. By obtaining the population ratio of different conformers one can calculate the energy difference that separates different conformational states.

1.6.6 Time correlation functions and transport coefficients

The MD simulations provides us with a trajectory (positions and velocities of all the atoms as a function of time) in phase space for the system with given initial configuration. This trajectory can be used to study the vibrational and transport properties of the system. Time correlation functions provide microscopic insight into the dynamics of the system. Experimentally measurable transport coefficients such as diffusion constant, viscosity, thermal conductivity, that are accessible from non-equilibrium MD, can also be calculated from equilibrium simulations [166,167]. This can be achieved using linear response theory that relates these transport coefficients to the time integral of the TCF of some dynamical variable.

The time correlation function of functions A and B is defined as

$$C_{AB}(t) = \langle A_0 B_t \rangle \tag{1.16}$$

where C_{AB} is the correlation coefficient. For identical phase functions, C_{AA}(t) is called an autocorrelation function and its time integral (from t=0 to t=∞) is a correlation time t_A. These functions are of great interest in computer simulation because they give a clear picture of the dynamics in a fluid, their time integrals t_A may often be related directly to macroscopic transport coefficients and their Fourier transforms $\widehat{C}_{AA}(\omega)$ may often be related to experimental spectra.

Transport coefficients are defined in terms of the response of a system to a perturbation. For example, the diffusion coefficient relates the particle flux to a concentration gradient, while the shear viscosity is a measure of the shear stress induced by an applied velocity gradient. Such perturbations can be introduced into the Hamiltonian and the distribution function may be calculated. The transport coefficient is obtained by the

integration of the auto time correlation function and is given by

$$\gamma = \int_0^\infty dt \langle \dot{A}(t)\dot{A}(0)\rangle \tag{1.17}$$

where γ is the transport coefficient and A is a variable appearing in the perturbation term in the Hamiltonian. Associated with the relations of this kind, one can also write an 'Einstein relation',

$$2t\gamma = \langle (A(t) - A(0))^2 \rangle \tag{1.18}$$

that is true at large t (compared with the correlation time of A).

Onsager's regression hypothesis which states that *the regression of microscopic thermal fluctuations at equilibrium follows the macroscopic law of relaxation of small non-equilibrium disturbances* [168] allows us to calculate the transport coefficients from equilibrium MD using time correlation functions.

The transport coefficients in computer simulations can be calculated from equilibrium correlation functions or by conducting suitable non-equilibrium simulations from first principles.

The diffusion coefficient D, which is an important property characterizing a liquid [169] is given (in three dimensions) by

$$D = \frac{1}{3}\int_0^\infty dt \langle \vec{v}_i(t) \cdot \vec{v}_i(0)\rangle \tag{1.19}$$

where $\vec{v}_i(t)$ is the centare-of-mass velocity of a single molecule. The corresponding Einstein relation that is valid at long times, is

$$2tD = \frac{1}{3}\langle |\vec{r}_i(t) - \vec{r}_i(0)|^2 \rangle \tag{1.20}$$

where $\vec{r}_i(t)$ is the molecule position. In the simulations, these averages would be computed for each of the particle and the results would be added together and divided by N to

improve the statistical accuracy.

The vibrational density of states (VDOS) can also be obtained by Fourier transforming the normalized velocity autocorrelation function. The power spectrum C(ω) is defined as

$$C(\omega) = \int_{-\infty}^{\infty} C(t) e^{-i\omega t} dt. \tag{1.21}$$

where C(t) is given by

$$C(t) = \frac{\langle \mathbf{v}(t) \cdot \mathbf{v}(0) \rangle}{\langle \mathbf{v}(0) \cdot \mathbf{v}(0) \rangle} \tag{1.22}$$

The shear viscosity η is given by

$$\eta = \frac{V}{k_B T} \int_0^{\infty} dt \langle P_{\alpha\beta}(t) P_{\alpha\beta}(0) \rangle \tag{1.23}$$

or

$$2t\eta = \frac{V}{k_B T} \langle (\zeta_{\alpha\beta}(t) - \zeta_{\alpha\beta}(0))^2 \rangle \tag{1.24}$$

In this case,

$$P_{\alpha\beta} = \frac{1}{V} \left(\sum_i p_{i\alpha} p_{i\beta} / m_i + \sum_i r_{i\alpha} f_{i\beta} \right) \tag{1.25}$$

is an off-diagonal ($\alpha \neq \beta$) element of the pressure tensor and

$$\zeta_{\alpha\beta} = \frac{1}{V} \sum_i r_{i\alpha} p_{i\beta} \tag{1.26}$$

1.7 Brief overview of Car Parrinello Molecular Dynamics

The main task in classical molecular dynamics simulations is the approximation of the interatomic interactions through classical means. These potentials are determined in advance. The full interaction, typically, is broken into two-body, three-body and many

body contributions, long-range and short-range terms that have to be represented by suitable functional forms. The elaborate interaction models and their representation in analytical form have been arrived at after decades of systematic research. Although very successful in studying the properties of a wide range of condensed phase systems [151, 152, 170–175], this approach fails significantly in the systems where many different atom or molecule types give rise to a myriad of different interatomic interactions that have to be parameterized and when the electron structure and thus the bonding pattern changes qualitatively in the course of the simulation.

Ab initio molecular dynamics successfully combines traditional molecular dynamics and the electronic structure methods. Several other names as Car-Parrinello [176], Hellmann-Feynman, first principles, quantum chemical, on-the-fly, potential-free etc. molecular dynamics are also in use currently. The basic idea underlying every *ab initio* molecular dynamics method is to compute the forces acting on the nuclei from electronic structure calculations that are performed "on-the-fly" as the molecular dynamics trajectory is generated.

Excellent reviews about this technique are available [177–191]. These *ab initio* calculations involves the quantum part that deals with electronic degrees of freedom and the classical dynamics of ions. *Ab initio* molecular dynamics method relies on the Born-Oppenheimer approximation that separates the electronic and ionic degrees of freedom based on the difference in the masses between the electron and the ions. In CPMD, the ground state electronic wavefunctions are evolved in time using Newton's equation of motion. CPMD simulations are based on the Hohenberg-Kohn-Sham density functional theory [192–194] (DFT) for electronic structure within a plane wave pseudopotential [195–203] implementation. *Ab initio* calculations can be used in the investigation of "chemically complex" systems, where the electronic structure can change in the course of simulation.

1.7.1 Representation of electronic orbitals

According to Blöch's theorem, each electronic wave function can be written as a sum of plane waves

$$\psi_i(\vec{r}) = \sum_k C_k^i e^{\vec{k}\cdot\vec{r}} \tag{1.27}$$

where, C_k^i's are the coefficients of expansion. Thus the electronic configuration is completely specified by a complete set of coefficients, $(c_{k1}^1, ..., c_{kmax}^1, ..., c_{k1}^n, ..., c_{kmax}^n)$, denoted by C. Then the minimization becomes the search in the space of all possible C for C_{opt}, such that $E(C_{opt})$, the electronic energy, is minimum energy for all C on the orthonormality constraint hypersurface, where the constraint hyperspace is the collection of all points in the hypersurface such that the orbitals are orthonormal. For the derivation of the equations of motion that result from the potential and constraint hypersurfaces, we define the coefficient velocities

$$\dot{c}_k^i = \frac{dc_k^i}{dt}, \tag{1.28}$$

where t is not real time but rather a construct to parameterize movement through coefficient hyperspace. The classical Lagrangian can then be defined as

$$L = T - V \tag{1.29}$$

with

$$T = \frac{1}{2}\mu \sum_i \sum_k (\dot{c}_k^i)^2 \tag{1.30}$$

and

$$V = E\{c_k^i\} \tag{1.31}$$

where T is the fictitious kinetic energy and μ is an arbitrary inertia or 'mass' that controls the speed and character of the motion through coefficient space. The Lagrange's equations

for this fictitious dynamics can be written as,

$$\frac{d}{dt}\frac{\partial L}{\partial \dot{c}_k^i} - \frac{\partial L}{\partial c_k^i} = 0 \tag{1.32}$$

The wave functions should also satisfy the orthonormality constraint equations,

$$\sigma_{ij} = \Omega^{-1} \int_{\mathrm{v}} d\vec{r}\psi_i^*(\vec{r})\psi_j(\vec{r}) - \delta_{ij} \tag{1.33}$$

Combining the above two equations we get

$$\mu \ddot{c}_k^i = -\frac{\partial E}{\partial c_k^i} - \sum_j \lambda_{ij}\frac{\partial \sigma_{ij}}{\partial c_k^i} \tag{1.34}$$

where λ_{ij} is Lagrange multiplier. The first term on the right hand side of the above equation tries to minimize the energy of the wavefunction, whereas the second term is the force due to the constraints.

1.7.2 Hohenberg-Kohn's theorem and Kohn-Sham formulation of DFT

According to Hohenberg and Kohn [192], "the total energy including exchange and correlation, of an electron gas is a unique functional of the electron density" and also "the minimum value of total energy functional is the ground state energy of the system, and the density that yields this minimum value is the exact single particle ground state density. Kohn and Sham then showed that it is possible to map a many body problem by an exactly equivalent set of self consistent one electron equations.

The Kohn-Sham total energy functional for a set of doubly occupied electronic states

ψ_i can be written as

$$\begin{aligned} E_{KS}[\{\psi_i(\overrightarrow{r})\}] &= \sum_i f_i \int \psi_i^*(\overrightarrow{r}) \left(\frac{-\hbar^2}{2m}\right) \nabla^2 \psi_i(\overrightarrow{r}) \mathbf{d^3 r} \\ &+ \frac{e^2}{2} \int\int \frac{\rho(\overrightarrow{r_1})\rho(\overrightarrow{r_2})}{|\overrightarrow{r_1} - \overrightarrow{r_2}|} \mathbf{d^3 r_1 d^3 r_2} + \int \varepsilon_{XC}\{\rho(\overrightarrow{r})\}\rho(\overrightarrow{r}) \mathbf{dr} \\ &+ E_{eI}([\psi_i(\overrightarrow{r})], \{\overrightarrow{R_I}\}) + U_I^O(\{\overrightarrow{R_I}\}) \end{aligned} \tag{1.35}$$

where, on the right hand side, the first term is the electronic kinetic energy, the second term represents electron-electron Coulomb energy, electron exchange correlation energy is represented by the third term, the fourth term is electron-ion interaction energy and the last term represents ion-ion interaction. Here $\rho(\vec{r})$ is the electron density given by

$$\rho(\vec{r}) = 2 \sum_i |\psi_i(\vec{r})|^2 \tag{1.36}$$

By minimizing E_{KS} with respect to single particle wavefunction, the ionic potential energy for the electrons in the ground state can be obtained.

1.7.3 Car-Parrinello equations of motion

Different *ab initio* methods differ in the way of evolving the system. In Born-Oppenheimer molecular dynamics (BOMD), E_{KS} is minimized at each step and the ions are evolved according to the Newton's equation of motion. The electronic orbitals remains at the ground state throughout the course of simulations. However in the Car-Parrinello method, the Kohn-Sham energy is minimized only at the beginning of the simulation and the electronic orbitals are evolved in time according to classical equations of motion. The

Car-Parrinello Lagrangian is given by

$$\begin{aligned} L_{CP} &= \mu \sum_i \int |\dot{\psi}_i(\overrightarrow{r})|^2 \mathbf{d^3 r} + \frac{1}{2} \sum_I M_I \dot{\overrightarrow{R_I}}^2 - E_{ks}[\{\psi_i\}, \overrightarrow{R_I}] \\ &\quad + \sum_{i,j} \Lambda_{ij} \left(\int \psi_i^*(\overrightarrow{r}) \psi_j(\overrightarrow{r}) \mathbf{dr} - \delta_{ij} \right) \end{aligned} \tag{1.37}$$

The first and second terms in the above equation are kinetic energy of electrons and ions respectively, third term is the Kohn-Sham energy functional and the last term ensures orthonormality of the wave functions. The fictitious electron mass μ has the units of energy$\times$time^2. The resulting equations of motion for electronic and ionic parts with holonomic constraints are,

$$\frac{d}{dt} \frac{\partial L_{CP}}{\partial \dot{\mathbf{R}}_\mathbf{I}} = \frac{\partial L_{CP}}{\partial \mathbf{R_I}} \tag{1.38}$$

$$\frac{d}{dt} \frac{\delta L_{CP}}{\delta \dot{\psi}^*} = \frac{\delta L_{CP}}{\delta \psi^*} \tag{1.39}$$

In CP dynamics, the time evolution of ions and electrons are given by

$$M_I \ddot{\mathbf{R}}_\mathbf{I}(t) = -\frac{\partial}{\partial \mathbf{R_I}} E_{KS} + \frac{\partial}{\partial \mathbf{R_I}} \{constraints\} \tag{1.40}$$

$$\mu_i \ddot{\psi}_i(t) = -\frac{\delta}{\delta \psi_i} E_{KS} + \frac{\delta}{\delta \psi_i} \{constraints\} \tag{1.41}$$

where μ_i are the fictitious masses assigned to the orbital degrees of freedom. The units of this mass parameter are energy times the squared time for reasons of dimensionality. The constraints within the total wavefunction lead to constraint forces in the equations of motion. The constraints in the equation of motion might be a function of both the set of orbitals $\{\psi_i\}$ and the nuclear coordinates $\{R_i\}$. Solving these equations, the unknown variables such as ψ_i(r,t), R_I(t), and λ_{ij}(t) can be estimated from the initial conditions on $R_I(0)$, $\dot{R}_I(0)$, $\psi_i(0)$, $\dot{\psi}_i(0)$, and $\lambda_{ij}(0)$.

The nuclei evolve in time at a temperature that is proportional to $\sum_I M_I \dot{\mathbf{R}}_\mathbf{I}^2$ according

to Car-Parrinello equations of motion, whereas a fictitious temperature that is proportional to $\sum_i \mu_i \langle \dot{\psi}_i | \dot{\psi}_i \rangle$ is associated with the electronic degrees of freedom. According to this terminology, low electronic temperature means that the electron is close to its instantaneous minimum energy that also means that it is close to the exact Born-Oppenheimer surface. Thus if the ground state wavefunction is optimized for the initial configuration of the nuclei it will stay close to its ground state also during the time evolution provided that it remains at a sufficiently low fictitious temperature.

1.7.4 Hellmann-Feynman theorem and its implications

Hellmann-Feynman theorem allows for the simplification of the calculation of the physical forces on the ions. The force on ion I is

$$f_I = -\frac{dE}{dR_I} \tag{1.42}$$

The changes in electron wavefunctions also contribute to the force on the ion. Therefore the force on the ion can be written as

$$f_I = -\frac{\partial E}{\partial R_I} - \sum_i \frac{\partial E}{\partial \psi_i}\frac{d\psi_i}{dR_I} - \sum_i \frac{\partial E}{\partial \psi_i^*}\frac{d\psi_i^*}{dR_I} \tag{1.43}$$

As $\frac{\partial E}{\partial \psi_i^*}$ is equal to $H\psi_i$, the last two terms can be written as

$$\sum_i \left\langle \frac{\partial \psi_i}{\partial R_I} \middle| H\psi_i \right\rangle + \sum_i \left\langle \psi_i H \middle| \frac{\partial \psi_i}{\partial R_I} \right\rangle \tag{1.44}$$

However, if each ψ_i is an eigenstate of the Hamiltonian

$$H\psi_i = \lambda_i \psi_i \tag{1.45}$$

Therefore,

$$\sum_i \left\langle \frac{\partial \psi_i}{\partial R_I} \middle| \lambda_i \psi_i \right\rangle + \sum_i \left\langle \psi_i \lambda_i \middle| \frac{\partial \psi_i}{\partial R_I} \right\rangle = \sum_i \lambda_i \frac{\partial}{\partial R_I} \langle \psi_i | \psi_i \rangle = 0 \tag{1.46}$$

since $\langle \psi_i | \psi_i \rangle$ is a constant by normalization

So, when each ψ_i is an eigenstate of the Hamiltonian, the partial derivative of the Kohn-Sham energy with respect to the position of an ion gives the real physical force of the ion.

1.7.5 Constants of motion

For the system with holonomic constraints, according to classical dynamics, there should be a conserved quantity. This conserved quantity serves as an extremely sensitive check for the molecular dynamics algorithm. The conserved energy in the case of CPMD is

$$E_{\text{cons}} = \sum_i \frac{1}{2} \mu_i \langle \dot{\psi}_i | \dot{\psi}_i \rangle + \sum_I \frac{1}{2} M_I \dot{\mathbf{R}}_\mathbf{I}^2 + \langle \psi_0 | H_{KS} | \psi_0 \rangle \tag{1.47}$$

where the first term represents the fictitious kinetic energy (T_e) of the electrons and the second term the kinetic energy of the ions.

$$T_e = \sum_i \frac{1}{2} \mu_i \langle \dot{\psi}_i | \dot{\psi}_i \rangle \tag{1.48}$$

$$E_{KS} = \langle \psi_0 | H_{KS} | \psi_0 \rangle \tag{1.49}$$

The physical energy is the sum of the ionic kinetic energy and the total potential E_{KS}.

$$E_{\text{phys}} = \sum_I \frac{1}{2} M_I \dot{\mathbf{R}}_\mathbf{I}^{\,2} + \langle \psi_0 | H_{KS} | \psi_0 \rangle = E_{cons} - T_e \tag{1.50}$$

The fictitious kinetic energy of the electrons is found to perform bound oscillations around a constant. This means that the electrons do not heat up in the presence of hot nu-

clei. T_e is a measure for deviations of the electronic wavefunctions from the exact Born-Oppenheimer surface. Usually, the conserved quantity E_{cons} will have very small standard deviation of the order of 10^{-6} from the mean value. The physical energy of the system is the difference between the conserved quantity and the fictitious kinetic energy of the electronic orbitals.

1.8 Scope and limitations of classical MD and CPMD

Classical MD has been successfully used to study a wide variety of systems including gaseous and condensed phase systems. These are based on empirical potential that has to be determined for the particular system. The form of the potential approximates the intermolecular interaction between the atoms, that usually includes pairwise interactions, three body interactions and many body interactions. The potential parameters that are determined based on the experimental results and *ab initio* calculations, remain fixed throughout the course of the simulation.

With the advent of faster computers and parallel computing, the size of the systems that can be simulated has increased to tens of nanometers thus giving access to the nanoscale properties within atomistic models. The time scales accessible in these simulations too have extended up to hundreds of nanoseconds for even complex systems of nanometric sizes. Models with united atom representation for a bunch of atoms, usually methyl or methylene group in the case of alkanes have been developed that allows the simulations of even bigger systems. For the study of very big systems like complex biological samples or polymers, coarse grained representations have been developed that allows for the probing of micrometer length scales and microsecond time scales. Here, however, the short length scale knowledge has to be sacrificed.

The main drawback of the classical molecular dynamics is that the results will be as good as the model used. One should have a very good model of the system in order to obtain proper results that could describe it accurately. For a new system with complex

intermolecular interactions, the form of the interaction and the potential parameters need to be determined. Transferability of the potential is also a main issue. Classical MD with hardwired potential is unable to predict the chemical reactions, where a bond can break and form a new bond.

Ab initio molecular dynamics addresses some of these issues. CPMD which is one of the AIMD method is the coupling of traditional MD with electronic structure calculations [204]. This is based on the Kohn-Sham formulation of DFT, and uses pseudopotentials to represent the interaction of valence electrons with the core electrons and the nuclei. Although CPMD is also not exact (due to deficiencies inherent to DFT (one electron treatment) and those present in XC functionals), the approximation here is at a higher level than that of the classical MD. In CPMD, there is no need for an empirical interaction potential. The forces on the ions are calculated on the fly based on the location of the other ions and electron density in the system. The potential of interaction between the ions continuously changes with time. Electronic degrees of freedom are taken into account that gives a better microscopic picture of the system. Some of the properties which in classical MD are indirectly built into the model and hence do not have significance can be calculated using CPMD. One such property is the frequency spectrum that can be calculated from the time evolution of velocities of the atom, does not have significance when calculated from MD trajectory since these are built into the model in the form of spring constants of harmonic bonds.

Despite these advantages over empirical potential MD, CPMD has some limitations. The accessible length and time scales are limited (tens of angstroms and tens of picoseconds) due to the requirement of intense computational resources for the calculations. The processes occurring at long time and length scales are hence totally inaccessible. The accuracy of the calculations also depends on the exchange and correlation functionals used. One needs to use large number of plane waves to accurately represent the pseudopotential, that also demands the computational resources. The dispersion forces are not taken into

account in these calculations. However in our studies we are looking at the structural changes that occurs at small length and time scales that are not very much affected due to the exclusion of these interactions.

Ionic liquids can be quite viscous. For instance, the viscosity of [bmim][PF_6] at room temperature is around 200 cP, i.e., two orders of magnitude larger than that of liquid water. Hence simulations of such ionic liquids will require long trajectories for a proper sampling of the configuration space. Generation of such long trajectories may be prohibitive in CPMD. Our CPMD simulations have been carried out mainly to study the reorganization of local structural motifs, at the length scales of the first coordination shell. Specifically, such CPMD simulations which were started from equilibrated classical MD configurations, help one to identify small rearrangements that take place in the near neighbor shell of a given species. It is in this spirit that these simulations are presented in this thesis.

1.9 Softwares and Hardwares used

All the classical molecular dynamics simulations reported in the thesis were carried out using PINY_MD [205] and LAMMPS [206] software. CPMD [207] software has been extensively used for performing the *ab initio* molecular dynamics simulations. Codes were developed for the calculation of structural and dynamical properties presented in the thesis during the course of research. All the analyses have been carried out using the home developed codes. Some of the structure optimizations, vibrational analysis and computations of binding energies were carried out using Gaussian [208] software and ADF-2006 software. Xmgr and Xmgrace softwares were used for plotting. Visualizations and some analyses were done with the visualization softwares xmovie, Molden [209], VMD [210] and Xcrysden [211]. All the softwares used, except for Gaussian and ADF-2006 are freely available softwares.

Since the thesis work included the generation of long trajectories for large systems

using classical MD and CPMD, intense computational resources were required. The simulations were carried out using dedicated clusters as well as from the resources that were available as central facilities. The dedicated clusters include a 8 node Beowulf cluster, 10 node Beowulf cluster and a 32 processor Beowulf cluster. Central facilities included a 12 node cluster, a 32 processor cluster, a teraflop facility at the Center for Development of Advanced Computing, a teraflop facility at CMSD, Hyderabad and a 512 core cluster at CCMS, JNCASR.

Bibliography

[1] L.A. Blanchard, D. Hancu, E.J. Beckman, J.F. Brennecke, *Nature*, **399**, 28 (1999).

[2] R.A. Sheldon, *Green Chem.*, **7**, 267 (2005).

[3] P.S. Shah, T. Hanrath, K.P. Johnston, B.A. Korgel, *J. Phys. Chem. B*, **108**, 9574 (2004).

[4] W. Leitner, *Nature*, **405**, 129 (2000).

[5] M. Poliakoff, P. King, *Nature*, **412**, 125 (2001).

[6] S.L. Wells, J.M. Desimone, *Angew. Chem. Int. Ed. Engl.*, **40**, 518 (2001).

[7] J.M. Desimone, *Science*, **297**, 799 (2002).

[8] J.M. Desimone, Z. Guan, C.S. Elsbernd, *Science*, **257**, 945 (1992).

[9] Q. Li, Z. Zhang, C. Zhong, Y. Liu, Q. Zhou, *Fluid Phase Equil.*, **207**, 183 (2003).

[10] M.A. Ribeiro, M.G. Bernardo-Gil, *J. Chem. Eng. Data*, **40**, 1188 (1995).

[11] T. Clifford, *Fundamentals of Supercritical Fluids* (Oxford Univerity Press, New York, 1999).

[12] M. Ji, X. Chen, C.M. Wai, J.L. Fulton, *J. Am. Chem. Soc.*, **121**, 2631 (1999).

[13] P.S. Shah, T. Hanrath, K.P. Johnston, B.A. Korgel, *J. Phys. Chem. B*, **108**, 9574 (2004).

[14] J.D. Holmes, P.A. Bhargava, B.A. Korgel, K.P. Johnston, *Langmuir*, **15**, 6613 (1999).

[15] P.S. Shah, J.D. Holmes, R.C. Doty, K.P. Johnston, B.A. Korgel, *J. Am. Chem. Soc.*, **122**, 4245 (2000).

[16] P.S. Shah, S. Husain, K.P. Johnston, B.A. Korgel, *J. Phys. Chem. B*, **106**, 12178 (2002).

[17] P. Licence, J. Ke, M. Sokolova, S.K. Ross, M. Poliakoff, *Green Chem.*, **5**, 99 (2003).

[18] M.J. Clarke, K.L. Harrison, K.P. Johnston, S.M. Howdle, *J. Am. Chem. Soc.*, **119**, 6399 (1997).

[19] K. Nagashima, C.T. Lee Jr., B. Xu, K.P. Johnston, J.M. DeSimone, C.S. Johnson Jr., *J. Phys. Chem. B*, **107**, 1962 (2003).

[20] B. Chen, J.I. Siepmann, M.L. Klein, *J. Phys. Chem. B*, **105**, 9840 (2001).

[21] S. Salaniwal, S.T. Cui, P.T. Cummings, H.D. Cochran, *Langmuir*, **15**, 5188 (1999); S. Salaniwal, S.T. Cui, H.D. Cochran, P.T. Cummings, *Langmuir*, **17**, 1773 (2001).

[22] S. Senapati, J.S. Keiper, J.M. DeSimone, G.D. Wignall, Y.B. Melnichenko, H. Frielinghaus, M.L. Berkowitz, *Langmuir*, **18**, 7371 (2002).

[23] M. Saharay, S. Balasubramanian, *J. Chem. Phys.*, **120**, 9694 (2004).

[24] M. Saharay, S. Balasubramanian, *ChemPhysChem*, **5**, 1442 (2004); **7**, 1167 (2006).

[25] M. Saharay, S. Balasubramanian, *J. Phys. Chem. B*, **111**, 387 (2007).

[26] M. Saharay, S. Balasubramanian, *J. Phys. Chem. B*, **100**, 3782 (2006).

[27] P. Anastas, J. Warner, *Green Chemistry: Theory and Practice* (Oxford University Press, New York, 1998).

[28] K.R. Seddon *Nature Mater.*, **2**, 363 (2003).

[29] R.D. Rogers, K.R. Seddon, *Science*, **302**, 792 (2003).

[30] T. Welton, *Chem. Rev.*, **99**, 2071 (1999).

[31] M.J. Earle, K.R. Seddon, *Pure Appl. Chem.*, **72**, 1391 (2000).

[32] D.R. Lide, *Handbook of chemistry and physics*, (CRC Press, Boca Raton, 2004).

[33] C.A. Angell, W. Xu, M. Yoshizawa, J.-P. Belieres, *Ionic Liquids*, Eds. H.Oye, A. Jagtoyen et. al. pp.389-398

[34] C.A. Angell, N. Byrne, J.-P. Belieres, *Acc. Chem. Res.*, (2007).

[35] P. Walden, *Bull. Acad. Imper. Sci. (St. Petersburg)*, 1800 (1914).

[36] S. Lee, *Chem. Commun.*, 1049 (2006).

[37] T. Nishida, Y. Tashiro, M. Yamamoto, *J. Flourine Chem.*, **120**, 135 (2003).

[38] J.G. Huddleston, A.E. Visser, W.M. Reichert, H.D. Willauer, G.A. Broker, R.D. Rogers, *Green Chem.*, **3**, 156 (2001).

[39] A.A. Fannin Jr., D.A. Floreani, L.A. King, J.S. Landers, B.J. Piersma, D.J. Stech, R.L. Vaughn, J.S. Wilkes, J.L. Williams, *J. Phys. Chem.*, **88**, 2614 (1984).

[40] P.J. Dyson, G. Laurenczy, C.A. Ohlin, J. Vallance, T. Welton, *Chem. Commun.*, 2418 (2003).

[41] P.A.Z. Suarez, S. Einloft, J.E.L. Dullius, R.F. de Souza, J. Dupont, *J. Chim. Phys. Phys. -Chim. Biol.*, **95**, 1626 (1998).

[42] P. Bonhote, A.P. Dias, N. Papageorgiou, K. Kalyanasundaram, M. Gratzel, *Inorg. Chem.*, **35**, 1168 (1996).

[43] J. Dupont, *J. Braz. Chem. Soc.*, **15**, 341 (2004).

[44] Q. Yang, D.D. *Journal of Photochemistry and Photobiology, A: Chemistry*,**165**, 229 (2004).

[45] S. Saha, P.K. Mandal, A. Samanta, *Phys. Chem. Chem. Phys.*, **6**, 3106 (2004).

[46] K.R. Seddon, A. Stark, M. Torres, *Pure Appl. Chem.*, **72**, 2275 (2000).

[47] M. Kanakubo, T. Umecky, T. Aizawa, Y. Kurata, *Chem. Lett.*, **34**, 324 (2005).

[48] P. Kolle, R. Dronskowski, *Eur. J. Inorg. Chem.*, 2313 (2004).

[49] M. Kanakubo, Y. Hiejima, K. Minami, T. Aizawa, H. Nanjo, *Chem. Commun.*, 1828 (2006).

[50] S. Chen, G. Wu, M. Sha, S. Huang, *J. Am. Chem. Soc.*, **129**, 2416 (2007).

[51] A.M. Scurto, W. Leitner, *Chem. Commun.*, 3681 (2006).

[52] M.J. Earle, J. M.S.S. Esperanca, M.A. Gilea, J.N.C. Lopes, L.P.N. Rebelo, J.W. Magee, K.R. Seddon, J.A. Widegren, *Nature*, **439**, 831 (2006).

[53] I. Krossing, J.M. Slattery, C. Daguenet, P.J. Dyson, A. Oleinkova, H. Weingartner, *J. Am. Chem. Soc.*, **128**, 13427 (2006); **129**, 11296 (2007).

[54] A.G. Fadeev, M.M. Meagher, *Chem. Commun.*, 295 (2001).

[55] P. Wasserscheid, T. Welton, Eds., *Ionic Liquids in Synthesis*, (Wiley-VCH, Weinheim, 2003).

[56] Q. Liu, M.H.A. Janssen, F. van Rantwijk, R.A. Sheldon, *Green Chem.*, **7**, 39 (2005)

[57] M.J. Earle, P.E. McCormac, K.R. Seddon, *Green Chem.*, **1**, 23 (1999).

[58] M. Badri, J.-J Brunet, R. Perron, *Tetrahedron Lett.*, **33**, 4435 (1992).

[59] C.J. Adams, M.J. Earle, G. Roberts, K.R. Seddon, *Chem. Commun.*, 2097 (1998).

[60] J.A. Boon, J.A. Levisky, J.L. Pflug, J.S. Wilkes, *J. Org. Chem.*, **51**, 480 (1986).

[61] R. Sheldon, *Chem. Commun.*, 2399 (2001).

[62] F. van Rantwijk, R.M. Lau, R.A. Sheldon, *Trends in Biotechnology*, **21**, 131 (2003).

[63] R. Hagiwara, T. Hirashige, T. Tsuda, Y. Ito, *J. Fluorine Chem.*, **99**, 1 (1999); *J. Electrochem. Soc.*, **149**, D1 (2002); R. Hagiwara, K. Matsumoto, T. Tsuda, Y. Ito, S. Kohara, K. Suzuya, H. Matsumoto, Y. Miyazaki, *J. Non-Crystalline Solids*, **312-314**, 414 (2002); R. Hagiwara, K. Matsumoto, Y. Nakamori, T. Tsuda, Y. Ito, H. Matsumoto, K. Momota, *J. Electrochem. Soc.*, **150**, D195 (2003); R. Hagiwara, Y. Nakamori, K. Matsumoto, Y. Ito, *J. Phys. Chem. B*, **109**, 5445 (2005).

[64] M. Yoshio, T. Mukai, H. Ohno, T. Kato, *J. Am. Chem. Soc.*, **126**, 994 (2004).

[65] S.N. Baker, T.M. McCleskey, S. Pandey, G.A. Baker, *Chem. Commun.*, 940 (2004).

[66] M.P. Scott, C.S. Brazel, M.G. Benton, J.W. Mays, J.D. Holbrey, R.D. Rogers, *Chem. Commun.*, 1370 (2002).

[67] B. Wu, R.G. Reddy, R.D. Rogers, *Proc. of Solar Forum*, April 21-25, Washington, DC, (2001).

[68] J.D. Roche, C.M. Gordon, C.T. Imrie, M.D. Ingram, A.R. Kennedy, F.L. Celso, A. Triolo, *Chem. Mater.*, **15**, 3089 (2003).

[69] P. Wasserscheid, *Nature*, **439**, 797 (2006).

[70] S.G. Kazarian; B.J. Briscoe; T. Welton *Chem. Commun.*, 2047 (2000).

[71] M. Kanakubo, T. Umecky, Y. Hiejima, T. Aizawa, H. Nanjo, Y. Kameda, *J. Phys. Chem. B*, **109**, 13847 (2005).

[72] C. Cadena, J.L. Anthony, J.K. Shah, T.I. Morrow, J.F. Brennecke, E.J. Maginn, *J. Am. Chem. Soc.*, **126**, 5300 (2004).

[73] X. Huang, C.J. Margulis, Y. Li, B.J. Berne, *J. Am. Chem. Soc.*, **127**, 17842 (2005).

[74] J.L. Anthony, J.L. Anderson, E.J. Maginn, J.F. Brennecke, *J. Phys. Chem. B*, **109**, 6366 (2005).

[75] A.M. Scurto, S.N.V.K. Aki, J.F. Brennecke, *J. Am. Chem. Soc.*, **124**, 10276 (2002).

[76] T. Takaya, S. Saha, H. Hamaguchi, M. Sarkar, A. Samanta, K. Iwata, *J. Phys. Chem. B*, **110**, 4291 (2006); S. Saha, H. Hamaguchi, *J. Phys. Chem. B*, **110**, 2777 (2006); R. Ozawa, S. Hayashi, S. Saha, A. Kobayashi, H. Hamaguchi, *Chem. Lett.*, **32**, 948 (2003).

[77] K.R. Harris, L.A. Woolf, M. Kanakubo, *J. Chem. Eng. Data.*, **50**, 1777 (2005); M. Kanakubo; K.R. Harris, N. Tsuchihashi, K. Ibuki, M. Ueno, *J. Phys. Chem. B*, **111**, 2062 (2007).

[78] J.L. Anderson, J.K. Dixon, E.J. Maginn, J.F. Brennecke, *J. Phys. Chem. B*, **110**, 15059 (2006); J.L. Anthony, E.J. Maginn, J.F. Brennecke, *J. Phys. Chem. B*, **105**, 10942 (2001).

[79] Z. Hu, C.J. Margulis, *J. Phys. Chem. B*, **110**, 11025 (2006); **111**, 4705 (2007).

[80] C. Pinilla, M.G. Del Popolo, R.M. Lynden-Bell, J. Kohanaoff, *J. Phys. Chem. B*, **109**, 17922 (2005); R.M. Lynden-Bell, *J. Phys. Chem. B*, **111**, 10800 (2007); M.G. Del Popolo, J. Kohanoff, R.M. Lynden-Bell, *J. Phys. Chem. B*, **110**, 8798 (2006).

[81] M.S. Kelkar, E.J. Maginn, *J. Phys. Chem. B*, **111**, 9424 (2007).

[82] M. Koel, *Proc. Estonian Acad. Sci. Chem.*, **49**, 145 (2000).

[83] H. Tokuda, K. Hayamizu, K. Ishii, A.B.H. Susan, M. Watanabe, *J. Phys. Chem. B*, **108**, 16593 (2004).

[84] J. Jacquemin, P. Husson, A.A.H. Padua, V. Majer, *Green Chem.*, **8**, 172 (2006).

[85] T.J. Gannon, G. Law, P.R. Watson, *Langmuir*, **15**, 8429 (1999).

[86] G. Law, P. R. Watson, *Langmuir*, **17**, 6138 (2001).

[87] G. Law, P.R. Watson, A.J. Carmichael, K.R. Seddon, *Phys. Chem. Chem. Phys.*, **3**, 2879 (2001).

[88] G. Law, P.R. Watson, *Chem. Phys. Lett.*, **345**, 1 (2001).

[89] T. Iimori, T. Iwahashi, H. Ishii, K. Seki, Y. Ouchi, R. Ozawa, H. Hamaguchi, D. Kim, *Chem. Phys. Lett.*, **389**, 321 (2004).

[90] J. Sung, Y. Jeon, D. Kim, T. Iwahashi, T. Iimori, K. Seki, Y. Ouchi, *Chem. Phys. Lett.*, **406**, 495 (2005).

[91] J. Bowers, M.C. Vergara-Gutierrez, J.R.P. Webster, *Langmuir*, **20**, 309 (2004).

[92] E. Sloutskin, B.M. Ocko, L. Tamam, I. Kuzmenko, T. Gog, M. Deutsch, *J. Am. Chem. Soc.* **127**, 7796 (2005); **127**, 18333 (2005).

[93] R.M. Lynden-Bell, J. Kohanoff, M.G. Del Popolo, *Faraday Discuss.*, **129**, 57 (2005).

[94] R.M. Lynden-Bell, *Mol. Phys.*, **101**, 2625 (2003).

[95] R.M. Lynden-Bell, M. Del Popolo, *Phys. Chem. Chem. Phys.*, **8**, 949 (2006).

[96] A. Chaumont, R. Schurhammer, G. Wipff, *J. Phys. Chem. B*, **109**, 18964 (2005).

[97] G. Chevrot, R. Schurhammer, G. Wipff, *Phys. Chem. Chem. Phys.*, **8**, 4166 (2006).

[98] E. Bart, A. Meltsin, D. Huppert, *Chem. Phys. Lett.*, **200**, 592 (1992).

[99] E. Bart, A. Meltsin, D. Huppert, *J. Phys. Chem.*, **98**, 10819 (1994); **98**, 3295 (1994); **99**, 9253 (1995).

[100] R. Karmakar, A. Samanta, *J. Phys. Chem. A*, **106**, 4447 (2002); **106**, 6670 (2002); **107**, 7340 (2003).

[101] R. Karmakar, A. Samanta, *Chem. Phys. Lett.*, **376**, 638 (2003).

[102] N. Ito, S. Arzhantsev, M. Heitz, M. Maroncelli, *J. Phys. Chem. B*, **108**, 5771 (2004).

[103] J.A. Ingram, R.S. Moog, N. Ito, R. Biswas, M. Maroncelli, *J. Phys. Chem. B*, **107**, 5926 (2003).

[104] S. Arzhantsev, N. Ito, M. Heitz, M. Maroncelli, *Chem. Phys. Lett.*, **381**, 278 (2003).

[105] G. Giraud, C.M. Gordon, I.R. Dunkin, K. Wynne, *J. Chem. Phys.*, **119**, 464 (2003).

[106] J.R. Rajian, S. Li, R.A. Bartsch, E.L. Quitevis, *Chem. Phys. Lett.*, **393**, 372 (2004).

[107] M.N. Kobrak, V. Znamenskiy, *Chem. Phys. Lett.*, **395**, 127 (2004).

[108] H. Shirota, A.M. Funston, J.F. Wishart, E.W. Castner Jr., *J. Chem. Phys.*, **122**, 184512 (2005).

[109] Y. Shim, J. Duan, M.Y. Choi, H.J. Kim, *J. Chem. Phys.*, **119**, 6411 (2003).

[110] Y. Shim, H.J. Kim, *J. Chem. Phys.*, **125**, 024507 (2006).

[111] C.G. Hanke, S.L. Price, R.M. Lynden-Bell, *Mol. Phys.*, **99**, 801 (2001).

[112] C.J. Margulis, H.A. Stern, B.J. Berne, *J. Phys. Chem. B*, **106**, 12017 (2002).

[113] T.I. Morrow, E.J. Maginn, *J. Phys. Chem. B*, **106**, 12807 (2002).

[114] J. de Andrade, E.S. Boes; H. Stassen *J. Phys. Chem. B*, **106**, 13344 (2002).

[115] C.J. Margulis, *Mol. Phys.*, **102**, 829 (2004).

[116] T. Yan, C.J. Burnham, M.G. Del Popolo, G.A. Voth, *J. Phys. Chem. B*, **108**, 11877 (2004).

[117] S.M. Urahata, M.C.C. Ribeiro, *J. Chem. Phys.*, **120** 1855 (2004).

[118] M.G. Del Popolo, G.A. Voth, *J. Phys. Chem. B*, **108**, 1744 (2004).

[119] Z. Liu, S. Huang, W. Wang, *J. Phys. Chem. B*, **108**, 12978 (2004).

[120] S. Alavi, D.L. Thompson, *J. Chem. Phys.*, **122**, 154704 (2005).

[121] S.U. Lee, J. Jung, Y Han, *Chem. Phys. Lett.*, **406**, 332 (2005).

[122] J.N.C. Lopes, J. Deschamps, A.A.H. Padua, *J. Phys. Chem. B*, **108**, 2038 (2004); **108**, 11250 (2004).

[123] J.N.C. Lopes, A.A.H. Padua, *J.Phys. Chem. B*, **108**, 16893 (2004).

[124] Z. Liu, X. Wu, W. Wang, *Phys. Chem. Chem. Phys.*, **8**, 1096 (2006).

[125] J.N.C. Lopes, A.A.H. Padua, *J. Phys. Chem. B*, **110**, 19586 (2006).

[126] T.G.A. Youngs, M.G. Del Popolo, J. Kohanoff, *J. Phys. Chem. B*, **110**, 5697 (2006).

[127] S. Tsuzuki, H. Tokuda, K. Hayamizu, M. Watanabe, *J. Phys. Chem. B*, **109**, 16474 (2005).

[128] Y. Wang, G.A. Voth, *J. Am. Chem. Soc.*, **127**, 12192 (2005).

[129] S.M. Urahata, M.C.C. Ribeiro, *J. Chem. Phys.*, **122**, 024511 (2005).

[130] P.A. Hunt, *Molec. Simulations*, **32**, 1 (2006).

[131] Y. Wang, H. Li, S. Han, *J. Phys. Chem. B*, **110**, 24646 (2006).

[132] C. Schroder, T. Rudas, O Steinhausser, *J. Chem. Phys.*, **125**, 244506 (2006).

[133] C. Rey-Castro, L.F. Vega, *J. Phys. Chem. B*, **110**, 14426 (2006).

[134] A.J. Arduengo, H.V. Rasika Dias, R.L. Harlow, M. Kline, *J. Am. Chem. Soc.*, **114**, 5530 (1992).

[135] J.D. Holbrey, W.M. Reichert, M. Nieuwenhuyzen, S. Johnston, K.R. Seddon, R.D. Rogers, *Chem. Commun.*, 1636 (2003).

[136] S. Hayashi, R. Ozawa, H. Hamaguchi, *Chem. Lett.*, **32**, 498 (2003).

[137] S. Saha, S. Hayashi, A. Kobayashi, H. Hamaguchi, *Chem. Lett.*, **32**, 740 (2003).

[138] A.R. Choudhury, N. Winterton, A. Steiner, A.I. Cooper, K.A. Johnson, *J. Am. Chem. Soc.*, **127**, 16792 (2005).

[139] S.M. Dibrov, J.K. Kochi, *Acta Cryst.*, **C62**, o19 (2006).

[140] A. Triolo, V. Arrighi, F. Juranyi, S. Janssen, C.M. Gordon, *J. Chem. Phys.*, **119**, 8549 (2003).

[141] C. Hardacre; J.D. Holbrey, S.E. Jane McMath, D.T. Bowron, A.K. Soper, *J. Chem. Phys.*, **118**, 273 (2003).

[142] C. Hardacre, S.E. Jane McMath, M. Nieuwenhuyzen, D.T Bowron, A.K. Soper, *J. Phys.: Condens. Matter*, **15**, S159 (2003).

[143] A. Triolo, A. Mandanici, O. Russina, V. Rodriguez-Mora, M. Cutroni, C. Hardacre, M. Nieuwenhuyzen, H. Bleif, L. Keller, M.A. Ramos, *J. Phys. Chem. B*, **110**, 21357 (2006).

[144] A. Triolo, O. Russina, C. Hardacre, M. Nieuwenhuyzen, M.A. Gonzalez, H. Grimm, *J. Phys. Chem. B*, **109**, 22061 (2005).

[145] J.L. Anthony, E.J. Maginn, J.F. Brennecke, *J. Phys. Chem. B*, **106**, 7315 (2002).

[146] S.N.V.K. Aki, B.R. Mellein, E.M. Saurer, J.F. Brennecke, *J. Phys. Chem. B*, **108**, 20355 (2004).

[147] J.M. Crosthwaite, S.N.V.K. Aki, E.J. Maginn, J.F. Brennecke, *J. Phys. Chem. B*, **108**, 5113 (2004).

[148] J. Deschamps, M.F. Costa Gomes, A.A.H. Padua, *ChemPhysChem*, **5**, 1049 (2004).

[149] J.K. Shah, E.J. Maginn, *J. Phys. Chem. B*, **109**, 10395 (2005).

[150] W.G. Hoover, *Computational Statistical Mechanics*, (Elsevier, New York, 1991).

[151] D. Frenkel, B. Smit, *Understanding Molecular Simulation* (Academic Press, San Diego, 1996).

[152] M. P. Allen, D. J. Tildesley, *Computer Simulation of Liquids* (Oxford, Clarendon, 1987).

[153] S.M. Bhabani, A. Chandra, *J. Chem. Phys.*, **125**, 234502 (2006); M.E. Tuckerman, A. Chandra, D. Marx, *Acc. Chem. Res.*, **39**, 151 (2006); S. Paul, A. Chandra, *J. Chem. Phys.*, **109**, 20558 (2005).

[154] D.A. McQuarrie, *Statistical Mechanics*, (Harper and Row, San Francisco, 1976).

[155] H.C. Andersen, *J. Chem. Phys.*, **72**, 2384 (1980).

[156] S. Nosé, *Mol. Phys.*, **52**, 255 (1984).

[157] S. Nosé, *J. Chem. Phys.*, **81**, 511 (1984).

[158] W.G. Hoover, *Phys. Rev. A*, **31**, 308 (1985).

[159] G.J. Martyna, M.L. Klein, M. Tuckerman, *J. Chem. Phys.*, **97**, 2635 (1992).

[160] G.J. Martyna, M.E. Tuckerman, D.J. Tobias, M.L. Klein, *Mol. Phys.*, **87**, 1117 (1996).

[161] C.J. Mundy, S. Balasubramanian, K. Bagchi, M.E. Tuckerman, G.J. Martyna, M.L. Klein, *Reviews in Computational Chemistry*, **14**, 291 (1999).

[162] M. Parrinello, A. Rahman, *Phys. Rev. Lett.*, **45**, 1196 (1980).

[163] M. Parrinello, A. Rahman, *J. Appl. Phys.*, **52**, 7182 (1981).

[164] M. Parrinello, A. Rahman, *J. Chem. Phys.*, **76**, 2662 (1982).

[165] G.J. Martyna, D.J. Tobias, M.L. Klein, *J. Chem. Phys.*, **101**, 4177 (1994).

[166] D.A. McQuarrie, *Statistical Mechanics* (University Science Books, Sausalito, 2003).

[167] B.J. Berne, R. Pecora, *Dynamic Light Scattering : With Applications to Chemistry, Biology, and Physics* (John Wiley & Sons, Inc., New York, 1976).

[168] L. Onsager, *Phys. Rev.*, **37**, 405 (1931); **38**, 2265, (1931).

[169] S.N. Chakraborty, C. Chakravarty, *J. Chem. Phys.*, **124**, 014507 (2006); A. Mudi, C. Chakravarty, R. Ramaswamy, *J. Chem. Phys.*, **122**, 104507 (2005).

[170] G. Ciccotti, D. Frenkel, I. R. Mc.Donald, *Simulation of Liquids and Solids : Molecular Dynamics and Monte Carlo Methods in Statistical Mechanics* (North Holland, Amsterdam, 1990).

[171] J. P. Hansen, G. Ciccotti, W. G. Hoover, *Molecular-Dynamics Simulation of Statistical-Mechanical Systems* (North-Holland, Amsterdam, 1986).

[172] A. R. Leach, *Molecular Modelling : Principles and Applications* (Prentice Hall, Harlow, 2001).

[173] A. K. Rappe, C. J. Casewit, *Molecular Mechanics Across Chemistry* (University Science Books, Sausalito, 1997).

[174] M. J. Field, *A Practical Introduction to Simulation of Molecular Systems* (Cambridge University Press, Cambridge, 1999).

[175] D. Marx, *NIC Series*, **31**, ISBN 3-00-017350-1, 195 (2006).

[176] R. Car, M. Parrinello, *Phys. Rev. Lett.*, **35**, 2471 (1985).

[177] G. Galli, M. Parrinello, *Science*, **250**, 1547 (1990).

[178] D. K. Remler, P. A. Madden, *Molec. Phys.*, **70**, 912 (1990).

[179] G. Pastore, E. Smargiassi, F. Buda, *Phys. Rev. A*, **44**, 6334 (1991).

[180] M. C. Payne, M. P. Teter, D. C. Allan, T. A. Aris, J. D. Joannopoulos, *Rev. Mod. Phys.*, **64**, 1045 (1992).

[181] M. Palummo, L. Reining, P. Ballone, *J. Phys. IV (Paris)*, **3:(C7)**, 1955 (1993).

[182] E. Deumens, A. Diz, R. Longo, Y. Ohrn, *Rev. Mod. Phys.*, **66**, 917 (1994).

[183] M. E. Tuckerman, M. Parrinello, *J. Chem. Phys.*, **101**, 1302, 1316 (1994).

[184] J. Hutter, M. Tuckerman, M. Parrinello, *J. Chem. Phys.*, **102**, 859 (1995).

[185] M. E. Tuckerman, P. J. Ungar, T. von Rosenvinge, M. L. Klein, *J. Phys. Chem.*, **100**, 12878 (1996).

[186] M. J. Gillan, *Contemp. Phys.*, **38**, 115 (1997).

[187] M. Parrinello, *Solid State Commun.*, **102**, 107 (1997).

[188] E. Sandre, A. Pasturel, *Mol. Simul.*, **20**, 63 (1997).

[189] D. Marx, *Nachr. Chem. Tech. Lab.*, **47**, 186 (1999).

[190] D. Marx, J. Hutter, '*Ab initio* Molecular Dynamics : Theory and Implementation', in http://www.fz-juelich.de/nic-series/ (2000).

[191] M. Parrinello, *Comput. Sci. Engg.*, **2**, 22 (2000).

[192] P. Hohenberg, W. Kohn, *Phys. Rev.*, **136**, B864 (1964).

[193] W. Kohn, L. J. Sham, *Phys. Rev.*, **140**, A1133 (1965).

[194] I. R. Stich, R. Car, M. Parrinello, S. Baroni, *Phys. Rev. B*, **39**, 4997 (1989).

[195] V. Heine, *Solid. St. Phys.*, **24**, 1 (1970).

[196] L. R. Kahn, W. A. Goddard, *J. Chem. Phys.*, **56**, 2685 (1972).

[197] G. B. Bachelet, D. R. Hamann, M. Schlüter, *Phys. Rev. B*, **26**, 4199 (1982).

[198] L. Kleinman, D. M. Bylander, *Phys. Rev. Lett.*, **48**, 1425 (1982).

[199] Y. Bar-Yam, S. T. Pantelides, J. D. Joannopoulos, *Phys. Rev. B*, **39**, 3396 (1989).

[200] A. Rappe, K. Rabe, E. Kaxiras, J. D. Joannopoulos, *Phys. Rev. B*, **41**, 1227 (1990).

[201] D. Vanderbilt, *Phys. Rev. B*, **41**, 7892 (1990).

[202] N. Trouillier, J. L. Martins, *Phys. Rev. B*, **43**, 1993 (1991).

[203] N. J. Ramer, A. M. Rappe, *Phys. Rev. B*, **59**, 12471 (1998).

[204] P.K. Chattaraj, S. Sengupta, *J. Phys. Chem.*, **100**, 16126 (1996); P.K. Chattaraj, U. Sarkar, *J. Quantum Chem.*, **91**, 633 (2003); P.K. Chattaraj, S. Sengupta, *J. Phys. Chem. A*, **101**, 7893 (1997).

[205] M.E. Tuckerman, D.A. Yarne, S.O. Samuelson, A.L. Hughes, G.J. Martyna, *Comput. Phys. Commun.*, **128**, 333 (2000).

[206] S.J. Plimpton, *J. Comp. Phys.*, **117**, 1 (1995); Web: http://lammps.sandia.gov

[207] J. Hutter, P. Ballone, M. Bernasconi, P. Focher, E. Fois, S. Goedecker, D. Marx, M. Parrinello, and M.E. Tuckerman, CPMD Version 3.9.1, Max Planck Institut fuer Festkoerperforschung, Stuttgart, and IBM Zurich Research Laboratory, 1990-2007.

[208] M.J. Frisch *et al*, Gaussian, Inc.: Pittsburgh, PA, 1998.

[209] G. Schaftenaar, J.H. Noordik, *J. Comput.-Aided Mol. Design*, **14**, 123 (2000).

[210] W. Humphrey, A. Dalke, K. Schulten, *J. Mol. Graph.*, **14**, 33 (1996).

[211] A. Kokalj, *J. Mol. Graphics Modelling*, **17**, 176 (1999).

Chapter 2

Intermolecular structure, dynamics and transport properties of an ionic liquid [mmim][Cl] using *ab initio* and classical molecular dynamics simulations

2.1 Introduction

Room Temperature Ionic Liquids (RTILs) have been studied extensively in recent years [1–8]. A considerable amount of research has been carried out by the group at the QUILL centre [9]. Neutron scattering studies of imidazolium ion based melts have been reported by Hardacre *et al* [10, 11]. A number of theoretical and computational studies on the structure and dynamics of these compounds have also appeared in the literature [12–17].

While Hardacre and coworkers [10] observed a larger coordination of the chloride anion in the plane of a central imidazolium ring, classical molecular dynamics simulations

predicted a reduced coordination of the same [12]. Del Pópolo *et al* and Buhl *et al* have reported an *ab initio* molecular dynamics study of 1,3-dimethylimidazolium chloride ([mmim][Cl]) melt [15, 18]. Performing calculations that were started from several initial configurations, Del Pópolo *et al* have obtained a better agreement with experiment in terms of the intermolecular structure than what was possible within classical MD simulations that used empirical potentials.

The present study consists of two parts. First part comprises of the studies on structure and vibrational dynamics of [mmim][Cl] using *ab initio* molecular dynamics method. The second part consists of the studies of transport properties of [mmim][Cl] using equilibrium classical molecular dynamics simulations. In the first part we have two fold objective of obtaining the intermolecular structure of the melt and specifically to identify any cation-cation orientational ordering and secondly, to study the vibrational dynamics of the system from first principles and to study the effects of the cation-anion hydrogen bonding on the internal modes of the cation. Using plane wave based *ab initio* molecular dynamics simulations, we obtain the intermolecular structure of [mmim][Cl] at 425K, and observe hydrogen bonding effects between the chloride anion and the acidic hydrogen of the imidazolium ion, a feature that is absent in classical MD simulations. Pointers on possible improvements in the empirical potential models are provided.

Most of the solvents used in chemistry are molecular in nature, for instance, water, acetonitrile, benzene etc. Hence considerable attention was devoted to the study of solvation dynamics in such media. However, the study of ionic solvents such as RTILs that are considered here may provide new insights about solvation in ionic environment. Samanta and coworkers [19–21] and Maroncelli *et al* [22] have observed that the dynamics of solvation is biphasic in RTILs. It should however be noted that the time constant of the ultrafast component (sub-picosecond) of solvation dynamics is undetermined in these experiments as their time resolution is larger [23]. This fast response can be captured using molecular dynamics simulations.

Apart from polarity, an important determinant for a solvent in its applicability as a reaction medium is viscosity. Very few experimental studies on RTILs are available on this important physical property, and its dependence on the length of the alkyl chain present in the imidazolium ion [24]. Similarly, another collective property, i.e., electrical conductivity too has not been extensively studied. Theoretical determination of these quantities for model systems are even more rare. It is in this spirit and to fill up this void that we present the transport properties, such as self diffusion coefficients, shear viscosity and electrical conductivity of a model of [mmim][Cl] in this chapter. Results are also presented for another collective quantity, *viz* the solvation dynamics of solutes in this solvent. As these ionic liquids are highly viscous (say, compared to liquid water), very long MD trajectories need to be generated. The current work examines the single particle and collective dynamical properties of the same melt through classical simulations. Anticipating our results, we observe the faster diffusion of anions compared to the cations, and a correlated ion motion. The calculated shear viscosity is larger than experimental estimates. We also offer a procedure to obtain the long time component of the decay of the solvation time correlation function, through an innovative use of the anion itself (that is intrinsic to the solvent) as a probe.

2.2 Methodology and Simulation details.

The classical MD simulations, using an explicit atom model that was developed recently by Padua and coworkers [17] were carried out in the canonical ensemble, using the PINY_MD code [25]. The simulated system consisted of 864 ion pairs (14688 atoms) in a cubic box of edge length 55.5082Å. Initial MD runs were carried out in the isothermal-isobaric ensemble at a pressure of 1 bar in order to determine the density of the simulated system. Electrostatic interactions were computed using the Ewald summation method with an α value of 0.27Å^{-1} [26]. 7073 reciprocal space lattice points were used in the calculation of the contribution of reciprocal sum to the Coulomb energy. Temperature control was

achieved using a Nosé-Hoover chain thermostat [27–29]. The reference system propagator algorithm (RESPA), a multiple time step method, was used to integrate the equations of motion [30]. Non-bonded interactions beyond and within 6Å were integrated with time steps of 3 fs and 1.5fs respectively. Torsional forces were evaluated every 0.75fs while stretching and bending degrees of freedom were integrated with a fine time step of 0.375fs. A cutoff of 13Å was used for the calculation of non-bonded forces and long range corrections were applied for the calculation of energy and pressure tensor. The melt was equilibrated for 5 ns and data in terms of configurations and velocities were accumulated in several blocks covering over 8ns, that were used for analyses. The energy conservation was 4 parts in 10^5 over 1 ns.

The *ab initio* MD simulations [31] were performed using the CPMD [32] code under constant temperature and density conditions of 425K and 1.174g/cc respectively. These are the conditions under which the neutron scattering experiments of Hardacre *et al* [10] were conducted. Since the accessible length and time scales in *ab initio* simulations are much smaller compared to that in classical MD, the size of the system was restricted to 32 ion pairs of 1,3-dimethylimidazolium chloride in a cubic box of edge length 18.17 Å. Thus the simulated system consisted of 544 atoms and 1472 valence electrons. The interaction between the nuclei and the core electrons was considered using a norm conserving pseudopotential of the Troullier-Martins form [33]. Gradient corrected exchange and correlation functionals prescribed by Becke [34] and Lee, Yang, Parr [35] respectively were employed. The initial configuration for the CPMD run was obtained from a classical MD simulation of 3ns duration. The electronic orbitals were expanded in a plane wave basis set with an energy cutoff of 70Ry. We performed geometry optimizations of a imidazolium-chlorine pair in gas phase at varying energy cutoff values of 50Ry, 60Ry, 70Ry, and 85Ry. We observed that the intramolecular distances and angles of the imidazolium ion as well as the chlorine atom position relative to the cation were converged at an energy cutoff value of 70Ry. Hence the CPMD simulations of the bulk liquid were carried out at this

cutoff value. Three dimensional periodic boundary conditions consistent with a cubic box were employed to obtain bulk behavior. The electronic degrees of freedom were quenched to the Born-Oppenheimer surface at the start of the CPMD run. The fictitious electron mass was chosen to be 500 a.u., that guaranteed an adiabatic separation between the electronic and ionic degrees of freedom. The kinetic energy of the electrons and ions were controlled using Nosé-Hoover chain thermostats [29]. All hydrogen atoms were assumed to be in deuterated form. The equations of motion were integrated with a time step of 4 a.u. (around 0.096 fs) over a length of 9.5 ps (including 5 ps of equilibration). The total energy was monitored over the entire trajectory and was found to be conserved to 5 parts in 10^8. Atomic configurations and velocities were stored at each time step that were later used for analysis. The *ab initio* simulations were performed on a dedicated 16 node Linux cluster. Although the run length for the CPMD simulations is small, the properties to be discussed in this chapter were found to be well converged within this time duration.

For the calculation of harmonic frequencies, plane wave structure optimization was carried out on a single isolated ion pair with 120Ry energy cutoff using the CPMD code, and the vibrational analysis was carried out using a finite difference method. The spectral assignments were made on the basis of visualization of atomic displacements using Molden software [36].

The shear viscosity at zero shear rate was calculated using the Green-Kubo relation [37],

$$\eta(t) = \frac{V}{k_B T} \int_0^t dt' \langle P_{\alpha\beta}(t'') P_{\alpha\beta}(t' + t'') \rangle \tag{2.1}$$

where V is the volume of the simulation box, and $P_{\alpha\beta}$ denote any of the three off-diagonal elements of the pressure (stress) tensor. The integrand is the stress-stress time correlation function (TCF), $C_P(t)$. The angular brackets denote an average over the arbitrary time origin, t'', at equilibrium. The integral of this TCF converges very slowly, and hence a considerable length of trajectory is required to calculate this quantity. Shear viscosity was calculated as the block average of ten different MD runs, in each of which a trajectory of

1 ns was generated, and the pressure tensor was stored at each time step.

Similarly, the zero-field electrical conductivity of the system that is given by the Green-Kubo relation as [38],

$$\sigma = \frac{1}{k_B T} \int_0^\infty \langle \vec{J}_\alpha(t) \cdot \vec{J}_\alpha(0) \rangle dt \tag{2.2}$$

where $\vec{J}_\alpha$ is given by

$$\vec{J}_\alpha = \sum q_i \vec{v}_{i\alpha} \ , \qquad \alpha = x, y, z \tag{2.3}$$

was calculated using the atomic velocity data stored every time step from eleven independent MD runs each of length 90 ps. From each run, the current-current time correlation function (the integrand in Equation 2.3) was calculated and these were averaged.

A microscopic quantity that is used widely in studying solvation dynamics is the vertical energy difference ΔE between two electronic states of a given solute that is caused due to a redistribution of its charge upon excitation with a laser pulse [39]. This is given by,

$$\Delta E = \Delta U + \Delta E^0 \tag{2.4}$$

where U is the solute-solvent interaction, and E^0 is the solute electronic energy in the ground state. Since the Lennard-Jones interaction between solute and the solvent is assumed to be independent of the electronic states of the solute, it does not contribute to ΔE. Hence the only contribution to it is from the Coulombic interactions.

In this scenario, the solvent dynamics of a solute is often described by a normalized time correlation function ($C_{\delta\Delta E}$(t) or simply, C_s(t)),

$$C_s(t) = \frac{\langle \delta\Delta E(t) \times \delta\Delta E(0) \rangle}{\langle (\delta\Delta E)^2 \rangle} \tag{2.5}$$

where

$$\delta\Delta E = \Delta E(t) - \langle \Delta E \rangle, \tag{2.6}$$

is the fluctuation of ΔE from its equilibrium average. The solvation dynamics of [mmim][Cl]

was studied through equilibrium molecular dynamics simulations of the system by using the cations and anions that are present in the melt, as intrinsic probes. One could thus categorize such calculations as the solvation dynamics of an ion. In addition, dipolar solvation dynamics in the melt was studied by performing separate MD runs in which a rigid dipole was introduced into the system [40]. The dipole probe consisted of two oppositely charged solute atoms, each of magnitude equal to electronic charge ($q = \pm e$). The mass of each of these sites was 100 a.m.u., and the interatomic separation was fixed at 3.5 Å. The Lennard-Jones parameters of each of the solute atoms were, σ=4 Å and $\epsilon/k_B = 100K$. Lorentz-Berthelot combination rules were employed to obtain interaction parameters between this dipole and the atomic sites of the ionic melt. Solvation dynamics of such a dipole was studied using ten different independent MD runs, each of duration 54 ps. We describe here the procedure adopted in one of these runs. A single dipole was inserted at an arbitrary position inside the melt. The system was then equilibrated for 400 ps during which each of the solute atoms of the dipole were assigned a mass of 10 a.m.u. so that the relaxation of the dipole could also contribute to the equilibration. After the initial equilibration, the dipole was further equilibrated for a short period of 15 ps, in which the masses were fixed to 100 a.m.u. Subsequent to these equilibration runs, the data required for the calculation of the solvation dynamics was generated.

In order to ensure that the dipolar solvation TCF is obtained from adequate sampling of the phase space, ten such independent MD runs (blocks) as described above, were performed. In each of these runs, the initial location of the dipolar probe was varied, arbitrarily. The dipolar solvation dynamics reported here is the average over all these blocks. Different combinations of six of these blocks yielded almost equivalent results, thus suggesting that the phase space is properly explored.

Error bars shown in graphs denote error on the mean.

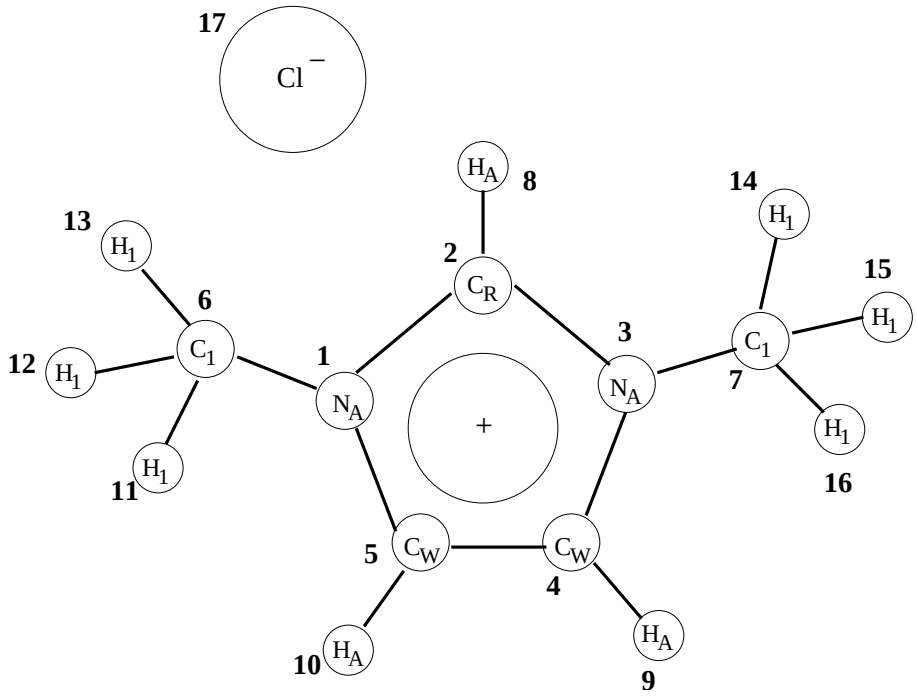

Figure 2.1: Schematic representation of 1,3-dimethylimidazolium chloride, along with the numbering scheme used in the discussion.

2.3 Results and Discussion

Intermolecular Structure:

In order to aid further discussion, we provide in Figure 2.1 a schematic of the cation, describing the atom indices and their connectivity. A few of the bond lengths and the bond angles, obtained from the crystal structure determined from x-ray diffraction [41] and the geometry optimized structure obtained from our CPMD calculations in the isolated (gas) phase are compared in Table 2.1. The calculated geometry of the imidazolium ion is in good agreement with the crystal structure. Most bond lengths are reproduced within 1.5% of experiment. The planarity of the ring too is reproduced in the *ab initio* calculations. The differences between theory and experiment in the cation-anion distance and the angle can be attributed to the fact that the theory is for the gas phase, while the experiment is for the crystalline system.

The partial radial distribution functions, g(r), calculated from classical molecular dy-

Table 2.1: Comparison between the geometry of 1,3-dimethylimidazolium chloride determined from x-ray crystal structure [41] and that from a CPMD optimized configuration in isolated (gas) phase .

Type	Bond Length [Å]	
	Experiment	CPMD
N1-C2	1.32	1.34
N1-C5	1.37	1.39
N3-C2	1.33	1.35
C4-C5	1.34	1.36
C2-H8	1.08	1.12
H8-Cl	2.65	1.98
Type	Angle [degree]	
	Experiment	CPMD
N1-C2-N3	108.3	107.6
N1-C5-C4	107.1	107.0
H8-C2-Cl	28.1	15.3

namics simulations as well as from CPMD are presented in Figure 2.2a. The cation-anion radial distribution function exhibits a peak at 4.6Å and a small hump at 5.8Å. The coordination number integrated up to the first minimum at 6.8Å, is 7.5. The first peaks in the cation-cation and chlorine-chlorine correlation functions are present at 4.1Å and 6.4Å respectively. In an earlier study [15], the first peak of the cation-cation g(r) was reported to be present around 5.1Å. A possible reason for the shorter distance observed in our sample is likely to be due to preferential ordering in cation orientations, a feature that will be discussed later. An additional reason could be the larger system size employed here. Although the first peak in the cation-cation function is present at a slightly lesser distance than the cation-anion one, the first coordination shell around the cation is overwhelmingly dominated by the anion, as expected. This is demonstrated in Figure 2.2b, that shows the running coordination number corresponding to the three distinct pairs of species. Thus, our results confirm that charge ordering prevails in this ionic melt, consis-

tent with the classical MD [16, 42] and the *ab initio* MD results [15]. The hump observed in the cation-anion g(r) at 5.8Å is due to chloride ions in the first coordination shell that are present along the direction of the methyl groups attached to the nitrogen atoms. This can be seen from Figure 2.3, that shows the atomic probability density map of locating chloride ions that are present between 5.5Å and 6.8Å from the geometric centre of the imidazolium ring (i.e., the distance range of the hump feature). It is clear that we find a finite probability for the presence of chloride ions only in the direction along the methyl groups.

The apparently good agreement between the pair correlation functions from classical MD and *ab initio* MD masks subtle, but crucial differences. Site-site g(r)s, in particular the pair correlation function between the chloride and the H8 hydrogen are distinctly different between the two simulations. Note that the H8 hydrogen is unique in the 1,3-dimethylimidazolium ion and it is known to be an acidic site. Even in the crystal, the C-H distance for this proton is 0.01Å larger than the C-H distances of the other two ring carbons. In Figure 2.4, we compare this pair correlation function between the two simulations and contrast its behavior with the g(r) of H9-Cl (or, that of H10-Cl). The latter hydrogens are also attached to carbons in the ring, but are not unique. The peak position of the RDF of chloride ions around the unique hydrogen has moved from 2.8Å in the classical MD simulations to 2.35Å in the CPMD simulations, suggesting the formation of a hydrogen bond between the unique hydrogen and the chloride ions, a feature that was also reported by Del Pópolo *et al* [15]. The coordination number of one, is evidence for the formation of such a bond. The distance between H9 and chloride too has shortened in the CPMD simulations relative to classical MD. These suggest the necessity of further refinement of the hydrogen-chlorine interaction potential.

The probability distribution of the chloride ions around the 1,3-dimethylimidazolium cation, $\Omega_{Cl}(r, \theta, \phi)$, calculated from MD simulations with the empirical potential is shown in Figure 2.5a. It can be seen that the probability of locating chlorine atoms is larger

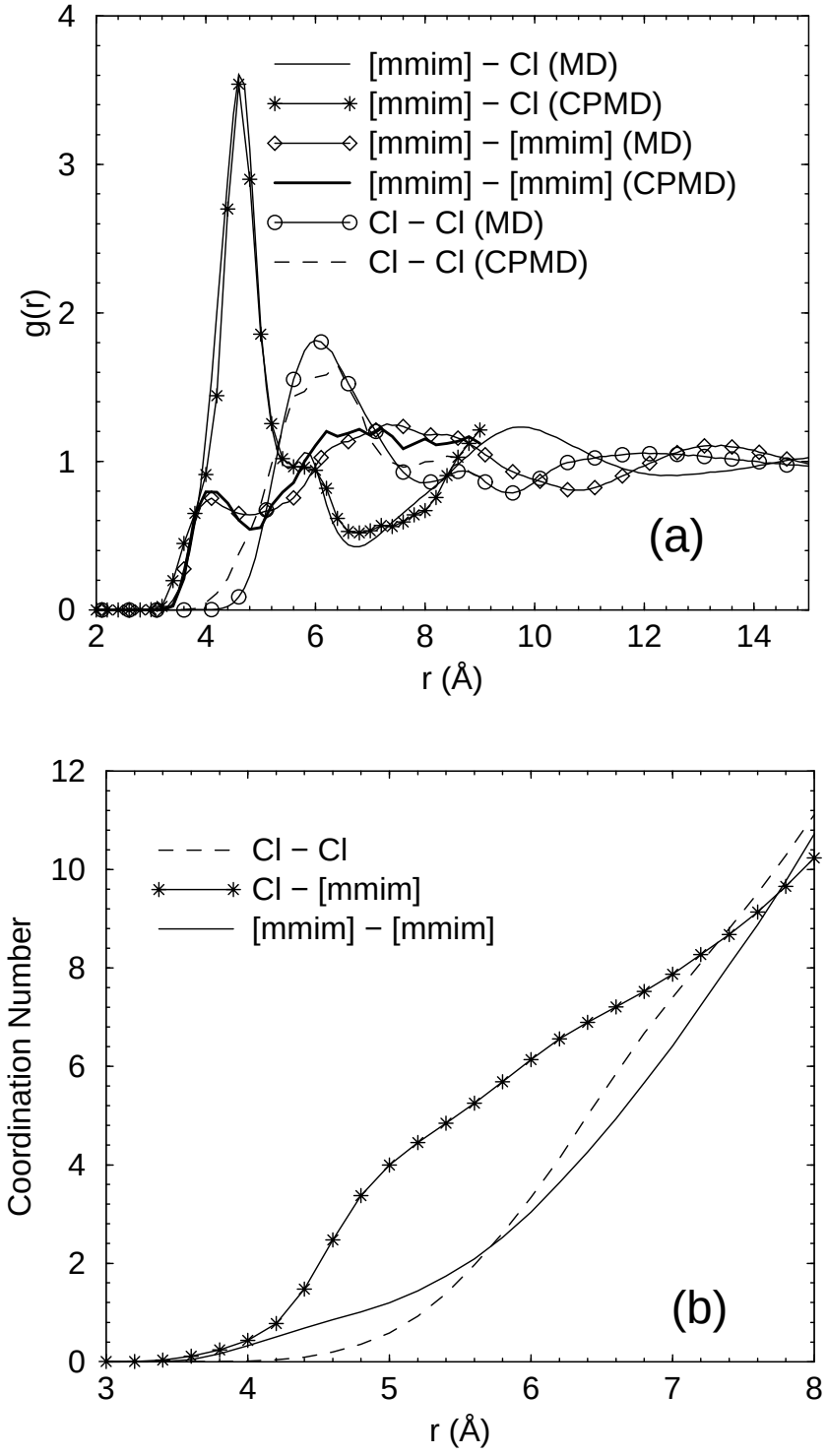

Figure 2.2: (a)Comparison of anion-anion, cation-anion, and cation-cation partial radial distribution functions, calculated from classical MD as well as from CPMD simulations. The cation position corresponds to the geometric centre of the imidazolium ring. Symbols are shown infrequently for clarity. (b) The running coordination number for the distinct pairs in [mmim][Cl] obtained from CPMD calculations

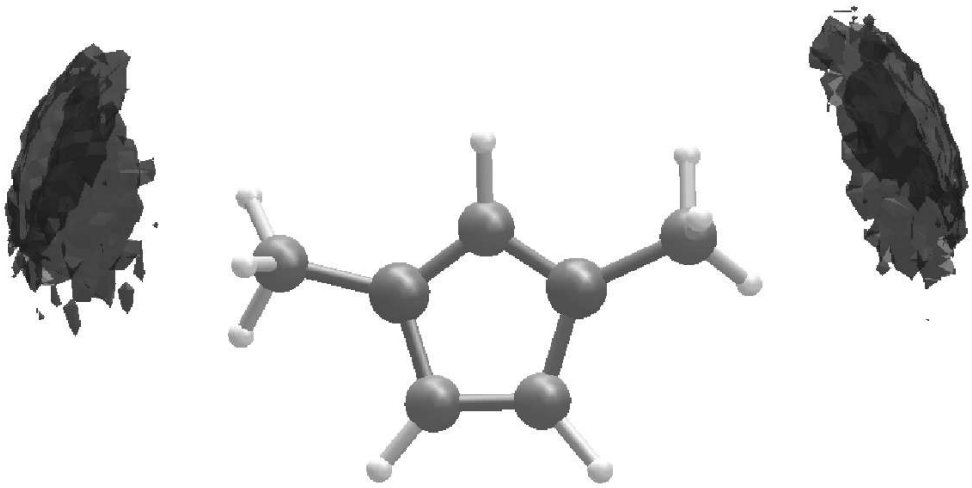

Figure 2.3: The spatial distribution of chloride ions present within a spherical shell of radii 5.5Å and 6.8Å, centered around the cation, obtained from the classical MD simulations. The isosurface at a density of $0.015/\text{Å}^3$, that is three times the average number density of the chloride ions is shown.

near the ring hydrogens. Strangely, the interaction model predicts a reduced probability just above the unique hydrogen that is connected to C2. The spatial density distribution obtained from the CPMD calculations shown in Figure 2.5b at the same contour level as the classical result, is revealing. Notably, the density hole seen above the acidic proton in classical simulations is filled up in the CPMD simulations, consistent with the recent *ab initio* work of Del Pópolo *et al* [15], and the neutron scattering data [10]. The density of chloride ions near the unique hydrogen as predicted by CPMD is more than three times larger than that from classical MD. This clearly indicates the formation of the hydrogen bond between the unique hydrogen and the chlorine. Our classical MD simulations were also repeated on a 32 ion pair system at the experimental density. These simulations too

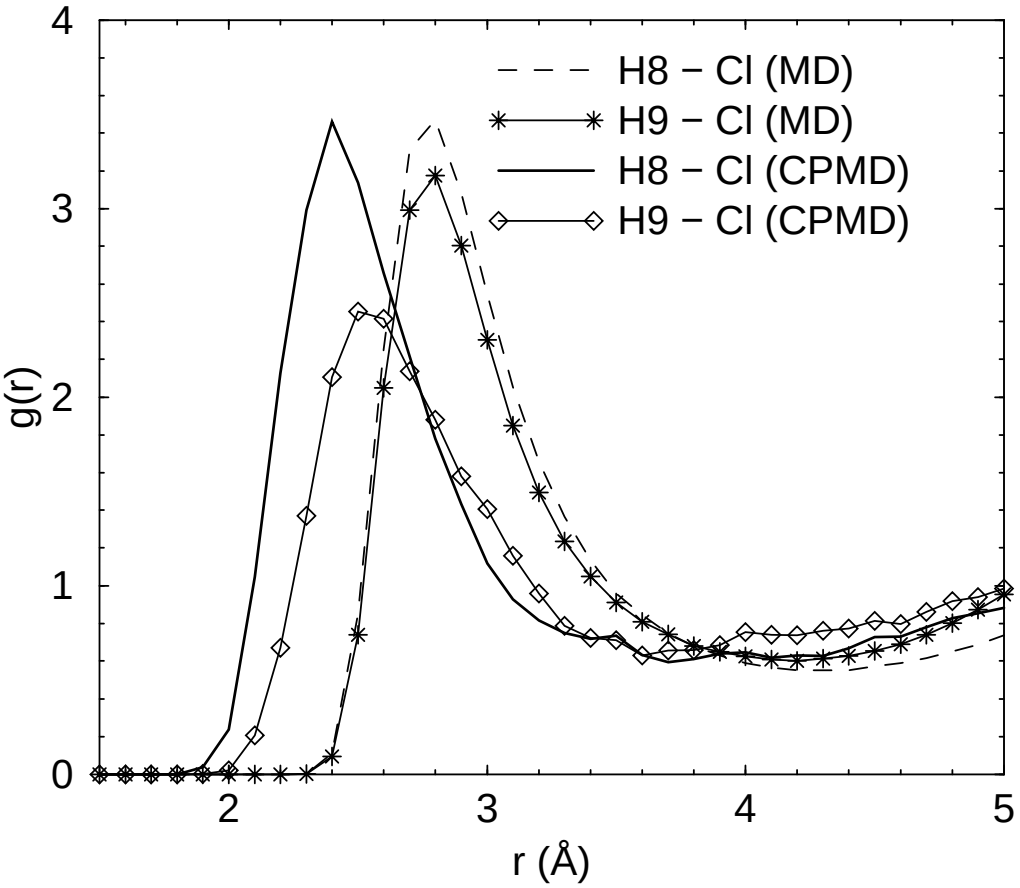

Figure 2.4: Comparison of the partial radial distribution functions of the chloride ions around the unique hydrogen (H8) of the imidazolium cation, calculated from classical MD as well as from CPMD simulations. The pair correlation functions of the non-unique hydrogen (H9) with chlorine are also shown. The behavior of H10-Cl g(r) is similar to that of H9-Cl and hence is not shown.

yielded a similar spatial distribution as the 864 ion pair system, eliminating the cause of difference as due to system size effects. Another major difference between the classical MD results and that from CPMD is illustrated in Figures 2.5c and 2.5d. These density distributions are the same as in Figures 2.5a and 2.5b, but are shown such that the plane of the central imidazolium ring is perpendicular to the plane of the paper. The difference between the classical MD result and CPMD is striking. While classical MD predicts two lobes of high occupancy for chloride ions in the plane of the cation along the two ring C-H vectors, CPMD predicts some occupation away from the ring plane also.

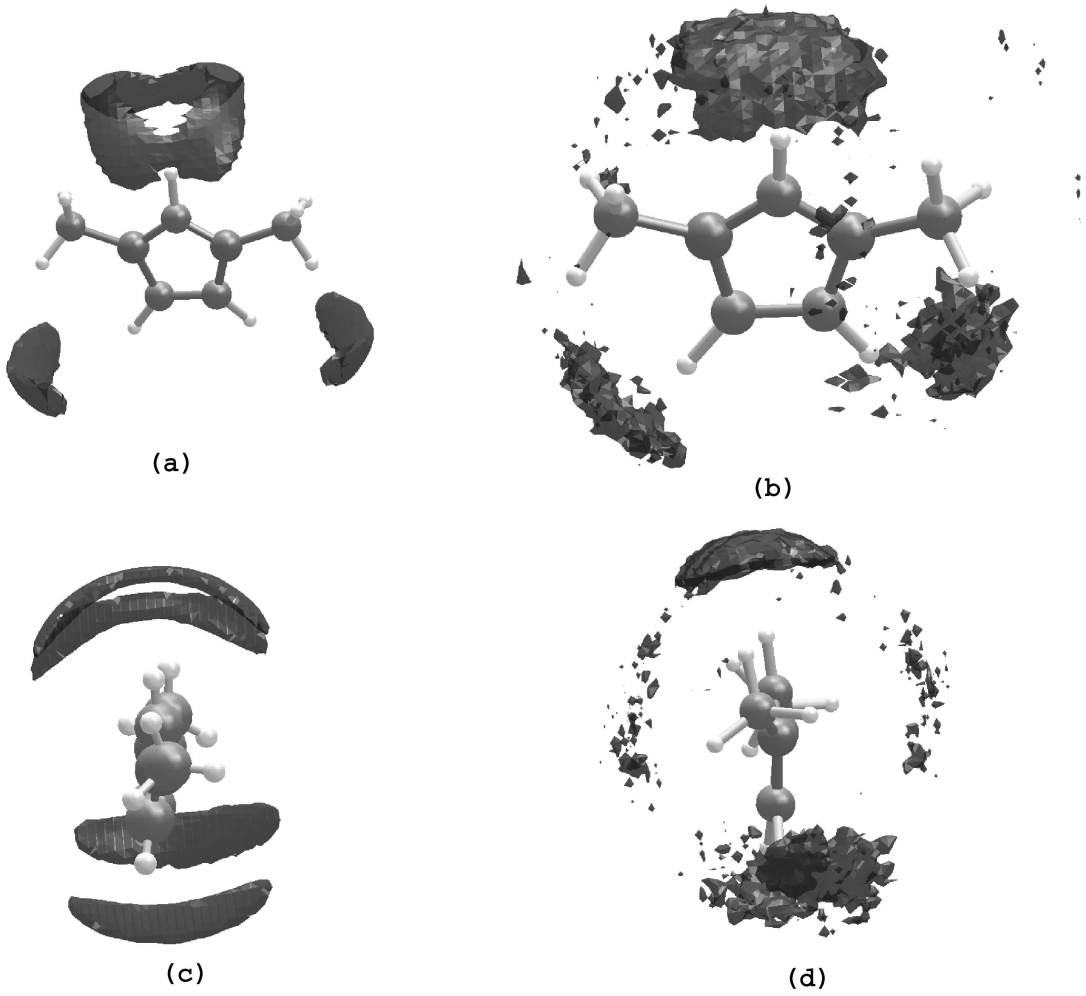

Figure 2.5: The spatial distribution of chloride ions around the cation, at an isosurface value of 0.0375/Å^3. (a) Top view from classical MD (b) Top view from CPMD (c) Side view from classical MD (d) Side view from CPMD.

As discussed earlier, the distribution of cation centers around a given cation is rather interesting, and exhibits a peak at 4.1Å. We would like to understand the orientational preferences (if any) between neighboring imidazolium rings. In Figure 2.6, we show the distribution of the angle between the normals to the ring planes of neighboring cations (i.e., cations within 4.8Å, the distance corresponding to the minimum of the first peak in the cation-cation g(r)). There is a clear preference for the neighboring rings to be parallel to each other – a feature that is likely to signify $\pi - \pi$ interactions between the imidazolium

rings. This fact is further demonstrated by calculating the spatial distribution of the cations around a cation within 4.8Å. Figure 2.7 presents the spatial distribution discussed above at an isosurface value of 0.0125Å^{-3} that is about 2.5 times the average number density of the cations. It is seen from the figure that the highest probability for the cation ring centers is above and below that of a cation ring within the first coordination shell. Since [mmim][Cl] is a planar molecule, the SDF suggests that the cation planes in the near neighborhood orient themselves parallelly. Such a parallel orientation is also observed in the crystal structure of [mmim][Cl]. Thus, the structure of the melt has many parallels with that of the crystal.

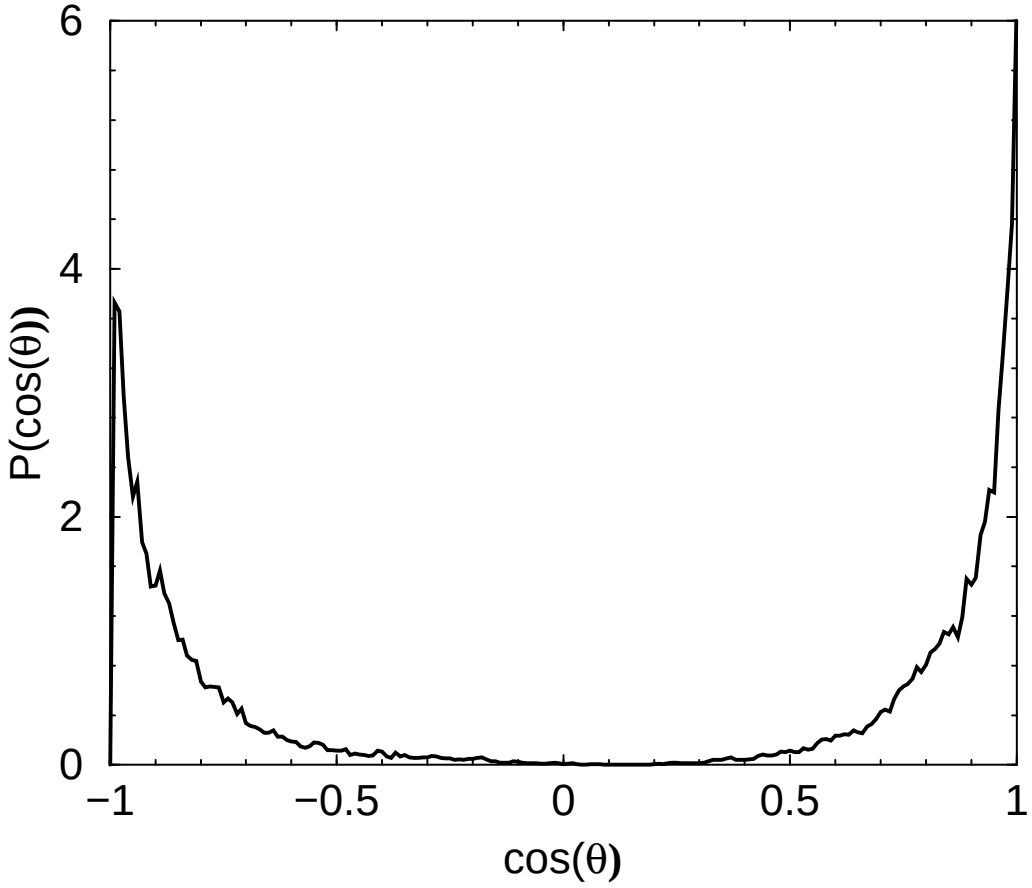

Figure 2.6: Probability distribution for the orientation of near-neighbor cations around a central cation. θ is the angle between the normals to the imidazolium ring of two neighboring cations.

It emerges from these analyses that the first coordination shell of anions surrounding

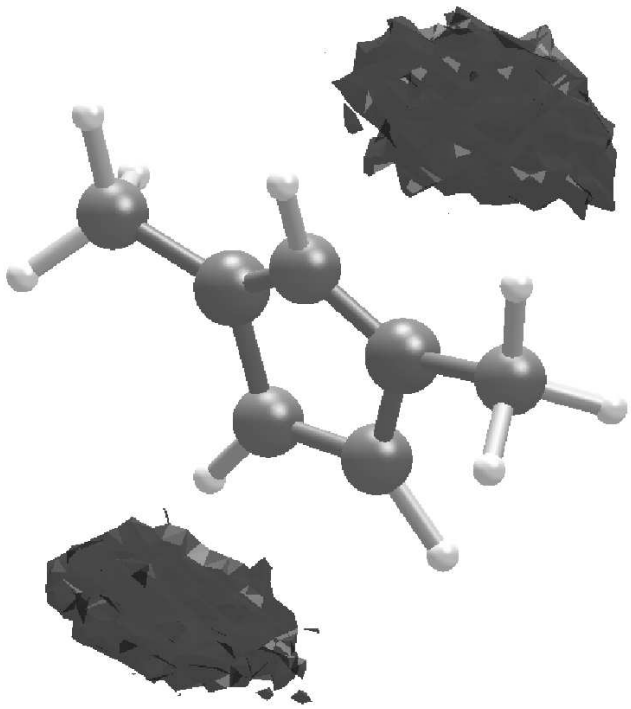

Figure 2.7: Spatial distribution of cation ring centers around a cation ring center within the first coordination shell at an isosurface value of 0.0125Å^{-3} that is 2.5 times the average number density of the cations.

the cation is rather anisotropic [11]. Two aspects contribute to this conclusion. Firstly, the shape of the cation influences the anion position along the direction of the methyl groups, so as to construct a non-spherical first coordination shell. Secondly, the hydrogen bond between the acidic proton (H8) and the anion too makes the chloride ion to approach the cation closer along that direction.

Frequency spectrum and spectral assignments:

The vibrational density of states (VDOS) of [mmim][Cl] melt was calculated as the Fourier transform of the normalized velocity autocorrelation function (VACF) of all the atoms in the system. In Figure 2.8, we show this result obtained from the CPMD tra-

jectory. The corresponding data from classical MD is not shown as most of the features in the spectrum arise from intramolecular vibrations that in any case are built into the parameter set of the empirical potential. Note that the CPMD calculations employed deuterium instead of hydrogen, and hence the modes associated with hydrogen are shifted towards lower frequencies. The features in the range of 2000-2400 cm^{-1} correspond to C-D stretch with the higher frequency peaks corresponding to the ring C-D stretch.

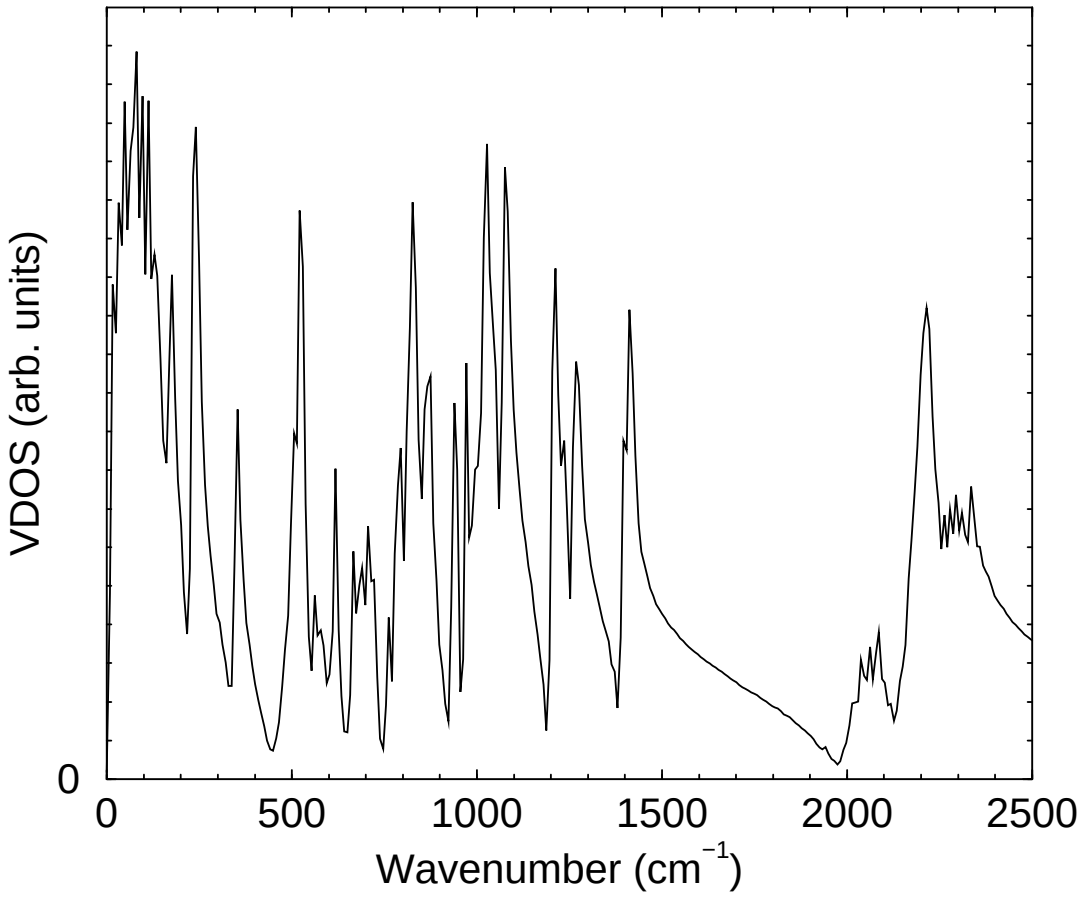

Figure 2.8: Power spectrum obtained as the Fourier transform of the velocity autocorrelation function of all the atoms from the CPMD run.

The formation of a cage around the chloride ions is evident from the presence of a clear peak at 115 cm^{-1} in its frequency spectrum, (Figure 2.9) corresponding to its rattling within the cage. Note that classical MD too is able to capture this frequency quite accurately.

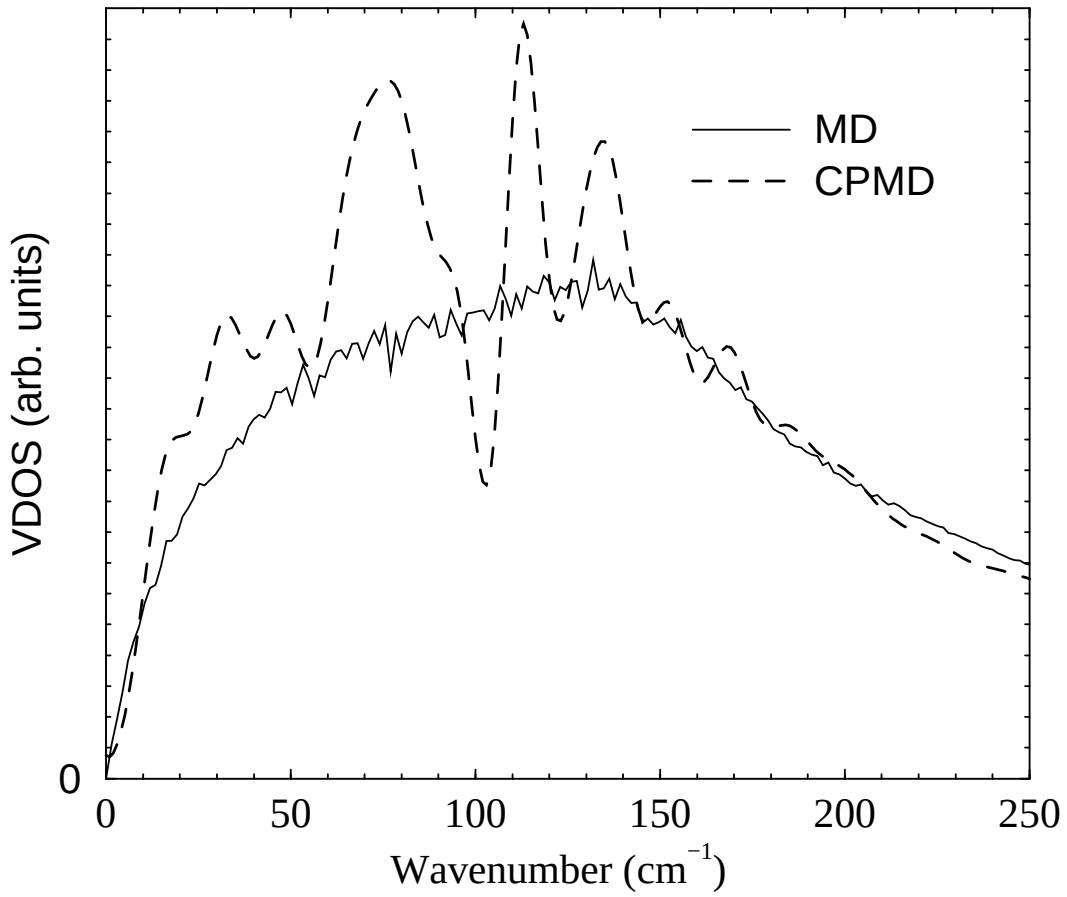

Figure 2.9: Power spectrum obtained as the Fourier transform of the velocity autocorrelation function of chlorine atoms. The spectrum corresponding to CPMD data has been smoothened using a cubic spline fit.

The frequencies associated with the nitrogen atoms are intense in the region around 1200 cm^{-1}, whereas the frequency corresponding to C_W-C_W stretch is present at 1430 cm^{-1}. The vibrations corresponding to the methyl C-D occur in the range of 2000 - 2150 cm^{-1}. From an analysis of the independent VACF's of the atoms, that gives frequencies associated with only those atoms, it was found that the C-D stretch corresponding to the unique hydrogen (H8) occurs at a lower frequency (2225 cm^{-1}) compared to the C-D stretches involving other hydrogen atoms (2335 cm^{-1}) of the ring (H9 and H10). The former forms a strong hydrogen bond than the latter, and consequently its C-D stretch frequency is red shifted, as seen in Figure 2.10. Such a red shift in the frequency of the intramolecular stretching mode is often used by spectroscopists to identify hydrogen bonding, or in gen-

eral, complexation or association of a molecule with another. We have thus been able to demonstrate the presence of the hydrogen bond between the H8 atom of the cation and the chloride ion not only through structural data but also through the vibrational dynamics of the cation. The latter is of direct relevance to experiments. However, it should be noted that DFT is found to under-estimate the frequencies and the length scales over which the data is averaged to obtain the vibrational density of states is also limited.

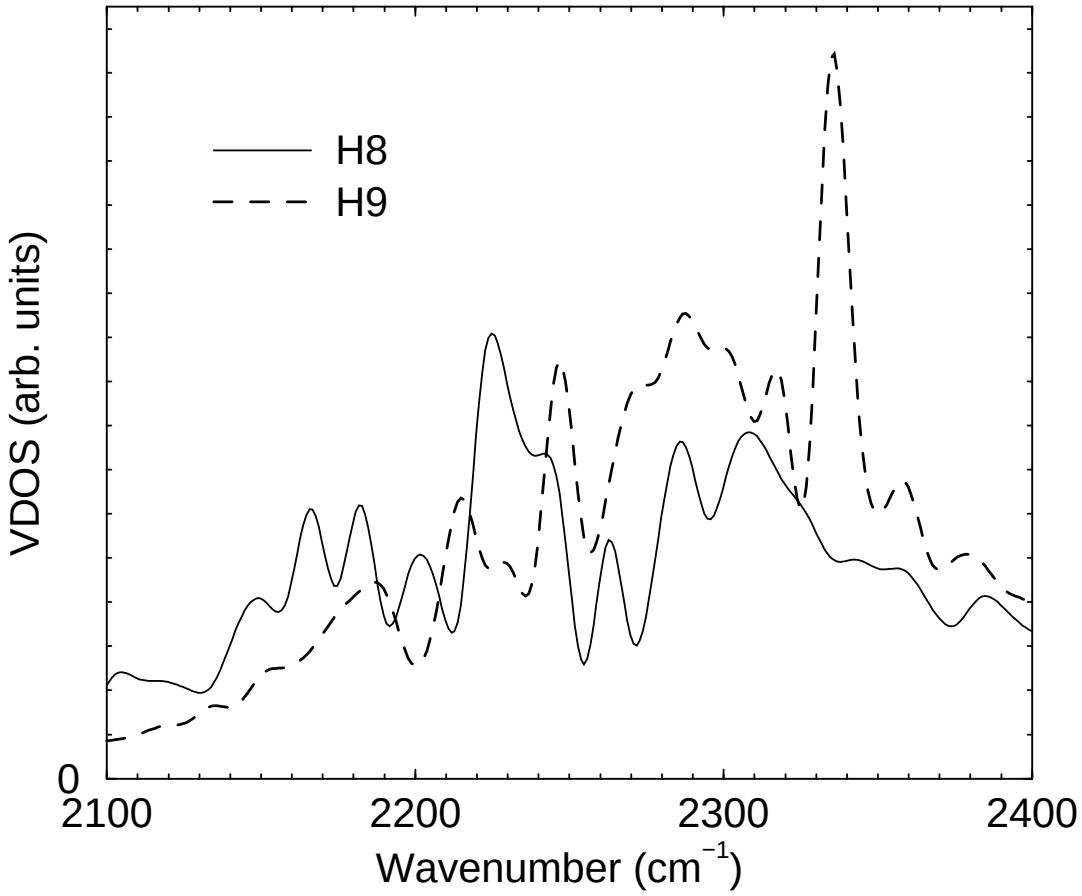

Figure 2.10: Power spectrum obtained as the Fourier transform of the velocity autocorrelation function of H8 and H9 (or H10) atoms. The spectra have been smoothened using a cubic spline fit.

In order to assign the various modes in the power spectrum, we have also performed Hessian analysis of the optimized geometry of an isolated [mmim][Cl] ion pair (gas phase) using the CPMD program. Atomic displacements obtained from that analysis were visualized using Molden software [36], and were used to assign the modes. Mode frequencies and

their assignments are provided in Table 2.2. The frequencies obtained here are consistent with spectroscopic experiments on similar kind of systems [43, 44].

2.4 Transport properties

2.4.1 Diffusion

The self diffusion coefficient of the cation and the anion are calculated from their mean squared displacements. The block average of mean squared displacement calculated from ten independent MD runs, along with the results from a single continuous MD run of 6 ns duration are shown in Figure 2.11. The cation, despite being heavier than the chloride ion, diffuses faster, that is also observed experimentally in similar systems [45]. Figure 2.11b shows the same data for a longer duration, that confirms this finding. This behavior in the diffusion can be reasoned from the average potential energies of the cation and that of the anion. The mean potential energies for the chloride ion and for the cation are calculated to be $-72 \times 10^3 K$, and $-23.6 \times 10^3 K$ respectively. Thus the chloride ion is locked in a deeper potential well compared to the cation and hence diffuses slower. However, in the short time range, inertial behavior is observed as expected, where the lighter chloride ion diffuses faster than cation (inset of Figure 2.11a). The crossover time at 425K is around 15 ps.

The self diffusion coefficient is given by the Einstein relation,

$$D = \frac{1}{6} \lim_{t \to \infty} \frac{d}{dt} \langle |\vec{r}_i(t) - \vec{r}_i(0)|^2 \rangle \tag{2.7}$$

The self diffusion coefficients for the anion and cation at 425 K are found to be $0.222 \times 10^{-10} m^2 s^{-1}$ and $0.313 \times 10^{-10} m^2 s^{-1}$ respectively. The diffusion co-efficients for [mmim][Cl] modeled using a different interaction potential by Hanke *et al* [12], are higher compared to our results. Apart from differences in the interaction potential, the length of

Table 2.2: Table of harmonic frequencies along with their assignment to different normal modes

Wavenumber (cm^{-1})	Assignment
103,131	CD_3 twist
172,259	cation-anion stretch
210	cation-anion bend
293,543	C_1 -N_A -C_R -N_A torsion
369	C_R -N_A -C_1 sym bend
538	C_R -N_A -C_W sym. bend, N_A -C_1 asym. stretch
562	C_R -N_A -C_W -D_A torsion
600	N_A -C_W -C_W -N_A torsion
639	N_A -C_W -C_W sym. bend
701	D_A -C_W -C_W -D_A torsion
772	D_A -C_R -N_A -N_A improper torsion
788	D_A -C_W -C_W sym. bend
825,841,858	N-C-D asym. bend
893	C_1 -N_A -C_R -C_W improper torsion
902	N_A -C_1 -D_1 sym. bend, ring o.p. bend
937	C_R -N_A -C_W sym. bend
1010	C_W -N_A -C_W i.p. bend, N_A -C_R sym. stretch
1020	C_W -C_W -N_A asym. bend, C_W -N_A -C_R sym. bend
1048,1055,1059,1062	D_1 -C_1 -D_1 sym. bend
1097	N_A -C_1 sym. stretch, D_1 -C_1 -D_1 sym. bend
1109	N_A -C_1 sym. stretch, D_1 -C_1 -D_1 sym. bend, C_W -C_W -N_A sym. bend
1273,1284	N_A -C_W sym. stretch, N_A -C_R -N_A sym. bend
1317	C-N sym. stretch
1451	ring i.p. asym. stretch
1474	C_W -C_W sym. stretch, C_R -N_A -C_W sym. bend
1881	C_R -D_A stretch
2113,2141	C_1 -D_1 sym. stretch
2247,2262,2266,2286	C_1 -D_1 asym. stretch
2365	C_W -D_A asym. stretch
2402	C_W -D_A sym. stretch

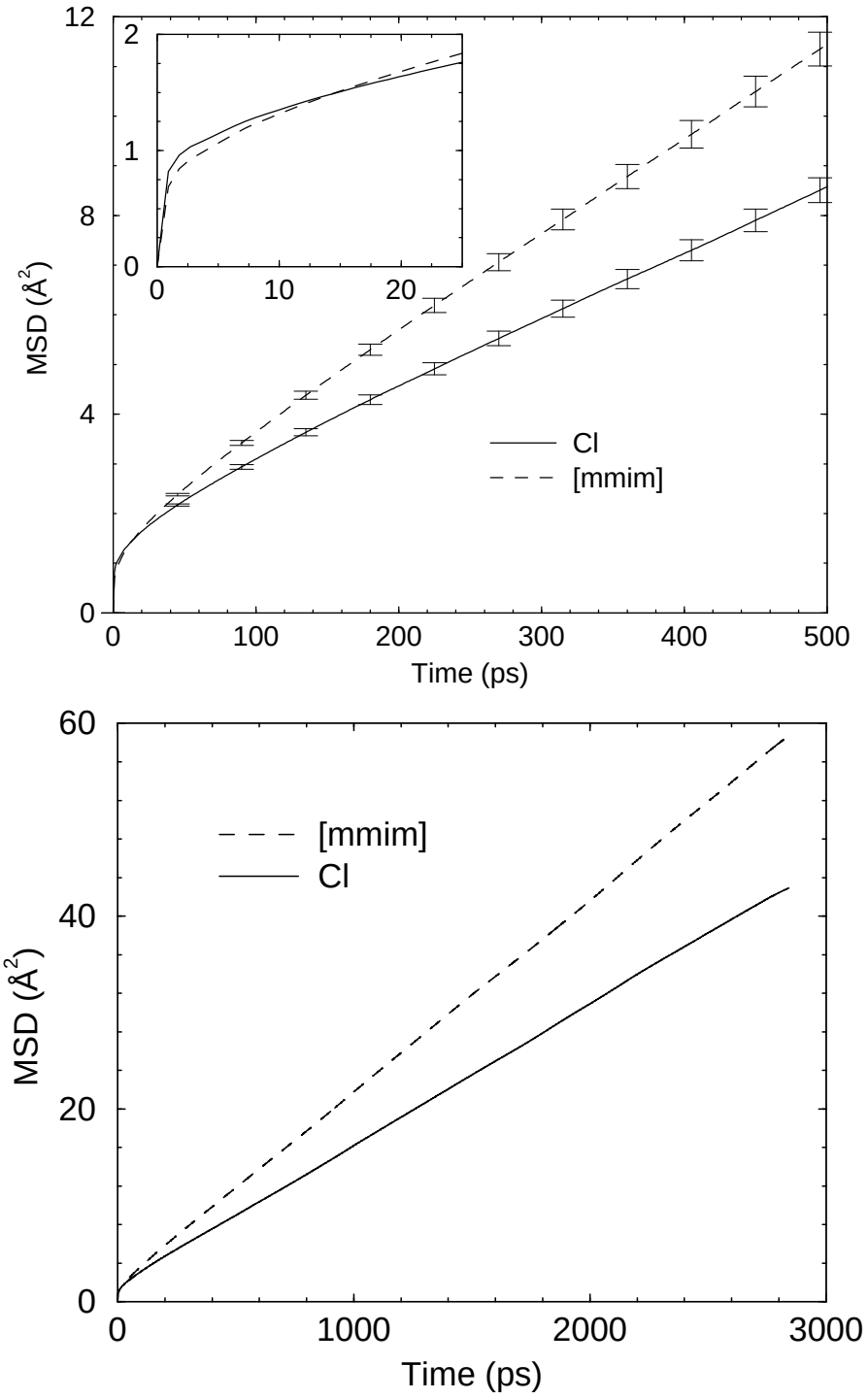

Figure 2.11: (a) Mean squared displacement data of [mmim][Cl] at 425K, as an average over ten independent blocks along with error bars. Inset shows the same data at short times. Note the larger inertial motion of chloride ions, as expected. (b) Mean squared displacement data of [mmim][Cl] at 425K, from a single long trajectory of 6 ns.

the simulations and the time range of the MSD data from which the coefficients (slope) are obtained could also contribute to the differences in the results. In general, it appears that the united atom model predicts lower self diffusion constants [12, 46].

2.4.2 Shear Viscosity

The short time behavior of the normalized stress-stress correlation function, $C_P(t)$ (the quantity within the angular brackets in Equation 2.1) is shown in Figure 2.12. The rapid oscillations arise from the high frequency intramolecular vibrational modes of the cation. Notice the overall slow decay of the curve, that indicates the timescales of relaxation of stress in this system.

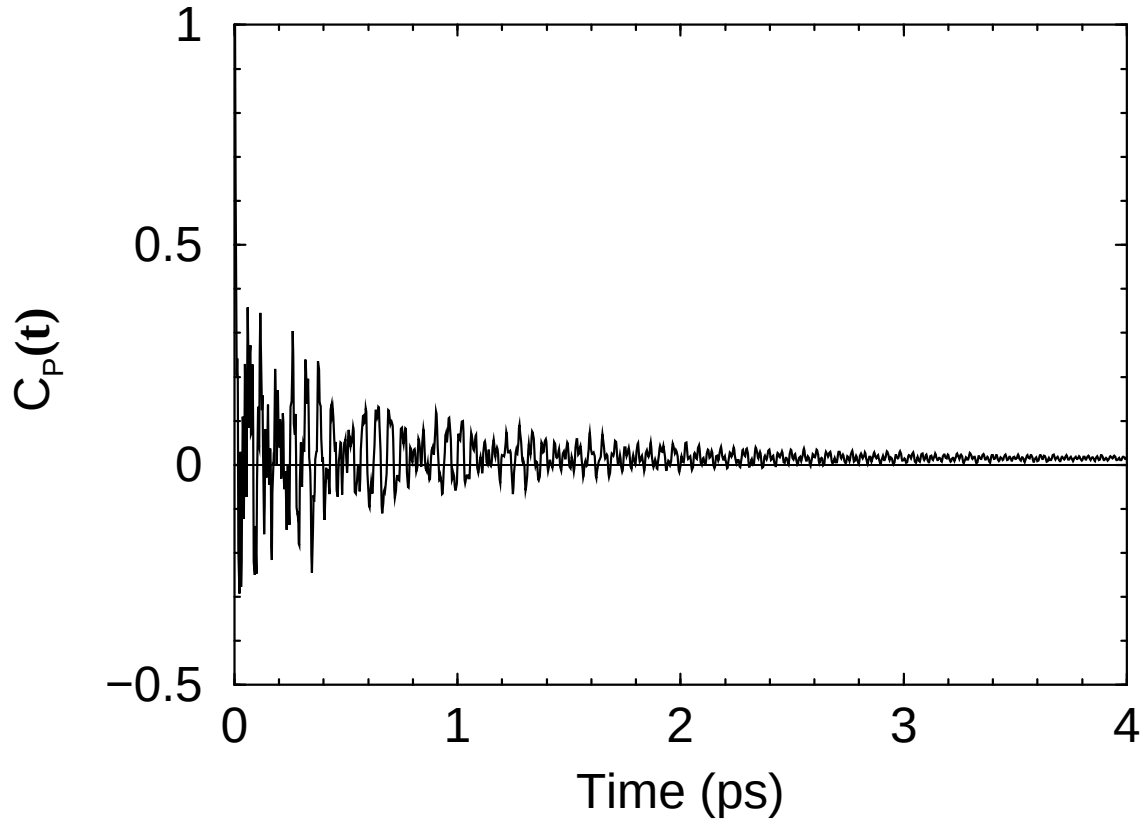

Figure 2.12: Self time correlation function of off diagonal components of the stress tensor at 425K, $C_P(t)$.

The running integral for the shear viscosity obtained from Equation 2.1 is presented

in Figure 2.13. We estimate the shear viscosity of [mmim][Cl] obtained from the current interaction model to be 0.048 ± 0.010 Pa.s at 425K. Experimental data on the viscosity of [mmim][Cl] is not available, however a comparison with the next member in the homologous series, i.e., 1-ethyl,3-methylimidazolium chloride, [emim][Cl] can be made. The latter is reported to have a viscosity of 0.018 Pa.s at 425K [24]. Note that [emim][Cl] has a lower molecular (point group) symmetry than [mmim][Cl] and hence it melts at a temperature of 357 K, [47,48] a clear 38 degrees lower than the melting point of [mmim][Cl]. Despite its higher melting point, [mmim][Cl] should actually have a lower viscosity than [emim][Cl] at a given temperature. This trend among the homologous 1,3-alkylimidazolium chlorides can be observed in the values of shear viscosity reported by Seddon *et al* [24], where the variation is monotonic, except for the compounds with high water contents. Voth *et al* [49] have studied the effect of electronic polarizability on diffusion constants and viscosity in the ionic liquid, [emim][NO_3]. They have found that the polarizable model predicts a diffusion constant that is three times higher than the non-polarizable model, and also predicts the viscosity of the system closer to experiment compared to the latter. They have concluded that the inclusion of polarizability make the ions more mobile, and is similar to performing the molecular dynamics of non-polarizable model at a higher temperature. Our results too point to the need for including polarizable interactions in order to obtain accurate model estimates of shear viscosity.

2.4.3 Electrical conductivity

In Figure 2.14, we provide the running integral corresponding to electrical (ionic) conductivity calculated as an average of 10 independent blocks from our simulations. The electrical conductivity of [mmim][Cl] is calculated to be 0.0089 Scm^{-1} at 425K, that is an order of magnitude smaller than the experimentally measured electrical conductivity at the same temperature, that is 0.106 Scm^{-1} [48]. It needs to be verified if this difference is due to deficiencies in the potential model. It should also be noted that ionic liquids such

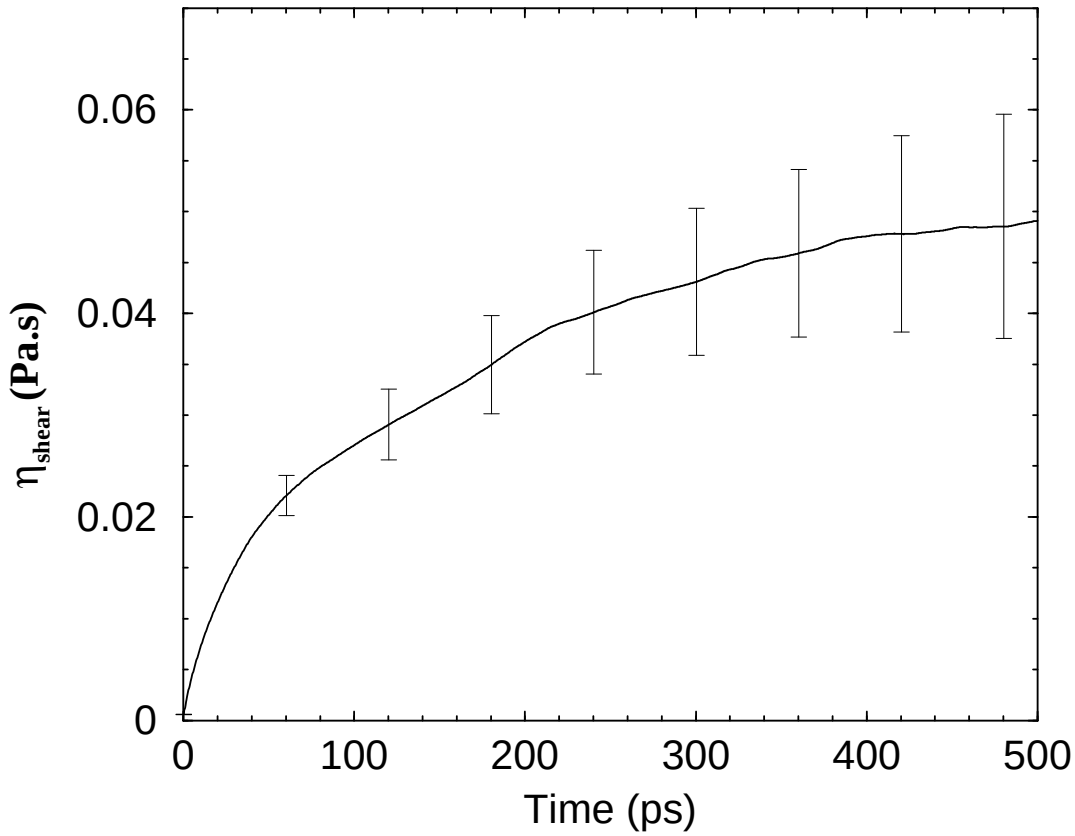

Figure 2.13: Running integral (see Equation 2.1) representing the shear viscosity of [mmim][Cl] at 425K.

as [mmim][Cl] are quite hygroscopic and readily absorb water. Hence further calculations such as those performed here must be carried out for other ionic liquids for which precise conductivity data has been experimentally determined for pure samples. However, it appears that the potential model underestimates ionic conductivity and overestimates shear viscosity of the melt, relative to experimental estimates. The inset to Figure 2.14 shows the mean running integral for σ obtained from individual blocks.

The ionic conductivity of a system can also be calculated using the Nernst-Einstein relation [38],

$$\sigma_{NE} = \frac{Ne^2 D_{self}}{Vk_B T} \tag{2.8}$$

where σ_{NE} is the ionic conductivity, N is the number of ions in the simulation cell, T is the temperature in Kelvin, e is the electronic charge, k_B is the Boltzmann's constant,

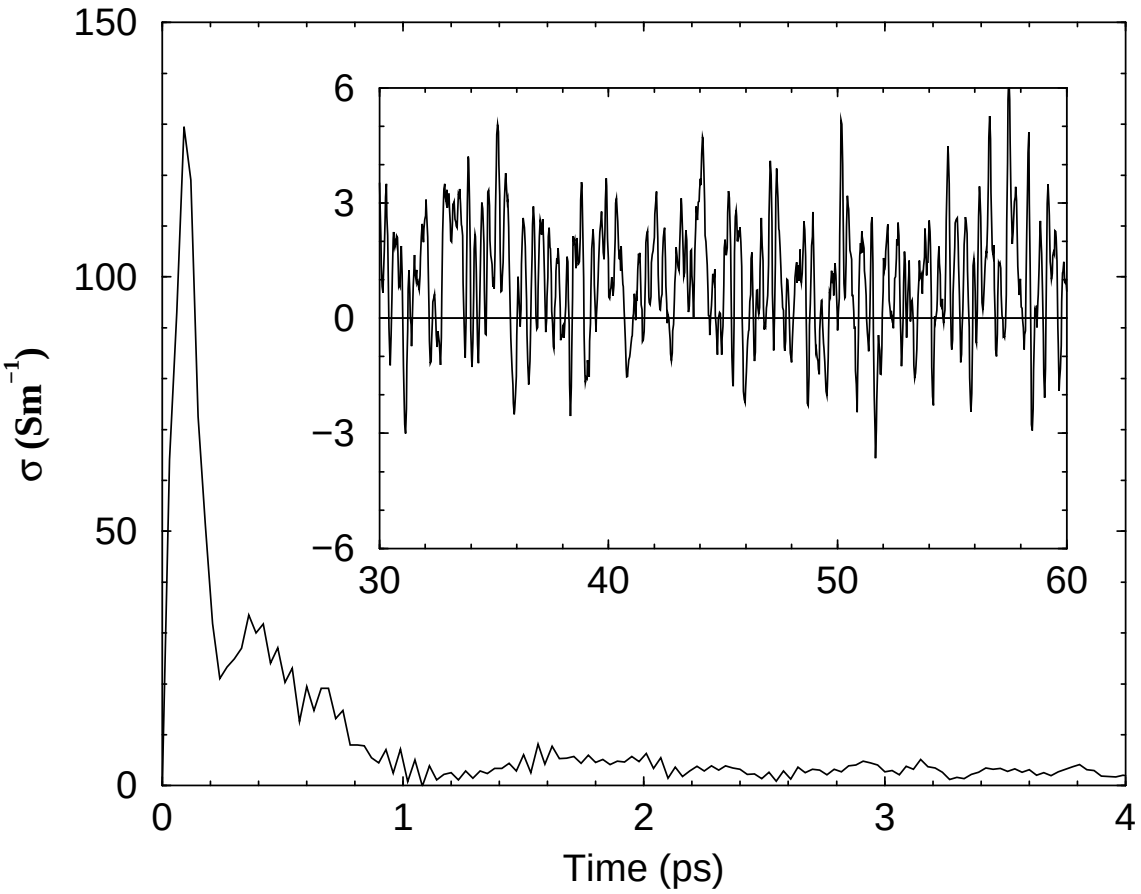

Figure 2.14: Running integral representing the electrical conductivity of [mmim][Cl] at 425K up to 4 ps (See equation 2.3). The inset is the same quantity shown between 30 and 60 ps.

D_{self} is the self diffusion coefficient, and V is the volume of the simulation cell. This relation is valid only under the condition that both diffusion of ions and their contribution to conductivity take place by the same mechanism. The conductivity calculated from Equation 2.8 is 0.0118 Scm^{-1}, that is 32.6% higher than the value obtained from Green-Kubo relation. The Nernst-Einstein relationship ignores cross correlations between the cationic and anionic currents. In addition, displacements of ion pairs together would contribute to the Nernst-Einstein estimate calculated through Equation 2.8, but would not lead to a measurable electrical conductivity. In this respect, [mmim][Cl] behaves similar to a conventional ionic melt such as sodium chloride [50]. Our conclusions are also in agreement with the findings of Voth and coworkers [49].

2.4.4 Solvation dynamics

Firstly, we discuss the calculation of the solvation dynamics TCF for the dipolar probe. As mentioned earlier, the solute atoms that constitute the dipole each have a mass of 100 a.m.u. Such a large mass is often necessary as the probe dipole could otherwise rotate or translate [40]. These motions can make the energy-energy correlation function (Eq. 2.5) to decay fast even if the solvent relaxation itself is slow. Under such conditions, an interpretation of the relaxation of this function as due to the solvent can be erroneous. In order to ensure that the solvation TCF can be unerringly associated with solvent dynamics, we have calculated the mean squared displacement of the probe dipole as a function of time, and found that it does not have any positive slope at long times (i.e., it is non-diffusive), and that the maximum displacement is only 1Å. Further, we have calculated the reorientational TCF of the dipole vector and have found that it does not decay with time. Hence it can safely be assumed that the solvation TCF calculated here is representative of the relaxation of the solvent. The large mass of the probe dipole and thus its restricted mobility imposes a constraint on adequate sampling of the solvation TCF. This fact necessitates that one performs MD runs from several independent starting configurations, in each of which the probe dipole is positioned at different locations of the liquid. As remarked in the section on Simulation Details, we have generated such trajectories from ten different initial configurations. The fluctuations in the Coulomb energy were calculated from the average over all the ten different configurations. The Coulomb energy of the dipole was calculated by summing up all of its interactions (from both its sites) with site charges located on the atoms of cations and anions. As mentioned earlier, the site charges on the solvent ions are obtained from the all-atom interaction model developed by Padua and coworkers [17]. The Coulomb energy so obtained was averaged over time and all the blocks to get the equilibrium energy. The time correlation function of the fluctuation of the instantaneous energy with respect to this average energy represents the solvent relaxation.

The equilibrium solvation TCF for the case of the dipole probe is shown in Figure 2.15. The total potential energy of the dipolar probe can be split into contributions arising from its interactions with the anions and the cations of the ionic liquid. Thus the total solvation TCF can be written as a sum of three partial time correlation functions – two of them that are self TCFs (anion-anion and cation-cation) and a third that is a cross time correlation function. These partial time correlation functions (normalized by the t=0 value of the total TCF) are also shown in Figure 2.15. The oscillations present in the total solvation TCF mirrors that seen in the anion contribution. The latter is a reflection of the rattling of the chloride in the cage formed by the imidazolium cations, a process that is observed at a frequency of 130 cm^{-1} in the power spectrum of the velocity autocorrelation function (VACF) of the anions. In the inset to Figure 2.15, we demonstrate this fact by comparing the VACF of the anions against the anion contribution to the dipolar solvation TCF.

The dipolar solvation TCF obtained above is truly representative of the solvent dynamics. However, obtaining these trajectories in the presence of a dipole for long times is tedious. It would be worthwhile if one could obtain an idea of the solvent dynamics as probed by dipolar solvation TCF, *without the use of a dipole*. We explore this possibility here. Figure 2.16 compares the decay of the solvation time correlation function for the cases of (i) the ionic dipole used as a probe, and (ii) the chloride ion intrinsic to the ionic liquid itself used as a probe.

Despite differences in the ultrafast region, the two TCFs are surprisingly similar for time values in the range of tens of picoseconds. Calculation of the solvation time correlation function through the use of an ionic dipole is more time consuming than the study of the pure solvent. In typical situations, one uses only one probe dipole for the entire system, and the initial location of the probe has to be varied to obtain a good sampling of the solvent dynamics. Thus the quality of the solvation TCF, particularly at large time values will not be good due to poor averaging. The close similarity between the two curves in Figure 2.16 validates the use of the anion itself as a probe for the study

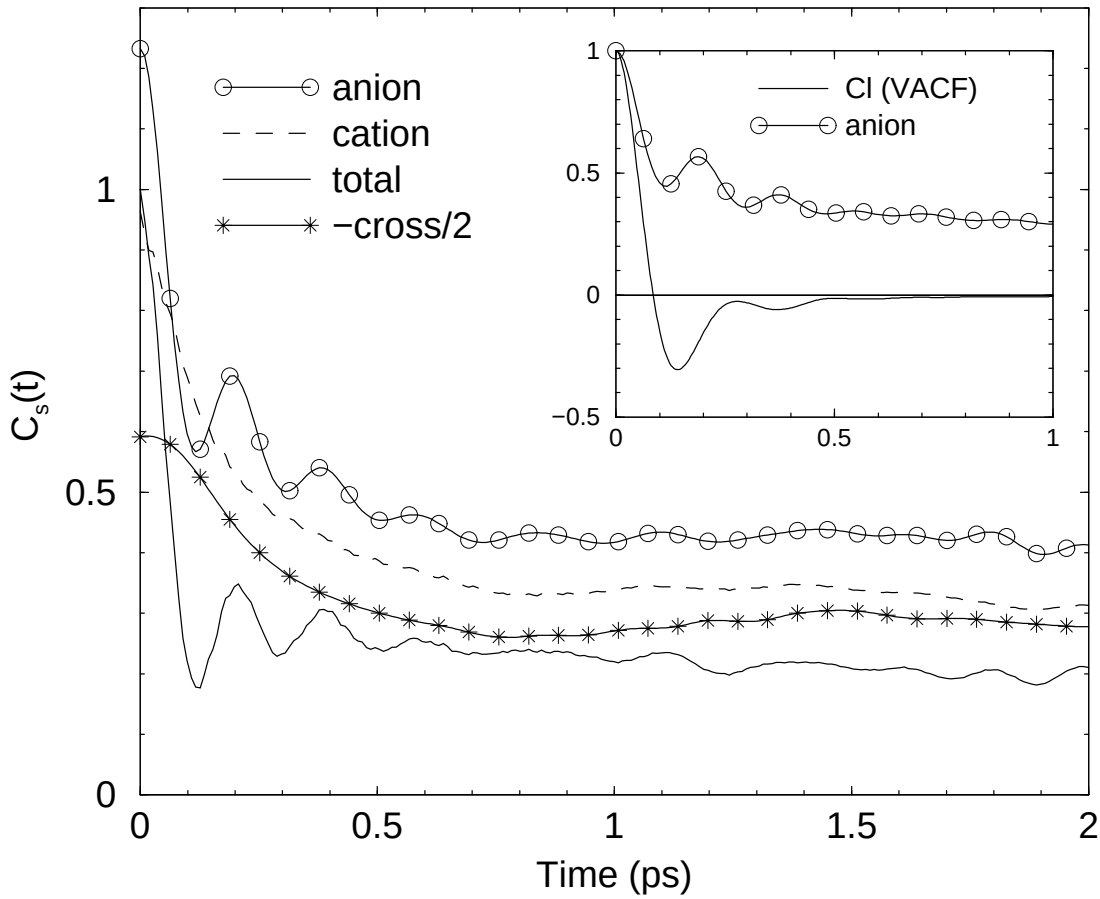

Figure 2.15: Solvent dynamics of an ionic dipole in [mmim][Cl], along with the contributions from the anions, cations, and the cross correlations between anion and cation. The contribution from the cross correlation function is multiplied by a factor of $-\frac{1}{2}$. Inset compares the anion contribution to solvation dynamics with the velocity auto time correlation of chlorine. Symbols are shown infrequently for clarity.

of solvation dynamics, particularly to obtain its long time component. This is advantageous as one can then obtain the relaxation of the solvent at long times, a feature that is very important for a proper comparison to experiments. The ultrafast (sub-picosecond) Gaussian relaxation of the solute is due to the rattling of chloride ions within their cage as well as the libration of methyl group, while the rotational reorientation of the bulky cations together with the diffusion of anions and cations account for the slow component of the decay. The correlation function (Equation 2.5) was fitted to a sum of a Gaussian

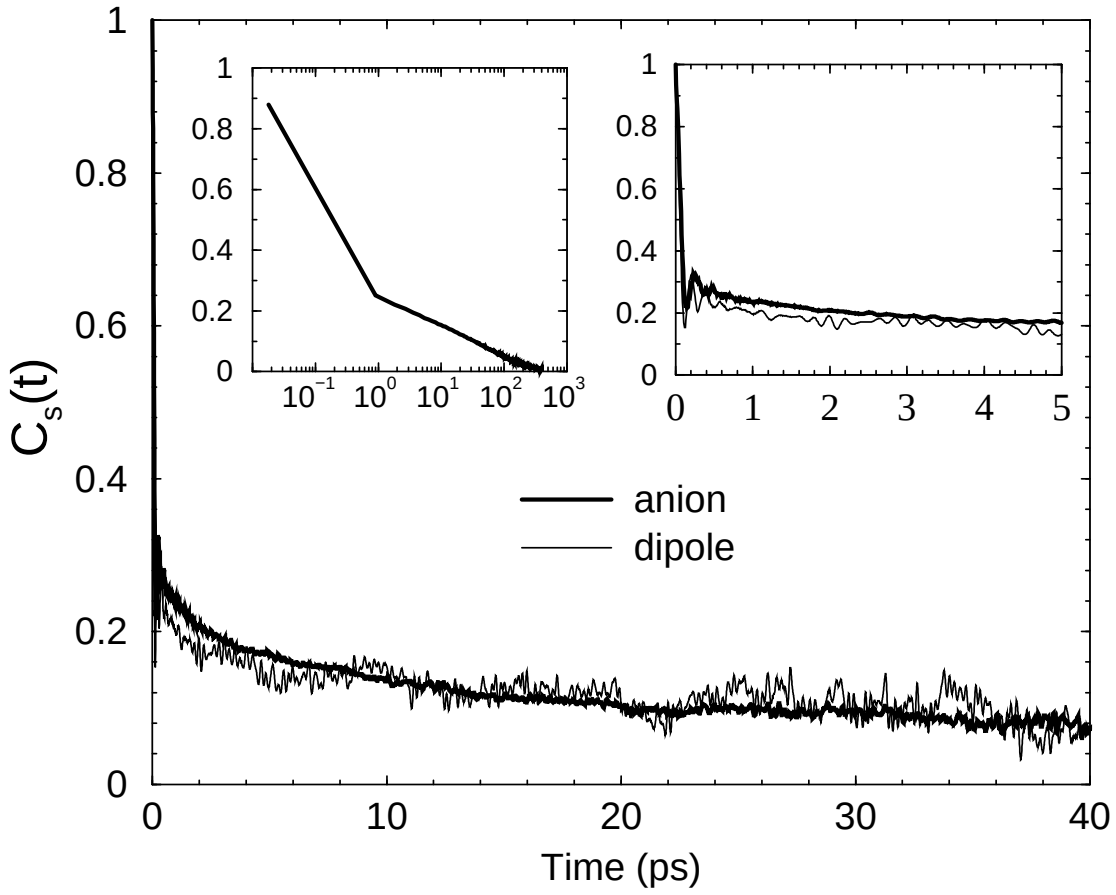

Figure 2.16: Comparison of the solvation time correlation function, $C_S(t)$ for the cases of an ionic dipolar probe and intrinsic anions. In the left inset is the log-linear plot of $C_S(t)$ for the anion shown for long times. The right inset compares $C_S(t)$ within 5 ps.

and two exponentials [51],

$$C_s(t) = a_1 exp(-0.5t^2/\tau_1^2) + a_2 exp(-t/\tau_2) + a_3 exp(-t/\tau_3) \tag{2.9}$$

The time constant for the Gaussian component was obtained by fitting the solvation TCF calculated from the trajectory with 9 fs resolution to Equation 2.9 for time values up to 0.12 ps. The remaining time constants for the ion solvation TCF were obtained by fitting the solvation TCF calculated from a 0.9 ps resolution trajectory to Equation 2.9. In this fit, the time constant of the ultrafast relaxation obtained from the high resolution data was frozen (constrained fit). However, its amplitude was left unconstrained. The

Probe	a_1 (%)	τ_1(ps)	a_2(%)	τ_2 (ps)	a_3(%)	τ_3(ps)	$\langle\tau\rangle$ (ps)
Cation	81.0	0.058	10.9	19.2	8.1	154.2	14.6
Anion	77.3	0.069	11.9	14.7	10.8	136.3	16.5
Dipole	76.3	0.054	8.2	1.87	15.5	67.3*	10.6

Table 2.3: The amplitudes and decay constants obtained by fitting the solvation time correlation function to Equation 2.9. ($\star$-Approximate estimate)

final parameters of fit for $C_S(t)$ are tabulated in Table 2.3. The average solvation time is calculated to be 16.5 ps in the case of anions and 14.6 ps in the case of cations. A similar procedure was employed to fit the solvation TCF of the dipolar probe. Note that the time constant of the long time component in the case of the dipolar probe (around 67 ps) can be considered only as an estimate, as the TCF itself has been calculated only up to 40 ps. The time constant for the Gaussian ultrafast component for dipolar solvation dynamics is comparable to that obtained for the intrinsic ionic probe. At intermediate time scales, ionic solvation proceeds slower than that of the dipole, while at long times their behavior are similar. The difference in the intermediate timescale may be due to the difference in the structural organization of the ions around dipole compared to that of the anion. The first coordination shell of the anion will be made up of cations, while that of the dipole will contain both anions and cations, that is in accordance with the theoretical predictions of Stillinger and coworkers on fused salts. [52]

Samanta and coworkers [19] have studied solvation dynamics in a similar system, [bmim][BF_4] at 300K in which the slow component of decay has a much longer time constant, in the order of nanoseconds. An exact comparison with their work is unfortunately not possible as the temperature in our simulations is 425K, and the ionic liquid too is different. The long time component that we report here (around 150 ps, see Table 2.3) has not so far been studied in simulations. Accounting for the difference in temperature between simulations and experiment, this component is likely to be the one observed in the nanosecond regime in experiments. It should also be noted that the ultrafast decay is

difficult to capture in experiments [19–23], and hence the simulation results are relevant from that viewpoint as well. Also, in our simulations the time constant of the slow decay could be an underestimate as our probe, i.e., the anion could diffuse in those time scales.

In a recent computer simulation study on the dependence of properties of the PF_6 ion based ILs on alkyl chain length, solvation dynamics has been found to be biphasic, with about 50% of the correlations decaying in about half a picosecond, and the decay of the full correlation is much slower, of the order of 100 ps [53]. Shim *et al* [40] have reported an ultrafast component in the solvent relaxation in [emim][Cl]. In their simulations, they have found that the main contribution to the total relaxation comes from the anion, and that the cation and cross terms do not contribute much. Kobrak and Znamenskiy [54], have performed simulations of betaine in [bmim][PF_6], and found that there is equivalent contribution from the anion and the cation towards the relaxation, in contradiction to the results of Shim *et al* [40]. While the former employed a rigid cation framework, the latter have employed a rigid imidazolium ring combined with a flexible butyl chain. This variation in the model construction could contribute to the differences in the results.

Time resolved emission spectroscopic experiments by Maroncelli and coworkers [22], have revealed that the ultrafast component of solvent relaxation is present only in the imidazolium based ionic liquids, while it is absent in the tetraalkyl ammonium and tetraalkyl phosphonium based ionic liquids. Our calculations are consistent with the results of Kobrak and Znamenskiy [54], and the experimental results of Maroncelli *et al* [22]. Although Shim *et al* have observed the dominance of the anion contribution to the ultrafast relaxation, our results allude specifically to the involvement of the anion rattling within the cation cage and also the libration of the methyl group of the cation. We provide evidence for the latter in terms of the time decay of correlation of the bisector vector of H-C-H of the cation's methyl group, $C_b(t)$ in Figure 2.17. We observe that more than 50% of the correlations have been lost before 1 ps. Since within this time the rotation or translation of the cation is negligibly small, the libration of the methyl group could also contribute

to the fast component of relaxation. It appears thus that *a consideration of all atoms explicitly and more importantly, allowing for a flexible model (as opposed to a rigid one) is vital for simulation studies on solvation dynamics, and the current work qualifies in these respects as one.*

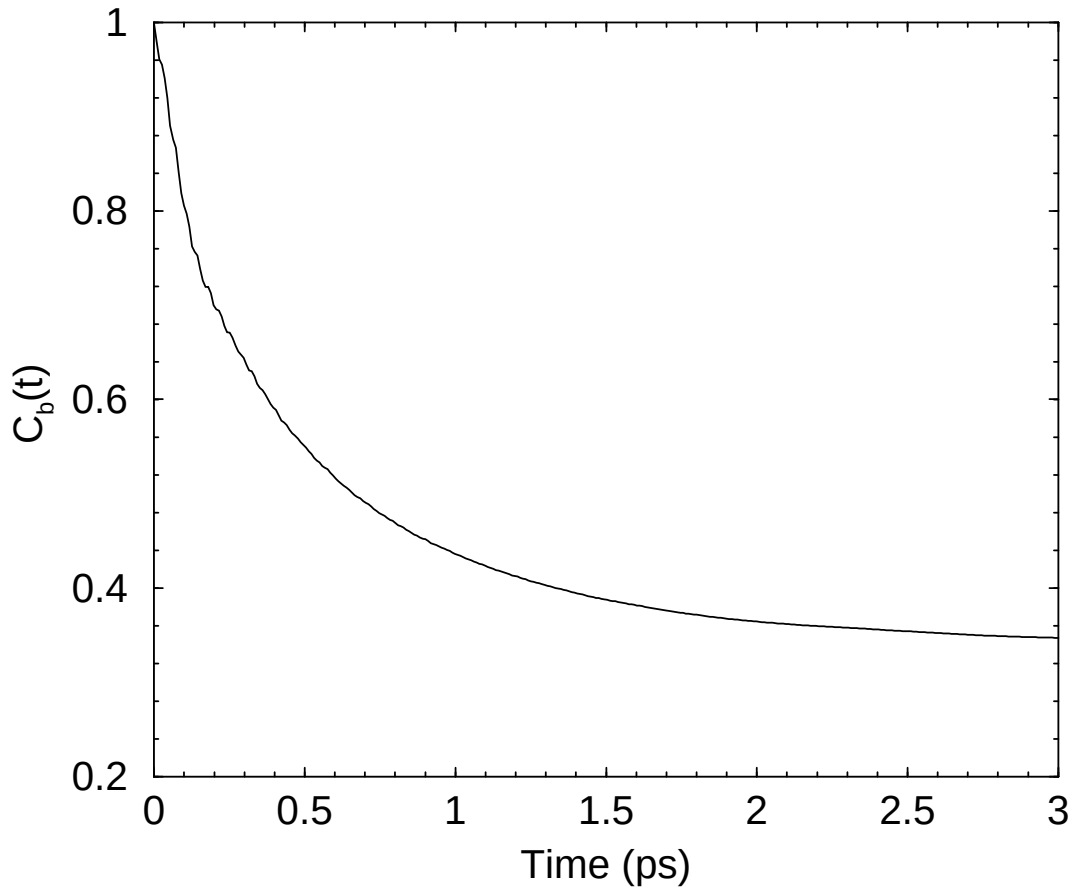

Figure 2.17: The time correlation function of the bisector vector of H-C-H belonging to the methyl group of the cations, $C_b(t)$.

The equilibrium solvation structure for the dipole is presented in Figure 2.18 as pair correlation functions between the center of the dipolar probe and the constituents of the solvent It shows that the chloride ions form a stronger cage around the dipole compared to the bulky imidazolium ions, that plays a major role in the relaxation process. The running coordination number of cations and anions around the dipole is shown as inset to Figure 2.18. It is found that three anions and approximately one cation surround the

neutral dipolar molecule in its first coordination shell. This strong local coordination shell is one of the underlying reason for the ultrafast decay.

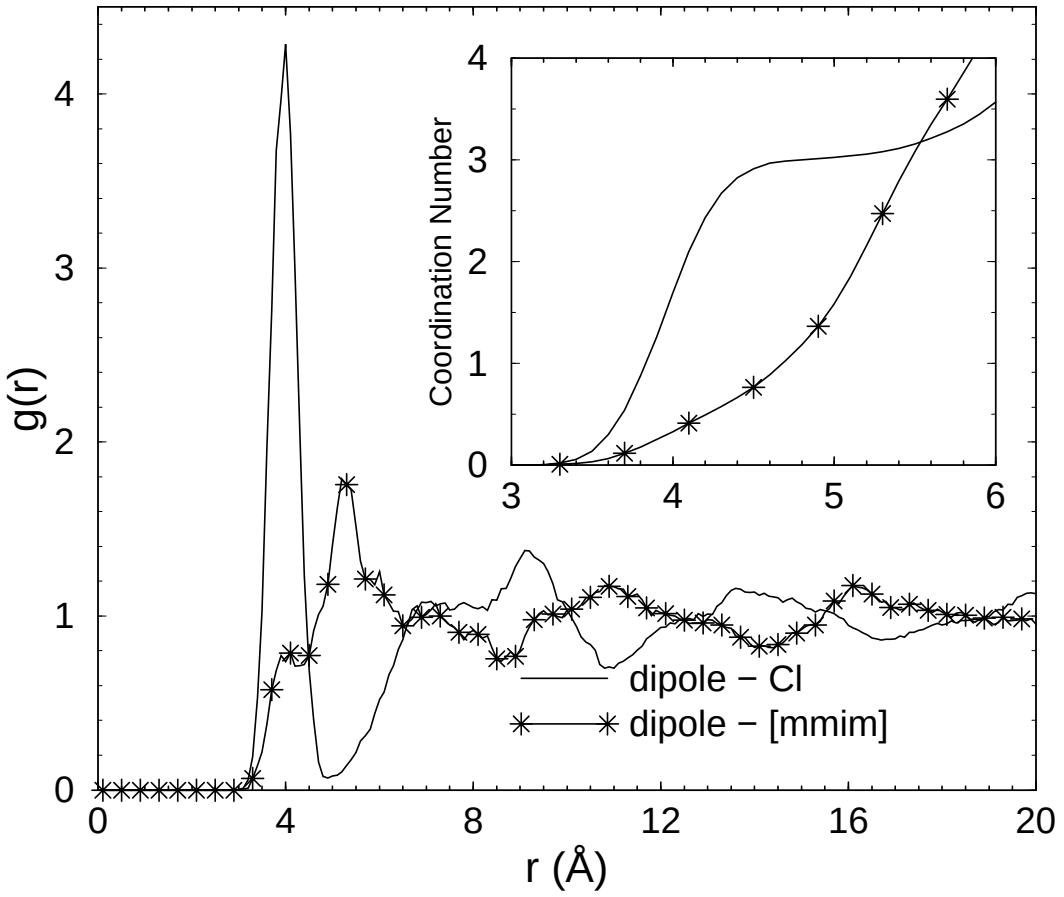

Figure 2.18: Radial distribution functions of anion and cation around the centre of mass of the probe dipole. The corresponding running coordination numbers are shown in inset. Symbols are shown infrequently for clarity.

Several dynamical processes in the ionic melt could contribute to the slowest component of the solvation TCF. We draw attention to one of the slow processes associated with the cation rotation here. We define $C_r(t)$ as,

$$C_r(t) = \langle \vec{r}_i(0).\vec{r}_i(t) \rangle \tag{2.10}$$

where $\vec{r}_i(0)$ is one of the three vectors defining the orientation of the cation. The angular bracket signifies an equilibrium average. This correlation function characterizes the rota-

tion of the cation along a particular axis. Three mutually perpendicular axes were defined as shown in the inset to Figure 2.19. Two of these are in the plane of the imidazolium ring, while the third was perpendicular to it. The correlation functions shown in the main body of Figure 2.18 were found to decay exponentially with time constants ranging from 300 to 360 ps. Hence, apart from the translation of anions and cations, cation rotation too could contribute to the slow component of the relaxation of the solvation time correlation function in these ionic melts.

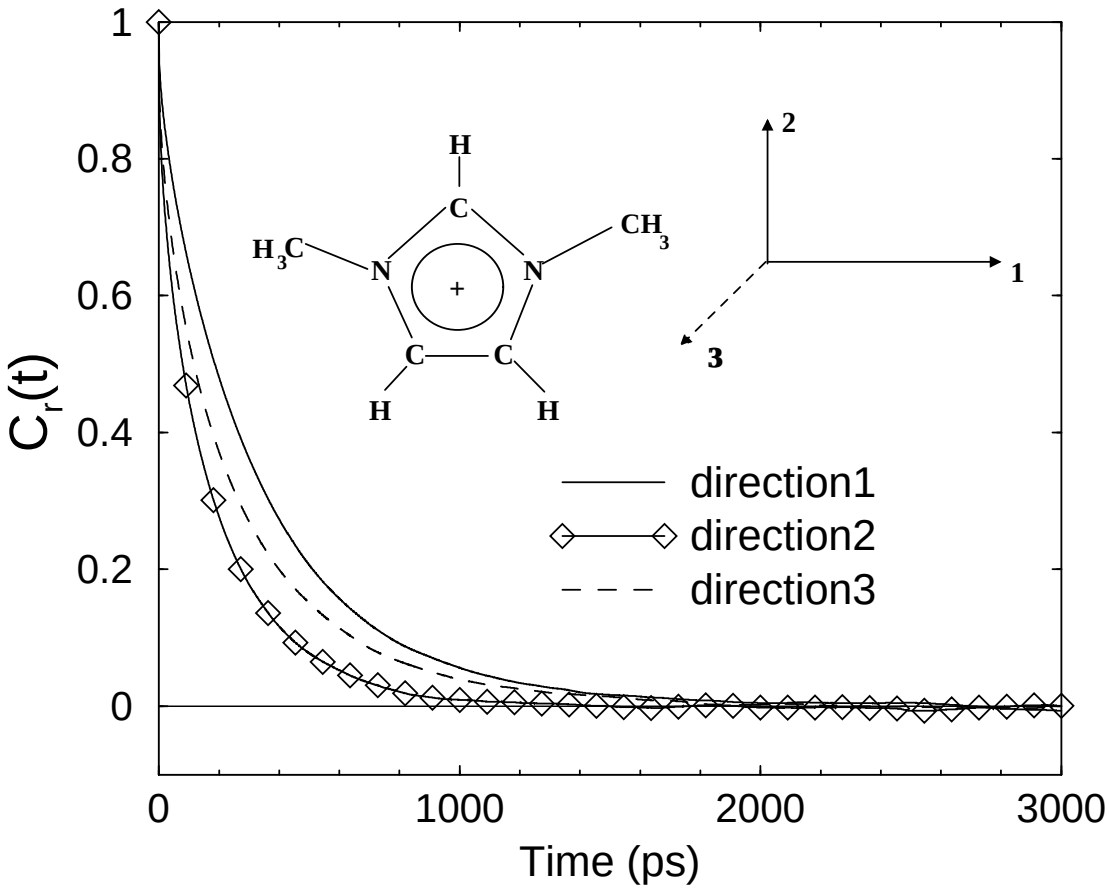

Figure 2.19: The rotational time correlation function about three orthogonal axes of the cation. Symbols are shown infrequently for clarity.

2.5 Conclusions

The intermolecular structure of a simple ionic liquid, 1,3-dimethylimidazolium chloride, has been studied using Car-Parrinello molecular dynamics and classical MD simulations. Density functional theory based CPMD calculations, using plane waves along with the exchange-correlation functionals of the BLYP kind are observed to predict the intramolecular structure of the imidazolium ion and structure of this melt well, in agreement with neutron scattering experiments [10]. Results on the *ab initio* derived vibrational spectrum of the melt too are in good agreement with spectroscopic data [43,44]. A crucial difference in the structure obtained between classical MD and the *ab initio* calculations is the hydrogen bonding of the unique hydrogen of the imidazolium to the chloride ion. The hydrogen bond is only weakly present in the classical data, suggesting a need for the refinement of the interaction potentials employed in classical simulations. The near neighbor chloride ions surrounding a cation are predominantly present in the plane of the imidazolium ring in classical MD simulations, while out-of-plane locations are also preferred in the *ab initio* calculations. Near neighbor cations are oriented such that their ring planes are parallel to each other. This signifies a strong $\pi - \pi$ interaction between them. The presence of the hydrogen bond between the acidic hydrogen (H8) and the chloride ion influences the C2-H8 stretching mode in a striking manner. In the current study, this mode has been demonstrated to red shift due to this association.

The earlier AIMD calculations of Del Pópolo *et al* [15] were performed on 8 or 24 ion pairs of [mmim][Cl] using a localized basis set. The current calculations are for 32 ion pairs in bulk using a plane wave basis set. Our results and conclusions on the structure of the liquid match the results of Del Pópolo *et al* to a large extent, despite the difference in methods, and the system size. However, crucially, our calculations differ from theirs in the position of the first peak in the cation-cation g(r). This difference might point to system size effects or to the difference in the basis set employed. Calculations that employ plane wave basis sets are generally more accurate than ones with localized sets,

and hence are more computationally demanding. Traditional ionic melts such as $ZnCl_2$ are non-molecular unlike the imidazolium salt studied here. Thus charge ordering in imidazolium melts needs to be understood along with the intramolecular structure of the cation. Certain sites on the cation can be closer to the geometric center of another cation rather than to the anion. Charge ordering in ionic melts can be rather long ranged [52], and hence it is crucial that reasonably large system sizes that accommodate at least a second neighbor shell are employed in atomistic simulations. Our work involving 32 ion pairs meets this expectation.

Transport properties including self diffusion co-efficients, shear viscosity and electrical conductivity of 1,3-dimethylimidazolium chloride have been calculated using molecular dynamics simulations that employ a recently developed fully flexible, all-atom interaction potential model by Padua and coworkers [17]. The imidazolium cations, despite being heavier than the chloride anions, are observed to diffuse faster. This fact is rationalized as due to the anions being present in a deeper potential well than the cation. The electrical conductivity of the melt is calculated using the Green-Kubo and Nernst-Einstein relations. Differences in the values obtained by these methods point to correlated ion motions in the melt. The current potential model predicts a rather large value for the shear viscosity and a low electrical conductivity for the [mmim][Cl] system, in comparison to experiments. Assuming that the experimental samples are devoid of moisture, our calculations point to the need for refining the interaction parameters further, in order to obtain quantitative agreement with experimental data on several of the important transport properties of the melt. It may also be pertinent to include the effect of charge polarization in developing better interaction potentials. These effects have been found to be important in the modeling of similar ionic melts [49, 55].

Apart from the transport properties, the relaxation of the solvent to a perturbation in the form of a charge redistribution in a solute is studied at equilibrium, through the solvation time correlation function. This process is examined both through an explicit

ionic dipole present in the melt, as well as through the regression of fluctuations of the potential energy of the anions intrinsic to the solvent. We find a rather good agreement between the two solvation TCFs within the timescales of our calculation. This indicates that the anions themselves could be used as probes of solvation dynamics, particularly to obtain the long time component. At least as far as this system is concerned, it appears that ion solvation (i.e., of the anion) proceeds in the same timescales as dipolar solvation. However, since the anions could diffuse (they move, on average by about 3Å in 500 ps) in these timescales, their use as probes of solvent dynamics need to be carried out with care. The time constant of the long time component presented in Table 2.3 should thus be interpreted as a lower bound. The inertial Gaussian response in the ultrafast (sub-picosecond) regime occurs on the same timescales for the dipolar and ionic probes. At intermediate time scales (between 1 and 10 ps), the solvation dynamics of these probes are different, with that of the anions proceeding slower than that of the dipolar probe. This is most likely due to differences in the near neighbor solvent structure. The rather close match between the solvation TCF of the dipolar and the intrinsic ionic probes at long times (greater than 10ps) is likely due to the slow, viscous modes that involve motions of the both cations and anions in the solvent. The sub-picosecond component in solvation dynamics of the ions arises from the cage vibrations of the anion. Methyl rotations in the cation that occurs in the same time scale, too could contribute to the decay of the solvation time correlation function. The use of intrinsic anions as probes enables us to study the long time component of solvent relaxation. We observe a long time component of around 150 ps in the relaxation of this function at 425K, that is likely to be related to the nanosecond time component observed in experiments on [bmim][BF_4] at 300K. The reorientational motion of the cation and the translational diffusion of both the anion and cation could contribute to this slow decay. Our work also emphasizes the need to employ fully flexible, all-atom potential models in order to accurately capture the dynamics of solvation.

Bibliography

[1] T. Welton, *Chem. Rev.*, **99**, 2071 (1999).

[2] M.J. Earle, K.R. Seddon, *Pure Appl. Chem.*, **72**, 1391 (2000).

[3] H.A. Every, A.G. Bishop, D.R. McFarlane, G. Oradd, M. Forsyth, *Phys. Chem. Chem. Phys.*, **6**, 1758 (2004).

[4] J.G. Huddleston, A.E. Visser, W.M. Reichert, H.D. Willauer, G.A. Broker, R.D. Rogers, *Green Chem.* **3**, 156 (2001).

[5] K.R. Seddon, A. Stark, M.J. Torres, *Pure Appl. Chem.*, **72**, 2275 (2000).

[6] J.L. Anderson, V. Pino, E.C. Hagberg, V.V. Sheares, D.W. Armstrong, *Chem. Commun.*, 2444 (2003).

[7] P. Wasserscheid, W. Keim, *Angew. Chem. Int. Ed.*, **39**, 3772 (2000).

[8] L.S. Ott, M.L. Cline, M. Deetlefs, K.R. Seddon, R.G. Finke, *J. Am. Chem. Soc.*, **127**, 5758 (2005).

[9] M.J. Earle, S.P. Katdare, K.R. Seddon, *Org. Lett.*, 6 707 (2004).

[10] C. Hardacre, J.D. Holbrey, S.E.J. McMath, D.T. Bowron, A.K. Soper, *J. Chem. Phys.*, **118**, 273 (2003).

[11] C. Hardacre, S.E.J. McMath, M. Nieuwenhuyzen, D.T. Bowron, A.K. Soper, *J. Phys.: Condens. Matter*, **15**, S159 (2003).

[12] C.G. Hanke, S.L. Price, R.M. Lynden-Bell, *Mol. Phys.*, **99**, 801 (2001).

[13] J. de Andrade, E.S. Boes, H. Stassen, *J. Phys. Chem. B*, **106**, 13344 (2002).

[14] S.M. Urahata, M.C.C. Rebeiro, *J. Chem. Phys.*, **122**, 024511 (2005).

[15] M.G. Del Pópolo, R.M. Lynden-Bell, J. Kohanoff, *J. Phys.Chem. B*, **109**, 5895 (2005).

[16] M.G. Del Pópolo, G.A. Voth, *J. Phys. Chem. B*, **108**, 1744 (2004).

[17] J.N.C. Lopes, J. Deschamps, A.A.H. Pádua, *J. Phys. Chem. B*, **108** 2038 (2004); **108**, 11250 (2004).

[18] M. Bühl, A. Chaumont, R. Schurhammer, G. Wipff, *J. Phys. Chem. B*, **109**, 18591 (2005).

[19] R. Karmakar, A. Samanta, *J. Phys. Chem. A*, **106**, 4447 (2002).

[20] R. Karmakar, A. Samanta, *J. Phys. Chem. A*, **107**, 7340 (2003).

[21] R. Karmakar, A. Samanta, *J. Phys. Chem. A*, **106**, 6670 (2002).

[22] S. Arzhantsev, N. Ito, M. Heitz, M. Maroncelli, *Chem. Phys. Lett.*, **381**, 278 (2003).

[23] J.A. Ingram, R.S. Moog, N. Ito, R. Biswas, M. Maroncelli, *J. Phys. Chem. B*, **107**, 5926 (2003).

[24] K.R. Seddon, A. Stark, M.J. Torres, in *Ionic Liquids As Green Solvents: Progress and Prospects*, Edited by K.R. Seddon, (ACS Symposium Series, Oxford University Press, Washington DC, 2002), p. 34.

[25] M.E. Tuckerman, D.A. Yarne, S.O. Samuelson, A.L. Hughes, G.J. Martyna, *Comput. Phys. Commun.*, **128**, 333 (2000).

[26] M.P. Allen, D.J. Tildesley, *Computer Simulation of Liquids* (Clarendon Press, Oxford, 1987).

[27] S. Nose, *J. Chem. Phys.*, **81**, 511 (1984).

[28] W.G. Hoover, *Phys. Rev. A.*, **31**, 1695 (1985).

[29] G.J. Martyna, M.E. Tuckerman, M.L. Klein, *J. Chem. Phys.*, **97**, 2635 (1992).

[30] M.E. Tuckerman, B.J. Berne, G. Martyna, *J. Chem. Phys.*, **97**,1990 (1992).

[31] R. Car, M. Parrinello, *Phys. Rev. Lett.*, **55**, 2471 (1985).

[32] J. Hutter, P. Ballone, M. Bernasconi, P. Focher, E. Fois, S. Goedecker, D. Marx, M. Parrinello, and M.E. Tuckerman, CPMD Version 3.9.1, Max Planck Institut fuer Festkoerperforschung, Stuttgart, and IBM Zurich Research Laboratory, 1990-2007.

[33] N. Troullier, J.L. Martins, *Phys. Rev. B*, **43**, 1993 (1991).

[34] A.D. Becke, *Phys. Rev. A*, **38**, 3098 (1988).

[35] C. Lee, W. Yang, R.G. Parr, *Phys. Rev. B*, **37**, 785 (1988).

[36] G. Schaftenaar, J.H. Noordik, *J. Comput.-Aided Mol. Design*, **14**, 123 (2000).

[37] D.J. Evans, G.P. Morriss, *Statistical Mechanics of Nonequilibrium Liquids* (Academic Press, London, 1990).

[38] J.P. Hansen, I.R. McDonald, *Theory of Simple Liquids* (Academic Press, London, 1976).

[39] M.S. Skaf, B.M. Ladanyi, *J. Phys. Chem.*, **100**, 18258 (1996).

[40] Y. Shim, J. Duan, M.Y. Choi, H.J. Kim, *J. Chem. Phys.*, **119**, 6411 (2003).

[41] A.J. Arduengo III, H.V.R. Dias, R.L. Harlow, M. Kline, *J. Am. Chem. Soc.*, **114**, 5530 (1992).

[42] S.M. Urahata, M.C.C. Rebeiro, *J. Chem. Phys.*, **120**, 1855 (2004).

[43] Y.U. Paulechka, G.J. Kabo, A.V. Blokhin, O.A. Vydrov, J.W. Magee, M. Frenkel, *J. Chem. Eng. Data*, **48**, 457 (2003).

[44] S. Tait, R.A. Osteryoung, *Inorg. Chem.*, **23**, 4352 (1984).

[45] T. Umecky, M. Kanakubo, Y. Ikushima, *Fluid Phase Equil.*, **228-229**, 329 (2005).

[46] S.M. Urahata, M.C.C. Rebeiro, *J. Chem. Phys.*, **122**, 024511 (2005).

[47] M. Koel, *Proc. Estonian Acad. Sci. Chem.*, **49**, 145 (2000).

[48] A.A. Fannin, Jr. D.A. Floreani, L.A. King, J.S. Landers, B.J. Piersma, D.J. Stetch, R.L. Vaughn, J.S. Wilkes, J.L. Williams, *J. Phys. Chem.*, **88**, 2614 (1984).

[49] T. Yan, C.J. Burnham, M.G. Del Popolo, G.A. Voth, *J. Phys. Chem. B*, **108**, 11877 (2004).

[50] A.Z. Borucka, J.O'M. Bockris, J.A. Kitchener, *J. Chem. Phys.*, **24**, 1282 (1956).

[51] R. Jimenez, G.R. Fleming, P.V. Kumar, M. Maroncelli, *Nature*, **369**, 471 (1994).

[52] F.H. Stillinger, J.G. Kirkwood, P.J. Wojtowicz, *J. Chem. Phys.*, **32**, 1837 (1960).

[53] C.J. Margulis, *Mol. Phys.*, **102**, 829 (2004).

[54] M.N. Kobrak, V. Znamenskiy, *Chem. Phys. Lett.*, **395**, 127 (2004).

[55] F. Hutchinson, M. Wilson, P.A. Madden, it Mol. Phys., **99**, 811 (2001).

Chapter 3

Layering at an Ionic Liquid-Vapor Interface: A Molecular Dynamics Simulation Study of [bmim][PF_6]

3.1 Introduction

The interface of a liquid with its vapor is a small component compared to its bulk, even then it plays a major role in many applications such as multiphasic catalytic reactions and hence its study is of primary importance [1]. Properties of liquids and ion concentrations at a liquid-vapor interface have been documented to be different than in bulk [2]. In the case of RTILs, a number of experimental investigations have been carried out to determine the location and orientation of the ions at the air-ionic liquid interface. [3–8]

Neutron reflectivity studies [6] indicate a possible layering of molecules in liquid [bmim][BF_4] that extends up to 40Å from the liquid-vapor interface. The ionic liquid-vapor interface has also been studied by using direct recoil spectroscopy (DRS) [4, 5] and sum frequency generation (SFG) techniques [7, 9]. While the SFG experiments conclude that the butyl tail of the cation points out of the surface with a certain tilt, DRS results

indicate that the plane of the imidazolium ring is perpendicular to the surface and that the butyl tails are parallel to the surface in liquid [bmim][PF_6] and perpendicular to it in [bmim][BF_4] [4, 5]. Recent SFG experiments by Rivera-Rubero and Baldelli [10] observe the butyl tail to project into the vapor phase and the ring plane to lie flat on the liquid surface. Obviously, there is a need to resolve these issues.

Deutsch and coworkers [8] have recently reported X-ray reflectivity and surface tension data for the [bmim][PF_6]-vapor interface. They observe a 10-12% increase in the density of electrons at the interface compared to that in bulk, and also conclude that this interface does not exhibit density oscillations, such as that observed in liquid metals [11] or in the MD simulations of a [mmim][Cl]-vapor interface [12, 13]. Very recent simulations of the liquid-vapor interfaces of [bmim][PF_6] and [bmim][BF_4] [14] too have observed oscillations in number and electronic densities, in apparent disagreement with the X-ray reflectivity experiments.

Our primary purpose is to try to resolve the apparent discrepancies between simulations and experiment on the nature of the electron density profile near the liquid-vapor interface of [bmim][PF_6]. Motivated by this aim, we present here results of fully atomistic molecular dynamics simulations of the liquid [bmim][PF_6]-vapor interface. Anticipating our results, we observe number density oscillations at the liquid-vapor interface in agreement with earlier simulations. However, the amplitude of the oscillations in the electron density profile are much lesser when compared to those in the number density profile, a feature that arises out of a near cancellation in the contribution to the former from the cations and the anions. This observation reconciles experiments and simulations. Further, we observe the liquid surface to possess a hydrophobic character.

We present details on the methodology and analyses employed in the next section, and discuss our results later.

3.2 Methodology and simulation details

Empirical potential molecular dynamics simulations were carried out on a planar liquid slab of 1-n-butyl-3-methylimidazolium hexafluorophosphate in equilibrium with its vapor. The simulations were carried out in the canonical ensemble using an all-atom model that was developed by Padua and coworkers [15] to study crystal forms of ionic liquids. We have employed this potential to study the structure and dynamics of liquid [mmim][Cl] [16] and have also employed it to generate initial configurations of an *ab initio* MD simulation [17] recently. Intramolecular interaction parameters for the $[PF_6]^-$ anion were adopted from the work of Borodin *et al* [18], making the model, a fully flexible one. The current simulations were carried out on two different system sizes at three temperatures using the PINY_MD [19] code. System A consisted of 256 ion pairs (8,192 atoms), while system B contained 512 ion pairs (16,384 atoms). The simulation of the latter with twice the number of ions along the z-direction as that in system A was necessitated to obtain a truly bulk-like region in the center of the liquid slab. For system A, a pre-equilibrated bulk configuration (equilibrated for 8 ns) of 256 ion pairs within a cubic box of edge length 44.83Å was placed at the center of a tetragonal supercell of dimensions 44.83Å, 44.83Å and 90.00Å, so that two ionic liquid - vacuum interfaces were present in a supercell. A similar procedure of equilibration in bulk was adopted for system B, and the size of the supercell in the z-direction for its interface calculations was chosen to be 150Å. Three-dimensional periodic boundary conditions were employed. The final configuration at each temperature was used as the starting configuration for the run at a subsequent lower temperature. Details on these simulations are summarized in Table 3.1. In addition to the above calculations, a second MD run starting from an independent configuration of 512 ion pairs at 400K was quenched to 300K. This system was equilibrated for 1.2 ns and a subsequent trajectory of duration 2.5 ns was obtained for analyses. We label this as Run C. Specifically, we obtained the mass and electron density profiles reported here as averages from Runs B and C.

Table 3.1: Details of simulated systems.

No. of ion pairs	Temperature (K)	Super cell dimensions b_x,b_y,b_z (Å)	Equilibration runlength (ns)	Analysis runlength (ns)
256	500	44.83, 44.83, 90.00	6.0	4.8
256	400	44.83, 44.83, 90.00	1.2	6.1
256	300	44.83, 44.83, 90.00	1.2	14.8
512	500	44.83, 44.83, 150.00	3.0	2.0
512	400	44.83, 44.83, 150.00	1.2	2.2
B. 512	300	44.83, 44.83, 150.00	1.2	31.1
C. 512	300	44.83, 44.83, 150.00	1.2	2.5

Ewald summation method with tinfoil boundary conditions was used for the computation of electrostatic interactions [20], and α values of 0.265Å^{-1} and 0.268Å^{-1} were employed for systems A and B respectively. 8581 and 12116 reciprocal vectors were used in the reciprocal space sum for the two systems that guaranteed convergence of the Coulomb energy. A Nosé-Hoover chain thermostat [21] was used to control the temperature. The equations of motions were integrated using the reference system propagator algorithm (RESPA) [22]. Nonbonded interactions within 13Å (the interaction cutoff) and beyond 6Å were integrated with time step of 3 fs, and a 1.5 fs time step was used to integrate nonbonded interactions within 6Å. Torsional forces were evaluated every 0.75 fs and stretching and bending degrees of freedom were integrated with time steps of 0.375 fs. The conservation in total energy was 7 parts in 10^5 over 1 ns at 300K.

In all the simulations carried out at 300, 400 and 500K, none of the ions were found to be exclusively in the vapor phase, a consequence of the negligible vapor pressure of this liquid at these temperatures.

Configurations from the MD trajectory were stored every 0.9 ps during the analysis phase of the simulation. For the calculation of various density profiles, a bin width of 1Å was used. At each instant, the center of mass of the system was translated to the origin before obtaining the profile. In some of the illustrations, the density profiles have been

averaged over the two interfaces, where the z-component of the center of mass is taken as the zero along the z-axis. The electron density profile was calculated by considering the total number of electrons of each atom and subtracting the partial charge associated with that atom corresponding to the interaction potential employed here. The results were not dependent on whether one subtracted the site partial charges or not, indicating the robustness of the profiles obtained. While calculating the orientation of different vectors with respect to the surface normal (z-axis), the interfacial region is taken to be that up to the first minimum in the mass density profile. The region between the center of mass and the first minimum is considered to be "bulk".

The surface tension γ was calculated using the diagonal components of the pressure tensor P_{ii} employing the formula, [23, 24]

$$\gamma = -b_z(P_{xx} + P_{yy} - 2P_{zz})/4 \tag{3.1}$$

where b_z is the length of the supercell in the direction parallel to the interface normal (z-axis), and the presence of the two equivalent interfaces is taken into account by introducing a factor of two in the denominator. The pressure tensor of the systems was stored every time step to calculate γ.

3.3 Results and Discussion

A schematic of the molecular structure of [bmim][PF_6] is presented in Figure 3.1 in order to aid the discussion.

3.3.1 Mass density

Simulations of an open interface provide a good means to estimate the bulk density of a liquid. In Figure 3.2a, we show the mass density profile along the z-axis for the two simulated systems at 300K. Note that the heights of the first peak on either interface of

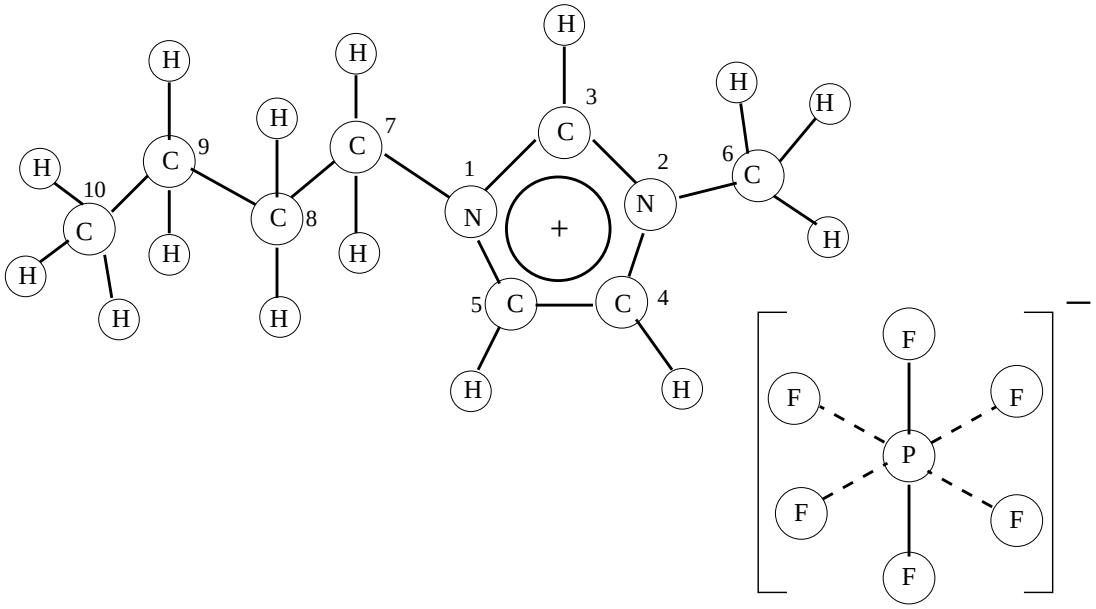

Figure 3.1: Schematic of [bmim][PF_6].

the larger system are comparable, signifying that the sample is well equilibrated. The mass density in the bulk region, estimated between z=-38Å and z=+38Å of system B is 1.34 g/cc, that is within 1.5% of the experimental value of 1.36 g/cc [25]. The profiles from the two system sizes overlap with each other in the bulk region. The density oscillations are quite strong and are discernible even for a distance of 20Å away from the interfaces. Figure 3.2b shows the symmetrized mass density profiles for the same system at the three temperatures. An expansion of the film with increasing temperature can be observed. The variation of the thickness (t) of the film in Angstrom, with temperature T in Kelvin, can be expressed as $t = 35.5 + 0.03T$. The thermal expansion coefficient of the film between 300K and 500K is obtained as $6.3 \times 10^{-4} K^{-1}$ that compares well with the experimentally determined value of $6.0 \times 10^{-4} K^{-1}$ [26].

3.3.2 Electron, number density

X-ray reflectivity studies on interfaces probe the depth profile of electron density. As discussed earlier, Deutsch and coworkers have recently concluded that the electron density

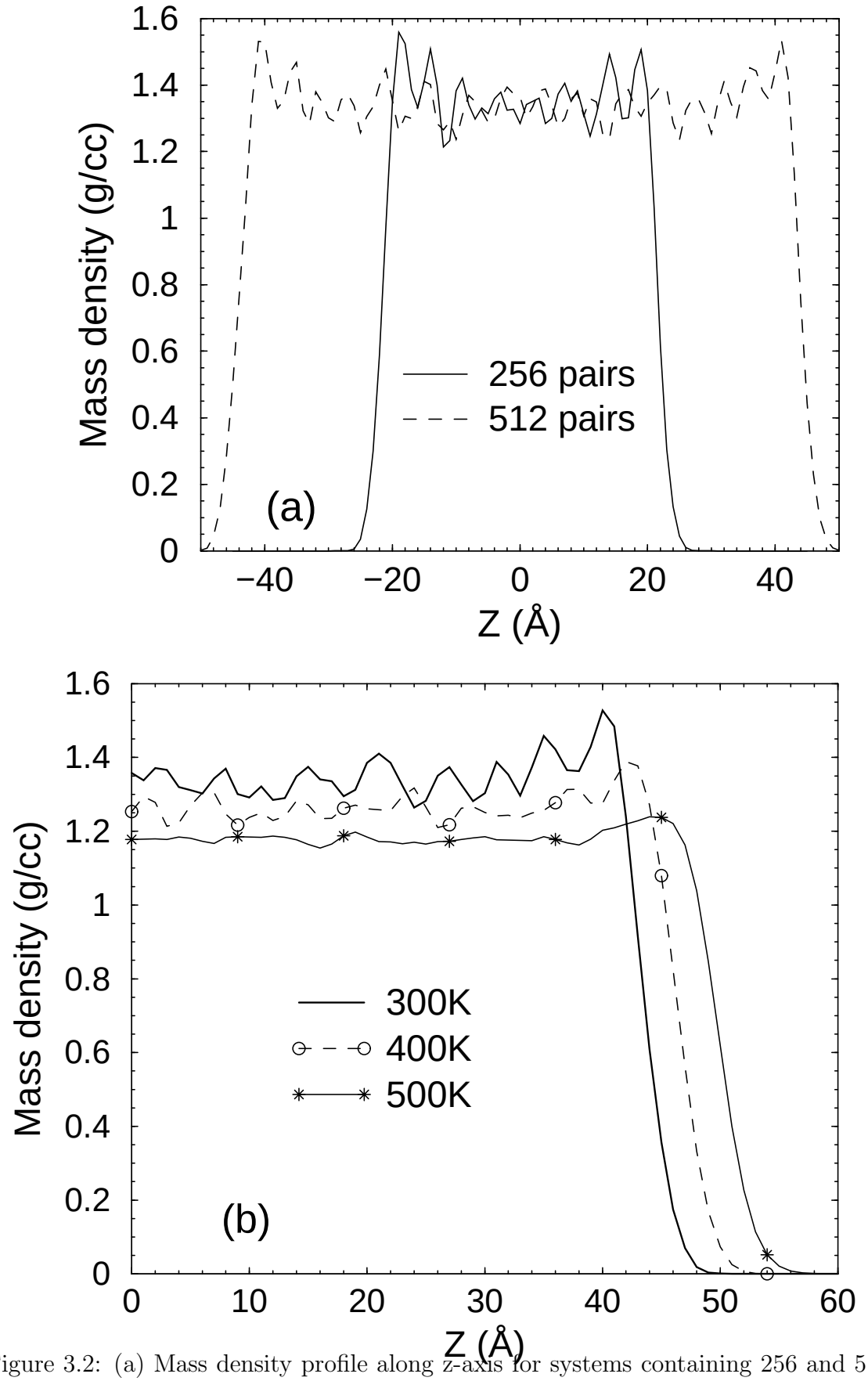

Figure 3.2: (a) Mass density profile along z-axis for systems containing 256 and 512 ion pairs at 300K. (b) Mass density profile along z-axis for the 512 ion pair system at different temperatures.

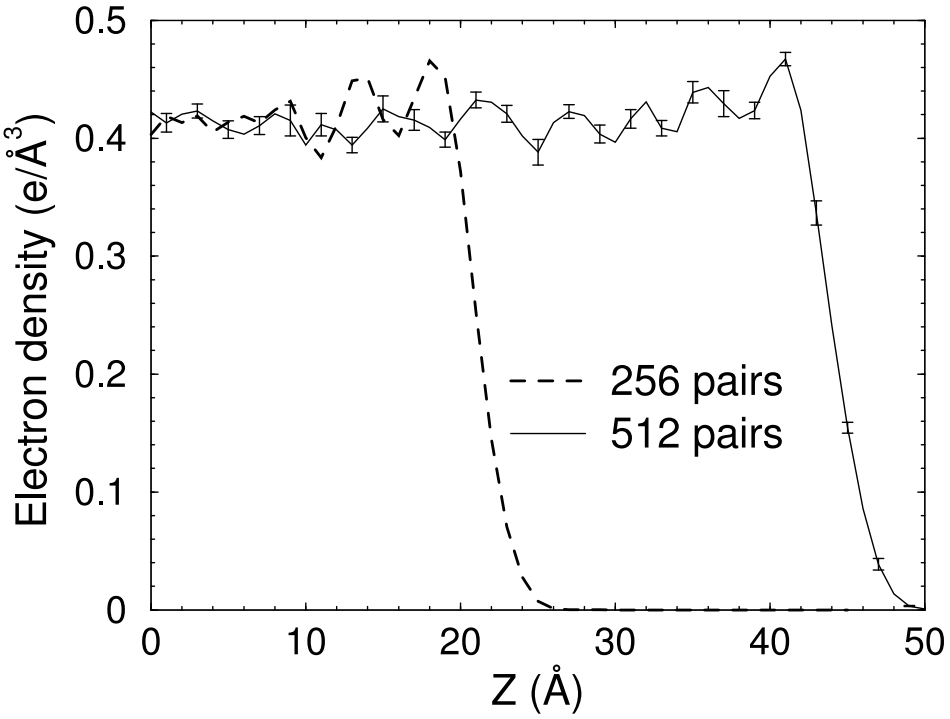

Figure 3.3: Electron density profile of 256 and 512 ion pair systems at 300K.

profile at a [bmim][PF_6]-vapor interface does not show oscillations [8]. In order to compare with these experiments, we show in Figure 3.3, the electron density profile along the z-axis for the 256 and 512 ion pair systems at 300K. The first thing to note is that there is a non-negligible increase in the electron density near the interface as compared to bulk.

Note that the peak height at the interface reaches a value of 0.47 e/$\mathring{A}^3$ that is comparable to the interfacial electron density of 0.50 e/$\mathring{A}^3$ obtained from experiments [8]. The average electron density in bulk for the 512 pair system at 300K is 0.41 e/$\mathring{A}^3$. Thus, the electron density at the interface is around 12% larger than in bulk, a result that is consistent with the X-ray reflectivity studies, that measured a 10-12% increase [8]. The enhancement in electron density at the interface over the bulk value at temperatures of 400K and 500K are around 9% and 5% respectively. Thus, the density differentials decrease with increasing temperature, as expected. The amplitude of the oscillations also

decreases with the increase in temperature, that is consistent with the observations of Lynden-Bell [12] on [mmim][Cl]. As we shall discuss later, the magnitude of such oscillations in the electron density profile in [bmim][PF_6] at 300K are much diminished when compared to that found in the number density profiles of the cation and anion.

Shown in Figure 3.4a are the number density profiles of the cation and anion centers at 300K from Run B. In the case of the cation, this is defined to be the ring center while the the coordinate of the phosphorus atom is taken as the center of the anion. Pronounced oscillations and layering are observed for both the ions. Notwithstanding the oscillations seen in the number density profiles of the cation ring centers and that of the anions, what matters to the total electron density profile shown in Figure 3 are the individual contributions from these two species that we study in Figure 3.4b. Here we show the contribution to the electron density profile obtained from the cations and from the anions separately. Their sum is the profile shown in Figure 3.3, that is reproduced also in Figure 3.4b for the sake of convenience. As expected from the behavior of the number density profiles, the electron density profiles of the cation and the anion exhibit oscillations. The position of the first peak in the profiles of the ions in figure 3.4b are similar. However, that of the second and subsequent peaks are out of phase. This behavior is clearly visible in the positions of the third and the fourth peaks of the cation profile, that coincide exactly with the minima in the electron density profile of the anions. As a consequence, the amplitude of the oscillations in the total electron density profile is diminished compared to those in the individual partial electron density profiles. *This is our central result that neatly relates the supposed absence of electron density oscillations in the experiments of Deutsch and coworkers [8], and the number density oscillations observed in our simulations as well as others [12, 14, 27].* Similar out of phase oscillations in the ion contributions to the electron density profile were observed in two other independent MD trajectories as well at 300K for the 512 ion pair system. The cross correlation between these two contributions has been evaluated to be -0.54 averaged over 3 independent MD trajectories of

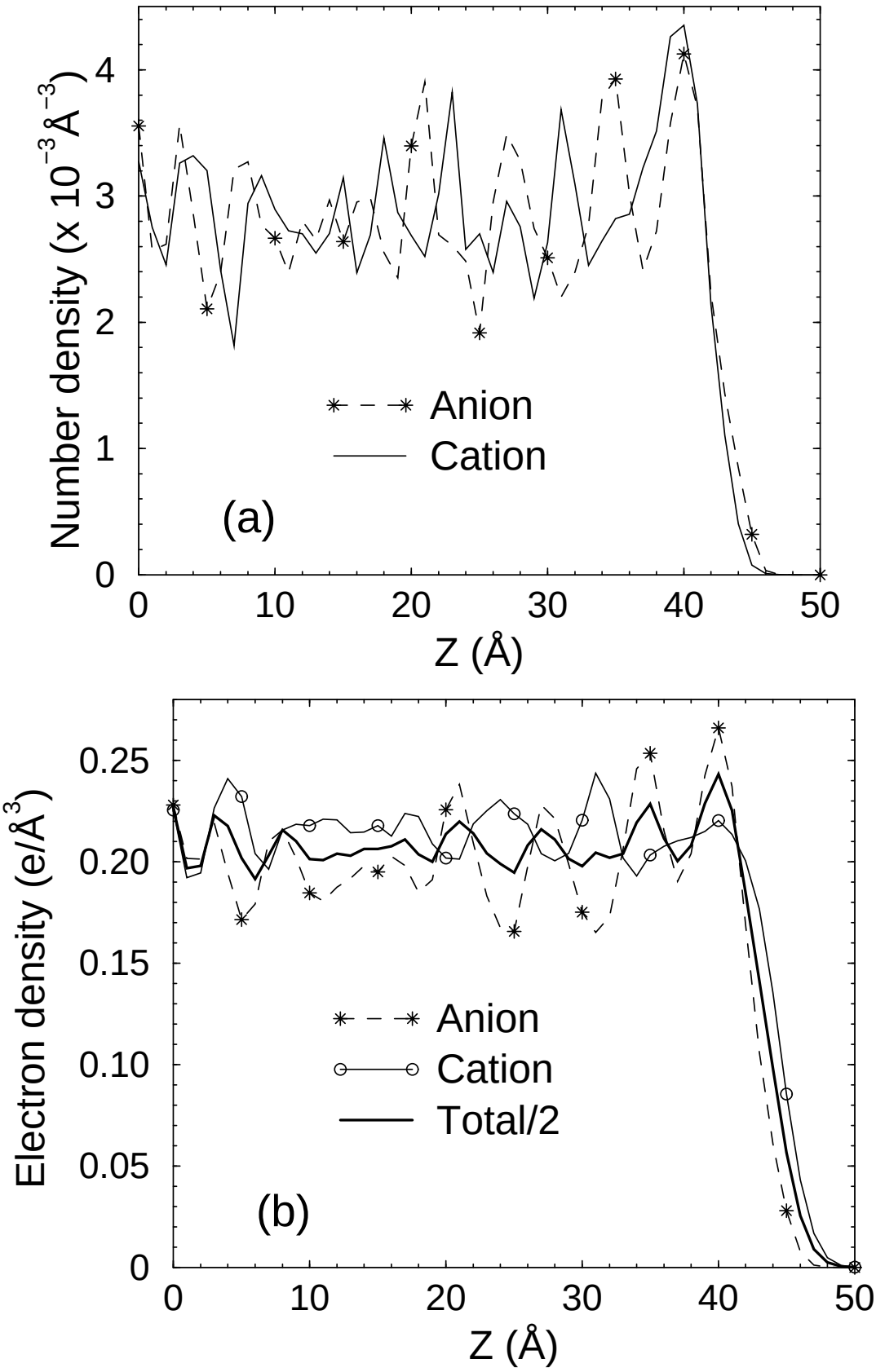

Figure 3.4: (a) Number density profiles of cation and anion for the 512 ion pairs system at 300K. (b) Profile of contribution from anions and cations to the total electron density.

the 512 ion pair system at 300K. A value of +1 and -1 would mean fully correlated and fully anti-correlated functions respectively. Thus the result of -0.54 obtained here quantifies our observation of out-of-phase oscillations in the anion and cation contributions as exemplified in Figure 3.4b.

The anion is found to be mainly responsible for the enhancement of the electron density at the interface as can be seen from Figure 3.4b. Although the number density profile for the cation shows a marginally taller peak at the interface compared to that of the anion (see Figure 3.4a), the contribution from the cation to the total electron density is nearly uniform with few oscillations, whose amplitudes are smaller than those present in the anion contribution. This result can be rationalized due to the higher molecular volume of the cation that results in its electron cloud being more distributed. The anion contribution to the total electron density profile mirrors its number density profile. The combination of these two factors leads to oscillations in the total electron density.

An enhancement in the molar fraction of the anions at the interface was predicted by Deutsch and coworkers [8] as anions are the only electron rich species that could account for the observed interfacial electron density of 0.5 e/Å^3. It turns out from our data that the anion contribution to the electron density enhancement is substantially larger than that of the cation. However, this fact need not imply that the anion number density at the interface has to be larger than that of the cation. Our observations indicate that the interpretation of the reflectivity experiments is nuanced. An increase in the interfacial electron density need not preclude an increase in the number density of cations at the interface over the bulk value. In addition, as stated earlier, the decreased amplitude of oscillations in the total electron density profile can be consistent with the presence of strong oscillations in the number density of ions.

3.3.3 Orientation of cation

Having reconciled this apparent disagreement between experiment and simulations, we proceed now to examine other properties of the interface. We study the orientation of the butyl tail for cations that are present at the interface. In Figure 3.5a, we present the distribution of the angle between the butyl chain (i.e., the N1-C10 vector) and the surface normal (z-axis). We observe that the most probable orientation of the butyl chain is to be parallel to the surface normal. Thus the outermost part of the surface of [bmim][PF_6] liquid is constituted by the butyl chains of the cation, and hence the surface should possess some degree of hydrophobic character. At 300K, a significant number of butyl chains possess a *gauche* defect in the central C-C bond. However, we have found that the percentage of such defects is only marginally increased for cations present at the interface when compared to those in bulk (Data not shown). We have also studied the orientation of the cation ring with respect to the surface normal. In Figure 3.5b, we show the probability distribution for the angle between the ring normal and z-axis. At the interface, there is a marked preference for the N-N vector of the cation to be parallel to the surface normal (z-axis), a result that is consistent with direct recoil spectrometry data [3]. However these distributions are rather wide and hence preferences in orientations are not very strong. Further, the liquid surface is rough at the length scales of a few Angstroms and hence preferences for specific orientations obtained from such distributions should not be used to build generic caricatures of the surface, in which structural motifs other than the preferred ones are absent.

Figure 3.6 summarizes the interfacial structure. The terminal methyl group of the butyl chain is present in the outermost part of the interface, followed by the nitrogen atom (N1) to which the butyl chain is attached, the anion, the center of the imidazolium ring, nitrogen atom to which the methyl group is attached (N2) and then the methyl group attached to the ring. A surface alignment of the cation is evident, with the most probable orientation being that where the butyl chains are aligned parallel to the surface

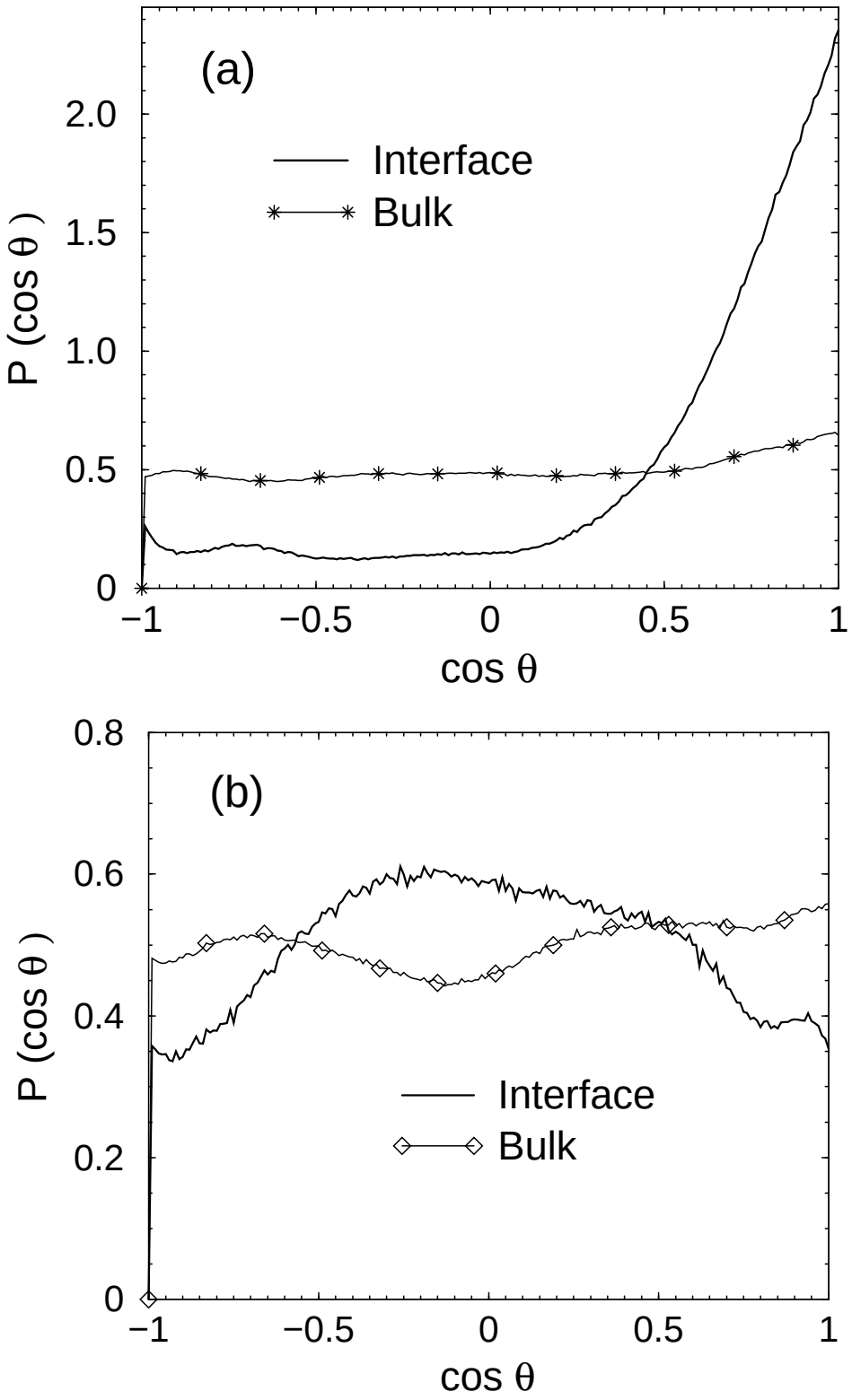

Figure 3.5: (a) Orientation of the chain vector with respect to the interface normal (z-axis) in the interfacial and bulk regions. θ is the angle between the vector N1-C10 and z-axis. (b) Orientation of the ring normal with respect to the interface normal (z-axis) in the interfacial and bulk regions. θ is the angle between the normal to the imidazolium ring plane and z-axis.

normal. The butyl tails of the cations at the interface are interspersed by the anions.

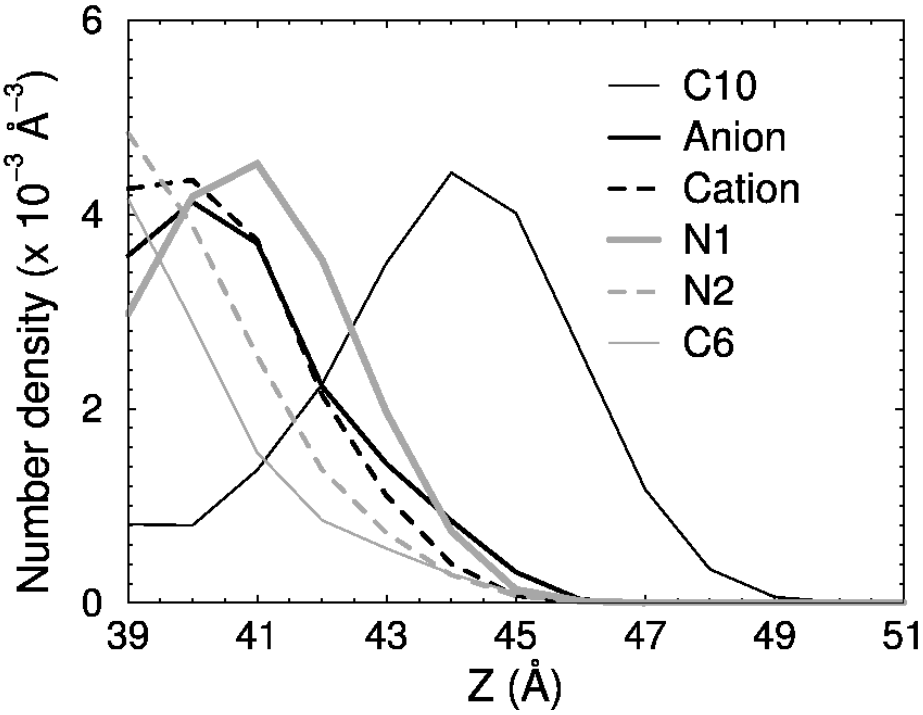

Figure 3.6: The number density profile of different sites on the cation and the anion at 300K for the 512 ion pair system.

The orientation of the cations in the system can be described by Legendre polynomials that are defined as $P_1(\cos\theta) = \cos\theta$ and $P_2(\cos\theta) = \frac{1}{2}(3\cos^2\theta - 1)$. Such functions enable us to obtain an idea of the range and extent of orientational preferences at the interface. The averages $\langle P_2(\cos\theta)\rangle$ for the NN vector, the butyl vector of the cation, and the normal to the imidazolium ring with respect to the z-axis are shown in Figure 3.7. The peak value for the butyl chain function at the interface is in the range of 0.4-0.5, that indicates the degree of orientational preference, relative to a value of unity expected for perfect ordering. The position dependence of the orientation of the N-N vector (i.e., the ring plane) with respect to the surface normal is interesting. Between z=43Å and z=46Å, the value of its P_2 function is negative implying that the ring plane is flat on the surface. This

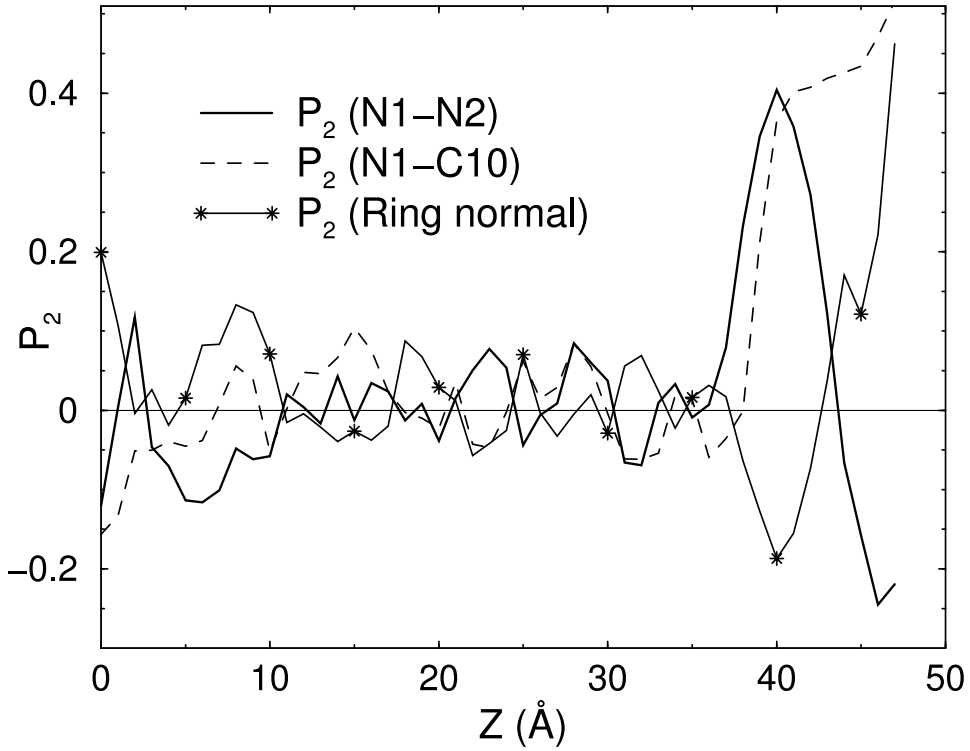

Figure 3.7: The averages $\langle P_2(\cos\theta)\rangle$ of the angle between the specified vector and the surface normal for 512 ion pair system at 300K.

can also be seen from Figure 3.6, where beyond z=45Å the number density profile of N1, N2 and the cation (center of the ring) that determine the plane of the ring, almost coincide that is a clear indication of the ring being aligned nearly parallel to the surface. Beneath this exposed surface lies a high density region in which the ring plane of the cation is perpendicular to the plane of the interface. This might explain the differences observed in the cation ring orientation between SFG [10, 28] and DRS experiments [4, 5]. The former observe the ring plane to be flat on the surface, while the latter report a perpendicular orientation. It should be noted however that the range of such an orientational preference is rather short with only the first layer at the surface exhibiting such preferences. In the bulk region, the second order Legendre polynomial for all the angles vanish due to its isotropicity, as expected.

The surface tension values for the 256 ion pair system were estimated to be 73, 38 and 36 mNm^{-1} respectively at temperatures of 300K, 400K and 500K. The value at 300K is larger than the experimental value of $45mNm^{-1}$ [8, 29]. The difference could point to deficiencies in the model potential as well as to the smaller surface area employable in simulations compared to experiments. Surface tension is a rather tough quantity to converge in equilibrium simulations. For instance, at 300K, the estimated standard deviation on the mean value of 73 mNm^{-1} is 222 mNm^{-1}! Non-equilibrium methods to obtain surface tension from atomistic simulations could be helpful.

3.4 Conclusions

The microscopic structure of liquid [bmim][PF_6]-vapor interface has been elucidated using atomistic molecular dynamics simulations. The potential model is found to predict the bulk density and thermal expansion coefficient of the liquid quite well, although the calculated surface tension is larger than the experimental value. We summarize our main results as follows.

(i) Density oscillations are observed at the interface – in the number density of cations and anions, in mass density, and also in the electron density. Oscillations in the electron density are much diminished when compared to the amplitude of oscillations in the number densities, due to a near cancellation in the contributions from the anions and that of the cations.

(ii) The electron density at the interface is around 12% larger than in the bulk. This result is in excellent agreement with conclusions drawn from X-ray reflectivity measurements [8].

(iii) The enhanced electron density at the interface is largely contributed by the anions, although both anions and cations enrich the surface. The cationic contribution to the electron density profile is nearly featureless, due mainly to its larger molecular volume.

(iv) The butyl chain of the cations present at the interface exhibits a preference to orient along the surface normal. Hence the surface could be expected to have a certain amount

of hydrophobic character. However, the hydrophobicity of this surface will be lesser than that of a *n*-alkane, due to the presence of charged groups in the vicinity.
(v) In the densest region of the interface, the cation ring plane is oriented parallel to the surface normal. Closer to the vapor phase that is rarer, the ring plane is parallel to the surface plane.

Surface density oscillations are a consequence of a finite molecular size and surface tension. Our estimates of surface tension tend to be larger than the experimental value. Could the density oscillations observed here be a consequence of the higher surface tension of the simulated interface? We discount this possibility, as such oscillations are observed in our systems at 400K and 500K as well, where our surface tension estimates are comparable to the experimental value (at 300K). This provides us confidence that density oscillations are indeed present in liquid [bmim][PF_6] at its vapor interface at 300K. However, simulations study much smaller samples than considered in experiments, and hence they do not include effects of capillary waves.

The observation of large amplitude oscillations in the number density at the interface is in apparent disagreement with the conclusions from X-ray reflectivity experiments [8]. The electron density profile obtained here exhibits oscillations with the same period as one of the profiles reported in Deutsch *et al* that was not selected for further analyses by them based on considerations of experimental resolution. On the other hand, in partial agreement with them, we find that the oscillations in the total electron density profile are diminished in amplitude relative to that found in the number density profile. The underlying reason for the observation of strong oscillations at the interface in the number densities of ions and a weak one in the electron density profile is the difference in the molecular sizes of the two species being appropriate to nearly cancel out their contributions to the total electron density. This central result is unlikely to change with the inclusion of polarizable interactions. Recent MD simulations on the liquid-vapor interface of a different IL, i.e., [emim][NO_3] at 400K [27] using a polarizable model exhibits similar

features of an out-of-phase oscillation in the number densities of cations and anions, a result that is crucial to the arguments enunciated in our work. Such a behavior in the number density profile can lead to similar effects in the contribution of ions to the total electron density profile, as reported here. It thus appears that our interpretation of the decreased amplitude in the electron density profiles of the liquid-vapor interfaces of ionic liquids possessing short side chains could be general.

Bibliography

[1] T. Welton, *Chem. Rev.*, **99**, 2071 (1999).

[2] P. Jungwirth, D.J. Tobias, *J. Phys. Chem. B*, **106**, 6361 (2002).

[3] T.J. Gannon, G. Law, P.R. Watson, *Langmuir*, **15**, 8429 (1999).

[4] G. Law, P.R. Watson, *Chem. Phys. Lett.*, **345**, 1 (2001).

[5] G. Law, P.R. Watson, A.J. Carmichael, K.R. Seddon, *Phys. Chem. Chem. Phys.*, **3**, 2879 (2001).

[6] J. Bowers, M.C. Vergara-Gutierrez, *Langmuir*, **20**, 309 (2004).

[7] T. Iimori, T. Iwahashi, H. Ishii, K. Seki, Y. Ouchi, R. Ozawa, H. Hamaguchi, D. Kim, *Chem. Phys. Lett.*, **389**, 321 (2004).

[8] E. Sloutskin, B.M. Ocko, L. Tamam, I. Kuzmenko, T. Gog, M. Deutsch, *J. Am. Chem. Soc.*, **127**, 7796 (2005); **127**, 18333 (2005).

[9] J. Sung, Y. Jeon, D. Kim, T. Iwahashi, T. Iimori, K. Seki, Y. Ouchi, *Chem. Phys. Lett.*, **406**, 495 (2005).

[10] S. Rivera-Rubero, S. Baldelli, *J. Phys. Chem. B.*, **110**, 4756 (2006).

[11] M.J. Regan, P.S. Pershan, O.M. Magnussen, B.M. Ocko, M. Deutsch, L.E. Berman, *Phys. Rev. B*, **54**, 9730 (1996).

[12] R.M. Lynden-Bell, *Mol. Phys.*, **101**, 2625 (2003).

[13] R.M. Lynden-Bell, J. Kohanoff, M.G. Del Popolo, *Faraday Discuss.*, **129**, 57 (2005).

[14] R.M. Lynden-Bell, M.G. Del Popolo, *Phys. Chem. Chem. Phys.*, **8**, 949 (2006).

[15] J.N.C. Lopes, J. Deschamps, A.A.H. Pádua, *J. Phys. Chem. B*, **108**, 2038 (2004); **108**, 11250 (2004).

[16] B.L. Bhargava, S. Balasubramanian, *J. Chem. Phys.*, **123**, 144505 (2005); **125**, 219901 (2006).

[17] B.L. Bhargava, S. Balasubramanian, *Chem. Phys. Lett.*, **417**, ,486 (2006).

[18] O. Borodin, G.D. Smith, R.L. Jaffe, *J. Comput. Chem.*, **22**, 641 (2001).

[19] M.E. Tuckerman, D.A. Yarne, S.O. Samuelson, A.L. Hughes, G.J. Martyna, *Comput. Phys. Commun.*, **128**, 333 (2000).

[20] Allen, M.P.; Tildesley, D.J. *Computer Simulation of Liquids* (Clarendon Press, Oxford, 1987).

[21] G.J. Martyna, M.L. Klein, M.E. Tuckerman, *J. Chem. Phys.*, **97**, 2635 (1992).

[22] M.E. Tuckerman, B.J. Berne, G.J. Martyna, *J. Chem. Phys.*, **97**, 1990 (1992).

[23] M. Rao, B.J. Berne, *Mol. Phys.*, **37**, 455 (1979).

[24] M. González-Melchor, F. Bresme, *J. Chem. Phys.*, **122**, 104710 (2005).

[25] J.G. Huddleston, A.E. Visser, W.M. Reichert, H.D. Willauer, G.A. Broker, R.D. Rogers, *Green Chem.*, **3**, 156 (2001).

[26] C. Cadena, J.L. Anthony, J.K. Shah, T.I. Morrow, J.F. Brennecke, E.J. Maginn, *J. Am. Chem. Soc.*, **126**, 5300 (2004).

[27] T. Yan, S. Li, W. Jiang, X. Gao, B. Xiang, G.A. Voth, *J. Phys. Chem. B.*, **110**, 1800 (2006).

[28] S. Rivera-Rubero, S. Baldelli, *J. Am. Chem. Soc.*, **126**, 11788 (2004).

[29] G. Law, P.R. Watson, *Langmuir*, **17**, 6138 (2001).

Chapter 4

Insights into the Structure and Dynamics of a Room Temperature Ionic Liquid: *Ab Initio* Molecular Dynamics Simulation Studies of [bmim][PF_6] and the [bmim][PF_6] - CO_2 Mixture

4.1 Introduction

Supercritical CO_2 that is being used in several synthetic processes has been suggested as a replacement for chlorofluorocarbons (CFCs) [1]. It is also one of the well studied systems through a combination of experimental [2,3] and computational [4–6] approaches. RTILs have many potential applications [7, 8] and have been widely studied [9–19]. A variety of computational methods, including simulations of RTILs, have provided a microscopic

picture of these systems [20–29]. RTILs too can have the potential to replace volatile organic solvents that are currently employed in several synthetic procedures [7]. However, the recovery or extraction of the products of a chemical reaction that is conducted in an ionic liquid *via* distillation is difficult due to the low volatility of the solvent [30]. The possibility of redressing this limitation by using $scCO_2$ has attracted much recent attention [31–34]. Furthermore, the interaction between the solute and the solvent in the mixture can impart new properties that the individual components may not possess [35]. The current focus of research on these mixtures is on the need to understand the molecular level interactions between the RTIL and CO_2 [36–42].

CO_2 is remarkably soluble in imidazolium based ionic liquids [31, 43–47]. On the other hand, the solubility of ILs in CO_2 is immeasurably low [31, 43]. This opens up the possibility of extracting products of an organic reaction or contaminants from ionic liquids, using CO_2. Brennecke and coworkers [33] have demonstrated the separation of organic compounds and water from ILs using CO_2.

The RTIL-CO_2 mixture has been studied from the viewpoint of understanding the molecular level interactions by Maginn and coworkers [38]. By examining the effect of varying the anion among different ILs, their experiments and computer simulations have shown that the anion influences the solubility of CO_2 to a larger extent than the cation. The nature of this anion-CO_2 interaction was probed using vibrational spectroscopic methods by Kazarian *et al* [36] who found evidence of a weak Lewis acid-base interaction between CO_2 and the anions of the ILs. Analyses of the void distribution in computer generated configurations of the IL-CO_2 mixture have shown that the CO_2 molecules are predominantly found to be located in pre-existing void spaces in the IL that reorganize to accommodate the CO_2 [40]. This observation offers a neat explanation for the negligible increase in molar volume of the solution compared to that of the pure IL. In a recent X-ray diffraction study [41], Kanakubo and coworkers have examined the intermolecular structure of the solution, in particular the location and orientation of the CO_2 molecule with

respect to the PF_6 anion. They concluded that the CO_2 molecule may not be tangential to the PF_6 sphere as was claimed in the computer simulation studies [38, 40]. Elucidating the intermolecular structure in a complex liquid such as [bmim][PF_6] is a challenging task that demands the combined use of experimental, computational and theoretical probes. In this effort, scattering experiments are handicapped by the lack of phase information. It is also quite difficult to obtain partial pair correlation functions of such systems, directly from experiments. Although atomistic computer simulation methods such as molecular dynamics (MD) or Monte Carlo that employ empirical potentials have redressed this lack of knowledge to a large extent, doubts on the transferability of the potential parameters across various condensed systems limit their capability to truthfully represent ILs.

Given this background and the importance of the systems involved, it is crucial that a reliable microscopic picture of the intermolecular structure of the mixture is obtained. *Ab initio* molecular dynamics simulations based on density functional theory have had considerable success in the recent past in the elucidation of the structure and dynamics in a variety of complex systems, including ionic liquids [48–54]. In this work, we report results of such a study on the CO_2-[bmim][PF_6] mixture in the hope that it will augment the current knowledge. As a reference system, we present results of Car-Parrinello MD simulations on pure [bmim][PF_6] as well. Our methods are detailed in the next section, followed by a presentation of the results. We end with conclusions drawn from our study.

4.2 Methodology and Simulation Details

A mixture of CO_2 and a room temperature ionic liquid, 1-*n*-butyl-3-methylimidazolium hexafluorophosphate was studied using *ab initio* molecular dynamics simulations. The simulated system consisted of 12 units each of [bmim] and [PF_6] ions and 28 CO_2 molecules, amounting to 70 mole percent of CO_2 in the mixture. The simulations were carried out at 298K at extrapolated experimental density [41, 43, 55, 56] using the CPMD [57, 58] code. This system with a total of 468 atoms was simulated in a cubic box of edge length

17.56 Å. The initial configuration for the CPMD run was generated by equilibrating the system at room temperature and experimental density for a duration of 8 ns using classical MD with a force field as mentioned later. Norm conserving pseudopotentials of the Troullier-Martins form [59] were employed to take into account the effect of the core electrons and the nuclei. Gradient corrected exchange and correlation functionals prescribed by Becke [60] and Lee, Yang, Parr [61] were employed. The initial configuration for the CPMD run was obtained from a classical MD simulation of 8 ns duration. A plane wave basis set with an energy cutoff of 90 Ry was used to expand the electronic orbitals. This value of the cutoff was chosen after checking for the convergence of the forces on ions as a function of increasing energy cutoff. Three dimensional periodic boundary conditions were applied to obtain bulk behavior. All the hydrogens in the system were substituted by deuterium, in order to enable the use of a larger time step of integration. Prior to the CPMD run, the electronic degrees of freedom were quenched to the Born-Oppenheimer surface. During the CPMD simulations, a fictitious electron mass of 700 a.u. was employed. The kinetic energy of the ions were controlled using the Nosé-Hoover chain thermostat [62]. The equations of motion were integrated with a time step of 5 a.u. (around 0.12 fs) over a length of 13.9 ps out of which the last 10.4 ps data was used for analysis. The conservation in total energy was 8 parts in 10^9 over a duration of 7 ps.

In order to study the differences in the structure and dynamics upon addition of CO_2 to [bmim][PF_6], an additional CPMD simulation of pure [bmim][PF_6] containing 12 ion pairs was carried out at room temperature and at a density of 1.36 g/cc. This system consisted of a total of 384 atoms within a cubic box of edge length 16.09 Å. The CPMD trajectory length was 11 ps, out of which the last segment of 7.9 ps duration was used for analysis. Other details of the run are the same as that for the mixture.

In addition to these CPMD calculations, classical molecular dynamics simulations (using empirical potentials) were carried out on a mixture containing 70 mole percent of CO_2. This system consisted of 324 ion pairs of [bmim][PF_6] and 756 CO_2 molecules,

together accounting for a total number of 12,636 atoms. The model was fully flexible with respect to the [bmim][PF_6] ion pairs, while the bond lengths of the CO_2 molecules were constrained in accordance to the EPM2 interaction potential [63]. The simulations were carried out in a cubic box of edge length, 53.0 Å with periodic boundary conditions consistent with the cubic symmetry. Nosé-Hoover chain thermostats [62] were used to maintain the temperature of the system at 298 K. The form of the interaction potential and parameters for the [bmim][PF_6] ion pair was adopted from the work of Lopes *et al.*, [64] that is consistent with OPLS/AA and AMBER schemes. The PF_6 ion was made fully flexible by adding the stretching and bending potentials derived from earlier work [65]. The interaction potential parameters for the CO_2 molecules were obtained from the work of Harris and Yung [63]. Cross interactions were treated using Lorentz-Berthelot rules. Based on the procedures outlined here, we have recently studied the liquid-vapor interface of [bmim][PF_6] [66]. Coulombic interactions were handled using the Ewald summation method. 10,239 reciprocal lattice space vectors were used to calculate the Coulomb energy. Non-bonded interactions were calculated up to a distance cutoff of 13 Å. The equations of motion were integrated using the multiple time step algorithm, RESPA [67], in which non-bonded interactions beyond 6 Å and within 13 Å were calculated with a time step of 3 fs, and those within 6 Å were calculated with a time step of 1.5 fs. The torsional forces were computed every 0.75 fs, and the bending and stretching degrees of freedom were integrated with a fine time step of 0.375 fs. The position of the atoms in the system were stored every 0.9 ps that were used for analysis.

A bin width of 0.2Å is used in the calculation of radial distribution functions, except for the crystalline RDFs for which a finer bin width of 0.001Å is used.

For the calculation of molecular dipole moments, 34 instantaneous configurations each of the pure [bmim][PF_6] system and of the mixture were selected and the centers of maximally localized Wannier orbitals [68–72] were obtained using the CPMD code. The dipole moment of molecules or ions were calculated by assigning a charge of -2e for the

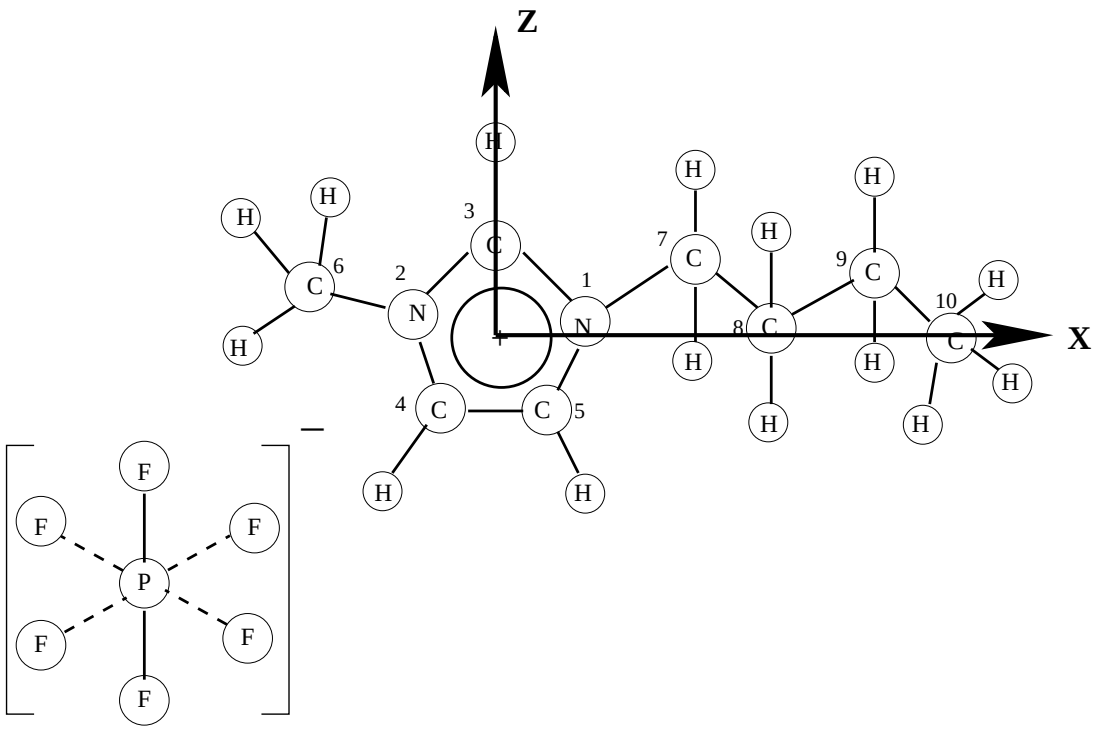

Figure 4.1: Schematic representation of [bmim][PF_6] along with the atom numbering scheme. The axes define the coordinate system employed in the calculation of the dipole moment of the cation. Y-axis is perpendicular to the plane of the imidazolium ring.

Wannier centers and atomic valence charges for the ion centers. The dipole moment for a charged system depends on the choice of the origin of the coordinate system. Here, we follow the earlier work of Lynden-Bell and coworkers [73] on a similar calculation performed for liquid 1,3-dimethylimidazolium chloride. The dipole moment in the classical system was calculated using the partial charges on the atoms.

4.3 Results and Discussions

A schematic of [bmim][PF_6] along with the atom numbering scheme and the coordinate system employed for the calculation of dipole moments is presented in Figure 4.1 in order to aid further discussion. A few of the bond lengths and bond angles, obtained from the geometry optimized structure of the cation or anion in gas phase (i.e., under isolated conditions) are compared against the values in the crystal [74] in Table 4.1. The geometry

Table 4.1: Comparison between the geometry of 1-*n*-butyl,3-methylimidazolium hexafluorophosphate determined from X-ray crystal structure [74] and that from a CPMD optimized configuration in gas phase (isolated conditions).

Type	Bond Length [Å]	
	Experiment	CPMD
N1-C3	1.33	1.35
N1-C5	1.38	1.39
N2-C3	1.32	1.34
N2-C6	1.47	1.48
N1-C7	1.47	1.50
C4-C5	1.35	1.37
C9-C10	1.52	1.54
P-F	1.60	1.71
Type	Angle [degree]	
	Experiment	CPMD
N1-C3-N2	108.8	108.9
N1-C4-C5	107.2	107.3
C3-N1-C7	125.6	125.6
C3-N2-C6	125.3	125.7

of the imidazolium ion is in good agreement with the crystal structure. Most bond lengths of the cation are reproduced within 1.5% of experiment. The planarity of the ring too is reproduced in the *ab initio* calculations. However, the calculated P-F distance is farther from that in the crystal by 6%. This appears to be a limitation of density functional theory [75]. We wish to note here that the fluorine pseudopotential itself was tested by optimizing the geometry of an isolated F_2 molecule. In F_2, F-F distance was found to be 1.435Å that is to be compared against a value of 1.4119Å in experiment [76].

Ab initio MD simulations of liquids demand large computational resources although the accessible time and length scales are rather limited. Under these circumstances, one needs to ensure that the duration of the trajectory allotted for equilibration and analyses are adequate. In addition, since ILs in general, and [bmim][PF_6] in particular, are viscous (with viscosity of around 200cP at 300K), it is conceivable that the properties obtained

Table 4.2: Maximum and mean squared displacement of CO_2 molecules and the ions over 8 ps.

Ion/ Molecule	Maximum displacement (Å)	Mean squared displacement (Å^2)
CO_2	5.6	4.7
PF_6	3.0	2.4
[bmim]	3.0	2.8

from such limited CPMD simulations could reflect that of the initial configurations. However, we have found several crucial structural quantities to differ between the classical MD and AIMD simulations. Hence the results reported here are less likely to be influenced by any bias in the initial configuration.

In the subsections that succeed, we present results on the arrangement of CO_2 molecules in the IL. It is thus natural to ask whether the CO_2 molecules sample the configuration space well. This can be answered by studying the magnitude of their displacements. The values of mean squared displacements of various species in the system, including that of CO_2 are provided in Table 4.2. Over a duration of 8 ps, the mean squared displacement of CO_2 has been calculated to be 4.7 Å^2 with a maximum displacement of 5.6Å. For the sake of completeness, the values obtained for the anion and the cation are also presented in Table 4.2.

Another quantity of interest that demonstrates the mobility of CO_2 molecules is the reorientational time correlation function of the CO_2 backbone that is shown in Figure 4.2. The P_1 and P_2 functions (first and second order Legendre polynomials) decay to values of around 0.4 in 4 ps indicating that, on average, every CO_2 molecule would have explored the local orientational landscape within the time scales for which we have simulated the mixture.

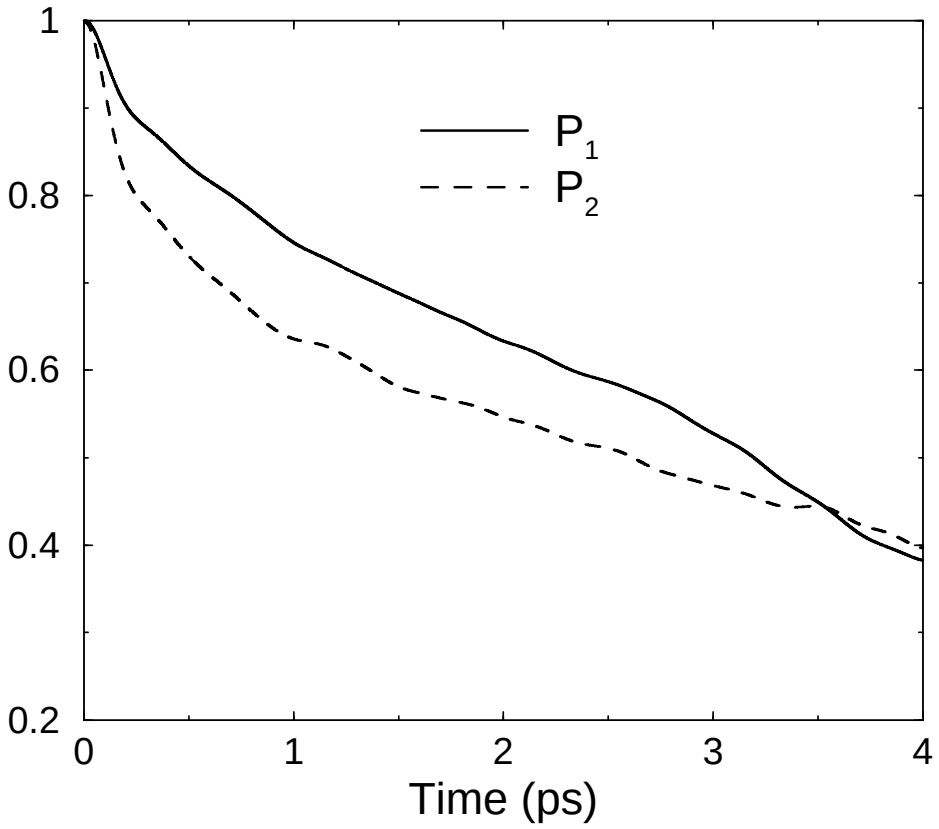

Figure 4.2: First (P_1) and second order (P_2) Legendre polynomial based rotational time correlation functions of the backbone vector of CO_2 molecules obtained from CPMD simulations of [bmim][PF_6] - CO_2 mixture.

4.3.1 Radial distribution functions

The partial radial distribution functions of the ions calculated from the CPMD, classical MD runs and the crystal for pure [bmim][PF_6] are presented in Figures 4.3a and 4.3b. Here, the anion is represented by the phosphorus atom, and the cation by the center of the imidazolium ring. The anion-anion radial distribution function obtained from CPMD exhibits significant differences with that from the classical MD simulation. The RDF for PF_6 - PF_6 seems to show a shoulder at around 6 Å that is absent in the classical MD data. Significantly, the anions approach each other closer in the CPMD trajectory. This may be attributed to the natural inclusion of electronic polarization of the anions in CPMD that is missing in the classical interaction potential [77]. A slight increase in

the intensity and a hump near 4.7Å are observed in the [bmim]-PF_6 RDF obtained from CPMD. Interestingly, the first peak in the crystalline RDF is also present at this distance. Relatively minor differences in the cation-cation g(r) between classical and CPMD data are ignored in the present discussion due to paucity of statistics. Comparison of CPMD data with that of crystal RDFs reveals strong similarities between the intermolecular structure in the liquid and that in the crystal.

Several MD simulation studies on the IL, [bmim][PF_6] using empirical potentials have been reported [78–81]. The partial radial distribution functions reported in these studies have been found to be different from one another and to varying extents with our *ab initio* results [39]. The potential model used by Morrow and Maginn [79] and Margulis *et.al.* [78] predict higher peak intensity for the C3-P radial distribution function compared to our *ab initio* results (data not shown).

The effect of CO_2 on the structure of IL in the mixture can be seen from Figure 4.3c, that compares various partial radial distribution functions obtained from CPMD simulations in the presence and in the absence of CO_2. In tune with earlier reports [38,40], there is no noticeable difference in the partial RDFs. However, the anion - anion RDF seems to be strongly influenced by the presence of CO_2. The corresponding coordination number at 8Å is 3.2 in the mixture compared to a value of 5.4 in the pure liquid. This decrease is likely due to the stronger anion-CO_2 interaction that is discussed in detail in the following sections. The existence of solvent (CO_2) separated ion pairs can be discerned from the marginal reduction in the intensity of the cation-anion RDF. The similarity between the RDFs of the mixture and of the pure IL can be rationalized. Physical measurements [55] and earlier simulations [40] have shown that the addition of CO_2 does not change the molar volume of the ionic liquid significantly. In particular, Berne and coworkers [40] have demonstrated that the CO_2 molecules prefer to occupy the void regions present in the IL.

Figure 4.4a compares the radial distribution functions, obtained from CPMD simula-

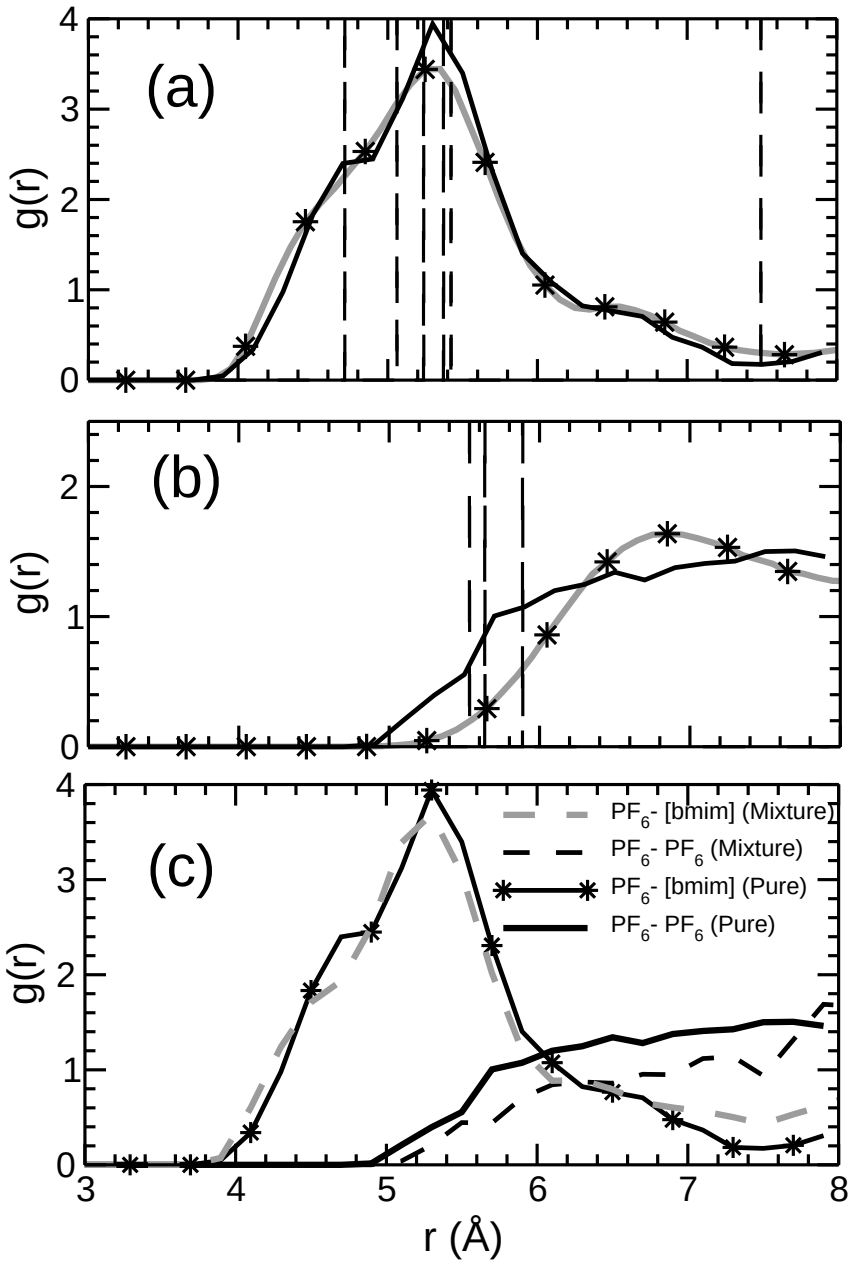

Figure 4.3: (a)&(b) Comparison of radial distribution functions obtained from classical MD and CPMD simulations in pure [bmim][PF_6] as well as in the [bmim][PF_6] crystal [74]. (a)[bmim] - [PF_6], (b) PF_6 - PF_6. Solid black line represents CPMD data, solid grey line with stars represents classical MD results, and the dashed black line corresponds to the crystal. (c) Comparison of radial distribution functions obtained from CPMD data in the presence and absence of CO_2. Symbols are shown infrequently for clarity.

tions, for fluorines of the anion around the ring hydrogen H(C3) in the mixture and in the pure liquid. The fluorine atoms are found to be nearer to the ring hydrogen H(C3) and the first peak height is more intense in the mixture by about 11% over its value in the pure system. A part of this change could also have arisen from the minor differences in the molar volume of the two systems studied.

Crucial differences are noticed in the RDF of the fluorine atoms of the anion and the ring hydrogen H(C3), between the CPMD and classical MD simulations of the mixture, as shown in Figure 4.4b. In the former, a clear shift towards smaller distances is observed in the position of the first peak. Further, a reduction in the peak height is also observed. It can thus be safely said that the ring proton H(C3) forms a hydrogen bond with the fluorine atoms of the anion. Some of the classical models [80] are found to overestimate the hydrogen bonding between the ring proton H(C3) and fluorines of the anion. In view of the distances involved, this hydrogen bond would be characterized as "weak" [82]. Based on a maximum H-F distance of 2.5Å and a minimum value for the C-H-F angle of 160 degrees to define a hydrogen bond, the fraction of cations in pure [bmim][PF_6] that form such H-bonds is estimated to be around 8%. This is to be compared against a value of 3.7% obtained from classical MD simulations. A snapshot of a part of the bulk system selected from the CPMD trajectory is shown in Figure 4.5 [83], as an example of the cation-anion hydrogen bond. Although empirical potential MD predicts nearly the same percentage of cation-anion hydrogen bonding in the mixture compared to the pure system, CPMD results show a marginal increase in the percentage of hydrogen bonding that is around 11.5% in the mixture. The [bmim][PF_6] crystal is reported to contain 7 hydrogen bonds per cation [74], based upon liberal hydrogen bond criteria, that the H-F bond length be less than 2.7Å and the C-H-F angle be greater than 90 degrees. Using these criteria, it was found that there are, on an average 10 hydrogen bonds per cation in the neat liquid simulated using CPMD. To summarize, although the density functional theory (DFT) based simulations predict a higher propensity of H-bonds in the ionic liquid

compared to classical simulations, their fraction and strength appear to be weak. This is particularly valid for an anion that is weakly basic such as the hexafluorophosphate studied here. The tetrafluoroborate anion could form a stronger cation-anion hydrogen bond. Formation of strong cation-anion hydrogen bonds have been reported earlier in another IL, 1,3-dimethylimidazolium chloride ([dmim][Cl]) [48–50,84,85]. We also observe a rather small, but non-negligible increase in the number of hydrogen bonds in the liquid upon addition of CO_2. This needs further examination.

The radial distribution of CO_2 molecules around the ions and CO_2 is shown in Figure 4.6. The narrower first peak in the case of the anion shows that the CO_2 molecules are more ordered around the anion than around the cation. CO_2 molecules are also proximal to the anion center rather than to the ring center of the cation. The first peak of the anion-CO_2 g(r) is at 4.3Å with a coordination number of 4.6 up to the first minimum at 5.9Å, whereas the cation-CO_2 g(r) peaks at 5.3Å with a coordination number of 8.7 up to the first minimum at 7.3Å. The difference in the mean PF bond distance between theory (1.7Å) and experiment (1.6Å) may have a minor effect on the radial distribution function between PF_6 and CO_2. In reality, the pair correlation function may be shifted by about 0.1Å with a marginal reduction in the P-C coordination number.

The coordination number of CO_2 around the anion, that is 4.6 compares with the value of 4.0 estimated from X-ray scattering experiments [41]. The reported [41] interatomic distance between phosphorus and carbon atom of CO_2 (P-C) is 3.59Å that is quite small when compared to the observed first peak position in our CPMD simulations and also earlier empirical potential MD simulations. Also, the interatomic distance of 3.59Å for P-C demands that the distance between the atoms of the anion and that of CO_2 to be less than the sum of their van der Waals radii. It is thus likely that the peak at 3.6Å observed in the total g(r) in scattering experiments is likely to come from CO_2 - CO_2 pairs rather than from CO_2 - PF_6 pairs.

However, our simulations also found that each CO_2 interacts with two PF_6 ions, in

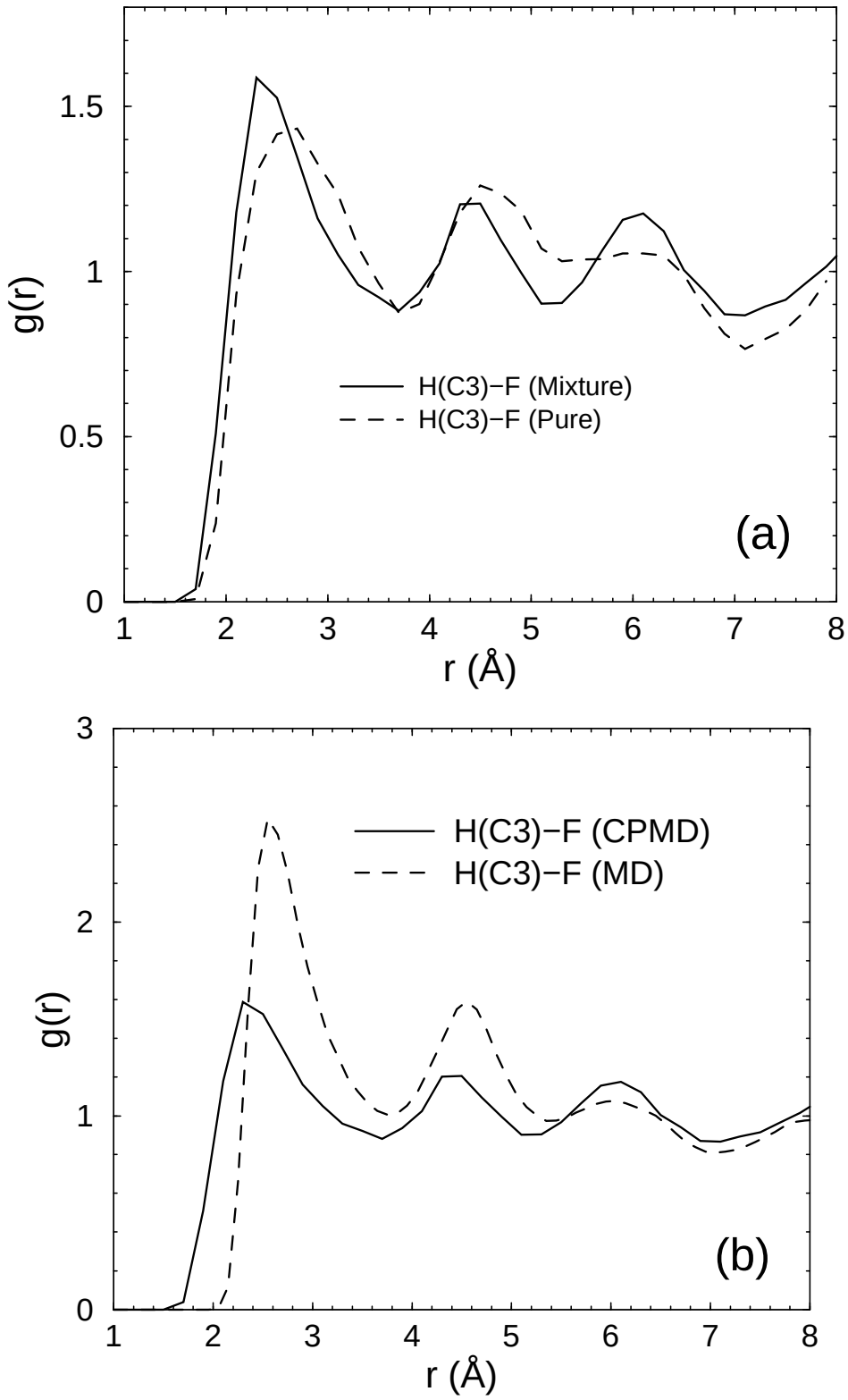

Figure 4.4: Comparison of radial distribution functions between (a) ring hydrogen H(C3) and fluorine obtained from CPMD simulations, in the presence and in the absence of CO_2. (b) ring hydrogen (H(C3)) and fluorine in the mixture obtained from CPMD and from classical MD simulations.

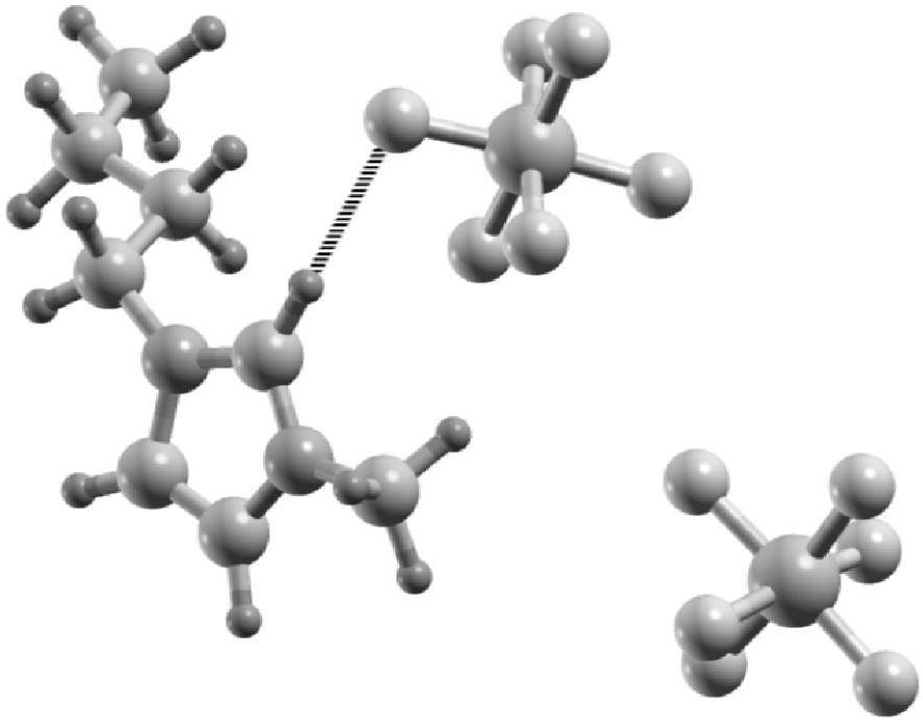

Figure 4.5: A snapshot of part of the pure [bmim][PF_6] system from the CPMD trajectory, showing the hydrogen bond between H(C3) and fluorine of the anion.

agreement with the experiments [41]. As discussed earlier, this strong coordination of CO_2 around the anion influences the anion-anion RDF in the mixture, that differs from that in the pure system. The CO_2 - CO_2 g(r) peaks at 3.7Å with a coordination number of 4.3 up to the first minimum at 5.9Å. ¿From the amplitude of the peaks in Figure 4.6, it is evident that the CO_2 molecules are preferentially found near the anion. Another novel finding of the current work is the characterization of the intermolecular structure between CO_2 and the cation. We have observed that among the ring hydrogens, the one attached to C3 is closest to the oxygen atom of CO_2. It exhibits a clearer coordination shell when compared to the other two ring hydrogens. Figure 4.7 compares the radial distribution function of the oxygen atoms of CO_2 around the ring hydrogen H(C3), obtained from classical and CPMD simulations. The increased interaction of the oxygens with H(C3) suggests the formation of a weak hydrogen bond in the CPMD simulations. Using the

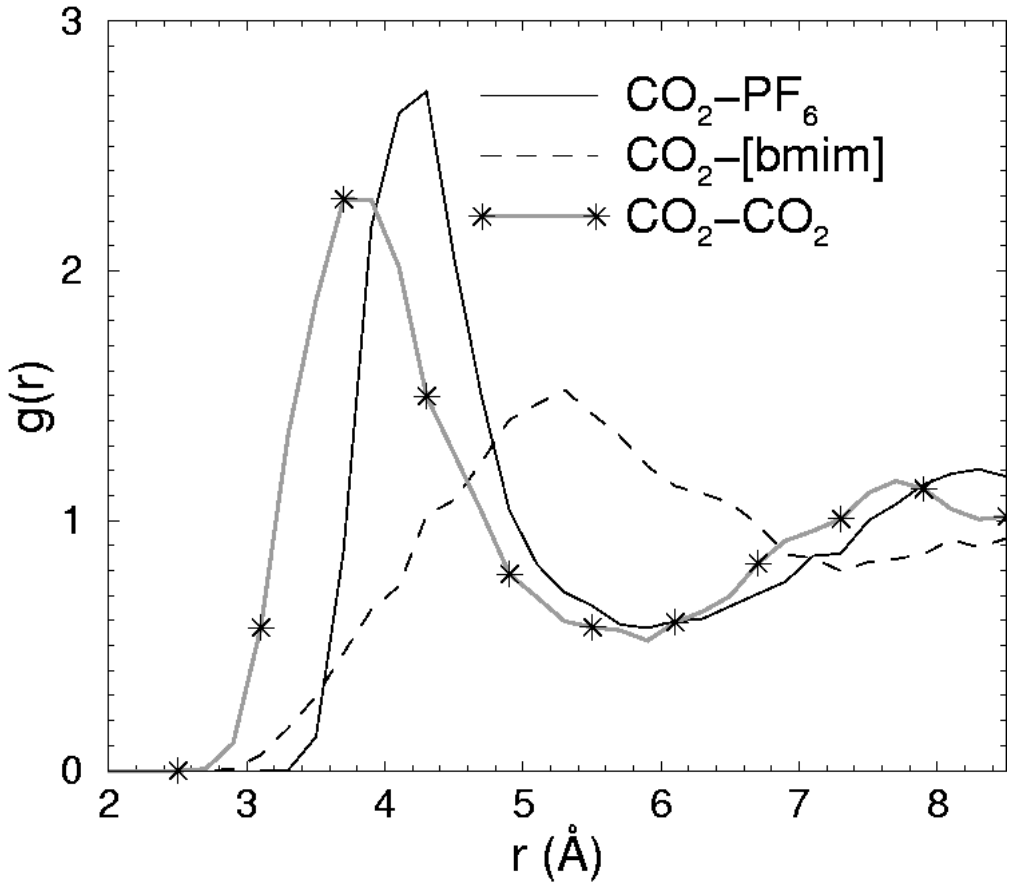

Figure 4.6: Partial radial distribution function of CO_2 around the cation, the anion and CO_2 in the mixture, obtained from CPMD simulations. The position of the carbon atom is taken to represent the CO_2 molecule. The cation is represented by the geometric center of the imidazolium ring while the phosphorus atom denotes the anion location.

liberal criteria for hydrogen bonding, i.e., H-O distance less than 2.7Å and C-H-O angle greater than 90 degrees, it was found that the oxygen atom of CO_2 was hydrogen bonded to the ring hydrogen H(C3) for about 5% of the time in CPMD against 2% in the classical MD simulations. The absence of such an interaction in the classical potential model is striking and needs to be redressed.

In Figure 4.8, we compare the intermolecular radial distribution functions (RDF) obtained from our simulations with the X-ray scattering results of Kanakubo et al [41]. A good agreement between simulation and experiment is observed for pure [bmim][PF_6] while the prominent oscillations found in the experimental data for the CO_2 - [bmim][PF_6]

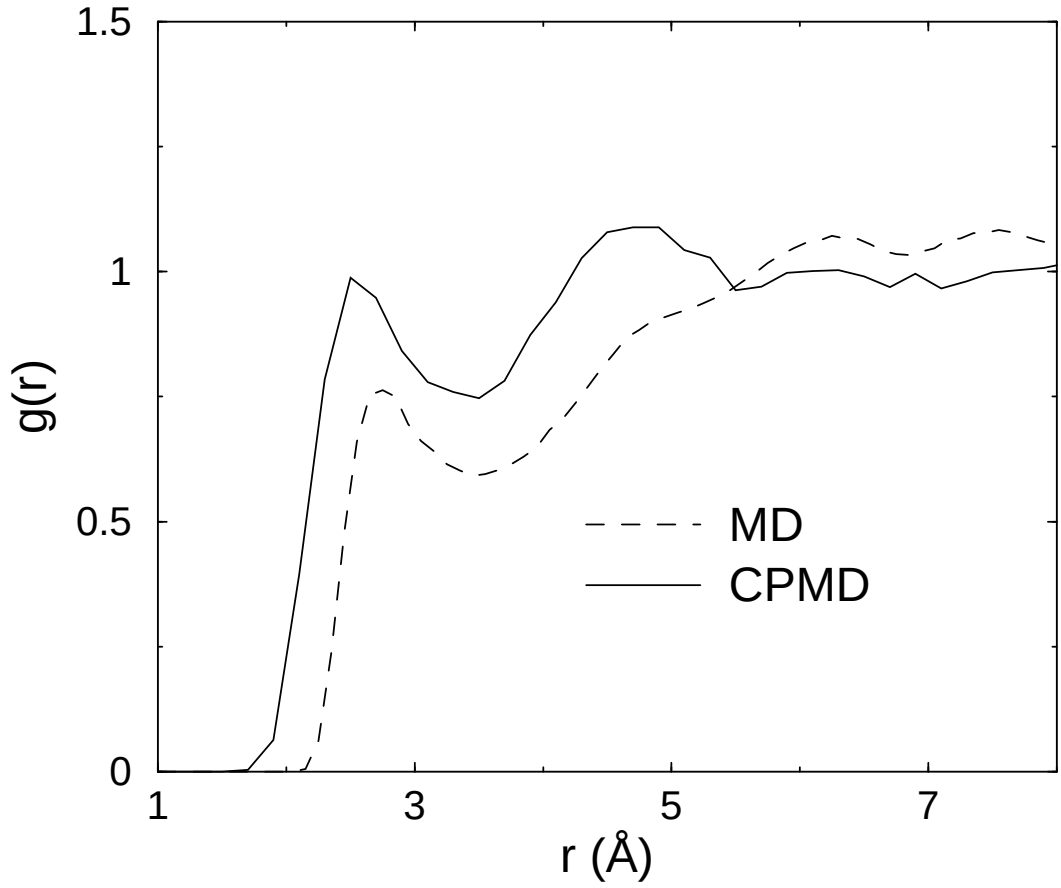

Figure 4.7: Comparison of the radial distribution function of oxygen atoms of CO_2 around the ring hydrogen H(C3) in the mixture obtained from CPMD and classical MD simulations.

mixture is not seen in the simulation. The reasons for this absence are unclear, and need to be investigated further. They could point to system size effects or due to limitations in DFT or due to numerical issues in obtaining the function from the scattering data in experiments. Note that the peaks are observed at the corresponding positions in the partial pair correlation functions obtained from simulations, however they are washed out during averaging to obtain the intermolecular RDF. Specifically, we can attribute the feature in the experimental data present at 3.1Å to intermolecular oxygen-oxygen distances between CO_2 molecules. It should be noticed that the trend seen in the experimental RDF between the pure system and the mixture is qualitatively reproduced in the simulation. The magnitude of increase in the intensity of the RDF upon adding CO_2 is smaller and

the oscillations are absent in the simulation.

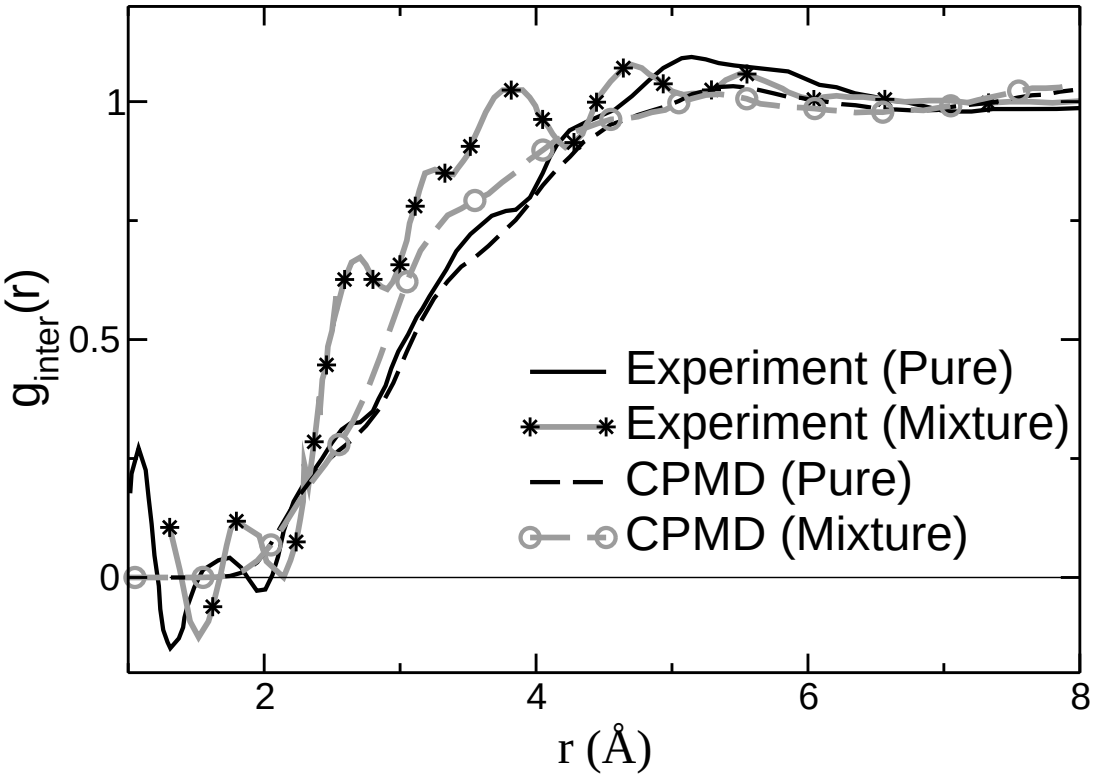

Figure 4.8: Comparison of the intermolecular radial distribution functions obtained from CPMD simulations with experiments [41] for pure [bmim][PF_6] and the CO_2[bmim][PF_6] mixture. The symbols are shown infrequently for clarity.

4.3.2 Intramolecular angle distribution of CO_2

Having obtained an understanding of the intermolecular structure of [bmim][PF_6] and the near neighbor environment around CO_2 in this IL, we turn our attention to its effect on the intramolecular structure of CO_2 molecules. As discussed in the Introduction, a polar neighborhood can force CO_2 molecules to adopt instantaneous non-linear geometries. Shown in Figure 4.9 are the probability distributions of the O-C-O angle of CO_2 molecules under various conditions. The classical MD data employing a harmonic bending potential predicts a distribution that is closest to a linear geometry. The CPMD data exhibit more propensity for instantaneous deviations from linearity. A striking feature is the

difference between the angle distributions obtained from the CPMD simulation when the CO_2 molecule is closer to and farther from the PF_6 anion. The former are more bent than the latter. We choose the position of the first peak of the C-P g(r), i.e., 4.3Å as a distance cutoff to distinguish between the two sets of CO_2 molecules. The figure illustrates this aspect for CO_2 molecules within 4.3Å from the phosphorus atom of an anion as well as for those CO_2 molecules that are at least more than 4.3Å away from every anion. Further, we observe that the extent of bending of CO_2 molecules that are within 3 Å from the acidic hydrogen (H(C3)) of the cations is similar to those that are present closer to the anions. It thus appears that the cation too is sufficiently capable of polarizing the electronic and geometric structure of CO_2 in order for it to adopt non-linear geometries.

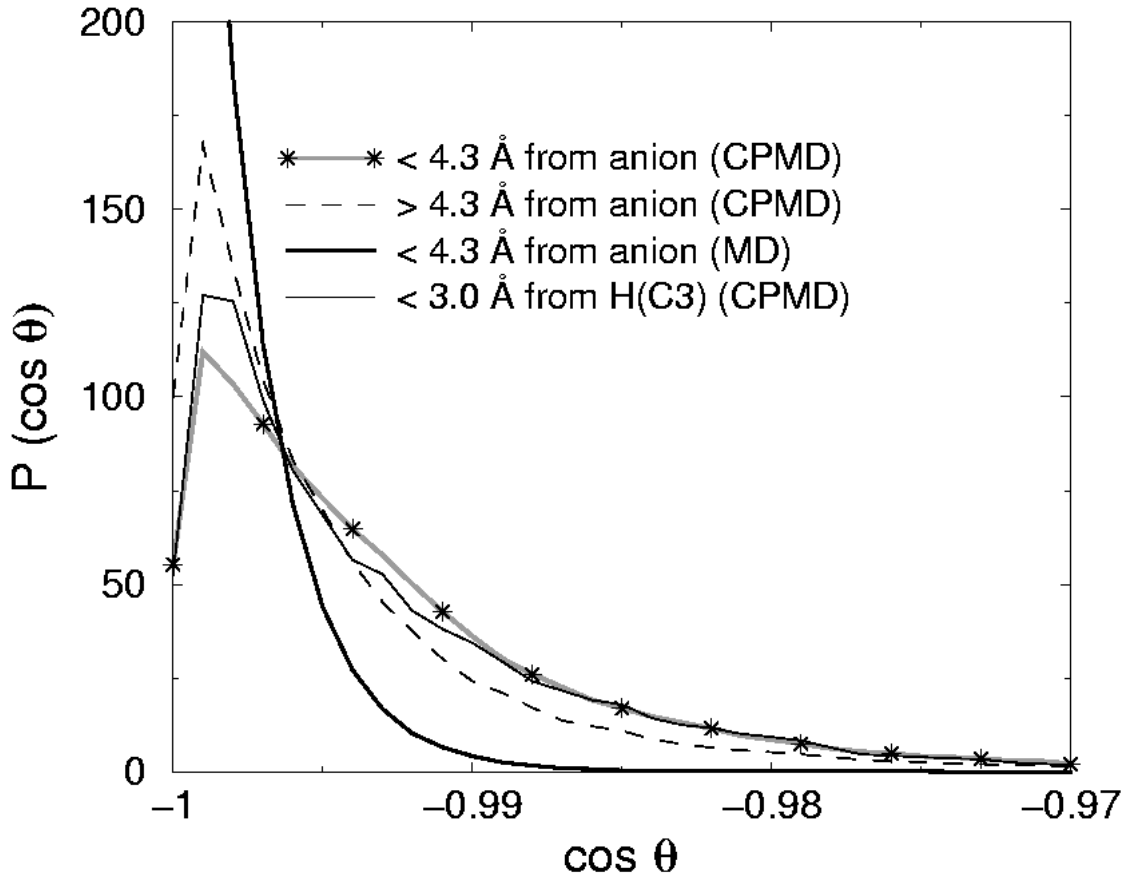

Figure 4.9: Intramolecular OCO angle distributions in the CO_2 molecule. The distances in the legend are those between the carbon atom of CO_2 and the phosphorus atom of the anion (or the H(C3) atom of the cation). Symbols are shown infrequently for clarity.

4.3.3 Orientation of CO_2 molecules

Orientation around anion

The orientational preference exhibited by a CO_2 molecule in the first coordination shell around the PF_6 anion in the CO_2 - [bmim][PF_6] solution has not been conclusive from the literature reports. Earlier MD simulation studies have concluded that the CO_2 molecule is aligned tangential to the spherical PF_6 anion [38, 40]. However, recent X-ray scattering experiments [41] argue that the CO_2 molecules penetrate the hollow voids in the PF_6 sphere. The *ab initio* MD results reported here agree with earlier simulations that were carried out using empirical potentials.

Plotted in Figure 4.10 are the probability distributions for the angle between the vectors connecting the two oxygen atoms of a CO_2 molecule and the vector that connects to the phosphorus atom of PF_6 to the carbon atom of CO_2. The probability of the CO_2 molecules to be located tangential to the anion is larger when they are closer to the anion. However this orientational preference decreases with an increase in the distance between the CO_2 and the anion. Shown in the figure are two distributions, one for CO_2 that are within 4.3 Å of the anion center and the other for which the CO_2 are present between 4.3 Å and 5.9 Å. The behavior of the function in classical MD is similar to that in CPMD. Given the fact that most CO_2 molecules would have undergone one or more complete rotations within the time scales of the CPMD run, it would be safe to conclude that the DFT based simulations reported here agree quite well with earlier classical simulations [38, 40].

Orientation of CO_2 with reference to fluorines of anion: In order to determine the most favorable location of the CO_2 molecules around the anion, we design a geometric analysis as follows. The three nearest fluorines of an anion that are present within 4.3Å (which is the position of the first peak position in the anion-CO_2 g(r)) of a CO_2 molecule were determined. Subsequently, the distributions of the angle between the C-P vector (where C is the carbon atom of the CO_2 molecule) and the three P-F vectors were determined. These are presented in Figure 4.11. The MD results are identical to the CPMD

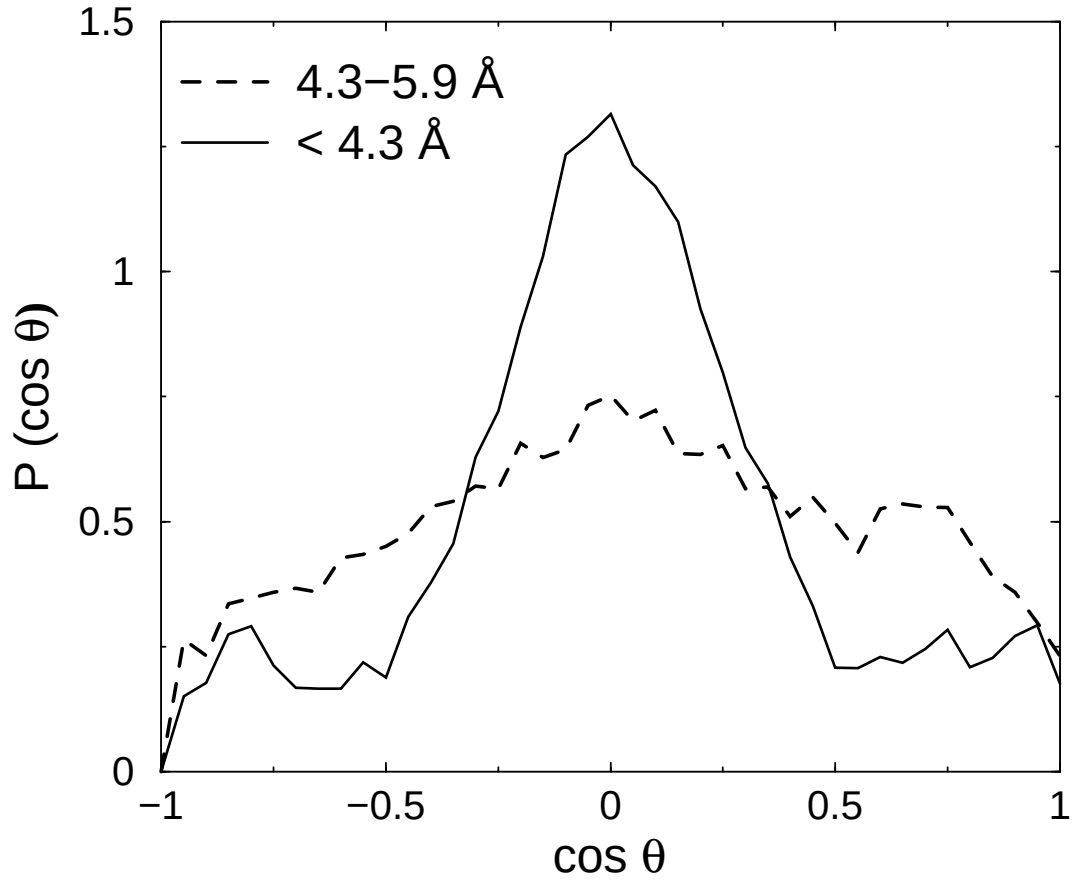

Figure 4.10: Orientation of the CO_2 molecules around the PF_6 anion in the mixture. θ is the angle between the backbone vector of CO_2 and the vector connecting the phosphorus atom of the anion to the carbon atom of CO_2 molecule, in the range of distances mentioned in the legend. The data are obtained from CPMD calculations.

data. All three distributions fall entirely in the positive domain of $cos(\theta)$ proving that the carbon atom of the CO_2 is present in the same octant defined by the three vectors. The most probable values of the angles are found to be 37, 53 and 66 degrees respectively. These values indicate that the carbon atom of the CO_2 molecule is likely to be present in the octahedral void of the anion formed by these three fluorine atoms. In view of the rather broad nature of the distribution related to the PF3 vector (the third nearest fluorine to the CO_2), we wish to caution the reader that this result should be construed only as indicative of a preference for the carbon atom to be present in octahedral hole. Not every carbon atom can be expected to occupy this site in a precise manner. In essence,

such distributions are the *raison d' etre* to perform computer simulations of the liquid state, as compared to quantum chemical calculations of isolated molecules or ion pairs. To summarize, we observe a strong preference for the carbon atom of CO_2 to be present in or around the octahedral voids of the anion.

There are eight such voids in the anion. As discussed earlier, at this mole fraction of CO_2, the anion is surrounded by about 4.6 CO_2 molecules within a distance of 6Å. This gives an effective percentage of occupation of the octahedral voids as 58%. Beyond this magnitude, CO_2 - CO_2 repulsion could be expected to dominate over the interaction strength with the anion. Note that the maximum solubility of CO_2 in [bmim][PF_6] is slightly more than 70 mol% [31,43]. We speculate that the underlying reason for this value of maximum solubility could be due to the fact that one has exhausted the maximum number of favorable sites near the anion that could be occupied. Further simulation studies (even classical MD simulations with refined potentials would do) as a function of CO_2 concentration could validate this conjecture.

4.3.4 Density maps

SDF of anion around cation

The spatial distribution function (SDF) of the anions around the cation in the case of pure [bmim][PF_6] obtained from classical MD and CPMD trajectories is presented in Figure 4.12. They show the probability density distribution of the anion (phosphorus) around the cation at an isosurface value of 0.0375 atoms/$\mathring{A}^3$, that is 13 times higher than the average density of the anions in the liquid. In the figure, (a) and (b) represent classical MD data whereas (c) and (d) are from CPMD. In Figure 4.12a and 4.12c, the ring plane of the cation is tilted to the plane of the paper around the C3-H vector. The classical MD data shows two clear lobes of density around H(C3), above and below the ring plane, that is also evident from figure 4.12b. Note that there is negligible presence of the anion exactly above the acidic proton. A considerable density of anions is also observed near the

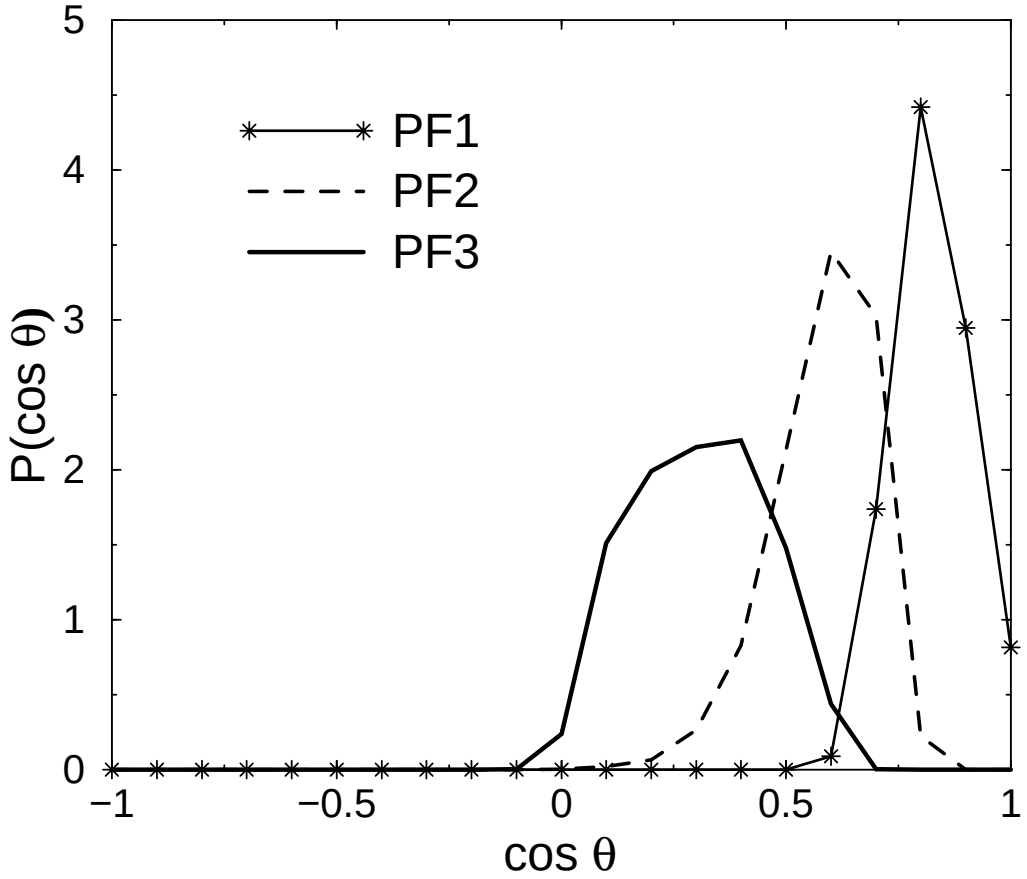

Figure 4.11: Distribution showing the preferred location of the CO_2 molecule around the anion obtained from CPMD simulations. θ is the angle between the vector joining the carbon atom of CO_2 with the phosphorus of the anions that are within 4.3Å, and the vector along the PF bond. F1, F2, F3 corresponds to the first, second and third nearest fluorine to the carbon respectively.

ring hydrogens H(C4) and H(C5). In contrast, the CPMD data shows a finite probability for the anions to be present above H(C3), that was also observed in our earlier work on [mmim][Cl] [50].

The angular distribution of anions around the cation, and the specific differences between the classical MD and CPMD data have been highlighted through the above analyses. We quantify this observation by studying the angle of approach of the anion as it forms a hydrogen bond with the H(C3) of the cation. Shown in figure 4.13e is the distribution of the angle between the vectors formed by C3-H(C3) and H(C3)-P, whenever

an anion is within 4.0 Å from H(C3). Significant differences are observed between the results of classical and CPMD simulations. While the latter shows a strong preference for the anion to approach the acidic hydrogen along its C-H bond vector, classical MD predicts a rather weaker orientational preference.

Within our statistical accuracy, no differences were observed in the SDF obtained for the pure [bmim][PF_6] and mixture from the CPMD data (not shown).

SDF of CO_2 around anion

The spatial distribution of the carbon and oxygen atoms of CO_2 molecules that are located around an anion is presented in Figures 4.14a and 4.14b. Black represents the oxygen density and grey the carbon density, obtained from classical MD simulations. The CPMD data is not shown due to paucity of statistics. Both carbon and oxygen densities are highest in the octahedral voids around the anions. Recall that the coordination number of CO_2 around the anion is 4.6, that suggests that not all the eight octahedral voids are occupied by CO_2 in every case, but only around half of them will be occupied by the CO_2 around each anion. However, eight distinct lobes are seen in Figure 4.14b, as the data is averaged over the anions and over the MD trajectory. Figure 4.14a shows the density of CO_2 around the anion in an orientation such that one of the P-F bond direction is perpendicular to the plane of the paper, and in Figure 4.14b, the same data is shown as seen from the top of an octahedral void. This distribution is favored as the carbon can interact with three of the fluorines *via* possibly an electron donor-acceptor interaction. At a given octahedral void location, the densities of both the carbon and oxygen atoms overlap as their distance from the central phosphorus atom is the same. This observation too supports the model of a tangential orientation of the CO_2 molecule around the spherical anion.

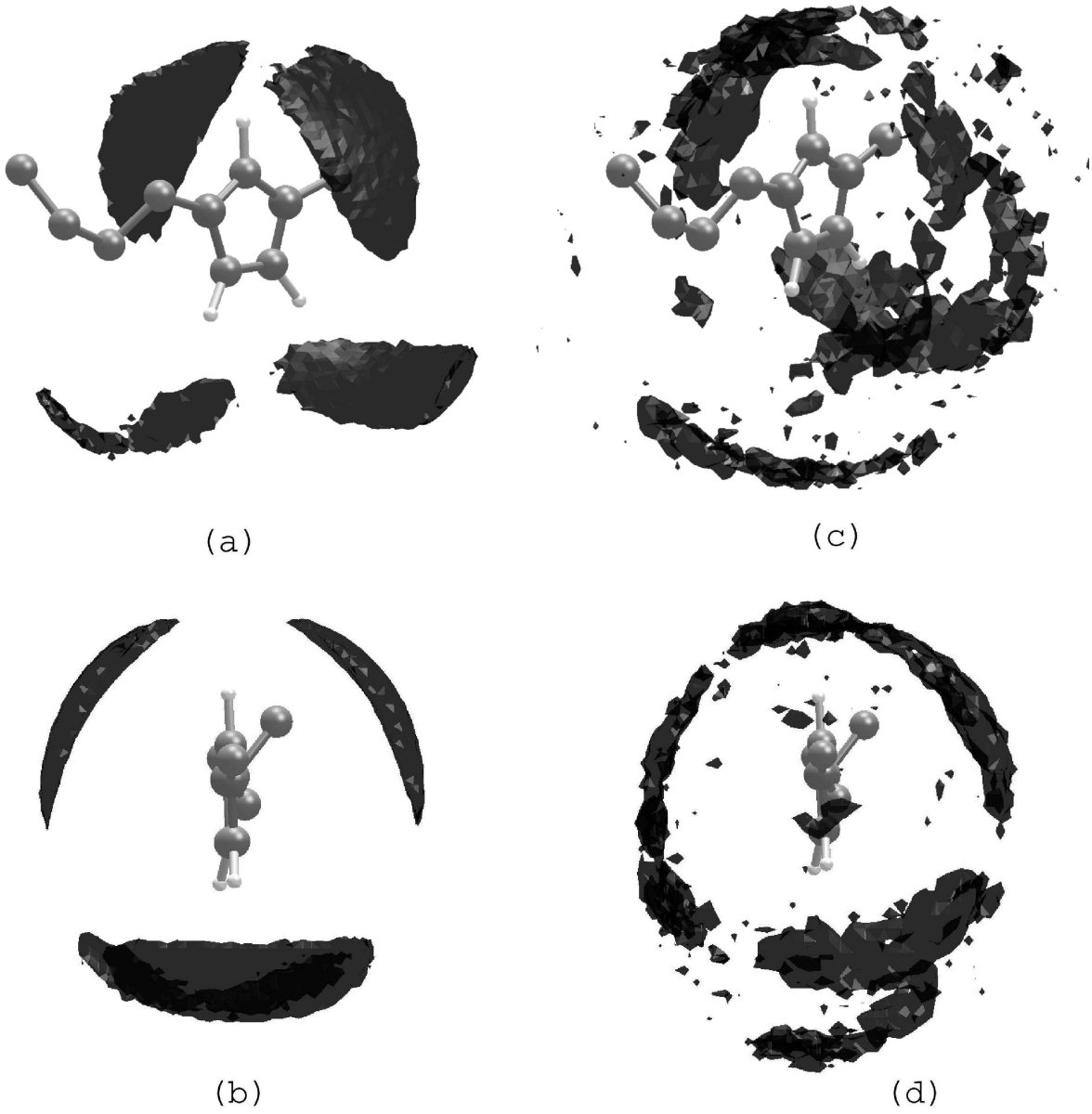

Figure 4.12: Spatial density distribution of the anions around the cation in pure [bmim][PF_6] obtained from classical MD and CPMD data at an isosurface value of 0.0375 atoms/$\mathring{A}^3$. (a) tilted view, classical MD, (b) side view, classical MD, (c) tilted view, CPMD and (d) side view, CPMD. The hydrogen atoms in the methyl and butyl groups are not shown for clarity.

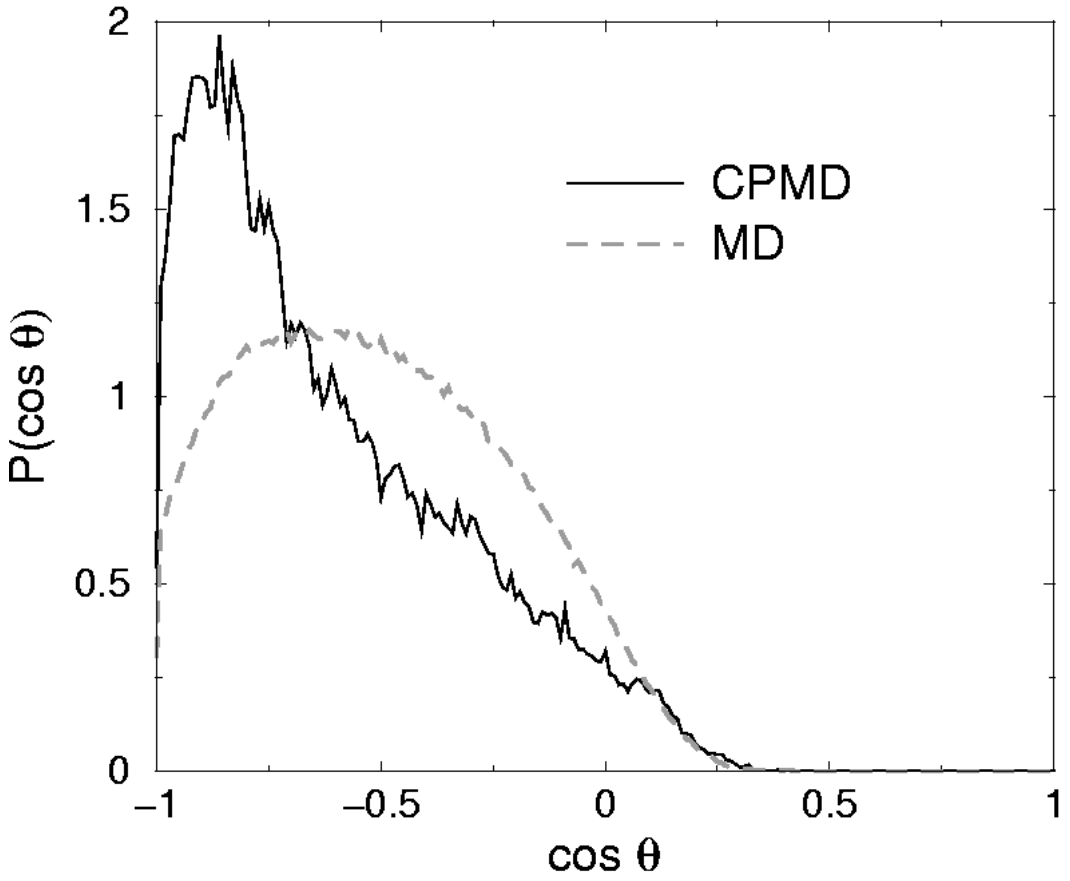

Figure 4.13: Distribution of the angle between the vectors connecting H(C3)-C3 and H(C3)-P, when the phosphorus atom is within 4.0Å from H(C3), obtained from classical MD and CPMD simulations.

4.3.5 Vibrational dynamics

The vibrational density of states obtained from the Fourier transform of velocity auto correlation function for the atoms of CO_2 is shown in Figure 4.15. The split in the bending mode of CO_2 is clearly seen, that is qualitatively consistent with the experiments of Kazarian and coworkers [36]. Density functional theory calculations are known to predict lower vibrational frequencies relative to experiment [86]. This has specifically been observed for supercritical CO_2 as well, earlier [87]. The splitting of the OCO bending mode can be rationalized as due to the interaction of the CO_2 molecules with the ions of [bmim][PF_6]. It should be noted that DFT is found to under-estimate the frequencies.

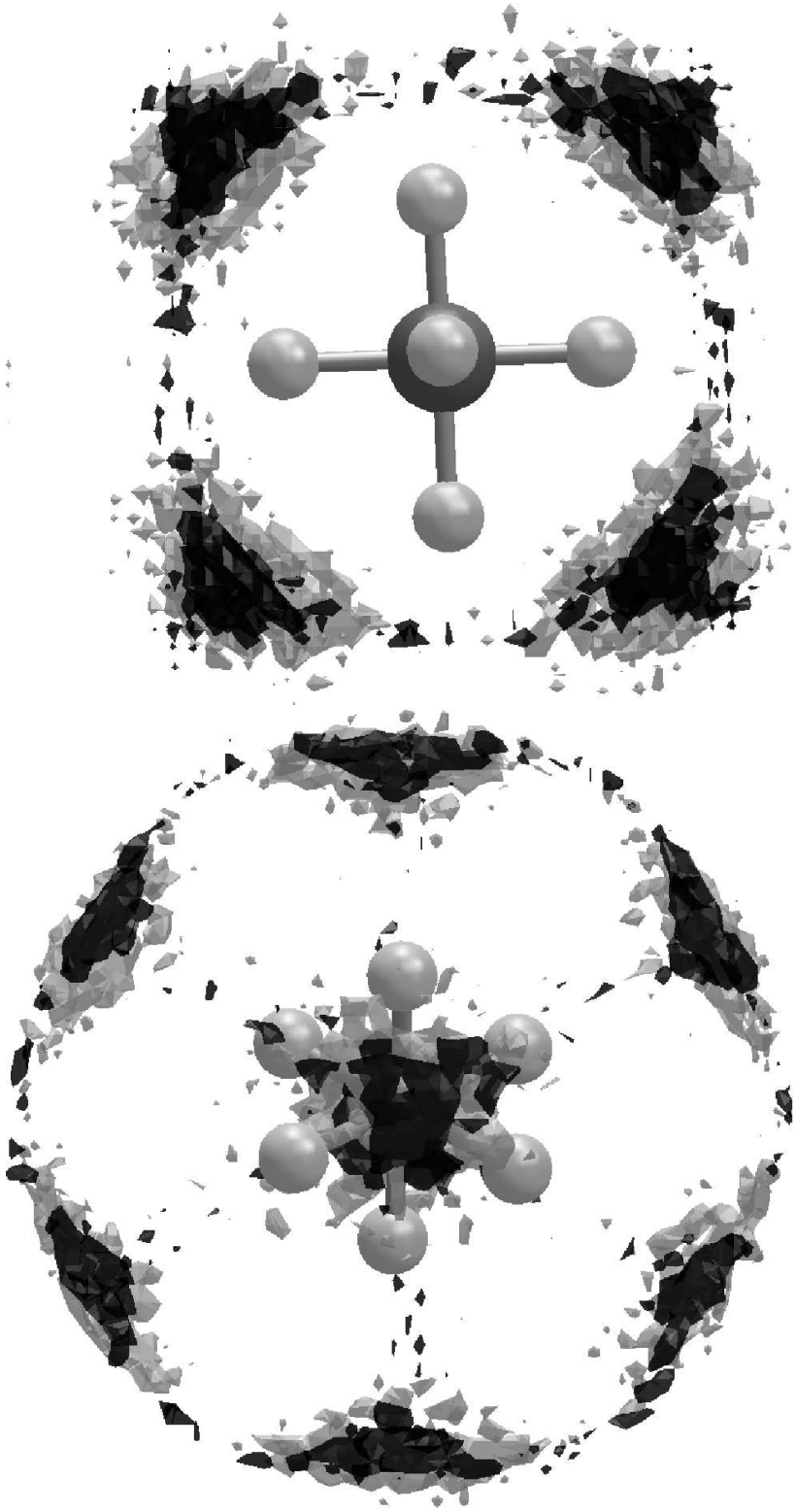

Figure 4.14: Spatial density distribution of the CO_2 molecules around anion in the mixture at an isosurface density of 0.02125 atoms/$\mathring{A}^3$ for carbon (grey) and 0.0425 atoms/$\mathring{A}^3$ for oxygen (black). The data is obtained from classical MD simulations.

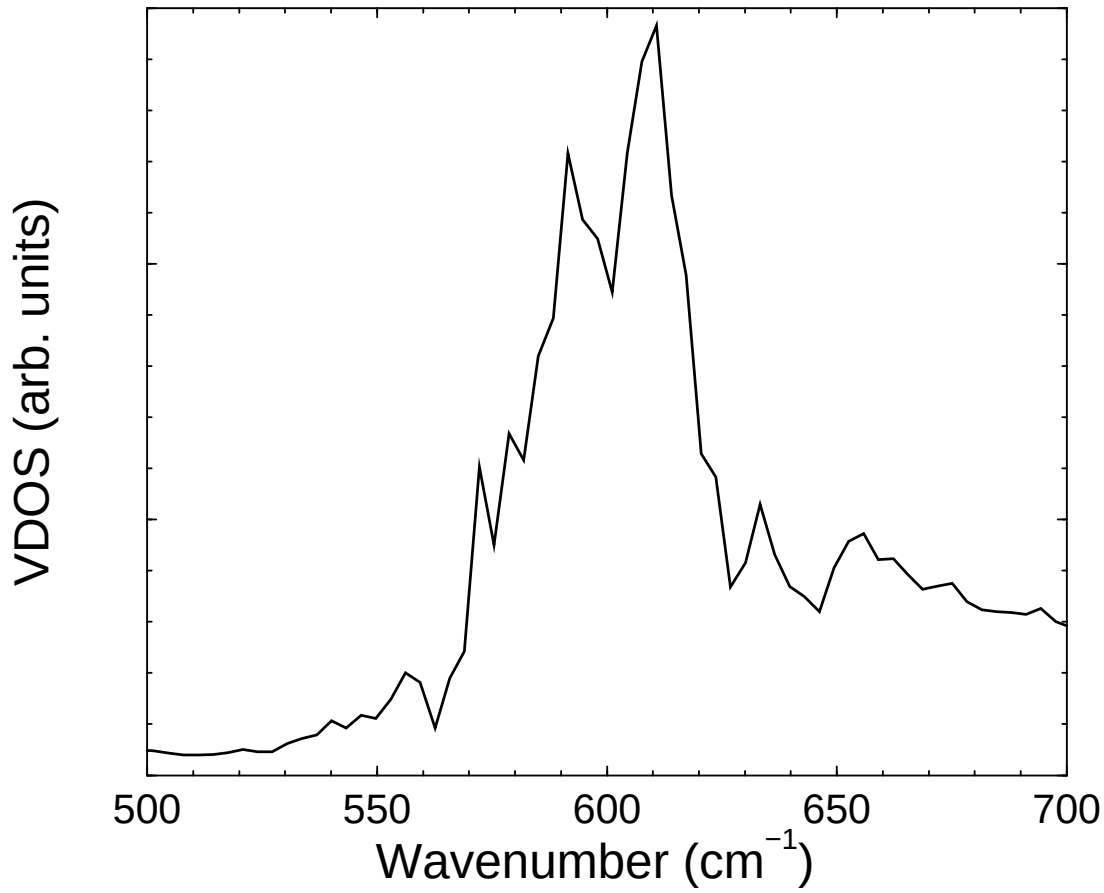

Figure 4.15: Vibrational density of states of CO_2 molecules in the CO_2 bending mode region.

4.3.6 Dipole moments

The instantaneous total dipole moment distribution of the anions and cations calculated from the Wannier centers obtained from CPMD code is presented in Figure 4.16. The coordinate axes chosen for the calculation are shown in Figure 4.1. The dipole moment for an ion is dependent on the choice of the coordinate system. Hence the values reported here need to be interpreted not for their absolute magnitudes, but for the trends that they exhibit. The geometric center of the imidazolium ring was chosen as its origin. The z-axis was along the line joining the center of the ring to C3, the y-axis was perpendicular to the ring plane and the x-axis was perpendicular to y and z-axes. The spherical PF_6 ion carries zero dipole moment under isolated conditions, as expected. However, thermal

fluctuations in its geometry as well as its capacity to be polarized in the ionic liquid environment leads to non-zero values of dipole moment for instantaneous configurations. The initial configuration for the geometry optimization procedure of the isolated cation (gas phase) was taken from the crystal structure [74]. Presented in Figure 4.17 are the distributions of the components of instantaneous dipole moment of the cations in pure [bmim][PF_6] obtained from CPMD simulations along with the corresponding value of the isolated cation mentioned above. The broad nature of the distribution of the x and y components is due to the many possible conformations of the butyl chain. The width in the z-component is due to these conformations as well as to the polarization of the C-H(C3) bond.

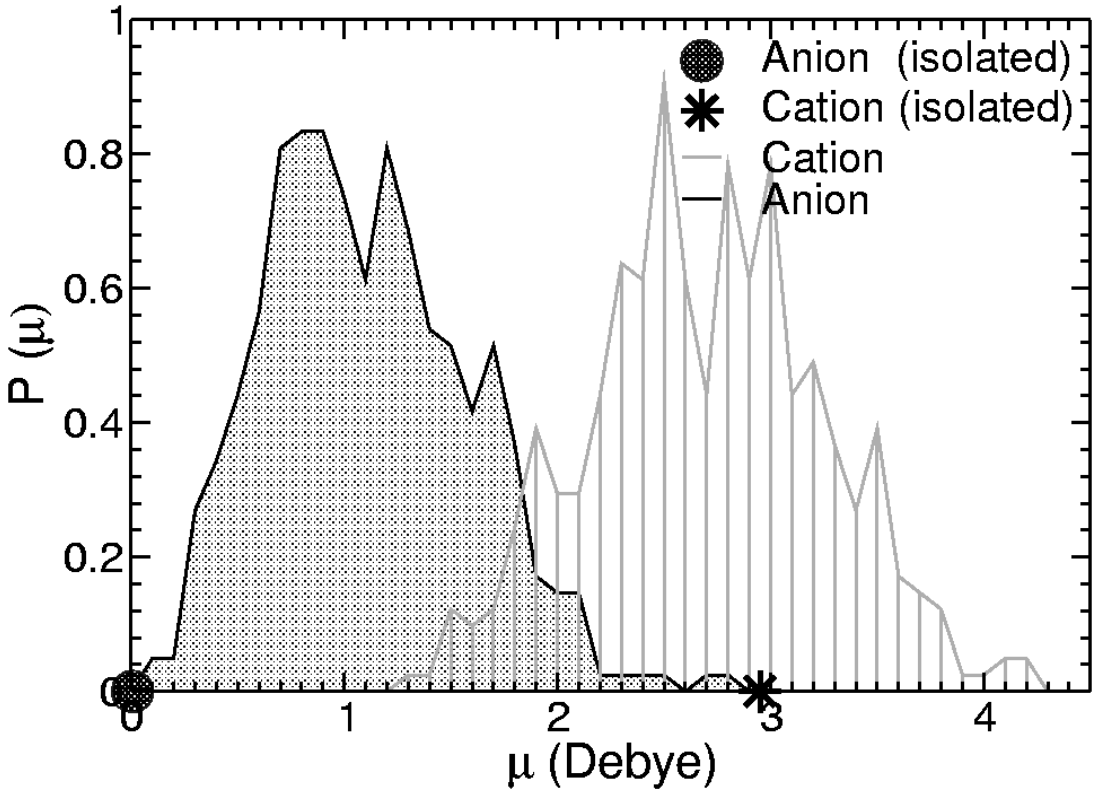

Figure 4.16: Distribution of instantaneous dipole moments of cation and anion in the pure [bmim][PF_6] system along with the values for structure optimized cation and anion, under isolated conditions.

Shown in Table 4.3 are the instantaneous total dipole moments and their components,

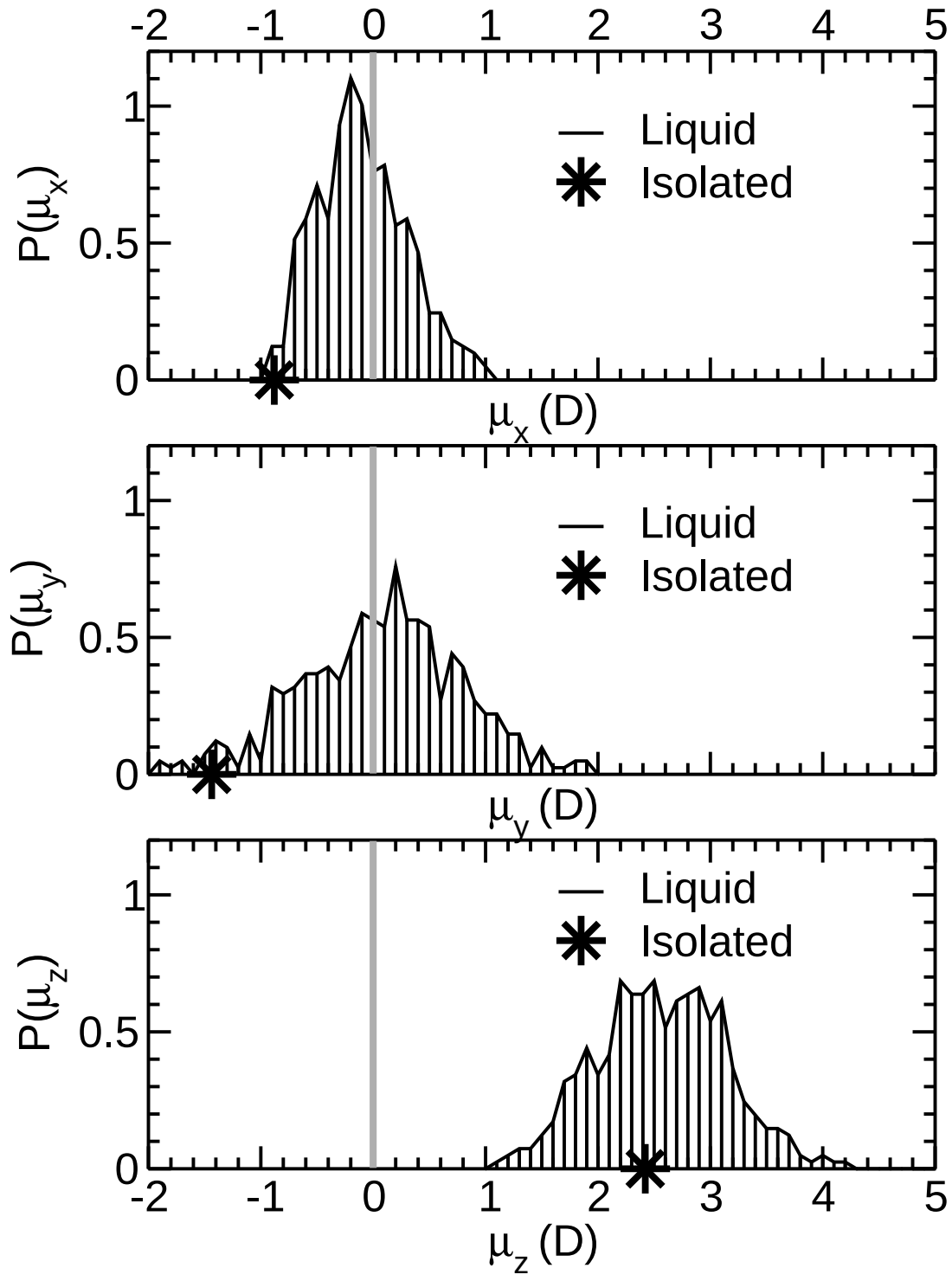

Figure 4.17: Distribution of components of instantaneous dipole moment of cation in the pure [bmim][PF_6] system along with the values for structure optimized cation, under isolated conditions.

Table 4.3: The ensemble average of instantaneous total dipole moment and its components for anion and cation obtained from classical and CPMD simulations of pure [bmim][PF_6] and structure optimized isolated ions.

Model/phase	ion	$\langle\mu_x\rangle$ (D)	$\langle\mu_y\rangle$ (D)	$\langle\mu_z\rangle$ (D)	$\langle\|\mu\|\rangle$ (D)
MD(liquid)	PF_6	0.01±0.19	0.00±0.19	0.00±0.19	0.31±0.13
MD(liquid)	[bmim]	-0.25±0.21	0.00±0.67	2.01±0.36	2.15±0.35
CPMD(liquid)	PF_6	0.07±0.71	0.11±0.65	0.02±0.63	1.06±0.48
CPMD(liquid)	[bmim]	-0.17±0.48	0.02±0.70	2.51±0.57	2.65±0.55
CPMD(isolated)	PF_6	-0.01	0.00	0.00	0.01
CPMD(isolated)	[bmim]	-0.88	-1.44	2.42	2.95

of anions and cations obtained from classical MD and CPMD data. The total dipole moment of the anion obtained from the classical MD data is 0.31±0.13 Debye that is very small compared to the CPMD value of 1.06±0.48 Debye. The dipole moment in the classical MD model with time independent charges arises only due to geometric fluctuations. However in CPMD, it arises from such fluctuations as well as due to changes in the electron distribution near the ions. The distributions of dipole moments obtained from CPMD calculations can guide the development of polarizable interaction models [20]. The cation is also found to possess a higher dipole moment compared to the classical values. Similar results were reported recently for another ionic liquid, [mmim][Cl] that was found to be more polarized in the liquid phase when compared to the gaseous environment [73]. It was also noticed that relative to pure [bmim][PF_6], the cations in the mixtures were marginally less polarized. (data not shown). This can be rationalized as due to the presence of charge neutral species CO_2 in the mixture that reduces the Coulombic forces felt by the cations.

4.4 Conclusions

Initial attempts made over the last few years to study the molecular organization in room temperature ionic liquids, using *ab initio* MD simulations have been successful [48–50]. These calculations were performed on [mmim][Cl] that melts only at 395K and is thus not so appealing to physical and synthetic chemists interested in room temperature properties. The work reported here has been carried out on an IL that is relevant to experimentalists [88] and further extends the existing knowledge on the microscopic details of these systems. In the absence of experimental data on the intermolecular structure of the pure IL and its solution with CO_2, the results of *ab initio* MD simulations will also be of great help for computational studies based on classical force field models. The structural data reported here can form a baseline for the refinement of empirical potentials [89] and can serve as an essential building block to construct hierarchical models that aid in studying larger length and time scales.

Results from the AIMD study of [bmim][PF_6] and its mixture with CO_2 show some significant differences with that from classical MD simulations. Although classical potential parameters predict the distribution of the ions around each other and that of CO_2 around the cation and anion to a good accuracy, they differ from the AIMD data in some respects. AIMD predicts the formation of a weak hydrogen bond between H(C3) of cation and fluorine atoms of the anion, a feature that is absent in the classical simulations. However in systems dominated by ionic interactions, the intermolecular structure may not be primarily dictated by the comparatively weaker hydrogen bonds. A liberal geometric definition of hydrogen bonds yields ten such bonds per cation in the pure liquid against seven present in the crystal [74]. A conservative estimate is one hydrogen bond per cation in the liquid. The distribution of dipole moment components and magnitudes of the ions show that they are polarized significantly in the liquid environment, compared to their electronic structure in the gas phase [20].

Previous AIMD simulations on [mmim][Cl] by Lynden-Bell and co-workers [48] using 8

and 24 ion pairs showed negligible system size effects. Their results were qualitatively similar to the results obtained from a 32 ion pair CPMD simulation performed by us [50]. In view of these, despite the rather small number of ion pairs employed in the current study, we believe that the intermolecular structure in terms of nearest neighbor arrangement is unlikely to differ with increasing system size. However, our AIMD simulation trajectory is much shorter than the structural and stress relaxation times of neat [bmim][PF_6]. Hence the results may have some memory of the initial configuration. Significant differences between AIMD and MD results have been observed by in some of the crucial pair correlation functions. This points to the fact that the intermolecular structure in the AIMD simulation has relaxed to some extent from the initial configuration. In addition, the cation-anion anion-cation structure obtained from the two independent AIMD simulations, one on pure [bmim][PF_6] and another on the mixture are similar. So, although the AIMD trajectory is short compared to common MD trajectory lengths, the fact that the two AIMD simulations provide similar data on pair correlation functions, makes these results believable. The butyl tails in [bmim][PF_6] can interact via van der Waals interactions, that may not be captured well within density functional theory. However, we believe that the intermolecular structure of ILs containing short alkyl chains are dominated mostly by electrostatics.

CO_2 molecules are found to be predominantly solvated by the anion rather than the cation. The most probable orientation of the CO_2 molecule is tangential to the PF_6 sphere, in agreement with previous classical MD simulations [40] and seemingly contradicts the conclusions drawn from X-ray scattering experiments [41]. The latter deduced that CO_2 molecules penetrate the octahedral voids of the anion. The most probable location of CO_2 around an anion has been determined using spatial distribution functions to be the octahedral voids around the anion. Out of the eight such voids, on average, only four are occupied for a given anion. A weak interaction of the oxygen of CO_2 molecule with the ring hydrogen H(C3) of the cation, is also observed. In order to explain the solubility of CO_2

in [bmim][PF_6], Berne and coworkers [40] have argued the importance of voids present in the neat IL to accommodate the CO_2 molecules. Our *ab initio* MD data is insufficient in spatial and temporal extents to add support to this thesis. The current work, however, also points to the role that specific interactions such as the hydrogen bond between the CO_2 and the ring hydrogen H(C3), could play in the solubility of CO_2 in ionic liquids. This was alluded to by Maginn and coworkers [38] who found a marginal change in the Henry's constants upon substituting a methyl group in the place of the hydrogen. We also differ from the conclusions of the X-ray scattering experiments [41] on the assignment of the 3.6Å peak in the total g(r) in the [bmim][PF_6] - CO_2 mixture. We contend that this peak arises from CO_2 - CO_2 pair distances rather than CO_2 - anion neighbors. Although the intermolecular radial distribution function obtained from CPMD simulation differs from the experimental data [41] for the CO_2[bmim][PF_6] mixture, we point out that they compares well for the pure [bmim][PF_6] system. In addition, the trend of changes in the RDF upon addition of CO_2 is reproduced in the simulation. Further work is necessary to resolve the minor differences between experiment and simulation in the presence (or absence) of oscillations in the RDF of the mixture.

CO_2 molecules that are present near the anions or the ring hydrogen H(C3) are found to deviate farther from a linear geometry than the rest of their kind. The change in geometry arises due to Lewis acid-base (or electron donor-acceptor) interactions in the former case, and the formation of a weak hydrogen bond in the latter. The fluorine atoms (Lewis base) can donate a partial electronic charge to the carbon atom (Lewis acid) of CO_2. The deviation from a linear structure results in the lifting of degeneracy in the bending mode of CO_2 that agrees qualitatively with spectroscopic experiments [36]. Thus, our results point out that apart from ion-quadrupole interactions that are expected between the anion and CO_2, ion-induced dipole interactions could also be important.

Bibliography

[1] J.M. DeSimone, Z. Guan, C.S. Elsbernd, *Science* **257**, 945 (1992).

[2] M.J. Clarke, K.L. Harrison, K.P. Johnston, S.M. Howdle, *J. Am Chem. Soc.* **119**, 6399 (1997).

[3] K. Nagashima, C.T. Lee, B. Xu, K.P. Johnston, J.M. DeSimone,C.S. Johnson, *J. Phys. Chem. B*, **107**, 1962 (2003).

[4] B. Chen, J.I. Siepmann, M.L. Klein, *J. Phys. Chem. B*, **105**, 9840 (2001).

[5] S. Salaniwal, S.T. Cui, P.T. Cummings, H.D. Cochran, *Langmuir*, **15**, 5188 (1999). S. Salaniwal, S.T. Cui, H.D. Cochran, P.T. Cummings, *Langmuir*, **17**, 1773 (2001).

[6] S. Senapati, J.S. Keiper, J.M. DeSimone, G.D. Wignall, Y.B. Melnichenko, H. Frielinghaus, M.L. Berkowitz, *Langmuir*, **18**, 7371 (2002).

[7] T. Welton, *Chem. Rev.*, **99**, 2071 (1999).

[8] M.J. Earle, K.R. Seddon, *Pure Appl. Chem.*, **72**, 1391 (2000).

[9] A. Triolo, A. Mandanici, O. Russina, V. Rodriguez-Mora, M. Cutroni, C. Hardacre, M. Nieuwenhuyzen, H. Bleif, L. Keller, M.A. Ramos, *J. Phys. Chem. B*, **110**, 21357 (2006).

[10] R.W. Berg, M. Deetlefs, K.R. Seddon, I. Shim, J.M. Thompson, *J. Phys. Chem. B*, **109**, 19018 (2005).

[11] C.G. Hanke, S.L. Price, R.M. Lynden-Bell, *Mol. Phys.* **99** 801 (2001).

[12] C.G. Hanke, N.A. Atamas, R.M. Lynden-Bell, *Green Chem.* **4**, 107 (2002).

[13] R.M. Lynden-Bell, N.A. Atamas, A. Vasilyuk, C.G. Hanke, *Mol. Phys.*, **100**, 3225 (2002).

[14] R.M. Lynden-Bell, *Mol. Phys.*, **101**, 2625 (2003).

[15] M.G. Del-Popolo, G.A. Voth, *J. Phys. Chem. B*, **108**, 1744 (2004).

[16] R.M. Lynden-Bell, J. Kohanoff, M.G. Del Popolo, *Faraday Discuss.*, **129**, 57-6 (2005).

[17] Z. Hu, C.J. Margulis, *Proc. Natl. Acad. Sci. U.S.A.*, **103**, 831 (2006).

[18] T. Yan, S. Li, W. Jiang, X. Gao, B. Xiang, G.A. Voth, *J. Phys. Chem. B*, **110**, 1800 (2006).

[19] R. Karmakar, A. Samanta, *J. Phys. Chem. A*, **107**, 7340 (2003).

[20] T. Yan, C.J. Burnham, M.G. Del Popolo, G.A. Voth, *J. Phys, Chem. B*, **108**, 11877 (2004).

[21] Y. Wang, G.A. Voth, *J. Am. Chem. Soc.*, **127**, 12192 (2005).

[22] S. Tsuzuki, H. Tokuda, K. Hayamizu, M. Watanabe, *J. Phys. Chem. B*, **109**, 16474 (2005).

[23] P.A. Hunt, *Mol. Sim.*, **32**, 1 (2006).

[24] S. Koβmann, J. Thar, B. Kirchner, P.A. Hunt, T. Welton, *J. Chem. Phys.*, **124**, 174506 (2006).

[25] P.A. Hunt, B. Kirchner, T. Welton, *Chem. Eur. J.*, **12**, 6762 (2006).

[26] P.A. Hunt, I.R. Gould, *J. Phys. Chem. A*, **110**, 2269 (2006).

[27] B.L. Bhargava, S. Balasubramanian, *J. Chem. Phys.*, **123**, 144505 (2005); **125**, 219901 (2006).

[28] L. Gong, W. Guo, J. Xiong, R. Li, X. Wu, W. Li, *Chem. Phys. Lett.*, **425**, 167 (2006).

[29] Y. Wang, H. Li, S. Han, *J. Chem. Phys.*, **124**, 044504 (2006).

[30] P. Wasserscheid, *Nature*, **439**, 797 (2006); M.J. Earle, J.M.S.S. Esperanca, M.A. Gilea, J.N.C. Lopes, L.P.N. Rebelo, J.W. Magee, K.R. Seddon, J.A. Widegren, *Nature*, **439**, 831 (2006).

[31] L.A. Blanchard, D. Hancu, E.J. Beckman, J.F. Brennecke, *Nature*, **399**, 28 (1999).

[32] D.J. Cole-Hamilton, *Science*, **299**, 1702 (2003).

[33] A.M. Scurto, S.N.V.K. Aki, J.F. Brennecke, *J. Am. Chem. Soc.*, **124**, 10276 (2002).

[34] A.M. Scurto, W. Leitner, *Chem. Commun.*, 3681 (2006).

[35] K.A. Fletcher, S.N. Baker, G.A. Baker, S. Pandey, *New J. Chem.*, **27**, 1706 (2003).

[36] S.G. Kazarian, B.J. Briscoe, T. Welton, *Chem. Commun.*, 2047 (2000).

[37] J. Lu, C.L. Liotta, C.A. Eckert, *J. Phys. Chem. A*, **107**, 3995 (2003).

[38] C. Cadena, J.L. Anthony, J.K. Shah, T.I. Morrow, J.F. Brennecke, E.J. Maginn, *J. Am. Chem. Soc.*, **126**, 5300 (2004).

[39] J. Deschamps, M.F. Costa Gomes, A.A.H. Pádua, *ChemPhysChem*, **5**, 1049 (2004).

[40] X. Huang, C.J. Margulis, Y. Li, B.J. Berne, *J. Am. Chem. Soc.*, **127**, 17842 (2005).

[41] M. Kanakubo, T. Umecky, Y. Hiejima, T. Aizawa, H. Nanjo, Y. Kameda, *J. Phys. Chem. B*, **109**, 13847 (2005).

[42] M.C. Kroon, E.K. Karakatsani, I.G. Economou, G. Witkamp, C.J. Peters, *J. Phys. Chem. B*, **110**, 9262 (2006).

[43] L.A. Blanchard, Z. Gu, J.F. Brennecke *J. Phys. Chem. B*, **105**, 2437 (2001).

[44] J.L. Anthony, E.J. Maginn, J.F. Brennecke, *J. Phys. Chem. B*, **106**, 7315 (2002).

[45] A.P. Kamps, D. Tuma, J. Xia, G. Maurer, *J. Chem. Eng. Data*, **48**, 746 (2003).

[46] P. Husson-Borg, V. Majer, M.F. CostaGomes, *J. Chem. Eng. Data*, **48**, 480 (2003).

[47] J.L. Anthony, J.L. Anderson, E.J. Maginn, J.F. Brennecke, *J. Phys. Chem. B*, **109**, 6366 (2005).

[48] M.G. Del Pópolo, R.M. Lynden-Bell, J. Kohanoff, *J. Phys. Chem. B*, **109**, 5895 (2005).

[49] M. Bühl, A. Chaumont, R. Schurhammer, G. Wipff, *J. Phys. Chem. B*, **109**, 18591 (2005).

[50] B.L. Bhargava, S. Balasubramanian, *Chem. Phys. Lett.*, **417**, 486 (2006).

[51] S. Raugei, M.L. Klein, *ChemPhysChem*, **5**, 1569 (2004).

[52] M. Boero, T. Ikeshoji, C.C. Liew, K. Terakura, M. Parrinello, *J. Am. Chem. Soc.*, **126**, 6280 (2004).

[53] B. Kirchner, A.P. Seitsonen, J. Hutter, *J. Phys. Chem. B.*, **110**, 11475 (2006).

[54] J.A. Morrone, K.E. Haslinger, M.E. Tuckerman, *J. Phys. Chem. B*, **110**, 3712 (2006).

[55] S.N.V.K. Aki, B.R. Mellein, E.M. Saurer, J.F. Brennecke, *J. Phys. Chem. B*, **108**, 20355 (2004).

[56] The solubility data of CO_2 in [bmim][PF_6] obtained from Ref. 55 was fitted to a second order polynomial, that yielded the volume expansion to be 1.312 for the 70 mole percent (CO_2) mixture of CO_2 - [bmim][PF_6] relative to pure [bmim][PF_6]. A value of 1.30 was chosen to arrive at the simulation density that agrees with the value that is used in Ref. 41.

[57] R. Car, M. Parrinello, *Phys. Rev. Lett.*, **55**, 2471 (1985).

[58] J. Hutter, P. Ballone, M. Bernasconi, P. Focher, E. Fois, S. Goedecker, D. Marx, M. Parrinello, M.E. Tuckerman, CPMD Version 3.11.1, Max Planck Institut fuer Festkoerperforschung, Stuttgart, and IBM Zurich Research Laboratory, 1990-2007.

[59] N. Troullier, J.L. Martins, *Phys. Rev. B*, **43**, 1993 (1991).

[60] A.D. Becke, *Phys. Rev. A*, **38**, 3098 (1988).

[61] C. Lee, W. Yang, R.G. Parr, *Phys. Rev. B*, **37**, 785 (1988).

[62] G.J. Martyna, M.L. Klein, M.E. Tuckerman, *J. Chem. Phys.*, **97**, 2635 (1992).

[63] J.G. Harris, K.H. Yung, *J. Phys. Chem.*, **99**, 12021 (1995).

[64] J.N.C. Lopes, J. Deschamps, A.A.H. Pádua, *J. Phys. Chem. B*, **108**, 2039 (2004); **108**, 11250 (2004).

[65] O. Borodin, G.D. Smith, R.L. Jaffe, *J. Comput. Chem.*, **22**, 641 (2001).

[66] B.L. Bhargava, S. Balasubramanian, *J. Am. Chem. Soc.*, **128**, 10073 (2006).

[67] M.E. Tuckerman, B.J. Berne, G. Martyna, *J. Chem. Phys.*, **97**, 1990 (1992).

[68] G.H. Wannier, *Phys. Rev.*, **52**, 191 (1937).

[69] S.F. Boys, *Rev. Mod. Phys.*, **32**, 296 (1960).

[70] R. Resta, *Rev. Mod. Phys.*, **66**, 899 (1994).

[71] R. Resta, S. Sorella, *Phys. Rev. Lett.*, **82**, 370 (1999).

[72] G. Berghold, C.J. Mundy, A.H. Romero, J. Hutter, M. Parrinello, *Phys. Rev. B*, **61**, 10040 (2000).

[73] C.E. Resende Prado, M.G. Del Pópolo, T.G.A. Youngs, J. Kohanoff, R.M. Lynden-Bell, *Mol. Phys.*, **104**, 2477 (2006).

[74] A.R. Choudhury, N. Winterton, A. Steiner, A.I. Cooper, K.A. Johnson, *J. Am. Chem. Soc.*, **127**, 16792 (2005); S.M. Dibrov, J.K. Kochi, *Acta Cryst. C*, **62**, o19 (2006).

[75] I.A. Guzei, J.M. Langenhan, *Acta Cryst. C*, **59**, i95 (2003).

[76] *CRC Handbook of Chemistry and Physics*, 81st ed. D.R. Lide, Ed.; (CRC Press, Boca Raton, FL, 2000) Chapter 9, p 20.

[77] P.A. Madden, M. Wilson, *Chem. Soc. Rev.*, **25**, 339 (1996).

[78] C.J. Margulis, H.A. Stern, B.J. Berne, *J. Phys. Chem. B*, **106**, 12017 (2002).

[79] T.I. Morrow, E.J. Maginn, *J. Phys. Chem. B*, **106**, 12807 (2002).

[80] Z. Liu, S. Huang, W. Wang, *J. Phys. Chem. B*, **108**, 12978 (2004).

[81] S.M. Urahata, M.C.C. Ribeiro, *J. Chem. Phys.*, **120**, 1855 (2004).

[82] *Crystal Design: Structure and Function. Perspectives in Supramolecular Chemistry*, G.R. Desiraju, Ed.; Wiley: Chichester, England, 2004; Vol. 7, p 6.

[83] A. Kokalj, *J. Mol. Graphics Modell.*, **17**, 176 (1999).

[84] C. Hardacre, J.D. Holbrey, S.E.J. McMath, D.T. Bowron, A.K. Soper, *J. Chem. Phys.*, **118**, 273 (2003).

[85] K. Dong, S. Zhang, D. Wang, X. Yao, *J. Phys. Chem. A*, **110**, 9775 (2006).

[86] G.S.M. Tong, A.S.C. Cheung, *J. Phys. Chem. A*, **106**, 11637 (2002).

[87] M. Saharay, S. Balasubramanian, *J. Chem. Phys.*, **120**, 9694 (2004).

[88] E. Sloutskin, B.M. Ocko, L. Tamam, I. Kuzmenko, T. Gog, M. Deutsch, *J. Am. Chem. Soc.*, **127**, 7796 (2005); **127**, 18333 (2005).

[89] B.L. Bhargava, R.Devane, M.L. Klein, S. Balasubramanian, *Soft Matter*, (2007); DOI: 10.1039/b710801j

Chapter 5

A refined potential model for atomistic simulations of an ionic liquid, [bmim][PF_6]

5.1 Introduction

The classical potential models for room temperature ionic liquids have some drawbacks while predicting the structure and dynamical properties of the system. Many *ab initio* studies, that are not based on empirical potential, of these systems have also been reported [1–6]. Several groups have been working on refining interaction potentials with varying degrees of success [7–12]. While some models predict a near-neighbor structure that is different from *ab initio* results on [mmim][Cl] or [bmim][PF_6] [1,3,9], others deviate in the prediction of density compared to experiments [9, 11, 13].

In the previous chapters we have seen that the potential model used, has several limitations. To overcome those limitations, we are refining it in this chapter. Here we build upon a well established interatomic potential for ionic liquids that are based on the imidazolium cation, developed by Lopes *et al* [14]. They had performed ab initio

calculations to obtain the torsional potential and to determine the partial charges on the atomic sites of the ions. The potential parameters were validated by condensed phase simulations. They have followed this work by presenting refinement of the potential for ILs containing anions such as chloride, bromide, dicyanamide [15]. In this chapter, we provide refined potential parameters for an important IL, 1-*n*-butyl,3-methylimidazolium hexafluorophosphate ([bmim][PF_6]), using their model as a template. The parameters are validated by quantitative reproductions of the intermolecular structure in the liquid by comparison to ab initio molecular dynamics (AIMD) simulation data that were carried out using the Car-Parrinello molecular dynamics (CPMD) method [4] and to experiments. Improvements in the representation of the model liquid include the ability to form the hydrogen bond between the cation and the anion, a better three dimensional coordination shell of the anion around the cation, and marked advancement in the transport properties.

Apart from this, we study the structural correlations and the charge ordering in RTILs, in particular [bmim][PF_6]. Aprotic room temperature ionic liquids (RTIL) exhibit characteristics of both molecular liquids and conventional inorganic ionic melts, and are thus unique. The intermolecular structure in RTILs is determined by the size and shape of the cation and anion as well as the manner in which the overall charge is distributed on the ions. Within the family of ionic liquids containing the imidazolium cation, structural studies have been carried out using X-ray and neutron scattering [16–21]. Experimental determination of intermolecular structure in complex liquids such as RTILs are aided by deuteration of the hydrogen atoms, either fully or partially. Such isotopic substitutions help in identifying the origin of specific features in the observed structure factor. Often, such experiments are augmented by theoretical analyses using the reverse Monte Carlo method, so as to obtain three dimensional atomistic structures of the liquid. Molecular dynamics (MD) simulations using empirical potentials too play a crucial and well acknowledged role in the precise interpretation of the structure factor obtained from experiments, in terms of intermolecular correlations [22]. Such comparisons between MD simulations

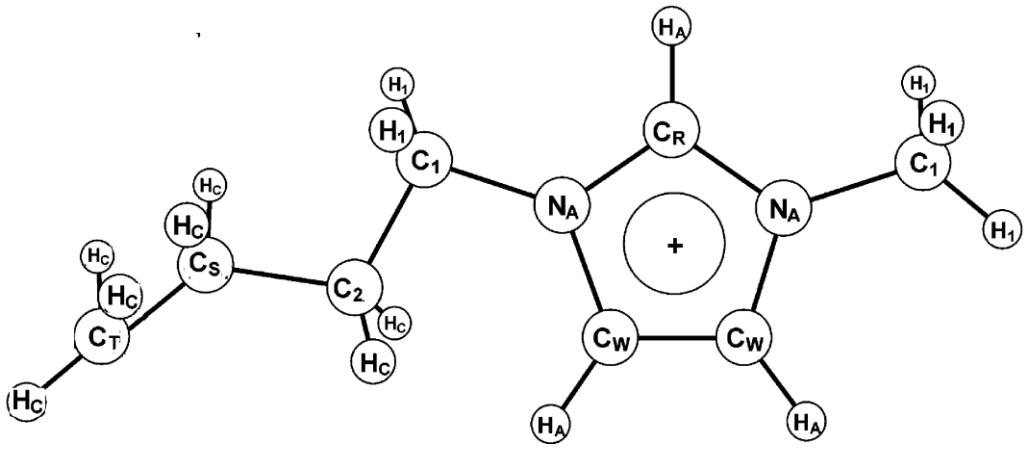

Figure 5.1: Schematic of [bmim] cation.

and scattering experiments, in turn, allow one to critically examine the shortcomings of model potentials and their ability to realistically represent the structure of the ionic liquid [23]. We focus on a precise comparison of the structure factor of the model liquid with experiment, the microscopic origin of the features observed, and on charge ordering in the IL.

5.2 Methodology and simulation Details

A schematic of [bmim][PF_6] is provided as Figure 5.1 along with the naming scheme for atoms in order to aid the discussion.

The form of the interatomic potential is the same as in Lopes *et al* [14] but is also provided here for the sake of completeness.

$$U = U_{intra} + U_{inter} \tag{5.1}$$

where U_{intra} and U_{inter} are defined in equations 5.2 and 5.3 respectively.

$$U_{intra} = \sum_{ij}^{bonds} \frac{k_{r,ij}}{2}(r_{ij} - r_{0,ij})^2 + \sum_{ijk}^{angles} \frac{k_{\theta,ijk}}{2}(\theta_{ijk} - \theta_{0,ijk})^2 + \sum_{ijkl}^{dihedrals} \sum_{m=1}^{6} V_{m,ijkl} \cos^m(\phi_{ijkl}) \tag{5.2}$$

$$U_{inter} = \frac{1}{2} \sum_{i} \sum_{j \neq i} \left\{ 4\epsilon_{ij} \left[\left(\frac{\sigma_{ij}}{r_{ij}} \right)^{12} - \left(\frac{\sigma_{ij}}{r_{ij}} \right)^{6} \right] + \frac{1}{4\pi\epsilon_0} \frac{q_i q_j}{r_{ij}} \right\} \tag{5.3}$$

The potential parameters for the intramolecular interactions that includes stretching, bending and dihedral terms are the same as in Lopes *et al* [14]. Parameters for the bond stretching and bending terms for the PF_6 anion were obtained from an earlier work [24].

Intermolecular interactions include Coulomb and Lennard-Jones terms. The original work of Lopes *et al* [14] provided potential parameters for a wide variety of ionic liquids, based on MD simulations of their crystalline and liquid forms. Our earlier investigations on [mmim][Cl] [25] and on [bmim][PF_6] [4,26] showed that the model parameters were not able to reproduce accurately, the cation-anion hydrogen bond. Further, ion transport in both the systems was found to be sluggish compared to experiment. The specific quantities of interest were shear viscosity, electrical conductivity and the diffusion coefficients of ions [25]. The calculated surface tension of liquid [bmim][PF_6] [26] was also found to be much larger than the experimental value. A comparison of our earlier results on the dynamics of [bmim][PF_6] using the Lopes *et al* model to experimental values led us to believe that a partial charge model could reduce the relatively strong contribution of Coulombic interaction to the potential energy. With this guideline, the total charge on the cation and anion in the new model has been chosen to be 0.8e and -0.8e respectively. A potential model with reduced cation and anion charges has also been used by Wipff

and coworkers to study the RTIL-water interface [27, 28], based on the original work of Morrow and Maginn [29]. In their model, the magnitude of the total charge on the ions was 0.904e, and the reduction from the value of unity was rationalized as due to charge transfer between the ions. In the present work, the refined model parameters were obtained by tuning the charges [30] so that the classical MD simulations reproduced the essential pair correlations obtained from our earlier Car-Parrinello MD calculations [4]. Some of the Lennard-Jones parameters were also tuned in this effort. The refinement of the site charges and LJ parameters were guided by the pair correlation functions obtained from ab initio MD simulations. Specifically, we were interested in obtaining a set of parameters which was able to reproduce the $H_A(C_R)$-F g(r) that signifies the cation-anion hydrogen bond. The partial charges on the atomic sites constituting the ions and the Lennard-Jones (L-J) parameters used in the present study are tabulated in Table 5.1. Note that the Lopes model prescribes a scaled 1-4 interaction, whereas the proposed refinement includes non-bonded intramolecular interaction terms only from 1-5 (and above) neighbors, without any scaling.

Lorentz-Berthelot mixing rules were employed to obtain L-J parameters for cross interactions. The details of the *ab initio* and classical MD simulations of the bulk liquid and that of the liquid-vapor interface are the same as in Ref. [4] and Ref. [26] respectively. They include an outer timestep of 3 fs within the RESPA scheme [31], Ewald summation method to handle Coulombic interactions, and Nosé-Hoover chain thermostats [32] for temperature control. A value of 1 ps was used as the time constant for the thermostat. Within the RESPA scheme, short range non-bonded interactions (within 6Å) were integrated with a timestep of 1.5fs, torsions at 0.75fs and bond stretch and angle interactions at 0.375fs.

For simulations of the liquid, the system was equilibrated in the isothermal-isobaric ensemble at one atmospheric pressure from which the densities were obtained. Simulations to calculate structural and transport properties were carried out in the NVT ensemble at

Table 5.1: Site charges and Lennard-Jones parameters of the refined model. The charges and the L-J parameters of Lopes *et al* model [14] are provided in brackets for sites whose parameters have been changed in the present model. Lorentz-Berthelot combination rules apply.

Species	Partial charge (e)	ϵ (kJ/mol)	σ (Å)
C_1	-0.089 (-0.17)	0.27615	3.50
C_2	-0.038 (0.01)	0.27615	3.50
C_R	0.060 (-0.11)	0.29289	3.55
C_S	-0.038 (-0.12)	0.27615	3.50
C_W	-0.020 (-0.13)	0.29289	3.55
C_T	-0.065 (-0.18)	0.27615	3.50
H_1	0.105 (0.13)	0.12553	1.92 (2.50)
H_A	0.096 (0.21)	0.12553	1.72 (2.42)
H_C	0.026 (0.06)	0.12553	2.50
N_A	0.052 (0.15)	0.71131	3.25
P	0.580 (1.34)	0.83680	3.94 (3.74)
F	-0.230 (-0.39)	0.25520	3.118

these densities. Since the viscosity of [bmim][PF_6] is very high (around 200 cP at 300K), the liquid was equilibrated at 500K for 2 ns and then gradually cooled to 300K in steps of 50K, so as to ensure proper equilibration. The system was equilibrated for a total of 8 ns and the production run was carried out for 4 ns. Simulations of the crystal were initiated from the experimental crystal structure [33, 34] and were carried out at a temperature of

173K at which the experimental structure was reported.

Simulations with the original model [14] and the refined model were performed with the same protocols. Liquid state simulations were carried out with 256 ion pairs of [bmim] and [PF_6] accounting for a total of 8192 atoms, at five different temperatures: 300K, 350K, 400K, 450K and 500K. As in earlier simulations, the liquid was initially allowed to equilibrate under constant NPT conditions from which the density of the system for the constant NVT conditions were fixed. The systems at 300K, 350K, 400K, 450K and 500K were then equilibrated in the canonical ensemble with cubic boxes of length 44.3, 44.78, 45.32, 45.91 and 46.51Å respectively. Nosé-Hoover chain thermostats [32] were used for the temperature control. Periodic boundary conditions consistent with the cubic symmetry were employed to obtain the bulk behavior. Ewald summation method was used to handle Coulombic interactions with an alpha value of 0.339 $Å^{-1}$. Coulomb energy in reciprocal space was calculated using 8538 reciprocal space vectors. Non-bonded interactions were calculated up to a distance cutoff of 13 Å. Multiple time step algorithm, RESPA [31] was used to integrate the equations of motion, wherein the non-bonded interactions beyond 6 Å and within 13 Å were integrated with a time step of 3 fs and those within 6 Å with a time step of 1.5 fs. Torsional forces were computed every 0.75 fs and the bending and stretching degrees of freedom were integrated with a time step of 0.375 fs. At each temperature, the system was equilibrated for at least 2 ns, and the trajectory was accumulated over more than 2 ns for analysis.

Simulations were also carried out at all temperatures mentioned above, using the intramolecular potential parameters for the PF_6 anion taken from the work of Lopes and Padua [35] to check whether the differences arise due to the new set of non-bonded parameters in the present model or due to the different intramolecular parameters used for the anion. No significant changes in the structure and dynamics of this system were observed relative to simulations carried out using intramolecular potential parameters for the anion which were used earlier [4], thus ruling out differences in the intramolecular

potential parameters as the cause for improved properties.

For the calculation of surface tension, a well equilibrated bulk liquid at 300K was placed in a supercell of dimensions 44.3, 44.3 and 90.0Å and further equilibrated for 1 ns. The surface tension of the liquid was calculated from the data obtained over a subsequent 1 ns trajectory. Three independent initial configurations were generated to obtain the trajectory for this calculation. Other procedures are as described in Ref. [26].

Figures 3 to 8 report results of simulations carried out at a temperature of 300K.

A larger system with 2048 ion pairs of [bmim][PF_6] (65,536 atoms) was also studied at 300K in a cubic box of length 88.6Å for the sake of comparison to results of the smaller system at 200K and also with experiments. The enthalpy of vaporization is an important quantity that can be calculated from simulations for comparison to experiments [36, 37]. Molecular dynamics simulations of a single ion pair of [bmim][PF_6] were carried out in isolated gas phase for the computation of enthalpy of vaporization. Starting from 10 different configurations, the average energy was computed over 3 ns for each trajectory. The calculated enthalpy of vaporization is 158.5±2.7 kJmol^{-1} compared to the experimental value of 145±10 kJmol^{-1} [38].

5.3 Results and discussions

5.3.1 Density

The density obtained from simulations using the refined model at different temperatures are compared with experimental data [39–41] in Table 5.3.1. The comparison is good, although the simulations predict densities higher than experiment by about 1.4%.

The coefficient of thermal expansion is defined as

$$\beta = \frac{1}{V}\left(\frac{\partial V}{\partial T}\right)_P = -\frac{1}{\rho}\left(\frac{\partial \rho}{\partial T}\right)_P \tag{5.4}$$

Table 5.2: Comparison of the liquid state density at zero pressure for [bmim][PF_6] between simulations using the refined model and experiment [33, 34, 39–41]. Density values predicted by the Lopes *et al* model [14] are given in parenthesis.

Temperature (K)	Density Simulation (kgm^{-3})	Density Experiment (kgm^{-3})	Percentage deviation
300	1389 (1334)	1369	1.4
350	1345 (1301)	1326	1.4
400	1297 (1262)	1282	1.2
450	1248 (1219)	1239	0.7
500	1200 (1184)	1195	0.4
Crystal at 173K	1560	1558	0.1

The calculated β ($6.85 \times 10^{-4} K^{-1}$) from the refined model compares well with the experimental value ($6.6 \times 10^{-4} K^{-1}$) [39] in the temperature range, 300-400K. The thermal expansion coefficient of [bmim][PF_6] has been reported to be $6.0 \times 10^{-4} K^{-1}$ by another group [42].

The variation of density with pressure was also calculated at 298.2 K. The computed densities at 105.6 MPa and 204.7 MPa were found to be 1435 and 1466 kgm^{-3} respectively which are within 2.0% of the experimental values [43].

5.3.2 Structure Factor and Charge Ordering

The partial structure factor was calculated between all distinct pairs of atoms using the formula,

$$S_{\alpha\beta}(q) = \delta_{\alpha\beta} + 4\pi\sqrt{\rho_\alpha \rho_\beta}\int_0^\infty r^2[g_{\alpha\beta}(r) - 1]\frac{\sin(qr)}{qr}dr \tag{5.5}$$

where $\rho_\alpha = \frac{N_\alpha}{V}$, N_α the number of atoms of type α, and V is the volume of the system. In practice, the upper limit in the integral was taken as half the simulation box length. The total X-ray structure factor is given by

$$S(q) = \sum_\alpha \sum_\beta c_\alpha c_\beta \frac{f_\alpha(q) f_\beta(q)}{\langle f(q)\rangle^2} S_{\alpha\beta}(q) \tag{5.6}$$

where c_α is the concentration of atom type α, f_α is the atomic form factor and $\langle f(q)\rangle = \sum_\alpha c_\alpha f_\alpha(q)$. For the calculation of neutron weighted structure factor, the atomic form factors in Eq. 5.6 were replaced by q-independent neutron scattering lengths of the atoms in equation. S(q) was calculated with a resolution in wave vector of 0.145Å^{-1} (for the 256 ion pair system), a value determined by the size of the simulation box.

The X-ray and neutron scattering factors obtained from the simulations [44] are compared with the experimental wide angle X-ray and neutron diffraction data [18] in Figure 5.2. The X-ray structure factor shows two peaks in the low wavevector region at around 1Å^{-1} and 1.5Å^{-1}. The peak intensity for the former is diminished compared to the latter in the experimental data. The X-ray structure factor obtained from simulations match very well with the experiments at all wave vectors. The neutron weighted structure factor of simulations presented in Figure 5.2 corresponds to a fully deuterated (i.e., perdeuterated) compound. The computed neutron structure factor agrees well with experiment. However, the intensity of the peak at 1Å^{-1} is slightly smaller in the simulation data when compared to experiments. It is particularly noteworthy that even the small shift in the position of the 1.5Å^{-1} peak between x-ray and neutron results, as observed in experiments, is reproduced in our simulations. The two features, at 1 and

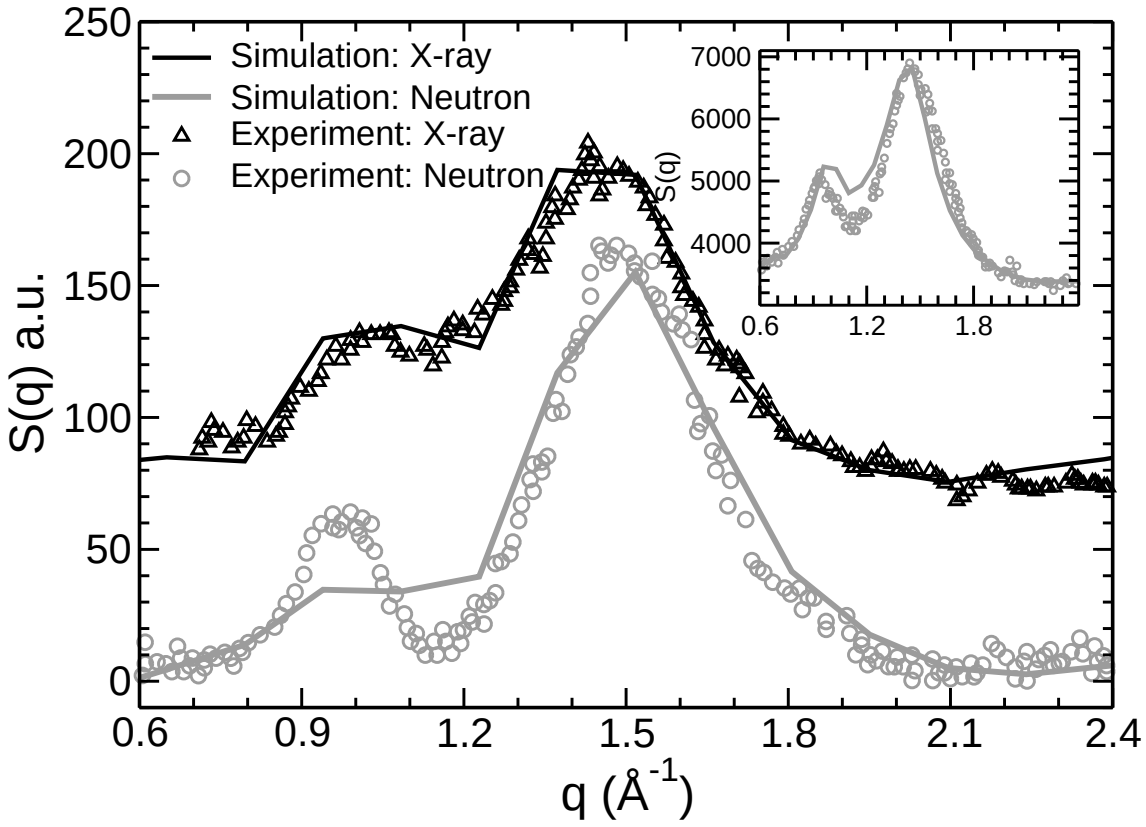

Figure 5.2: Comparison of X-ray and neutron structure factors between simulations and experiments [18] for perdeuterated [bmim][PF_6] at 200K. Data corresponding to X-ray structure factor have been shifted by 50 units along the y-axis. Inset shows a similar comparison of the neutron structure factor at 300K, where the simulation data is from the 2048 ion pair system.

1.5Å^{-1} correspond to real space distances of 6.3Å and 4.2Å respectively. In the inset, we compare the results of simulations (from the 2048 ion pair system) at 300K against that from wide angle neutron scattering experiment [18]. Once again, we observe a good agreement between the two. As expected, the increase in temperature causes the higher wave vector peak to shift to lower values, i.e., to around 1.45Å^{-1} compared to the data at 200K. Features beyond 1.5Å^{-1} arise from intramolecular correlations and hence are not discussed here.

Based on the satisfactory comparison to experiment in terms of both neutron and X-ray weighted structure factors, we proceed now to determine the origin of these peaks by analyzing the partial structure factors between different atom pairs in the system. The

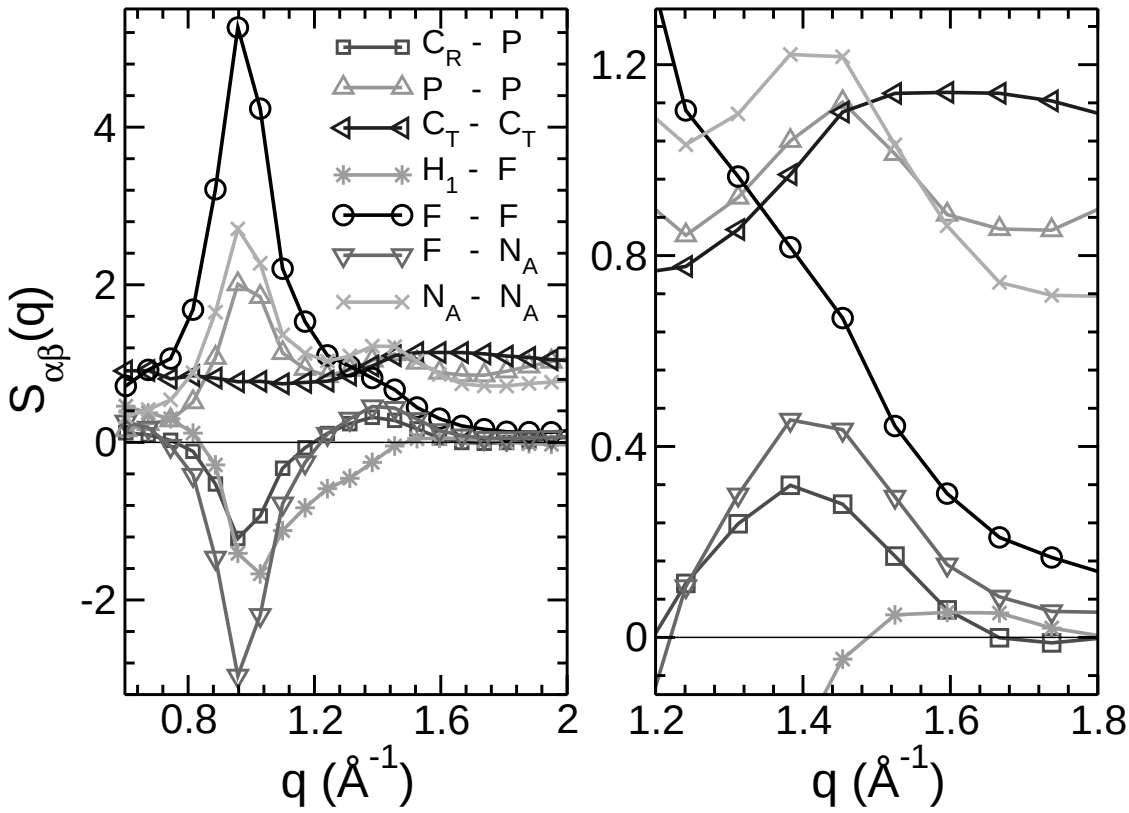

Figure 5.3: Partial structure structure factors between selected pairs of atoms of [bmim][PF_6] at 300K from the 2048 ion pair system. Zero X-axis is also shown in the figure. P and F refer to phosphorus and fluorine atoms of the anion respectively. For a description of other atom types, see Figure 5.1.

unweighted partial structure factors for several pairs of atom types are shown in Figure 5.3. The feature at 1Å^{-1} in the total structure factor arises mainly out of correlations between anion-anion or between the ring atoms belonging to different cations. In particular, we find the intensity of scattered X-rays in this region of wave vector to be dominated by correlations between fluorine atoms of the anion. Cross correlations between the carbon atoms of the imidazolium ring and the anion as well as those between the methylene hydrogens and fluorine atoms contribute negatively to this peak. In contrast, the 1.5Å^{-1} peak in the total S(q) is dominated by correlations of the type, nitrogen-nitrogen (of the cations), correlations between tails of adjacent cations and cross-correlations between the atoms of anion and cation. This feature corresponds to a real space length scale of about

4.2Å – the distance between alkane chains in crystalline n-alkanes [45]. These assignments agree with conventional expectations, as well as with data obtained by us on on this liquid using a coarse grained model [46].

The picture that emerges from these analyses strongly suggests that the real space structure of RTILs resembles conventional ionic melts, i.e., one of charge ordering. The presence of coordination shells of oppositely charged ions is a characteristic of such melts. We demonstrate this fact by presenting the three-dimensional spatial density distribution of the cations and anions around a given anion in Figure 5.4. The number density value for the isosurfaces shown are 0.00017 $Å^{-3}$ for cations and 0.00007 $Å^{-3}$ for anions, corresponding to 7 and 3 times the average density of these entities in the liquid. Black represents the most probable locations of anions around PF_6 while grey locates that for the cation ring center. The ring carries a large fraction of the positive charge of the cation, and hence it is appropriate that one studies the spatial location of its center with respect to the anion. The data is shown in two different orientations. The cations lie near the octahedral holes formed by the three PF bond vectors, 4.6 to 5.0Å away from the central phosphorus atom, whereas the anions are preferably located along the PF bond vectors at a distance between 5.75 and 6.0Å from the center of the anion. Note that these are time and ensemble averaged data, and hence not every preferred site is expected to be populated around a chosen anion present in the liquid. For instance, the anion-cation coordination number (at 6Å) is close to 4. Thus, on average, only half of the locations shown in grey are likely to be occupied in the liquid state. The intermolecular structure in the liquid is characterized by ordering of charges, in both translational and an orientational sense.

In summary, X-ray and neutron weighted structure factors for the ionic liquid [bmim][PF_6] have been computed from molecular dynamics simulations and compared with experimental scattering data [18]. Results of our simulations agree very well with experiments in terms of both peak positions and intensity. In the region corresponding to short range

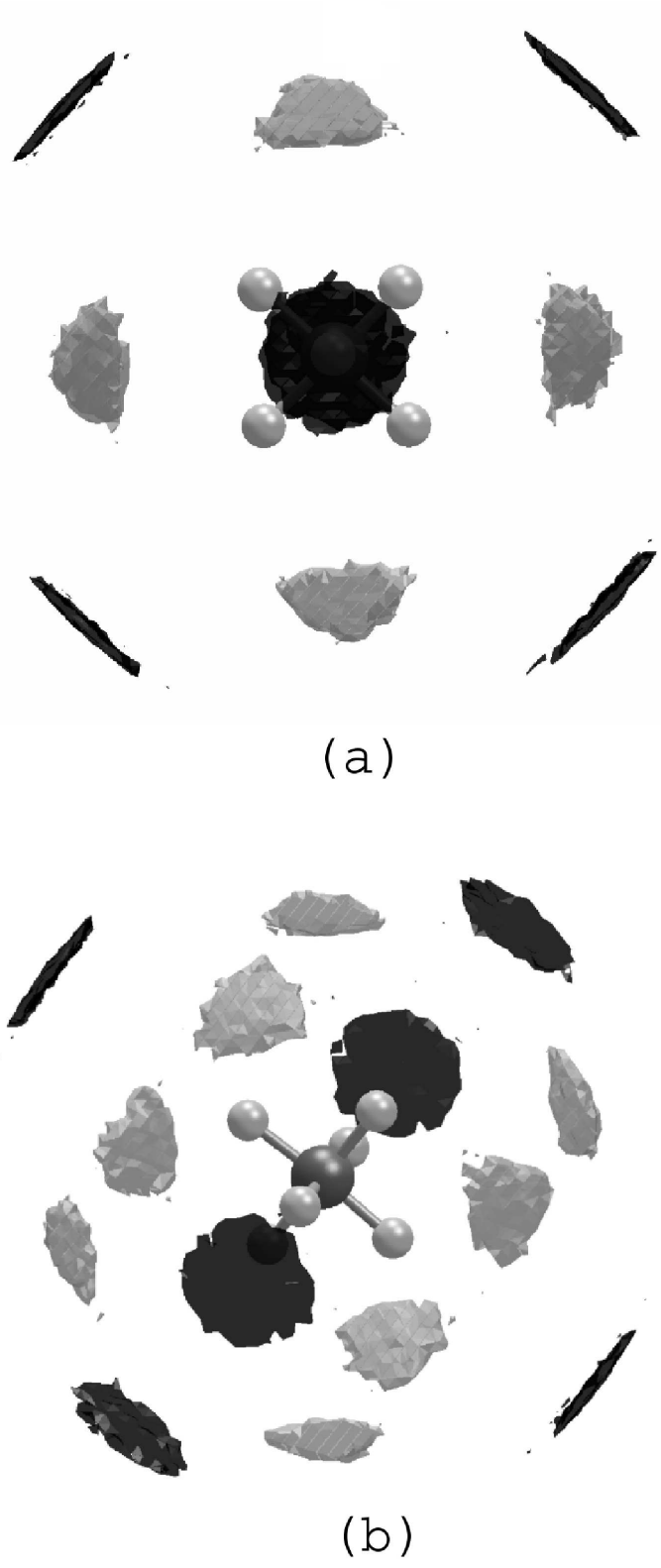

Figure 5.4: (a) The spatial distribution of cations and the anions present within 6.3Å around an anion. Black and grey regions represent density isosurfaces at values 7 and 3 times the average density of anions and cations respectively. (b) Same as (a), in a different orientation.

intermolecular correlations, two peaks are observed in the experimental data. The origin of these two peaks has been analyzed using partial structure factors. It is found that anion-anion and ring-ring (of the cations) correlations are mainly responsible for the peak at 1Å^{-1}. The feature at 1.5Å^{-1} is contributed by anion-anion, tail-tail and tail-cation correlations. The charge ordering behavior reported here for [bmim][PF_6] is expected to be present in other ionic liquids as well.

5.3.3 Radial distribution functions

Cation-anion and anion-anion partial radial distribution functions obtained from the refined model are compared with those from AIMD simulations in Figure 5.5. The comparison is good and the peak positions also match experimental data on the liquid state structure [18, 47].

The radial distribution function of fluorine atoms of the anion around $H_A(C_R)$ is shown in Figure 5.6. The data from the current model is very close to that of AIMD results. This is not surprising as it was one of the functions used to refine the potential parameters. Earlier works have reported differences in the RDF between the hydrogen atom (H_A) attached to the carbon in between the two nitrogens (C_R) of the imidazolium ring and the chloride ion, as obtained from classical and AIMD simulations [1–3, 48]. This acidic hydrogen is believed to be capable of forming a weak hydrogen bond with the anion and hence it is important to capture this feature in the classical MD model, which the refined potential reported here does. Although a classical model was proposed by Youngs *et al* [11] to overcome this deficit for [mmim][Cl], it predicted a much higher density compared to experiment.

5.3.4 Spatial distribution functions

The spatial distribution function of the anions around the cation obtained from the present model is compared with those obtained from the AIMD simulations and with the Lopes

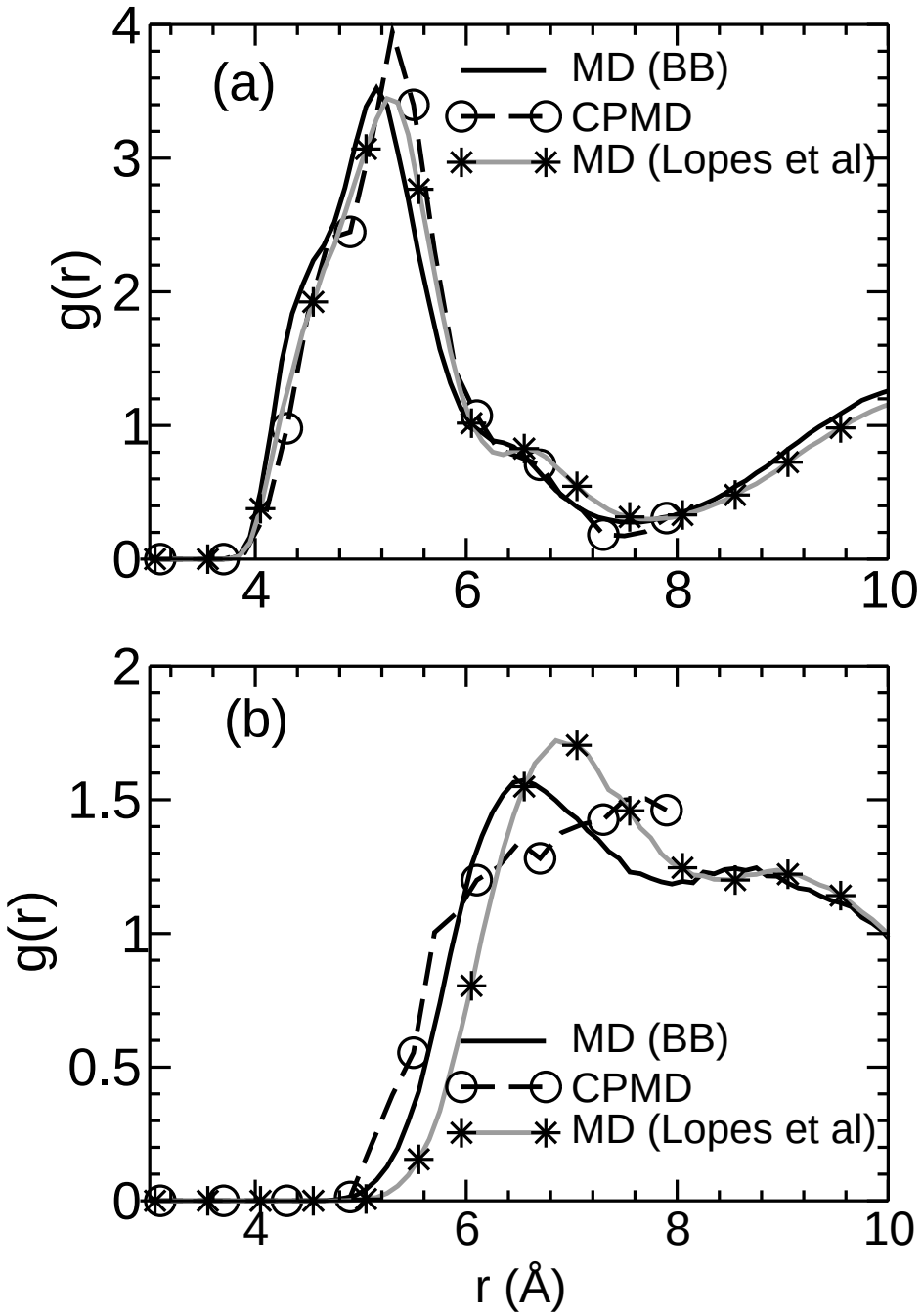

Figure 5.5: Comparison of partial radial distribution functions obtained from the present model, Lopes *et al* model [14] and the AIMD simulations [4]. (a) anion - cation and (b) anion - anion. Results pertaining to our model presented in this figure and the subsequent ones are obtained from simulations performed at 300K and a density of 1.389 g/cc.

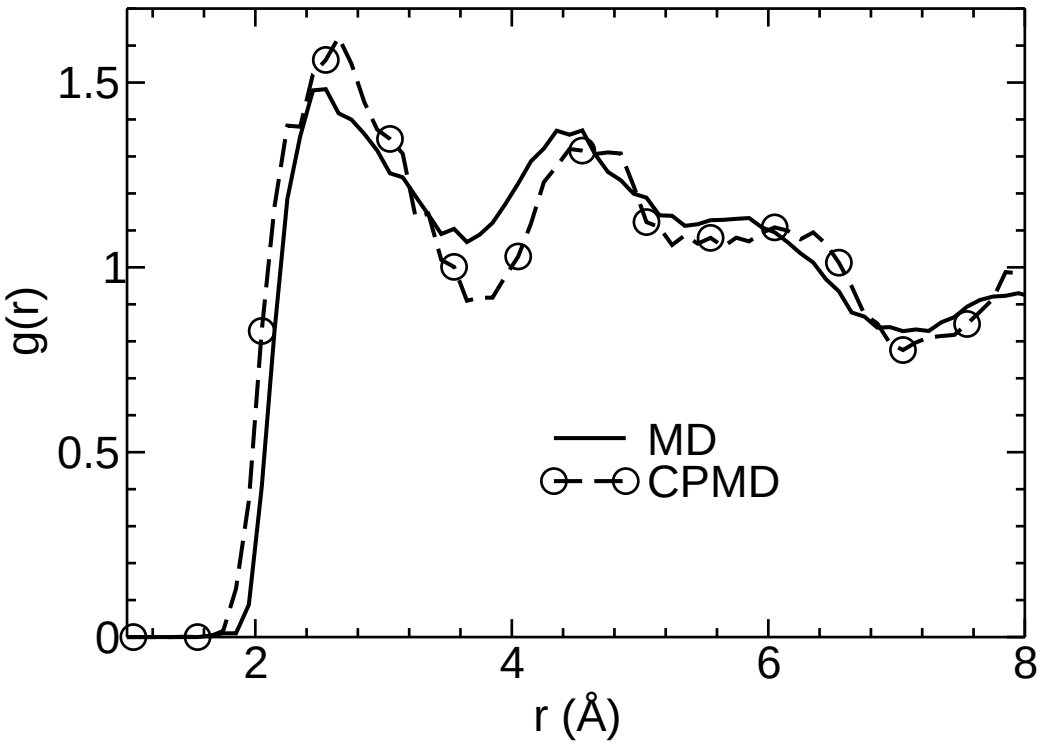

Figure 5.6: Radial distribution function of fluorine atoms of PF_6 around $H_A(C_R)$ obtained from the present model, Lopes *et al* model [14] and AIMD simulations [4].

et al model in Figure 5.7. The isosurface value of the anion density presented in the figure is 0.0375 $\mathring{A}^{-3}$, which is around thirteen times higher than the average density of anions in the liquid. All the three figures are presented with the same orientation of the cation. On the cations, only the hydrogen atoms attached to the ring carbon atoms are shown for a clearer view.

The CPMD data shows substantial probability of anions to be present above the $H_A(C_R)$ atom (Fig. 5.7b). The SDF shows that the anions are also present above and below the ring plane. The probability is also significant near the $H_A(C_W)$ that is closer to the methyl group. The probability is diminished near the second $H_A(C_W)$ that is closer to the butyl group. This can be rationalized as due to the steric hindrance offered by the butyl chain that can attain different conformations, thus inhibiting the presence of anions in that region. The results from Lopes *et al* model exhibits lesser probability for the anions to be present near the $H_A(C_R)$ that was also seen in another compound of the

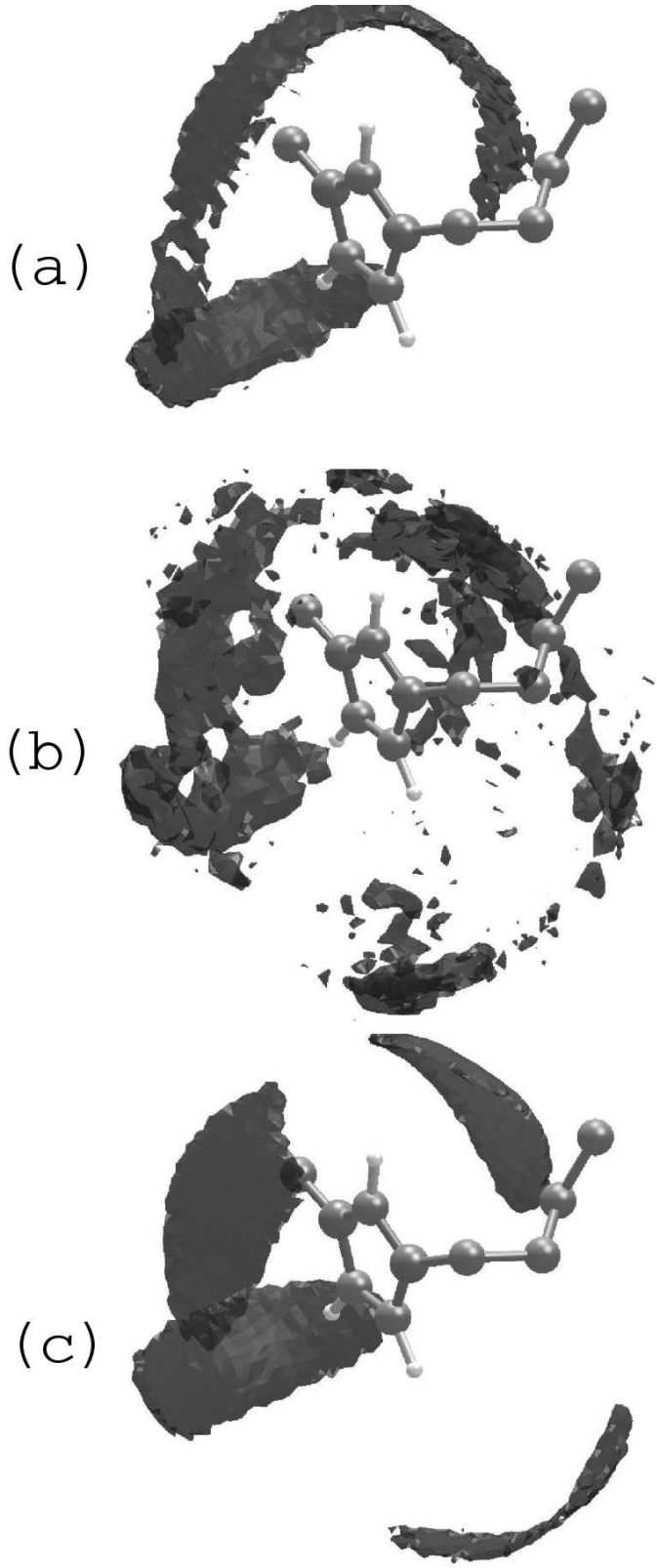

Figure 5.7: Spatial distribution function of the anions around the cation at an isosurface value of 0.0375 $\mathring{A}^{-3}$. (a) Present model, (b) CPMD [4] (c) Lopes *et al* model [14]. The hydrogen atoms on the methyl group and butyl group of the cation are not shown for clarity.

same family, [mmim][Cl] [3].

The present model compares very well with the AIMD results. There is substantial density of anions near the $H_A(C_R)$ atom as predicted by CPMD. Also, the anions are present above and below the ring and the isosurface assumes a semicircular form above the $H_A(C_R)$ in the SDF. But the density of anions near the $H_A(C_W)$ closer to the butyl chain is less than that seen in CPMD and hence is not seen in this figure at the chosen isosurface value. Since the CPMD data in that region is quite noisy, it can be safely assumed that the present model predicts the structure close to that of CPMD simulations.

We have studied the approach (directionality) of the anion towards the cation. To characterize this, we identify the phosphorus atoms that are within 4Å from $H_A(C_R)$ and compute the distribution of the angle formed between the vectors C_RH_A and $H_A(C_R)P$. This distribution is shown in Figure 5.8. Consistent with the discussion on the SDF, we find that the refined model predicts the cation-anion hydrogen bond angle to be more linear than the original model.

5.3.5 Diffusion coefficients

The self diffusion coefficient of the ions has been obtained from the Einstein relation through the slope of the mean squared displacement in the long time regime. We observe that the [bmim] cation, despite being bulky and asymmetric, diffuses faster than the spherical $[PF_6]$ anion. This result that was also observed in our previous study on [mmim][Cl] [3], as well as in several other computational studies [8, 29, 49, 50] has also been reported experimentally [39, 51].

The diffusion co-efficients obtained from the slope of the mean squared displacement data in the duration 400-500ps, for the ions at different temperatures are presented in Table 5.3.5. The diffusion coefficients obtained from the Lopes *et al* model at the temperatures 300, 350, 400, 450 and 500K have also been included in Table 5.3.5 for the sake of comparison. Various workers have stressed the importance of long trajectories in the cal-

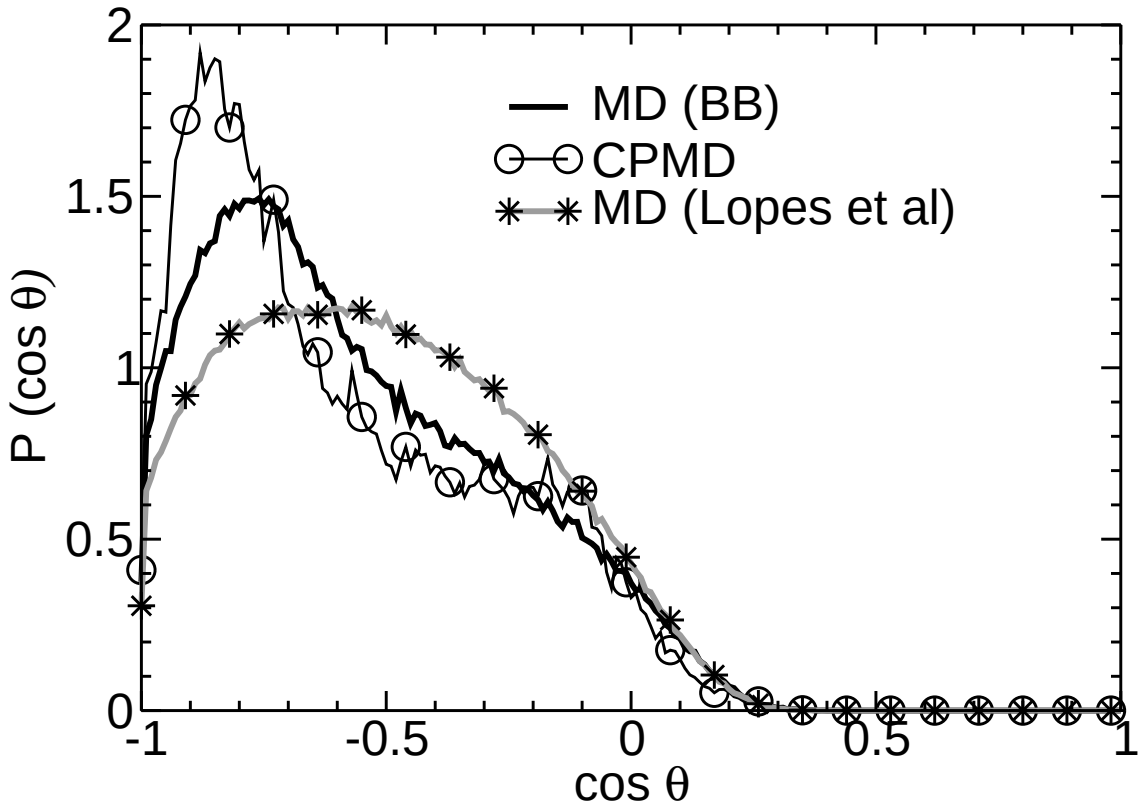

Figure 5.8: Distribution of the angle between the vectors connecting $H_A(C_R)$-C_R and $H_A(C_R)$-P, when the phosphorus atom is within 4.0Å from $H_A(C_R)$, as obtained from the present model (BB), CPMD simulations [4] and Lopes *et al* model [14]. Symbols are shown infrequently for clarity.

culation of diffusion coefficients [29, 50], as the nature of the mean squared displacement curve need to be linear in order to obtain these coefficients using the Einstein relation. It can be noted from the table that the original model with unit positive and negative charges on the cation and the anion, predicts slower diffusion of the ions compared to experiment. The reported values corresponding to the present model are obtained as an average over 3 to 5 independent MD trajectories, whereas the values reported for the Lopes *et al* model [14] are the average over two independent MD trajectories. The values obtained from the MD simulations are compared against the values reported from the experimental studies of Tokuda *et al* [39] in which the temperature dependence of the diffusion co-efficients is fitted to the Vogel-Fulcher-Tammann (VFT) equation. Kanakubo

Table 5.3: Diffusion co-efficients of anion and cations at different temperatures. Values obtained from the Lopes *et al* model [14] are provided in parenthesis for comparison.

.

Temperature	D_{an} ($\times 10^{-12}$ m^2s^{-1})		D_{cat} ($\times 10^{-12}$ m^2s^{-1})	
	simulation	experiment	simulation	experiment
300	4.7 (0.85)	5.9	6.7 (1.58)	8.0
350	52.7 (5.0)	51.4	77.6 (7.7)	64.2
400	205.0 (28.8)	178.6	244.2 (35.2)	209.2
450	374.4 (102.2)	401.3	387.0 (150.9)	447.3
500	685.0 (238.8)	707.9	774.4 (295.7)	760.5

Table 5.4: VFT equation parameters for the diffusion coefficient data.

Ion	$D_0(\times 10^{-8})$ m^2s^{-1}	B (10^2 K)	T_0 (K)
Anion	2.83	14.31	116
Cation	5.90	18.84	67

and coworkers too have experimentally determined the diffusion co-efficients [51]. The results from our simulations are within 20% of the reported experimental values.

The diffusion co-efficients obtained at different temperatures were fitted to the Vogel-Fulcher-Tammann equation given by [52]

$$D = D_0 \exp\left(-\frac{B}{T - T_0}\right) \tag{5.7}$$

The VFT equation parameters for the anion and the cation that best fit the simulation results are presented in Table 5.4.

5.3.6 Surface tension

The surface tension γ was calculated using the diagonal components of the pressure tensor P_{ii} employing the formula [53, 54],

$$\gamma = -b_z(P_{xx} + P_{yy} - 2P_{zz})/4 \tag{5.8}$$

where b_z is the length of the supercell in the direction parallel to the interface normal (z-axis), and the presence of the two equivalent interfaces is taken into account by introducing a factor of two in the denominator. The pressure tensor of the systems was stored every time step to calculate γ.

The average surface tension obtained from three independent runs is found to be 47 mN/m against the experimental value of 42.3 mN/m at 300K [55, 56]. The Lopes *et al* model [14] predicts a value of 74 mN/m at 300K.

5.4 Conclusions

In a timely article, Lopes *et al* presented an interaction potential model for several room temperature ionic liquids [14]. The virtue of that model is its capability to model a wide variety of cations and anions and thus their salts. In the present study, within a narrower aim, we refine that model for a specific IL, [bmim][PF_6], in order to accurately obtain its structural and dynamical properties. In essence, the refined model employs +0.8e and -0.8e as the total charge on the cation and anion respectively. Classical molecular dynamics simulations at different temperatures have been carried out to validate the parameters. The density of the liquid predicted by the model is within 1.4% of experiment at all temperatures. The thermal expansion co-efficient obtained from the density differentials with temperature too agrees very well with the values reported in the literature. The structure of the liquid characterized by the radial distribution function of anion and cation around themselves and around each other, and the spatial distribution functions

compare very well with the *ab initio* MD results reported earlier by our group [4]. Specifically, the present model captures the weak hydrogen bonding between the anion and the cation, something that has been a sore thumb of many earlier studies [1–3]. The diffusion co-efficients obtained are within 20% of the experimentally reported values at all the temperatures studied. The refined model also predicts a surface tension value of 47 mN/m at 300K compared to the experimental value of 42.3 mN/m [55, 56]. Such a lowering of surface tension and a better agreement with experiment on the transport properties has also been reported by Voth and coworkers, however using a polarizable model [57, 58]. The advantage of the Lopes et al [14] approach is the generality of the force field that can be used for many ionic liquids. Their model works well to reproduce experimental static properties, while the model presented here is for a specific IL, [bmim][PF_6].

The parameters for non-bonded interactions of the potential proposed here may not be unique; the properties of the IL may probably be reproduced by another set too. However, in our empirical search, quite a large number of trial simulations were run. Also, the refined model is able to predict both structure and dynamics at several temperatures, reasonably well. Importantly, this model is able to capture the local intermolecular structure predicted by AIMD simulations and "non-local" experimental quantities such as density, thermal expansion coefficient, diffusion coefficients and surface tension. In view of these, we believe that the potential is robust and contains some elements of transferability as well. Further simulations employing the present model in solutions are underway.

Bibliography

[1] M.G. Del Pópolo, R.M. Lynden-Bell, J. Kohanoff, *J. Phys. Chem. B*, **109**, 5895 (2005).

[2] M. Bühl, A. Chaumont, R. Schurhammer, G. Wipff, *J. Phys. Chem. B*, **109**, 18591 (2005).

[3] B.L. Bhargava, S. Balasubramanian, *Chem. Phys. Lett.*, **417**, 486 (2006).

[4] B.L. Bhargava, S. Balasubramanian, *J. Phys. Chem. B*, **111**, 4477 (2007).

[5] P.A. Hunt, *J. Phys. Chem. B.*, **111**, 4844 (2007).

[6] P.A. Hunt, B. Kirchner, T. Welton, *Chem. Eur. J.*, **12**, 6762 (2006).

[7] J. de Andrade, E.S. Boes, H. Stassen, *J. Phys. Chem. B*, **106**, 3546 (2002).

[8] C.J. Margulis, H.A. Stern, B.J. Berne, *J. Phys. Chem. B*, **106**, 12017 (2002).

[9] S.M. Urahata, M.C.C. Rebeiro, *J. Chem. Phys.*, **120**, 1855 (2004).

[10] Z. Liu, S. Huang, W. Wang, *J. Phys. Chem. B*, **108**, 12978 (2004).

[11] T.G.A. Youngs, M.G. Del Pópolo, J. Kohanoff, *J. Phys. Chem. B*, **110**, 5697 (2006).

[12] N.M. Micaelo, A.M. Baptista, C.M. Soares, *J. Phys. Chem. B*, **110**, 14444 (2006).

[13] S. Alavi, D.L. Thompson, *J. Chem. Phys.*, **122**, 154704 (2005).

[14] J.N.C. Lopes, J. Deschamps A.A.H. Pádua, *J. Phys. Chem. B*, **108**, 2038 (2004); **108**, 11250 (2004).

[15] J.N.C. Lopes, A.A.H. Pádua, *J. Phys. Chem. B*, **110**, 19586 (2006).

[16] C. Hardacre, J.D. Holbrey, S.E.J. McMath, D.T. Bowron, A.K. Soper, *J. Chem. Phys.* **118**, 273 (2003).

[17] C. Hardacre, S.E.J. McMath, M. Nieuwenhuyzen, D.T. Bowron, A.K. Soper, *J. Phys.: Condens. Matter* **15**, S159 (2003).

[18] A. Triolo, A. Mandanici, O. Russina, V. Rodriguez-Mora, M. Cutroni, C. Hardacre, M. Nieuwenhuyzen, H. Bleif, L. Keller, M.A. Ramos, *J. Phys. Chem. B* **110**, 21357 (2006).

[19] M. Deetlefs, C. Hardacre, M. Nieuwenhuyzen, A.A.H. Padua, O. Sheppard, A.K. Soper, *J. Phys. Chem. B* **110**, 12055 (2006).

[20] M. Kanakubo, T. Umecky, Y. Hiejima, T. Aizawa, H. Nanjo, Y. Kameda, *J. Phys. Chem. B* **109**, 13847 (2005).

[21] A. Triolo, O. Russina, H. Bleif, E.D. Cola, *J. Phys. Chem. B* **111**, 4641 (2007).

[22] P. Hunt, *Mol. Sim.*, **32**, 1 (2006).

[23] R. Ludwig, *ChemPhysChem*, **7**, 1415 (2006).

[24] O. Borodin, G.D. Smith, R.L. Jaffe, *J. Comput. Chem.*, **22**, 641 (2001).

[25] B.L. Bhargava, S. Balasubramanian, *J. Chem. Phys.*, bf 123, 144501 (2005).

[26] B.L. Bhargava, S. Balasubramanian, *J. Am. Chem. Soc.*, **128**, 10073 (2006).

[27] A. Chaumont, R. Schurhammer, G. Wipff, *J. Phys. Chem. B*, **109**, 18964 (2005).

[28] G. Chevrot, R. Schurhammer, G. Wipff, *Phys. Chem. Chem. Phys.*, **8**, 4166 (2006).

[29] T.I. Morrow, E.J. Maginn, *J. Phys. Chem. B*, **106**, 12807 (2002).

[30] A search in the Lennard-Jones parameter space with the magnitude of the total charge on the ions as 0.9e (instead of 0.8e) was not able to reproduce the structural quantities to the extent as is reported here.

[31] M.E. Tuckerman, B.J. Berne, G.J. Martyna, *J. Chem. Phys.*, **97**, 1990 (1992).

[32] G.J. Martyna, M.L. Klein, M.E. Tuckerman, *J. Chem. Phys.*, **97**, 2635 (1992).

[33] A.R. Choudhury, N. Winterton, A. Steiner, A.I. Cooper, K.A. Johnson, *J. Am. Chem. Soc.*, **127**, 16792 (2005).

[34] S.M. Dibrov, J.K. Kochi, *Acta Cryst. C*, **62**, o19 (2006).

[35] J.N.C. Lopes, A.A.H. Pádua, *J. Phys. Chem. B*, **108**, 16893 (2004).

[36] L.M.N.B.F. Santos, J.N.C. Lopes, J.A.P. Coutinho, J.M.S.S. Esperanca, L.R. Gomes, I.M. Marrucho, and L.P.N. Rebelo, *J. Am. Chem. Soc.* **129**, 284 (2007).

[37] R. Ludwig, and U. Kragl, *Angew. Chem. Int. Ed.* **46**, 6582 (2007).

[38] Y.U. Paulechka, G.J. Kabo, A.V. Blokhin, O.A. Vydrov, J.W. Magee, M. Frenkel, *J. Chem. Eng. Data* **48**, 457 (2003).

[39] H. Tokuda, K. Hayamizu, K. Ishii, A.B.H. Susan, M. Watanabe, *J. Phys. Chem. B*, **108**, 16593 (2004).

[40] J.G. Huddleston, A.E. Visser, W.M. Reichert, H.D. Willauer, G.A. Broker, R.D. Rogers, *Green Chem.*, **3**, 156 (2001).

[41] J. Jacquemin, P. Husson, A.A.H. Padua V. Majer, *Green Chem.*, **8**, 172 (2006).

[42] C. Cadena, J.L. Anthony, J.K. Shah, T.I. Morrow, J.F. Brennecke, E.J. Maginn, *J. Am. Chem. Soc.*, **126**, 5300 (2004).

[43] Z. Gu, J.F. Brennecke, *J. Chem. Eng. Data*, **47**, 339 (2002).

[44] To compare with wide angle scattering experiments, a parabolic function in wave vector [59] has been subtracted from the S(q) obtained from simulation. The parameters of the function were chosen to ensure a nearly constant baseline for the simulation result, consistent with the experimental data.

[45] D.M. Small, *The Physical Chemistry of Lipids: From Alkanes to Phospholipids*, Plenum, New York, **1986**, pp 21-33.

[46] B.L. Bhargava, R. Devane, M.L. Klein, S. Balasubramanian, *Soft Matter* **2007**, (In Press); DOI: 10.1039/b710801j

[47] I. Billard, G. Moutiers, A. Labet, A. El Azzi, C. Gaillard, C. Mariet, K. Lutzenkirchen, *Inorg. Chem.*, **42**, 1726 (2003).

[48] A. Bagno, F. D'Amico, G. Saielli, *ChemPhysChem*, **8**, 873 (2007).

[49] C.G. Hanke, S.L. Price, R.M. Lynden-Bell, *Mol. Phys.*, **99**, 801 (2001).

[50] M.G. Del Pópolo, G.A. Voth, *J. Phys. Chem. B*, **108**, 1744 (2004).

[51] M. Kanakubo, K.R. Harris, N. Tsuchihashi, K. Ibuki, M. Ueno, *J. Phys. Chem. B*, **111**, 2062 (2007).

[52] H. Vogel, *Phys. Z.*, **22**, 645 (1921); G.S. Fulcher, *J. Am. Ceram. Soc.*, **8**, 339 (1923).

[53] M. Rao, B.J. Berne, *Mol. Phys.*, **37**, 455 (1979).

[54] M. González-Melchor, F. Bresme, F. *J. Chem. Phys.*, **122**, 104710 (2005).

[55] E. Sloutskin, B.M. Ocko, L. Tamam, I. Kuzmenko, T. Gog, M. Deutsch, *J. Am. Chem. Soc.*, **127**, 7796 (2005); **127**, 18333 (2005).

[56] G. Law, P.R. Watson, *Langmuir*, **17**, 6138 (2001).

[57] T. Yan, C.J. Burnham, M.G. Del Pópolo, G.A. Voth, *J. Phys. Chem. B*, **108**, 11877 (2004).

[58] T. Yan, S. Li, W. Jiang, X. Gao, B. Xiang, G.A. Voth, *J. Phys. Chem. B*, **110**, 1800 (2006).

[59] L. Hennet, I. Pozdnyakova, A. Bytchkov, V. Cristiglio, P. Palleau, H.E. Fischer, G.J. Cuello, M. Johnson, P. Melin, D. Zanchi, S. Brassamin, J.-F. Brun, D.L. Price, M.-L.Saboungi, *Rev. Sci. Instrum.*, 053903 (2006).

Chapter 6

Nanoscale Organization in Room Temperature Ionic Liquids: A Coarse Grained Molecular Dynamics Simulation Study

6.1 Introduction

Room temperature ionic liquids (RTIL) containing the imidazolium cation and an inorganic anion have been shown to possess interesting intermolecular arrangements [1–3]. Of recent interest has been the study of their structure at nanometric length scales [4–8]. In this regard, compounds with 1,3-dialkylimidazolium as the cation and a variety of inorganic species as the counterion have been investigated. Within this family, cations with alkyl tails longer than C_{10} have been shown to possess liquid crystalline phases [9] and are thus expected to show some of that character in the liquid phase as well. However, the liquid state structure of ILs possessing alkyl groups of intermediate lengths (C_4 to C_{10}) continues to be studied. Atomistic [4, 7] and coarse grained [5, 6] computer simula-

tions have shown the possibility of nanoscale segregation of polar (i.e., cation ring and anions) and non-polar (alkyl tail groups) moieties in the liquid. These liquids are believed to possess intermediate scale ordering in the length scales of a few nanometre. It has been conjectured that such an ordering might even template the formation of nanomaterials [10]. These simulation studies have been complemented by neutron diffraction, wide angle x-ray and neutron scattering experiments [11–13]. They showed that the liquid state structure of [bmim][PF_6] possesses many similarities with that of its crystal. Quite recently, studies on a series of ionic liquids based on the Cl or BF_4 anion demonstrated the organization of molecules at length scales beyond 1.5nm [8]. Triolo and coworkers found a peak at low wave vectors (below 1 $Å^{-1}$) whose position depended on the length of the alkyl tail as well as on temperature. Interestingly, this feature shifted to lower wave vectors with decreasing temperature indicating that it arose from diffusive processes. Such a structural ordering can cause a heterogeneity in dynamics as well [14].

Our aim is to develop a coarse grain (CG) model for molecular dynamics (MD) simulations which will enable one to probe length scales larger than the capability of current atomistic simulations. In this work, we study the nanoscale ordering in ionic liquids of the type 1-*n*-alkyl-3-methylimidazolium hexafluorophosphate, [$C_n$mim][PF_6]. Our recent *ab initio* MD simulations of [bmim][PF_6] [15] enabled us to develop a refined atomistic potential for this compound [16]. In the present work, we build a coarser molecular model for the ions, using the results of *ab initio*, and atomistic simulations *as well as* experimental data as reference. This hierarchical approach yields excellent predictive capabilities on the physical properties of these liquids and offers considerable insight into their nanoscale structure.

6.2 Details of Model and Simulation

The coarse grain model was constructed with the following principles: (i) the alkyl tail was represented in the same fashion as in Shinoda et al [17], who studied aqueous surfactant

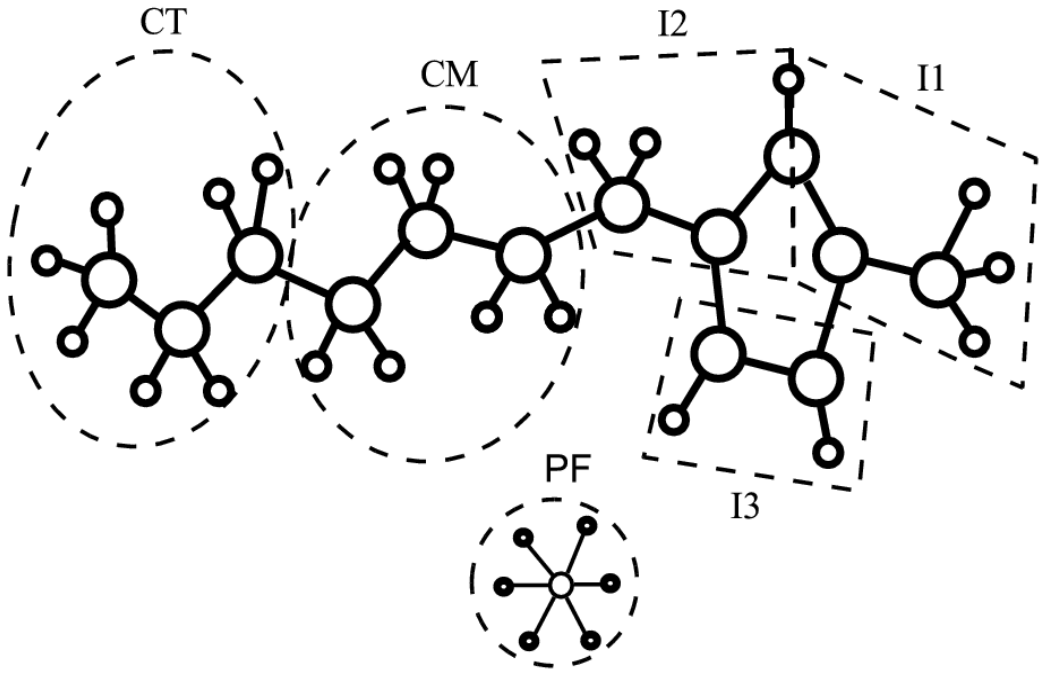

Figure 6.1: Schematic of $[C_7mim][PF_6]$, illustrating the mapping of atoms to coarse grain beads.

solutions, (ii) around three carbon or nitrogen atoms along with any hydrogen atoms bonded to them were coarsened into one bead, (iii) the CG model should reproduce the pair correlation functions obtained from all-atom simulations. With these guiding principles, the CG prototype was constructed for $[bmim][PF_6]$.

The schematic in Figure 6.1 represents a mapping between the all atom (AA) molecule and the CG one, for the case of $[C_7mim][PF_6]$. Note that one of the carbon and an hydrogen atom in the AA model is shared equally among the I1 and I2 beads. The charges on the bead were taken as the sum of the charges of their respective atom constituents from the AA model, with appropriate weights in cases where an atom contributed partially to the construction of a bead. The CM and CT beads were charge neutral, consistent with Shinoda et al [17]. The same procedure was followed to calculate the masses of the CG beads. The coordinates of the CG beads were obtained from mass-weighted atom coordinates of the AA molecule. The form of the intramolecular potential (U_{intra}) is the

same as in Shinoda et al [17] and is given here for the sake of completeness.

$$U_{intra} = \sum^{Bond} k_b(r - r_0)^2 + \sum^{Angle} k_\theta(\theta - \theta_0)^2 \tag{6.1}$$

where k_b and k_θ are force constants, r_0 and θ_0 are the equilibrium bond length and bond angle respectively. Effective potentials for the bead bond lengths and angles were calculated from their probability distributions within all-atom simulations. These effective potentials were fitted to Eq. 6.1 to obtain the force constants and equilibrium lengths or angles. Based on preliminary CG simulations, marginal adjustments were made to these parameters in order to reproduce the mean values of the all-atom distributions. The refined values are provided in Tables 6.1 and 6.2.

Beads within the same molecule separated by more than two bonds and those belonging to different molecules interacted via a non-bonded interaction ($U_{nonbond}$)which included a 9-6 type Lennard-Jones potential and Coulombic interaction between the charges. It is given by,

$$U_{nonbond} = \frac{27}{4}\epsilon\left[\left(\frac{\sigma}{r}\right)^9 - \left(\frac{\sigma}{r}\right)^6\right] + \frac{1}{4\pi\epsilon_0}\frac{q_i q_j}{r_{ij}} \tag{6.2}$$

where ϵ and σ are Lennard-Jones parameters, q_i and q_j are charges on the beads i and j respectively.

We employed a real space cutoff of 15Å for the nonbonded interactions and the potential is not shifted at that distance. Initial values of ϵ between beads were taken to be the sum of ϵ values of their atomic constituents from the AA model. This is justified based on the additivity of atomic polarizabilities to obtain group polarizability [18]. Initial values of σ of the beads of the head group were based on its geometry. These parameters were refined so as to reproduce the pair correlation function between the CG beads as obtained from all-atom simulations, the density and surface tension of [bmim][PF_6] under ambient conditions.

The parameters of the potential model are provided in Tables 6.1, 6.2, 6.3. Values for

the beads belonging to the alkyl tail, prescribed by Shinoda et al [17] have been retained.

Table 6.1: Bond parameters

Bead Pair	k_b [kcal/mol/Å^2]	r_0 [Å]
I1-I2	179.54	2.97
I1-I3	223.75	2.30
I2-I3	230.65	2.27
I2-CM	7.98	3.225
CM-CM	6.160	3.64
CM-CT	6.160	3.65
CT-CT	6.955	3.71

Table 6.2: Angle parameters

Bead Triplet	k_θ [kcal/mol/rad^2]	θ_0 [degree]
I1-I2-I3	932.5	51.22
I1-I3-I2	433.26	81.88
I3-I1-I2	748.7	50.39
I1-I2-CM	4.91	143.82
I3-I2-CM	1.40	147.83
I2-CM-CM	2.21	170.17
CM-CM-CT	1.190	175.0

Molecular dynamics simulations were performed using the LAMMPS code [19]. Simulations to obtain the density of the ionic liquids were carried out in the NPT ensemble using Nosé-Hoover thermo- and barostats with time constants of 500fs and 3000fs respectively. The equations of motion were integrated with a timestep of 4fs. Coulombic interactions were handled using the particle-particle particle-mesh (PPPM) solver, with an accuracy of 1 part in 10^5 for bulk simulations and 1 part in 10^6 for the calculations on the liquid-air interface.

Simulations of the liquid-vapor interface to calculate surface tension were carried out with 256 ion pairs, under NVT conditions in a box whose length in the z-direction was

Table 6.3: Non-bonded 9-6 Lennard-Jones interaction parameters and bead charges. Interaction cutoff for all pairs is 15Å.

Bead Pair	ϵ [kcal/mol]	σ [Å]
I1 - I1	0.3757	4.1000
I1 - I2	0.3604	4.0500
I1 - I3	0.2740	4.0500
I1 - CM	0.3483	4.3000
I1 - CT	0.3914	4.3400
I1 - PF	0.0857	5.1000
I2 - I2	0.3457	4.1000
I2 - I3	0.2628	4.0500
I2 - CM	0.3341	4.3000
I2 - CT	0.3754	4.3400
I2 - PF	0.0857	5.1000
I3 - I3	0.1998	3.6000
I3 - CM	0.2540	3.7600
I3 - CT	0.2854	3.8000
I3 - PF	0.1989	4.8500
CM - CM	0.4200	4.5060
CM - CT	0.4440	4.5455
CM - PF	0.4274	4.9030
CT - CT	0.4690	4.5850
CT - PF	0.4801	4.9430
PF - PF	0.5656	5.2000

	I1	I2	I3	CM	CT	PF
q[e]	0.356	0.292	0.152	0.0	0.0	-0.8

90Å. Surface tension was calculated in the usual manner from the difference between the average of P_{xx} and P_{yy} with P_{zz}. This value was averaged over three independent simulation trajectories. Calculations for the density reported here were obtained from simulations of 256 ion pairs in the case of [bmim][PF_6] and 3375 ion pairs for [C_7mim][PF_6] and [C_{10}mim][PF_6]. Results on structure were obtained from systems of 6912 ion pairs for [bmim][PF_6] and 3375 ion pairs for [C_7mim][PF_6] and [C_{10}mim][PF_6]. An equilibrated configuration from an all-atom MD simulation containing 256 (or 125) ion pairs was used to obtain the initial positions of coarse grain beads in these systems. This configuration

was further equilibrated within the CG potential. The larger system was constructed from this trajectory by replicating the small system 27 times, i.e., thrice in each of the Cartesian directions. For each compound, the larger system was equilibrated at 450K for over 15ns, and cooled slowly to 300K in steps of 50K, under NPT conditions. In summary, the system was cooled from 450K to 300K at a rate of about 200ps/K. At 300K, structural quantities were averaged for over 15ns after a considerable period of equilibration. The box lengths of the [bmim][PF_6], [C_7mim][PF_6], and [C_{10}mim][PF_6] systems at 300K were 134.0598, 113.2778, and 120.172Å respectively. For [bmim][PF_6], simulations were also carried out at 200K for a comparison of the structure factor with experiment.

Partial pair correlation functions were obtained between all distinct pairs of bead types, with a bin width of 0.03Å, up to a distance of half the box length. These were then transformed into partial structure factors defined as,

$$S_{\alpha\beta}(q) = \delta_{\alpha\beta} + 4\pi\sqrt{\rho_\alpha \rho_\beta}\int_0^\infty r^2[g_{\alpha\beta} - 1]\frac{sin(qr)}{(qr)}dr \tag{6.3}$$

where $\rho_\alpha = \frac{N_\alpha}{V}$. N_α is the number of beads of type α and V is the volume of the system, δ is the Kronecker delta function and g(r) is the radial distribution function. The upper limit in the integral was replaced with half the box length. The total x-ray structure factor is defined as,

$$S(q) = \sum_\alpha \sum_\beta c_\alpha c_\beta \frac{f_\alpha(q) f_\beta(q)}{\langle f(q)\rangle^2} S_{\alpha\beta}(q) \tag{6.4}$$

where c_α is the concentration of bead type α in the system. f_α is the form factor (or scattering length) of bead α and $\langle f(q)\rangle = \sum_\alpha c_\alpha f_\alpha(q)$.

The minimum value of q in the simulations is set by the linear dimension of the simulation box. The box length for the three systems in our simulations ranged between 110Åand 120Å. Hence the minimum value of q is around 0.05 to 0.06 $Å^{-1}$.

Since the coarse grained beads correspond to more than one atom, the structure factor from simulations cannot be compared with experimental data at very large values of q. In

our CG model, the length scale of coarsening is approximately 3Å. Thus, the maximum value of q for which a comparison can be made is $\frac{2\pi}{3} \approx 2\text{Å}^{-1}$.

The x-ray form factors for the beads were obtained as the sum of the form factors of atoms that constitute the bead. Obviously, there is no formal manner to obtain the x-ray form factors and hence the suitability of this approach can only be gauged from the quality of the results it provides. The total neutron structure factor was obtained in a similar fashion, with the q-independent neutron scattering lengths of the beads replacing the form factors in Eq. 6.4. A similar procedure is followed to obtain scattering length densities of molecules (or groups of atoms) in the analysis of data in wide angle neutron scattering [20].

6.3 Results and discussion

Table 6.4 compares the density of the ionic liquids calculated from the coarse grained simulations with experiment. Under ambient conditions, the agreement with experiments is good, while at high pressures the maximum difference in density is less than 4%. At such pressures, the internal structure of the molecules would influence near neighbor intermolecular structure, and the lack of this fine structure in the CG model is the reason for the larger difference in density. The calculated surface tension at 300K of [bmim][PF_6] was 39 mN/m, compared to the experimental value of 42.5 mN/m [21].

In order to benchmark the capabilities of the CG model in predicting the intermolecular structure at short range, we have calculated the structure factor of the [bmim][PF_6] liquid. Shown in Figure 6.2 are the structure factors obtained from simulations weighted by appropriate bead form factors or scattering lengths. These are to be compared with the small angle scattering data of Triolo and coworkers [11]. In the range of wave vectors between 0.6 and 2.4Å^{-1}, two prominent features are observed – one at 1.45Å^{-1} and another at 0.98Å^{-1}. The CG model predicts a decreased intensity of the latter in the

Table 6.4: Comparison of the density ρ in units of kg/m^3, of the simulated ionic liquids with experiment at 300K.

System	Temperature [K]	Pressure [MPa]	Simulation	Experiment*	$\delta\rho$ [%]
[bmim][PF_6]	300.0	0.0	1365	1359	0.4
	343.2	0.0	1330	1324	0.4
	298.2	104.2	1439	1408	2.2
	298.2	202.1	1487	1438	3.4
	323.2	102.8	1426	1394	2.3
[C_7mim][PF_6]	300.0	0.0	1257	1257	0.0
[C_{10}mim][PF_6]	300.0	0.0	1186	1166	1.7

*: Ref. [22] for data on [bmim][PF_6]; [C_7mim][PF_6]: Interpolated value based on densities of [bmim][PF_6], [C_6mim][PF_6] and [C_8mim][PF_6] from Ref. [23]; [C_{10}mim][PF_6]: Extrapolated value based on densities of ILs with shorter tails [24].

x-ray structure factor relative to that in neutron scattering, in agreement with experiment. Partial structure factors between various pairs of bead types (not shown) indicates that correlations between alkyl tails and that between the tail and the anion contribute significantly to the 1.5Å^{-1} peak. Other contributions to this peak include the partial structure factors of the following pairs: I1-PF, I1-CT, PF-PF. The 0.98Å^{-1} feature arises from anion-anion and I1-I1 correlations, resembling the near-neighbor arrangement in the crystal [25]. This interpretation is in line with that of other simulations as well [4, 7]. The peaks in the structure factor obtained from simulations are narrower than those from experiments, again due to the fact that the internal structure of the real molecules allows the possibility of many more orientations of near neighbors than what is possible in the coarse grain model. Note however that the positions of the peaks obtained from simulation are quite close to the experimental results. Thus the agreement in the physical properties and the structure factor data to experiments allows us to place some level of confidence in the CG model.

We now move on to examine the structure factor obtained from simulations at smaller wave vectors, corresponding to length scales beyond 1 nm, for which purpose the coarse

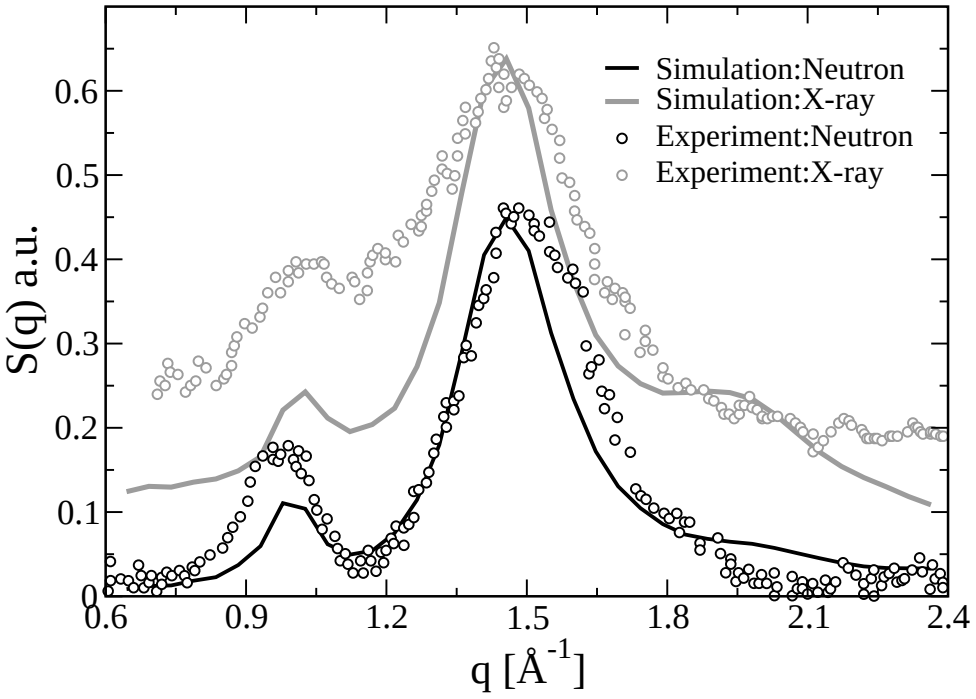

Figure 6.2: Comparison between neutron and x-ray scattering structure factors obtained from simulation [26] and experiment [11] for [bmim][PF_6] at 200K. Density of the simulated liquid is 1431 kg/m^3.

grained simulations were carried out. Figure 6.3 shows the total neutron structure factors for fully protiated [bmim][PF_6], [C_7mim][PF_6], and [C_{10}mim][PF_6] at small wave vectors. The resolution in wave vector as determined by the box lengths of the simulations, is less than 0.03Å^{-1}, and hence one can safely interpret any features beyond, say, 0.1Å^{-1} and not be worried that they could be due to truncation errors. We observe a peak at 0.29Å^{-1} in the structure factor of [C_{10}mim][PF_6] while that for [C_7mim][PF_6] shows a broad feature around 0.41Å^{-1}. These correspond to distances of 21.6Å and 15.3Å respectively. These correlations could arise from ordering of alkyl tails as well as from ordering of other species in the IL. Unlike the total S(q) for the fully protiated liquid, the neutron scattering structure factor for the perdeuterated [C_{10}mim][PF_6] does not exhibit the low wave vector peak, as the scattering lengths of all the beads are somewhat similar for a perdeuterated sample. In the inset to Figure 6.3, the x-ray scattering total structure factor is shown which exhibits features similar to those discussed for the neutron data for

the protiated sample.

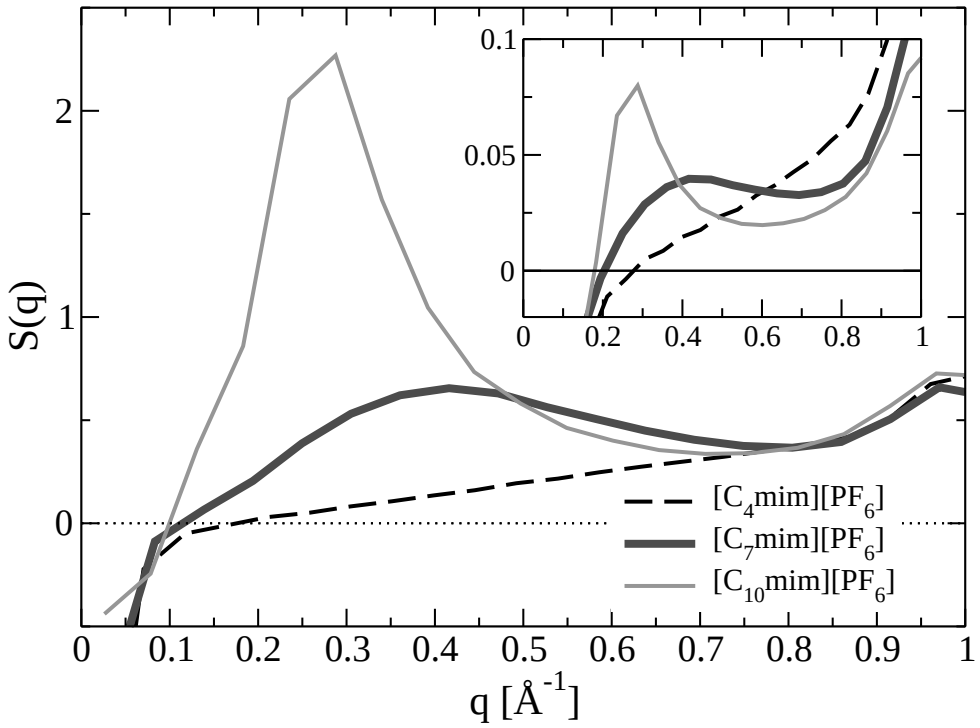

Figure 6.3: Neutron structure factor calculated from fully protiated ionic liquids at 300K. Inset: Calculated x-ray structure factor at 300K.

To understand the origin of the low angle feature, we examine the partial structure factors in Figure 6.4. It shows the unweighted partial structure factor between various pairs of bead types that are relevant to the discussion here for the IL, $[C_{10}mim][PF_6]$. At $0.29Å^{-1}$, one finds strong positive correlations for CT-CT, I1-I1, I1-PF, and PF-PF pairs, suggesting the existence of intermediate range order for these pairs. Such large positive correlations in the partial structure factors were also observed for $[C_7mim][PF_6]$ at $0.41Å^{-1}$.

Armed with the knowledge of the partial structure factors, we can now interpret the differences in the calculated total S(q) shown in Figure 6.3. The scattering lengths of beads belonging to the cation are much reduced by protiation relative to that in a perdeuterated liquid. However, the value for the anion remains unchanged. Hence, relative to the scattering from a deuterated sample, the contribution from the anion-anion partial S(q)

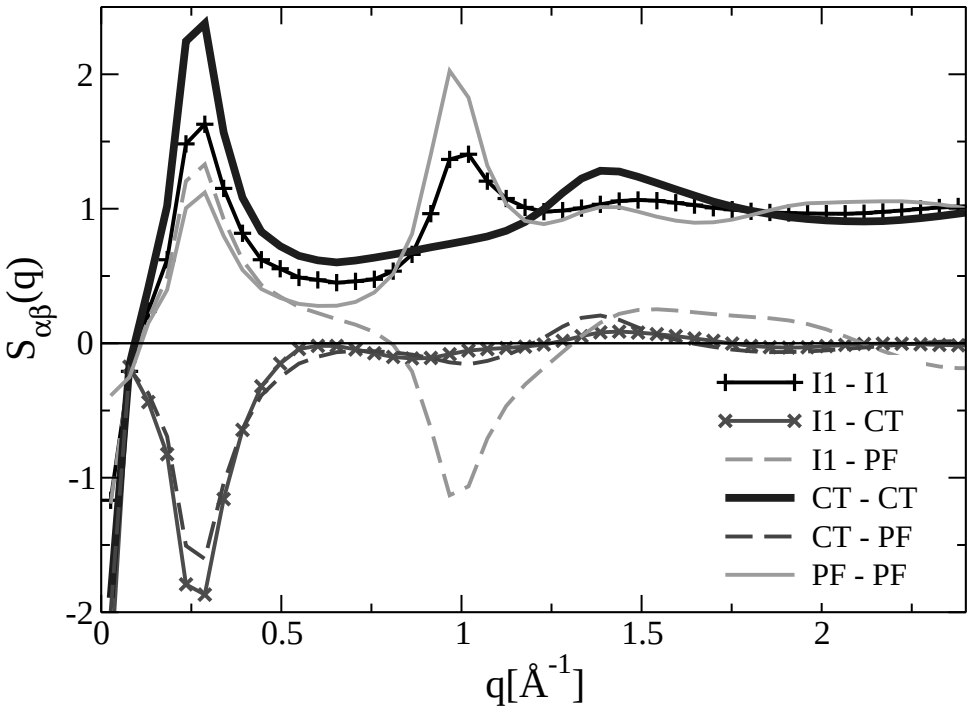

Figure 6.4: Partial structure factors of $[C_{10}mim][PF_6]$at 300K.

to the total neutron S(q) is enhanced leading to the increase in the peak height of the low wave vector peak in the fully protiated sample. Thus, although $S_{CT-CT}(q)$ has the largest peak height at 0.29Å^{-1} (Figure 6.4), it is $S_{PF-PF}(q)$ which contributes most to the feature as observed in wide angle x-ray or neutron scattering experiments on protiated samples.

The low angle feature in any of the partial structure factors of $[C_{10}mim][PF_6]$ occurs at the same wave vector, *viz* 0.29Å^{-1}. This fact indicates that the real space structure underlying this feature is likely to come from a collective organization or ordering of all the species involved and is unlikely to arise out of ordering between a pair of just a specific kind. The amplitude of the low angle feature in the total x-ray (neutron) structure factor is determined not only by the amplitude of the peak in the unweighted partial structure factors, but also by the respective bead form factors. To a first approximation, the latter are directly proportional to the number of electrons belonging to the bead. Thus, the PF anion by virtue of its 69 electrons, contributes the most to this feature in the total

x-ray structure factor shown in the inset to Figure 6.3. A simple verification of this hypothesis was carried out by replacing a selected partial pair correlation function with an uniform value of unity, and recalculating the total x-ray S(q). The low angle peak in the S(q) vanished when the PF-PF g(r) was thus altered, while it was nearly unchanged when the CT-CT or I1-I1 g(r) were modified. It can be concluded that the predominant contribution to x-ray scattering at these wave vectors comes from the ordering between anions.

As discussed before, the 0.29Å^{-1} peak in the total S(q) translates to a real space distance of 22.4Å. Given that the intramolecular distance between I1 and CT beads in [C_{10}mim][PF_6] is around 12Å, it is tempting to associate the feature with twice the molecular length. This idea is not far fetched when one examines the crystal structures of [$C_n$mim][PF_6] [9, 27]. In the crystal, anions are present in layers surrounded by 5 cation rings within 5.1Å. Sheets of anions are separated by the alkyl tails of the cation, and the interlayer distance in crystalline [C_{10}mim][PF_6] is 20.65Å which is very close to the correlation distance observed in our simulation [9, 27]. In the liquid, the PF-I1 coordination number at the minimum in their g(r) is 4.6, close to the value for the crystal. Shown in Figure 6.5a, is a snapshot from our simulations of a small region of the [C_{10}mim][PF_6] liquid. Two anions separated by a distance of about 22Å are shown, along with the beads present in their immediate neighborhood. The tails of the cation interdigitate with those from a neighboring "layer". The ionic liquid contains many such molecular level arrangements which contribute to the low angle peak in the structure factor. It is interesting to envisage the morphological implications of such a molecular organization. In Figure 6.5b, we show density isosurfaces of PF and CT beads. Their topology resembles a bicontinuous phase, one in which the polar moieties of the ionic liquid are located in regions distinct from the non-polar entities such as the CT bead. The respective regions are more or less continuous and span the entire simulation box. To summarize, the anion (or, non-polar) sheets that were ordered in the crystal can be

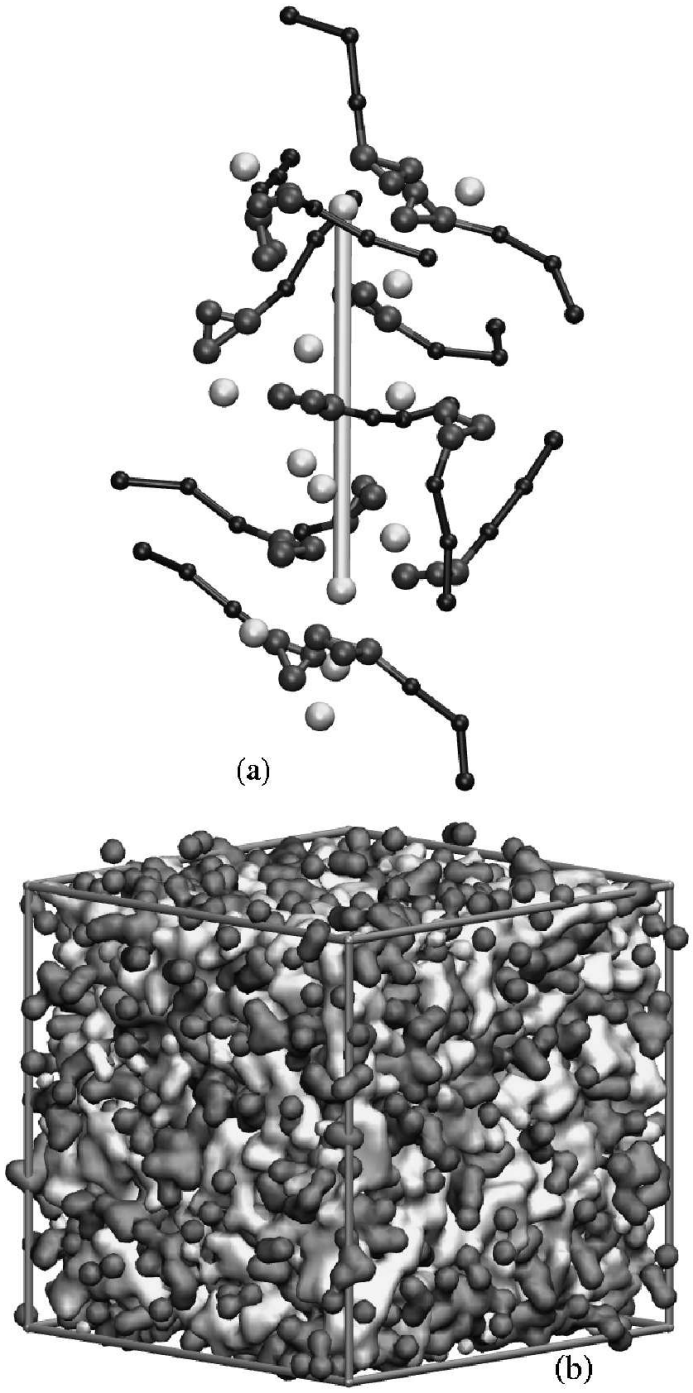

Figure 6.5: (a) Snapshot of a region from liquid [C_{10}mim][PF_6]. PF beads are in a light shade. Two of them separated by 22.1Å, are connected by a pseudo bond aligned vertical in the figure. Anions and cations present within a 8Å radius of this pseudo bond are shown, along with the cations present within the first coordination shell of the two anions. Beads belonging to the head group of the cation form a triangle, which are connected to the CM and CT beads that form the alkyl tail. Graphics created with VMD [28]. (b) Bicontinuous morphology of liquid [C_{10}mim][PF_6]. Light and dark shades represent density isosurfaces of PF and CT beads, at a value of 0.0019 beads/Å^3, which is the mean density in the liquid. The length of the simulation box edge is 120.172Å.

visualized as being disordered in the liquid state.

6.4 Discussion and conclusions

We have presented a new coarse grained model for simulations of the family of ionic liquids, 1-*n*-alkyl-3-methylimidazolium hexafluorophosphate. The model has been employed to study the intermolecular and intermediate range structure in such liquids. Simulations show the existence of a bicontinuous morphology in the liquid, whose character is influenced by the length of the alkyl group. The molecular origin of this behavior lies in the formation of disordered or winding sheets of anions between which the interdigitated alkyl groups are sandwiched. The nanoscale ordering leads to a prominent feature in the structure factor which can be captured in both wide angle neutron and x-ray scattering experiments. Although several partial structure factors possess this strong feature at low wave vectors, the correlation between anions appears to dominantly contribute to the low angle peak observed in such experiments. These results are consistent with other simulations [4–7] as well as recent x-ray scattering experiments on similar ionic liquids [8]. Neither wide angle x-ray nor neutron scattering experimental data are available for the specific ionic liquids simulated here. We hope that our results on the intermediate range ordering as well as the insights offered for the observed differences in the structure factor with protiation or deuteration will be borne out by future experiments.

It is pertinent to note that the crystal of the ionic liquid is a lamellar phase, while the liquid is bicontinuous, and possibly more phases could exist, particularly in ionic liquids possessing longer alkyl tails.

Bibliography

[1] C.G. Hanke, S.L. Price and R.M. Lynden-Bell, *Mol. Phys.*, **99**, 801 (2001).

[2] C. Hardacre, J.D. Holbrey, S.E.J. McMath, D.T. Bowron and A.K. Soper, *J. Chem. Phys.*, **118**, 273 (2003).

[3] C.J. Margulis, H.A. Stern and B.J. Berne, *J. Phys. Chem. B*, **106**, 12017 (2002).

[4] S.M. Urahata and M.C.C. Rebeiro, *J. Chem. Phys.*, **120**, 1855 (2004).

[5] Y. Wang and G.A. Voth, *J. Am. Chem. Soc.*, **127**, 12192 (2005).

[6] Y. Wang and G.A. Voth, *J. Phys. Chem. B*, **110**, 18601 (2006).

[7] J.N.A. Canongia Lopes and A.A.H. Padua, *J. Phys. Chem. B*, **110**, 3330 (2006).

[8] A. Triolo, O. Russina, H.-J. Bleif and E. Di Cola, *J. Phys. Chem. B*, **111**, 4641 (2007).

[9] C.M. Gordon, J.D. Holbrey, A.R. Kennedy and K.R. Seddon, *J. Mater. Chem.*, **8**, 2627 (1998).

[10] Z.H. Li, Z.M. Liu, Z.L. Zhang, B.X. Han, J.M. Du, Y.N. Gao and T. Jiang, *J. Phys. Chem. B*, **109**, 14445 (2005).

[11] A. Triolo, A. Mandanici, O. Russina, V. Rodriguez-Mora, M. Cutroni, C. Hardacre, M. Nieuwenhuyzen, H.-J. Bleif, L. Keller and M.A. Ramos, *J. Phys. Chem. B*, **110**, 21357 (2006).

[12] C. Hardacre, S.E.J. McMath, M. Nieuwenhuyzen, D.T. Bowron and A.K. Soper, *J. Phys. Condens. Matt.*, **15**, S159 (2003).

[13] M. Kanakubo, T. Umecky, Y. Hiejima, T. Aizawa, H. Nanjo and Y. Kameda, *J. Phys. Chem. B*, **109**, 13847 (2005).

[14] P. Mandal, M. Sarkar, A. Samanta, *J. Phys. Chem. A*, **108**, 9048 (2004); Z.H. Hu and C.J. Margulis, *Proc. Nat. Acad. Sci.*, **103**, 831 (2006).

[15] B.L. Bhargava and S. Balasubramanian, *J. Phys. Chem. B*, **111**, 4477 (2007).

[16] B.L. Bhargava and S. Balasubramanian, *J. Chem. Phys.*, **127**, 114510 (2007).

[17] W. Shinoda, R. Devane and M.L. Klein, *Mol. Sim.*, **33**, 27 (2007).

[18] K.J. Miller, *J. Am. Chem. Soc.*, **112**, 8533 (1990).

[19] S.J. Plimpton, *J. Comp. Phys.*, **117**, 1 (1995). Web: http://lammps.sandia.gov

[20] Small Angle Neutron Scattering tutorials at: http://www.ncnr.nist.gov/programs/sans/tutorials/inde

[21] E. Sloutskin, B.M. Ocko, L. Tamam, I. Kuzmenko, T. Gog and M. Deutsch, *J. Am. Chem. Soc.*, **127**, 7796 (2005).

[22] Z. Gu and J.F. Brennecke, *J. Chem. Eng. Data*, **47**, 339 (2002).

[23] K.R. Seddon, A. Stark and M.J. Torres, *Clean Solvents ACS Symposium Series*, **819**, 34 (2002).

[24] S. Chun, S.V. Dzyuba and R.A. Bartsch, *Anal. Chem.*, **73**, 3737 (2001).

[25] A.R. Choudhury, N. Winterton, A. Steiner, A.I. Cooper and K.A. Johnson, *J. Am. Chem. Soc.*, **127**, 16792 (2005). S.M. Dibrov and J.K. Kochi, *Acta Cryst. C*, **62**, o19 (2006).

[26] To compare with wide angle scattering experiments, a parabolic function in wave vector [29] has been subtracted from the S(q) obtained from simulation.

[27] W.M. Reichert, J.D. Holbrey, R.P. Swatloski, K.E. Gutowski, A.E. Visser, M. Nieuwenhuyzen, K.R. Seddon and R.D. Rogers, *Cryst. Growth Des.*, **7**, 1106 (2007).

[28] W. Humphrey, A. Dalke and K. Schulten, VMD: Visual Molecular Dynamics, *J. Mol. Graph.*, **14**, 33 (1996).

[29] L. Hennet, I. Pozdnyakova, A. Bytchkov, V. Cristiglio, P. Palleau, H.E. Fischer, G.J. Cuello, M. Johnson, P. Melin, D. Zanchi, S. Brassamin, J.-F. Brun, D.L. Price and M.-L. Saboungi, *Rev. Sci. Instrum.*, **77**, 053903 (2006).

Chapter 7

Probing Anion-Carbon dioxide Interactions in Room Temperature Ionic Liquids: Gas Phase Cluster Calculations

7.1 Introduction

Room temperature ionic liquids (RTILs) are currently being investigated as alternate chemical reaction media due to their ability to solvate a wide variety of compounds, and to their benign environmental attributes [1–3]. As RTILs possess a low vapor pressure, distillation may not be an easy route to extract products of a chemical reaction conducted in them [4]. However, supercritical CO_2 ($scCO_2$) has been found to be able to extract such products from ILs [5]. CO_2 is highly soluble in many of the RTILs but RTILs are almost insoluble in the CO_2 phase [5]. Since these early results, several experimental studies [6–8] have been carried out to determine the phase behavior of these mixtures. In addition, x-ray scattering [9], vibrational spectroscopy [10], and solvatochromic shift experiments [11,

12] have explored the specific interactions in the IL-CO_2 mixtures that contributes to the high solubility of CO_2. The effect of anions of RTILs on the solubility of different gases in general [7] and of CO_2 in particular [6] have been studied by Brennecke and coworkers. These studies have concluded that the nature of anion influences the solubilities of gases in ILs, rather than the cation. This conclusion and also the computational studies [14–16] on ionic liquid-CO_2 mixtures substantiates the earlier findings of vibrational spectroscopic studies by Kazarian *et al* [10, 13]. Computational studies [14–16] on ionic liquid-CO_2 mixtures. Earlier works have also highlighted the role of Lewis acid-base interaction in complexes involving CO_2 [17,18]. Gas phase calculations on the geometrical and electronic structure have also examined the interactions between cations and anions constituting several ionic liquids [19–22]. Studies on the interaction of CO_2 with ionic liquids also gain importance in light of the recent synthesis of ILs in scCO_2 medium [23].

The geometries of the interacting anion-CO_2 pairs and the relationship between the interaction strength and solubility has not been explored yet. In this Letter, we report density functional theory (DFT) based zero Kelvin calculations that explore minimum energy structures of several anion-CO_2 pairs in gas phase. Anticipating our results, we find that among ILs containing fluorinated anions, the solubility of CO_2 is inversely proportional to the anion-CO_2 binding energy. The distortion in the geometry of CO_2 due to this interaction and its consequence on the vibrational modes of CO_2 are also discussed.

In chapter 4 we have discussed the structure and dynamics in [bmim][PF_6] - CO_2 mixture. Since it is difficult to carry out bulk simulations on all the ionic liquids with CO_2, we have chosen to study them through *ab initio* gas phase calculations that are presented in this chapter.

7.2 Simulation details

Structure optimizations of 14 different anions each with a single CO_2 molecule were carried out within DFT using the CPMD code [24]. The anions used for the study were fluo-

ride (F^-), chloride (Cl^-), bromide (Br^-), iodide (I^-), nitrate (NO_3^-), tetrafluoroborate (BF_4^-), perchlorate (ClO_4^-), acetate (CH_3COO^-), trifluoroacetate (CF_3COO^-), hexafluorophosphate (PF_6^-), dicyanamide ($[N(CN)_2]^-$), trifluoromethanesulphonyl ($[CF_3SO_3]^-$), bis-(trifluoromethylsulphonyl)imide, ($[N(CF_3SO_2)_2]^-$) and methide ($[C(CF_3SO_2)_3]^-$).

For each of the anion, three or four initial configurations were constructed for geometry optimization, in each of which the CO_2 molecule was placed at a different location around the anion. In this manner, we were able to explore the potential energy surface better. The structures and binding energies reported here are those corresponding to the lowest energies. The calculations were carried out under isolated conditions. Norm conserving pseudopotentials of the Trouiller-Martins form [25] were employed to treat the effect of core electrons. Gradient corrected exchange and correlation functionals prescribed by Becke [26] and Lee, Yang, Parr [27] respectively were employed. A plane wave energy cutoff of 90 Ry was used. We have recently reported results of ab initio molecular dynamics simulations on the intermolecular structure of an important IL, [bmim][PF_6] and its solution with CO_2 using similar procedures as adopted here [16]. Cluster boundary conditions [28] and a Hockney Poisson solver [29] consistent with calculations for an isolated system were employed. However, the use of plane waves as basis set requires the use of a simulation box. Here, we used a cubic box of edge length 15Å for all ion-CO_2 pairs except for the methide and bis-(trifluoromethylsulphonyl)imide (Tf_2N), for which a 16Å box was used, that is larger than the largest extent of the molecular pairs. The binding energy of each pair was obtained by subtracting the total energy of the isolated anion and that of an isolated CO_2 molecule from the total energy of the pair. Harmonic frequencies were obtained by performing the vibrational analysis using a finite difference method on the minimum energy configurations of the anion-CO_2 pair. The vibrational modes so obtained were visualized using Molden [30] for assignment.

In order to verify the invariance of the properties of interest as a function of box length, we performed additional calculations on the trifluoroacetate-CO_2 pair in boxes of

different lengths ranging from 13-17Å. These calculations showed that the the binding energy and the frequency split were converged for the value of the box length used in the simulations. Similar calculations were also carried out for the methide-CO_2 pair (the pair that is largest in size) with varying boxlengths ranging from 14 to 18Å in steps of 1Å to confirm the convergence of the binding energy.

For the sake of comparison, structure optimization and subsequent frequency calculations were carried out for some of the anion-CO_2 pairs at MP2 (Moller-Plasset perturbation) level with 6-311+G* basis set using the Gaussian 03 software [31].

7.3 Results and discussions

Of all the anions studied, only fluoride was found to spontaneously react with the CO_2 molecule to form FCO_2^-, with a F-C distance of 1.585Å. This distance is larger compared to the average F-C bond length of 1.355Å in carbon tetrafluoride, yet the formation of a chemical bond was clear. The CO_2 entity in the complex was highly distorted from linearity with a O-C-O angle of 139.4 degrees. The binding energy of the complex was found to be -118.3 kJ/mol. The complex had a distorted planar trigonal structure. The CO_2 molecule was found to bend away from the F^- ion so that the interaction between the electronegative fluorine and the oxygens is minimized.

A systematic trend in the distance of the carbon from the ion, the OCO angle, and the binding energy was observed in CO_2 - halide complexes as can be seen from Table 7.1. The anion-carbon distance and the OCO angle increase with increasing halogen size, while the binding energy decreases. The structure optimized configuration for the chloride-CO_2 dimer is shown in Figure 7.1. The geometry of the dimer was similar in the case of other halogen anions except for the C-X distance and the OCO angle. All the monoatomic anions were found to lie in the plane of the CO_2 molecule. The latter was bent away from the anions so as to minimize the repulsive interaction of the oxygen atoms with the halide ions.

Table 7.1: Data obtained from optimized geometries of CO_2 - anion complexes. The nearest distance of CO_2 from the anion in the corresponding complex, the OCO angle, the binding energy of the complex and the frequency split in the CO_2 bending mode upon complexation as determined through a Hessian analysis are shown. Values in brackets are obtained from MP2 calculations using 6-311+G* basis set.

Anion	Minimum distance(Å)	OCO angle (degrees)	Binding energy (kJ/mol)	Frequency split (cm^{-1}) (Bending mode of CO_2)
F^-	1.59 (1.59)	139.4 (139.4)	-118.3 (-82.8)	28.5 (63.2)
Cl^-	2.75	162.2	-26.9	97.0
Br^-	3.09	167.6	-20.7	97.3
I^-	3.50	171.8	-15.0	68.0
NO_3^-	2.79 (2.75)	171.2 (172.6)	-24.8 (-25.9)	32.3 (37.7)
BF_4^-	2.90 (2.77)	175.0 (175.1)	-19.9 (-18.8)	13.4
ClO_4^-	3.08	175.6	-14.5	18.4
CH_3COO^-	2.39	163.0	-35.0	104.9
CF_3COO^-	2.72 (2.75)	171.4 (172.7)	-23.8 (-25.4)	55.3 (36.1)
PF_6^-	3.01 (2.80)	176.3 (176.1)	-14.2 (-13.8)	12.5 (16.4)
$[N(CN)_2]^-$	3.55	177.2	-9.0	4.0
$CF_3SO_3^-$	3.09 (2.91)	175.3 (175.4)	-14.6 (-17.7)	21.8
$[N(CF_3SO_2)_2]^-$	3.06	176.8	-9.9	21.6
$[C(CF_3SO_2)_3]^-$	3.10	177.3	-5.6	17.5

The other anions that exhibited a greater affinity towards CO_2 molecules were acetate, chloride, nitrate and trifluoroacetate, in the order of decreasing bind energies. The extent of distortion of CO_2 from a linear geometry upon complexation was found to be roughly proportional to the binding energy. Not unexpectedly, the frequency split of the bending mode of CO_2 is also found to vary linearly with the deviation in the angle of CO_2 from linearity. These are presented in Figure 7.2. In the case of anions based on the trifluoromethylsulphonyl group, the binding energy for the anion-CO_2 dimer decreases with the number of such groups present in the anion that can be observed from Table 7.1. Not surprisingly, the extent of distortion in the geometry of the CO_2 molecule shows the same trend.

Minimum energy geometries of CO_2 with different anions are displayed in Figure 7.3.

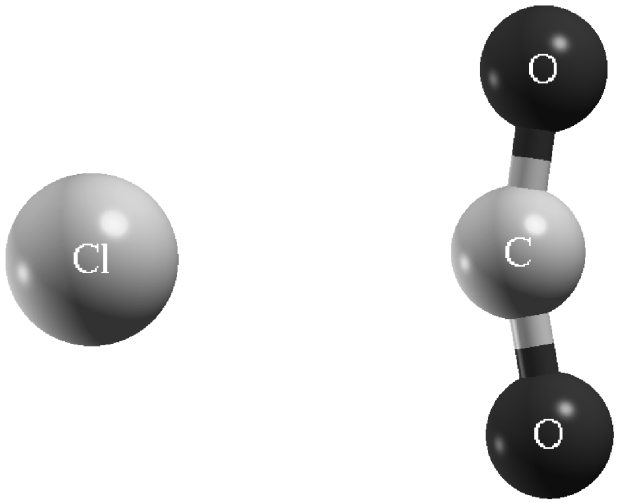

Figure 7.1: Minimum energy structure for the chloride-CO_2 dimer.

In the complex with nitrate, CO_2 is located such that it is equidistant from the two oxygens of the nitrate ion. CO_2 is perpendicular to the plane of the nitrate anion, with the carbon of CO_2 lying in the plane of the anion. Also, the oxygens of the CO_2 are bent outwards to reduce the repulsive interaction with the electronegative oxygens of nitrate ion. The minimum energy structures of CO_2 interacting with several polyatomic anions show some similarities. In the tetrafluoroborate-CO_2 complex (Figure 7.3b), the carbon of CO_2 lies in the plane formed by two BF bond vectors and the CO_2 molecule is perpendicular to this plane just as in the case of nitrate ion. The minimized structure of perchlorate ion with CO_2 was similar to that of the BF_4-CO_2 complex. Similar principles influence the structure of the PF_6-CO_2 complex shown in Figure 7.3e. In the case of the dicyanamide-CO_2 dimer, the carbon of CO_2 is out of the plane of dicyanamide by 2.2^o (Figure 7.3c). CO_2 location with respect to acetate (Figure 7.3d) is similar to that in the nitrate complex. However, the distortion in its OCO angle is larger. The structure of the trifluoroacetate-CO_2 complex is similar to that of acetate and hence is not shown.

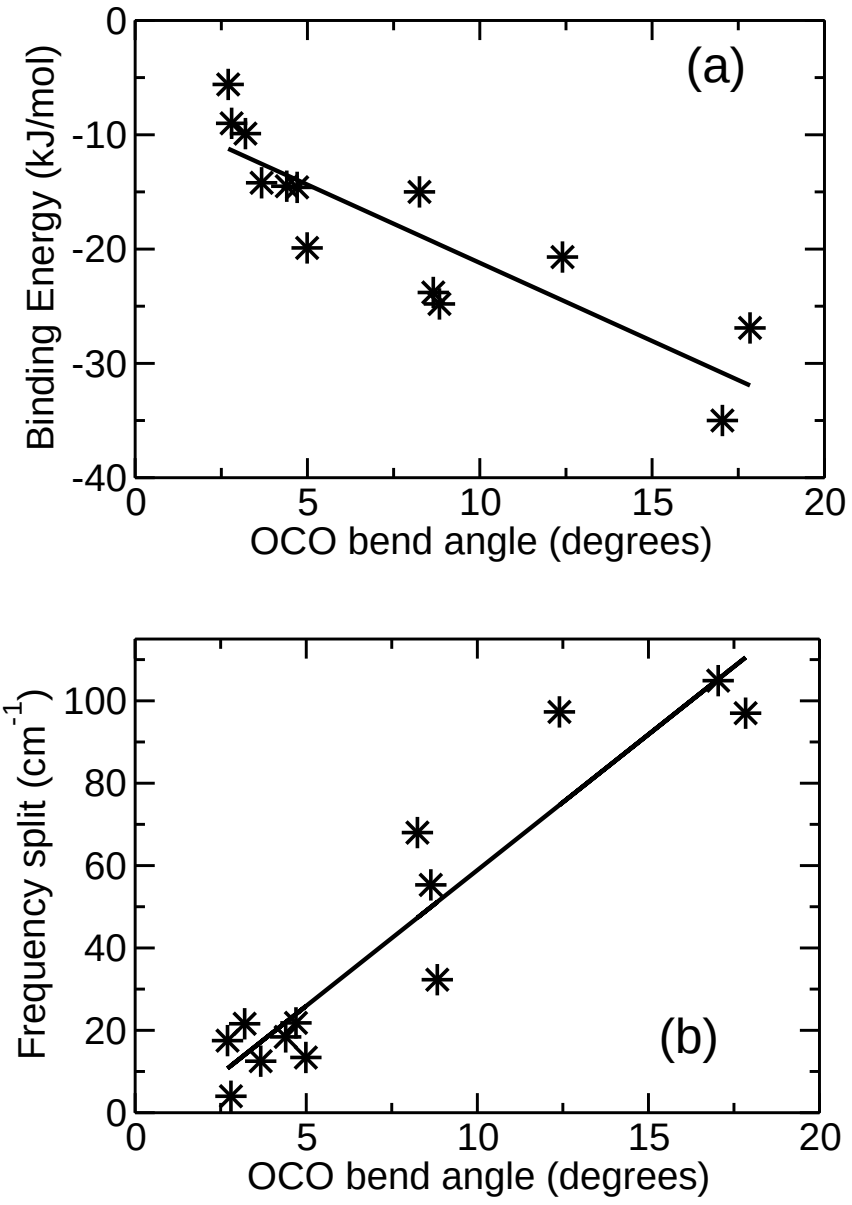

Figure 7.2: (a) Binding energy of the anion-CO_2 dimer vs. the deviation of OCO angle of CO_2 molecule from 180^o in various complexes. The fluoride-CO_2 dimer is excluded since the fluoride was found to chemically bond with CO_2. Stars represent various anions. The continuous line is the best linear fit to the data. (b) Same as (a), but with the extent of frequency split in the bending mode of CO_2 as the y-axis.

The geometry of the complex with bulky anions like Tf_2N is similar to the ones with lighter anions. The preferred site for CO_2 is near the SO_2 group of the anion that can be seen in Figure 7.3f. The dimer showed a minimum energy with the CO_2 molecule orienting perpendicular to the plane formed by two SO bonds and the carbon lying on that plane, that is similar to that observed for the acetate ion. Trifluoromethanesulphonyl and methide ions that have one and three such SO_2 groups also exhibit minimum energy configurations in which the CO_2 is located around the SO_2 group and the orientation is exactly as in Tf_2N.

Presented in Table 7.1 are the distance of the CO_2 molecule to the nearest atom of the anion, the OCO angle of CO_2, binding energy of the dimer and the calculated frequency split of the CO_2 bending mode.

The optimized structures of anion-CO_2 complexes appear to be dominated by Lewis acid-base interactions, with the carbon atom of CO_2 as the electron acceptor (acid) and the anion as the donor (base). This interaction leads to varying degrees of distortion of the CO_2 molecule. The extent of bending of CO_2 will be a measure of the basicity of the anion. The magnitudes of bending of CO_2 in BF_4^- and PF_6^- complexes qualitatively agrees with the spectroscopic results of Kazarian and coworkers [10]. Leaving the fluoride ion that forms a complex with CO_2 the binding energy decreases in the following order: acetate, chloride, nitrate, trifluoroacetate, and bromide. In gas phase, the ν_2 bending mode of CO_2 is doubly degenerate. The doublet observed in the complexes studied here arises due to the deviation of the CO_2 geometry from linearity, and can be ascribed to in plane and out of plane bending modes.

Experimentally obtained solubility data of CO_2 in ILs [6] suggests a relationship between the molar volume of the anion and the solubility. The latter increases with the increase in the molar volume of the anion for the ILs based on the [bmim] cation and different anions presented in Figure 7.4. The studies of Anthony *et al* [7] too suggests the role of entropy in the solubility of CO_2 and other gases in the RTILs.

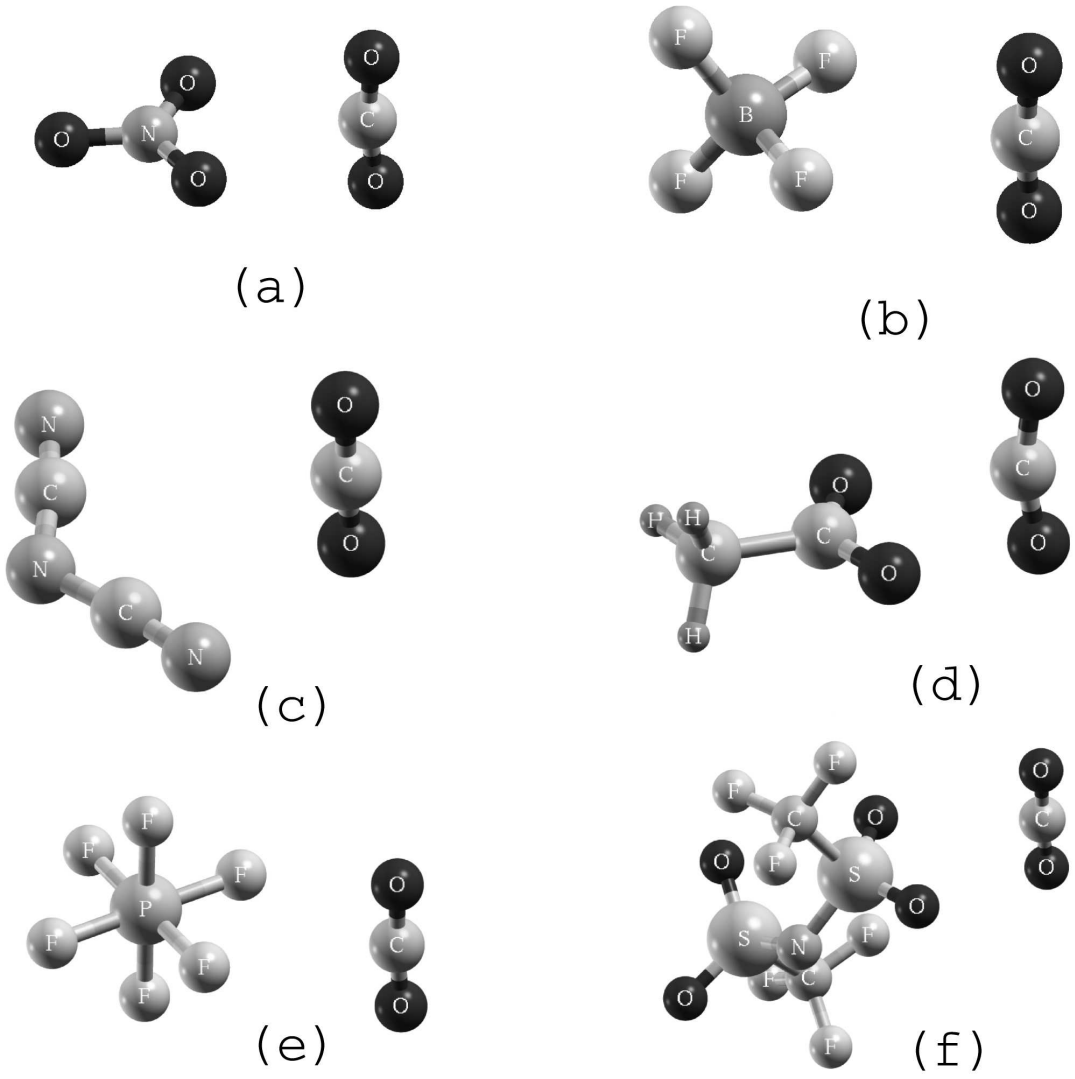

Figure 7.3: Minimum energy structure of different anion-CO_2 complexes. (a) NO_3^-, (b)BF_4^-, (c)$[N(CN)_2]^-$, (d) CH_3COO^-, (e) PF_6^- and (f) $[N(CF_3SO_2)_2]^-$.

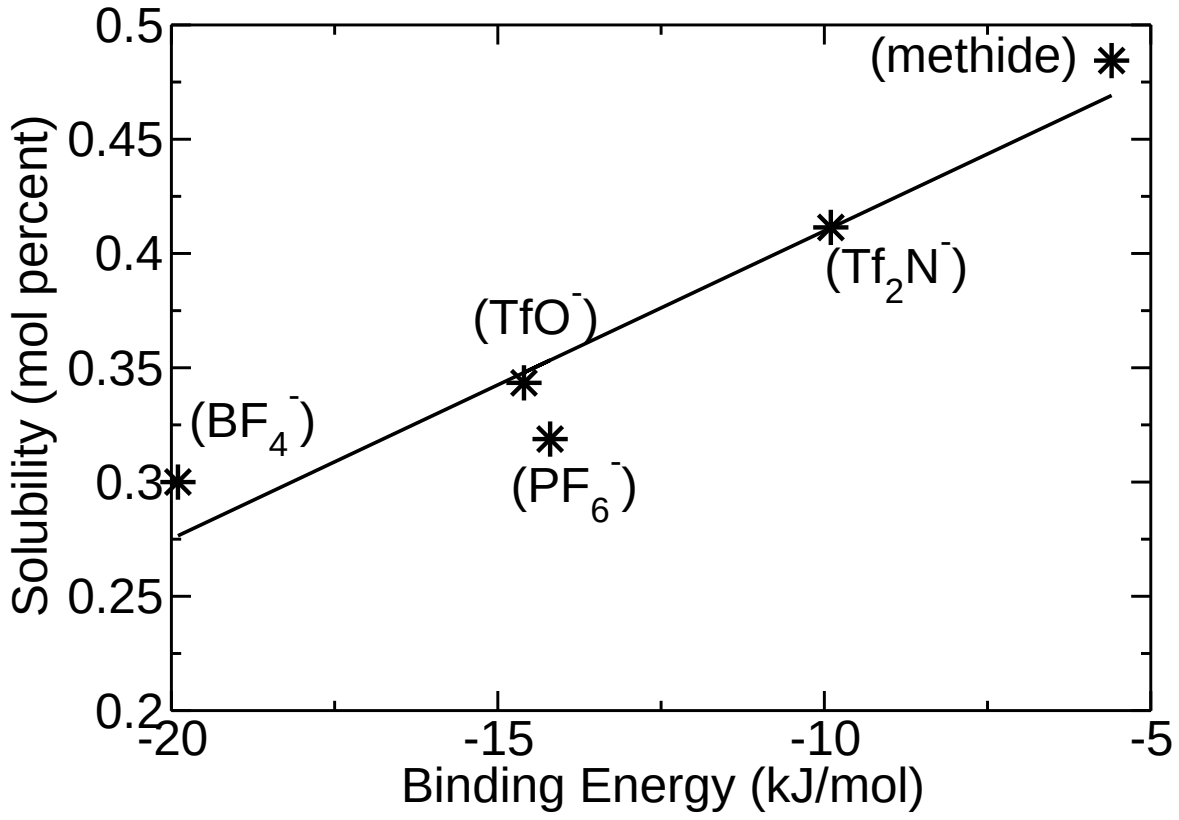

Figure 7.4: Variation of experimentally measured [6] solubility of CO_2 in ionic liquids containing different fluorinated anions and the same cation ([bmim]), at 298K and 20.7 bar, against the binding energy of the corresponding anion - CO_2 dimer calculated in this work. The continuous line is the best linear fit to the data.

Recent measurements on the solubility of CO_2 in ionic liquids that contain the same cation [bmim], but with different anions have shown the following sequence of increasing solubility: tetrafluoroborate, hexafluorophosphate, trifluoroacetate, acetate, bis(trifluoromethylsulphonyl)imide and methide [6]. In Figure 7.4, we show a plot of the mole fraction of CO_2 at 298K and 20 bar in fluorinated ILs as reported in Ref. [6] versus the binding energies of CO_2 with anions of such ILs calculated in our work. Within this data set, we observe increasing levels of CO_2 solubility with decreasing binding energies. Needless to state, pair energies alone may not determine CO_2 solubility [32] and hence the correlation observed here may be fortuitous; such a trend in solubility also correlates with increasing molecular size of the anion. Monte Carlo simulations [33] can be performed

to calculate the solubility of CO_2 in these ILs. These could allow one to distinguish the contributions from molecular size and anion-CO_2 binding towards solubility. It should also be noted that the larger anions such as Tf_2N and methide possess two or three preferred sites for binding CO_2 that could also play an important role in their ability to dissolve larger amounts of CO_2.

Results from MP2 level calculations using 6-311/G* basis set for six of the anion - CO_2 clusters exhibited similar qualitative characteristics in quantities such as the binding energy and the frequency split (calculated for four anion-CO_2 clusters) in the bending mode of CO_2 compared to the DFT-BLYP calculations. Except for the case of fluoride-CO_2 that was found to undergo a reaction, the binding energies predicted by MP2 level calculations are comparable to the DFT study. Optimized structures obtained by the two methods resulted in similar geometries (as discussed above in the case of DFT calculations), further strengthening our observations.

7.4 Conclusions

The interaction of CO_2 molecules with various anions used in many RTILs have been studied using density functional theory. The optimized geometries point to the role of Lewis acid-base type of interaction between CO_2 and the anions, whose strength was found to be directly proportional to the basicity of the anion. Such an interaction also distorts the CO_2 molecule away from linearity, in turn lifting the degeneracy of its bending mode. The difference in the calculated frequencies of the bending modes agrees qualitatively with infrared spectroscopic data [10]. In the case of halides, the interaction strength decreases with increasing size of the anion. In complexes containing multi-nuclear anions studied here, CO_2 prefers the location near the anion in which its carbon atom can interact with two electronegative atoms of the anion. This location and orientation was found to be the minimum energy configuration for all the polyatomic anions studied here. The binding energy of CO_2 complexing with fluorinated anions is found to be inversely correlated with

the experimentally measured solubilities of CO_2 in ILs containing such anions. We believe that the number of preferred locations for the CO_2 to be present near the anion may also influence its solubility.

Ab initio calculations on selected anion-CO_2 pairs performed at a higher level of theory (MP2 level) qualitatively agree with our conclusions.

Bibliography

[1] T. Welton, *Chem. Rev.*, **99**, 2071 (1999).

[2] M.J. Earle, K.R. Seddon, *Pure Appl. Chem.*, **72**, 1391 (2000).

[3] R.A. Sheldon, *Green Chemistry*, **7**, 267 (2005).

[4] M.J. Earle, J.M.S.S. Esperanca, M.A. Gilea, J.N.C. Lopes, L.P.N. Rebelo, J.W. Magee, K.R. Seddon, J.A. Widegren, *Nature*, **439**, 831 (2006).

[5] L.A. Blanchard, D. Hancu, E.J. Beckman, J.F. Brennecke, *Nature*, **399**, 28 (1999).

[6] S.N.V.K. Aki, B.R. Mellein, E.M. Saurer, J.F. Brennecke, *J. Phys. Chem. B*, **108**, 20355 (2004).

[7] J.L. Anthony, J.L. Anderson, E.J. Maginn, J.F. Brennecke, *J. Phys. Chem. B*, **109**, 6366 (2005).

[8] Y.S. Kim, W.Y. Choi, J.H. Jang, K.P. Yoo, C.S. Lee, *Fluid Phase Equilib.*, **228-229**, 439 (2005).

[9] M. Kanakubo, T. Umecky, Y. Hiejima, T. Aizawa, H. Nanjo, Y. Kameda, *J. Phys. Chem. B.*, **109**, 13847 (2005).

[10] S.G. Kazarian, B.J. Briscoe, T. Welton, *Chem. Commun.*, 2047 (2000).

[11] J. Lu, C.L. Liotta, C.A. Eckert, *J. Phys. Chem. A*, **107**, 3995 (2003).

[12] C.P. Fredlake, M.J. Muldoon, S.N.V.K. Aki, T. Welton, J.F. Brennecke, *Phys. Chem. Chem. Phys.*, **6**, 3280 (2004).

[13] L. Cammarata, S.G. Kazarian, P.A. Salter, T. Welton, *Phys. Chem. Chem. Phys.*, **3**, 5192 (2001).

[14] C. Cadena, J.L. Anthony, J.K. Shah, T.I. Morrow, J.F. Brennecke, E.J. Maginn, *J. Am. Chem. Soc.*, **126**, 5300 (2004).

[15] X. Huang, C.J. Margulis, Y. Li, B.J. Berne, *J. Am. Chem. Soc.*, **127**, 17842 (2005).

[16] B.L. Bhargava, S. Balasubramanian, *J. Phys. Chem. B*, **111**, 4477 (2007).

[17] J.C. Meredith, K.P. Johnston, J.M. Seminario, S.G. Kazarian, C.A. Eckert, *J. Phys. Chem. A*, **100**, 10837 (1996).

[18] P. Raveendran, Y. Ikushima, S.L. Wallen, *Acc. Chem. Res.*, **38**, 478 (2005).

[19] P.A. Hunt, *Mol. Sim.*, **32**, 1 (2006).

[20] P.A. Hunt, B. Kirchner, T. Welton, *Chem. Eur. J.*, **12**, 6762 (2006).

[21] S. Tsuzuki, H. Tokuda, K. Hayamizu, M. Watanabe, *J. Phys. Chem. B*, **109**, 16474 (2005).

[22] Y. Wang, H. Li, S. Han, *J. Chem. Phys.*, **124**, 044504 (2006).

[23] W. Wu, W. Li, B. Han, Z. Zhang, T. Jiang, Z. Liu, *Green Chem.*, **7**, 701 (2005).

[24] J. Hutter, P. Ballone, M. Bernasconi, P. Focher, E. Fois, S. Goedecker, D. Marx, M. Parrinello, and M.E. Tuckerman, CPMD Version 3.11.1, Max Planck Institut fuer Festkoerperforschung, Stuttgart, and IBM Zurich Research Laboratory, 1990-2007.

[25] N. Troullier, J.L. Martins, *Phys. Rev. B*, **43**, 1993 (1991).

[26] A.D. Becke, *Phys. Rev. A*, **38**, 3098 (1988).

[27] C. Lee, W. Yang, R.G. Parr, *Phys. Rev. B*, **37**, 785 (1988).

[28] R.N. Barnett, U. Landman, *Phys. Rev. B*, **48**, 2081 (1993).

[29] R. W. Hockney, *Methods Comput. Phys.*, **9**, 136 (1970).

[30] G. Schaftenaar, J.H. Noordik, *J. Comput.-Aided Mol. Design*, **14**, 123 (2000).

[31] Gaussian 03, Revision C.02, M.J. Frisch, G.W. Trucks, H.B. Schlegel, G.E. Scuseria, M.A. Robb, J.R. Cheeseman, J.A. Montgomery, Jr., T. Vreven, K.N. Kudin, J.C. Burant, J.M. Millam, S.S. Iyengar, J. Tomasi, V. Barone, B. Mennucci, M. Cossi, G. Scalmani, N. Rega, G.A. Petersson, H. Nakatsuji, M. Hada, M. Ehara, K. Toyota, R. Fukuda, J. Hasegawa, M. Ishida, T. Nakajima, Y. Honda, O. Kitao, H. Nakai, M. Klene, X. Li, J. E. Knox, H.P. Hratchian, J.B. Cross, C. Adamo, J. Jaramillo, R. Gomperts, R.E. Stratmann, O. Yazyev, A.J. Austin, R. Cammi, C. Pomelli, J.W. Ochterski, P.Y. Ayala, K. Morokuma, G.A. Voth, P. Salvador, J.J. Dannenberg, V.G. Zakrzewski, S. Dapprich, A.D. Daniels, M.C. Strain, O. Farkas, D.K. Malick, A.D. Rabuck, K. Raghavachari, J.B. Foresman, J.V. Ortiz, Q. Cui, A.G. Baboul, S. Clifford, J. Cioslowski, B.B. Stefanov, G. Liu, A. Liashenko, P. Piskorz, I. Komaromi, R.L. Martin, D. J. Fox, T. Keith, M.A. Al-Laham, C.Y. Peng, A. Nanayakkara, M. Challacombe, P.M.W. Gill, B. Johnson, W. Chen, M.W. Wong, C. Gonzalez, and J.A. Pople, Gaussian, Inc., Wallingford CT, 2004.

[32] P. Raveendran, S.L. Wallen, *J. Phys. Chem. B*, **107**, 1473 (2003).

[33] J.K. Shah, E.J. Maginn, *J. Phys. Chem. B*, **109**, 10395 (2005).

Chapter 8

A molecular dynamics study of CO_2 - [bmim][PF_6] mixture: Effect of CO_2 concentration

8.1 Introduction

Room temperature ionic liquid (RTIL) - CO_2 mixtures have been studied previously from the microscopic perspective in order to understand molecular level interactions [1]. By observing the effects of varying the anion among different ionic liquids (ILs), Maginn and coworkers [1] have shown that anion influences solubility of CO_2 in ionic liquids to a greater extent compared to cation. In a pioneering work, the nature of anion-CO_2 interaction has been probed using vibrational spectroscopy by Kazarian *et al* [2]. They report a weak Lewis acid-base interaction between CO_2 and anions of the ILs. Computer simulation studies have demonstrated that CO_2 occupies pre-existing void spaces in the IL that reorganize to accommodate CO_2 [3], which accounts for the negligible increase in the molar volume of the mixture compared to pure ILs at low concentration of CO_2. X-ray diffraction experiments were carried out by Kanakubo and coworkers [4] to examine the

intermolecular structure of the solution, in particular the location and orientation of the CO_2 molecule with reference to the anion. Based on these experiments, they concluded that the CO_2 molecule may not be exactly tangential to the PF_6 sphere.

Having obtained an understanding of the intermolecular structure and arrangement of the CO_2 in the [bmim][PF_6] - CO_2 mixture using *ab initio* molecular dynamics simulations, we now attempt to study the mixture at different concentrations of CO_2. For this study we employ the refined force field model for [bmim][PF_6] discussed earlier. We present the methods in the next section, which is followed by the results and end with the conclusions drawn from our study.

8.2 Methodology and simulation Details

Molecular dynamics simulations were carried out on [bmim][PF_6] - CO_2 mixtures with varying concentration of CO_2 at 300K using the PINY_MD code [5]. The form of the interatomic potential and the potential parameters for the [bmim] and [PF_6] ions are adapted from our previous work [6]. The model has been found to predict the structure very close to that of *ab initio* structure [7] along with the diffusion co-efficients, density and surface tension close to that of experiments. For the CO_2 molecules, the EPM2 model [8] is used. Lorentz - Berthelot mixing rules were employed to obtain the Lennard-Jones parameters for cross interactions. The model is fully flexible for [bmim] and [PF_6] ions. However the bond distances in the CO_2 has been constrained consistent with the EPM2 model for CO_2.

Five different systems with 0, 10, 30, 50 and 70 mol % of CO_2 in 256 ion pairs of [bmim][PF_6] were simulated first in the isothermal-isobaric ensemble and later in the canonical ensemble. The number of CO_2 molecules for the 10, 30, 50 and 70 mol % of CO_2 turns out to be 28, 110, 256 and 595 respectively. The pressure of the system was determined based on experimental data [9]. The isothermal-isobaric ensemble simulations were carried out to determine the density of the system for the given system. Later, the

Table 8.1: Details of simulations

CO_2 mol %	Pressure (MPa)	Boxlength (Å)	Density (kgm^{-3})
0	0.0	44.30	1389
10	0.6	44.56	1388
30	2.0	45.38	1378
50	4.4	46.81	1360
70	15.0	49.92	1320

system was equilibrated in the canonical ensemble for atleast 2 ns and the trajectory was stored over next 2 ns, every 0.9 ps for analysis. The pressure applied in the isothermal-isobaric ensemble simulation, converged boxlength for that pressure and final densities have been provided in Table 8.1.

Nosé-Hoover chain thermostats [10] were used for temperature control. Periodic boundary conditions consistent with cubic symmetry were employed to obtain the bulk behavior. Ewald summation method was used to handle Coulombic interactions with an alpha value of 0.339 $Å^{-1}$. Non-bonded interactions were calculated up to a distance cutoff of 13 Å and long range corrections were applied for the calculation of energy and pressure tensor. The multiple time step algorithm, r-RESPA [11] was used to integrate the equations of motion, in which the non-bonded interactions beyond 6 Å and within 13 Å were integrated with a time step of 3 fs and those within 6 Å with a time step of 1.5 fs. Torsional forces were computed every 0.75 fs and the bending and stretching degrees of freedom were integrated with a time step of 0.375 fs. The energy conservation was monitored through the simulations and was found to be 3 parts in 10^5 over 1 ns.

Table 8.2: Comparison of volume expansion of [bmim][PF_6] - CO_2 mixture at different concentrations of CO_2 obtained from simulations and experiment [9]

Concentration of CO_2 (mol %)	Volume expansion (%) Computation	Volume expansion (%) Experiment
10	1.8	1.5
30	7.5	6.9
50	18.0	16.8
70	43.1	31.2

8.3 Results and discussions

8.3.1 Volume Expansion

CO_2 is highly soluble in some of the ionic liquids. It has been demonstrated that it is soluble up to 75 mol% in [bmim][PF_6] [12]. Previous studies [3] have indicated that CO_2 occupies pre-existing void spaces in the ionic liquids, which is the reason for the low volume expansion on its addition to the RTILs. Voronoi analysis was used to conclude that the cation and the anion rearrange in the ionic liquid to form small number of large voids from large number of small voids to accommodate the added CO_2. The volume expansion predicted by the current model at different concentrations of CO_2 along with the experimental values [9] is provided in Table 8.2. The latter are the best fit values obtained by fitting the experimental data to a quadratic equation.

The experimental data was available only in the range of CO_2 concentrations between 0 and 56.7 mol %. It can be noticed from the table that the values obtained from the computation are close to experimental results within this range. The volume expansion for the 70 mol % mixture is quite high in the simulations than the best fit to the experimental data. One of the reasons for this difference may be due to errors in extrapolation.

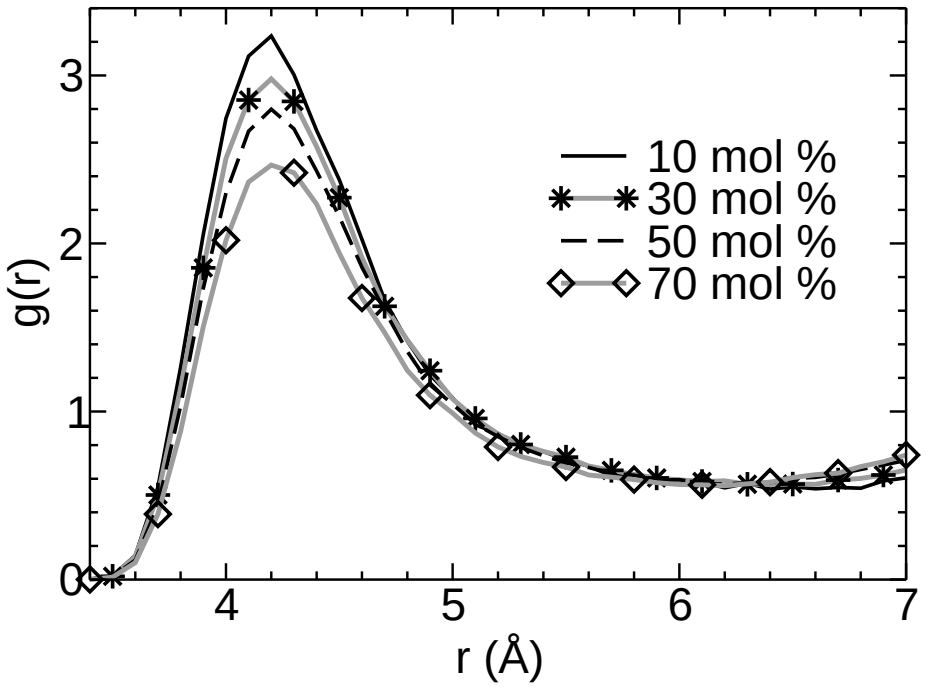

Figure 8.1: Radial distribution functions of CO_2 around the PF_6 anion for different CO_2 concentration in the [bmim][PF_6] - CO_2 mixture. Symbols are shown infrequently for clarity.

8.3.2 Radial distribution functions

PF_6 - CO_2 RDF

The anion - CO_2 radial distribution functions (RDF) are presented in figure 8.1. The RDF peaks at 4.2 Å at all the concentrations studied. The first minimum is present at 6.4 Å for the 50 and 70 mol % mixtures, while it is present at 6.2 Å for the 10 and 30 mol % mixtures. Figure 8.1 clearly shows that there is no shift in the peak positions with the change in the CO_2 concentration, although the peak heights are different. The coordination number up to 6.3 Å (up to the location of first minimum) are 0.3, 1.2, 2.4 and 4.2 respectively for 10, 30, 50 and 70 mol % mixtures. The increase in the coordination number with the increase in the CO_2 concentration is reasonable. The coordination number up to the first minimum suggests that the CO_2 molecules interact with atleast two of the anions. This is evident as the number of CO_2 that are within the first coordination shell is almost

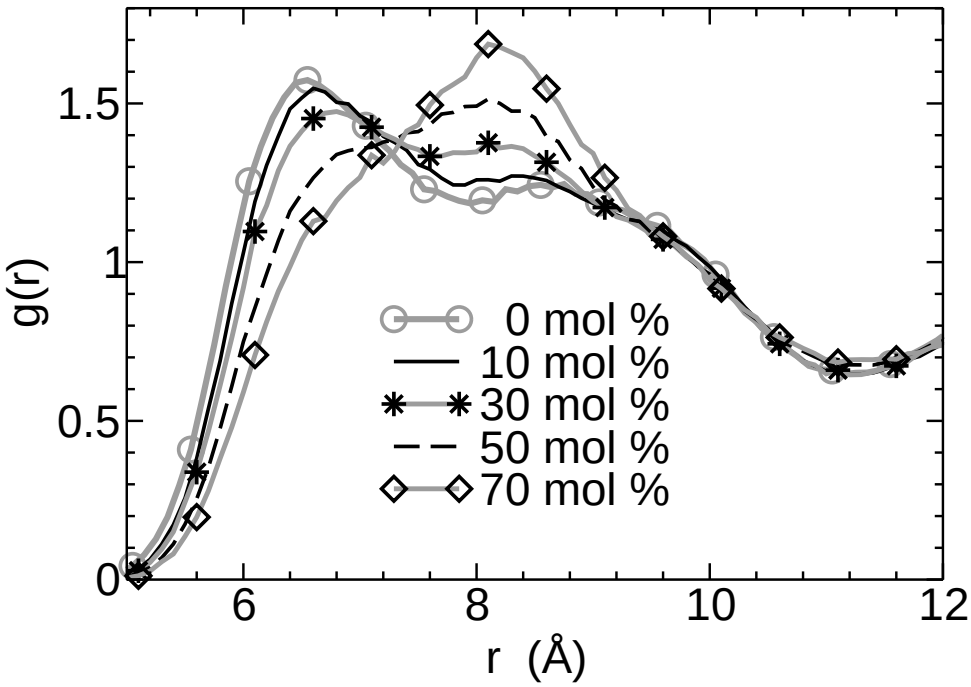

Figure 8.2: PF_6PF_6 radial distribution functions at various CO_2 concentrations in the [bmim][PF_6] - CO_2 mixture. Symbols are shown infrequently for clarity.

thrice that of the average number of CO_2 per anion available in the system. This can also be rationalized as the coordination shell of an anion is not exclusive, i.e., the first coordination shell of one anion can overlap with that of the other. In the case of 10, 30, 50 and 70 mol % mixtures, the coordination number is 3, 3, 2.5 and 2 times greater than the average number of CO_2 per anion respectively. This suggests that the number of CO_2 that can be present in the first coordination shell around the anion is limited by the CO_2 - CO_2 repulsion. It has been demonstrated in our previous studies that CO_2 occupies the octahedral voids around the anions. Although there are eight such voids, the number of CO_2 present around the anion is not eight, suggesting that steric repulsion plays a major role at higher concentrations of CO_2.

PF_6 - PF_6 RDF

Figure 8.2 presents the PF_6 - PF_6 radial distribution functions. The anion-anion radial distribution function varies significantly with increase in CO_2 concentration. Slight differences can be observed even on addition of 10 mol % of CO_2 to the ionic liquid. The differences also increase with increase in CO_2 concentration. The peak shifts towards right at higher mol % of CO_2. The position of the peak shifts from 6.5Å in the case of pure [bmim][PF_6] to a value of 8.1Å at the highest concentration of CO_2. The RDF in case of pure [bmim][PF_6] is sharper to the left of the peak whereas it is broader to the right. The curves gradually broaden in the left as the concentration of CO_2 in the mixture increases and it is broadest in the case of 70 mol % mixture. Anions move away from each other with increase in CO_2 concentration in the mixture. This can be rationalized as due to specific interaction between CO_2 and PF_6 that diminishes PF_6 - PF_6 interactions. As can be seen from the figure, near neighbor organization of anions with reference to other anions changes significantly with increase in CO_2 concentration. However the first minima that is located at 11.2 Å remains the same in case of all concentrations, which means that the increased CO_2 in mixture affects only near neighbor environment of anions.

Since the anion move away from each other with introduction of CO_2 it is expected that coordination number of anions will be less in case of mixture with highest concentration of CO_2. Coordination number up to 7.2 Å (location where the intensity of all the RDF peaks is same) are 3.3, 2.9, 2.3 and 1.7 respectively for 10, 30, 50 and 70 mol % mixture. Same values up to the first minimum (at 11.2Å) are 16.0, 15.2, 14.0 and 11.7 respectively. Since RDF of anions around an anion are very broad, it is reasonable to compare the coordination numbers at 7.2Å.

[bmim] - PF_6 RDF

Cation - anion RDF is presented in Figure 8.3. RDFs at all concentration of CO_2 are similar. All of them peak at 5.6 Å with their first minima at 7.6 Å. The coordination

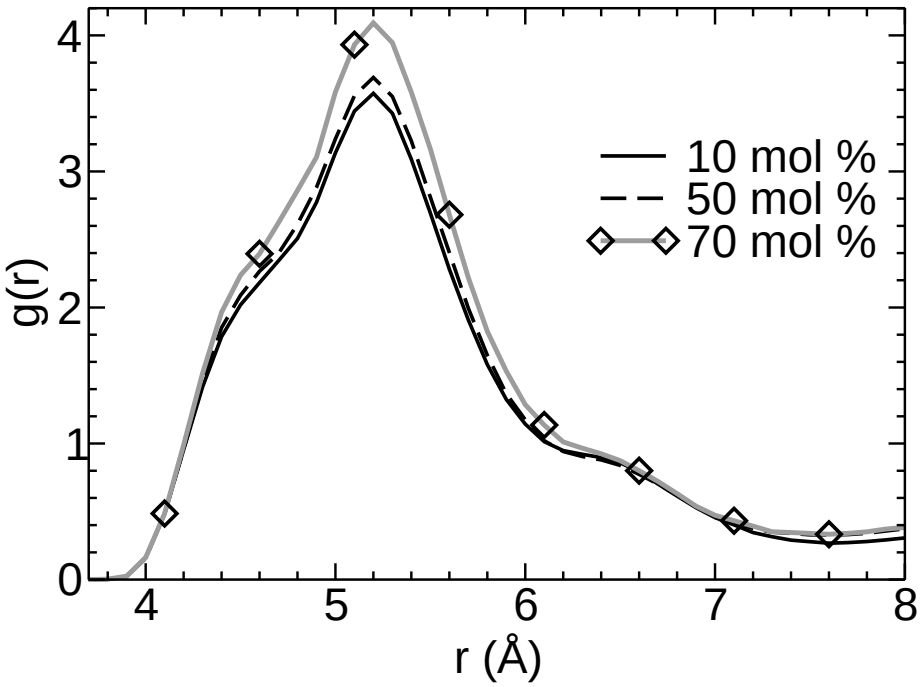

Figure 8.3: Radial distribution functions of PF_6 anions around the the cation ring center for various CO_2 concentrations in the [bmim][PF_6] - CO_2 mixture. Symbols are shown infrequently for clarity.

numbers up to the first minima are 5.7, 5.5, 5.1 and 4.6 respectively for 10, 30, 50 and 70 mol % mixtures of CO_2[bmim][PF_6]. Here also it can be noted that coordination number decreases with the increase in CO_2 concentration. This is similar to that seen in anion-anion RDF, where specific interaction between anion and CO_2 was said to be the reason for decrease in coordination number. However it should be noted that decrease in coordination number in case of cation-anion is small when compared to anion-anion coordination number, where the coordination number at 7.2 Å at 10 mol % CO_2 concentration was twice when compared to the same quantity at 70 mol %, suggesting that the anion interaction with CO_2 is mainly responsible for separation of ions.

In the figure 8.3, data is shown only for 10, 50 and 70 mol %. The curve for 30 mol % lies in between the curves for 10 and 50 mol % and that for the pure [bmim][PF_6] it is marginally below the curve corresponding to 10 mol %.

The large changes observed in the behavior of anion-anion RDFs and the lack thereof

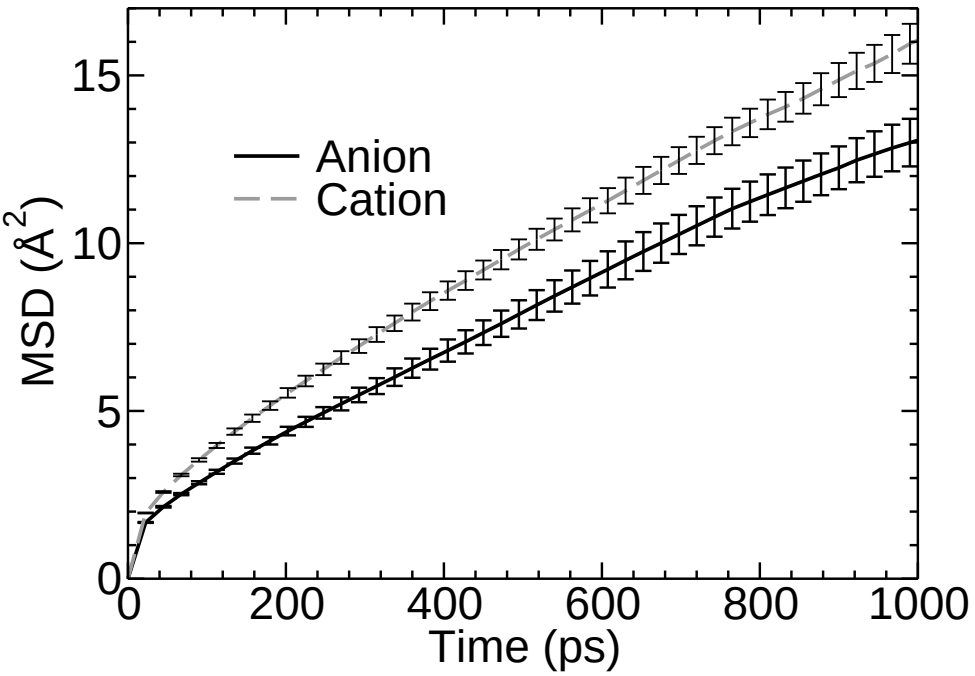

Figure 8.4: Mean squared displacement of anion and cation at 300K in the 30 mol % mixture of CO_2 - [bmim][PF_6] obtained as an average of 5 independent blocks along with error bars.

in the anion-cation RDFs, as a function of CO_2 concentration provides conclusive evidence that for the interaction between CO_2 and anion.

8.3.3 Diffusion Coefficients

The mean squared displacement of anion and cation in the 30 mol % mixture that is obtained as an average over 5 independent configurations is presented in Figure 8.4, along with error bars. It can be seen from the figure that the mixture does not show glassy behavior at this state point. Diffusion coefficients were calculated for all concentrations of CO_2 studied, as the long time regime slope of mean squared displacement curve (between 400 and 500 ps). The mean squared displacement curves themselves were obtained as an average over 3 to 5 independent trajectories at different concentration of CO_2 in mixture.

Diffusion coefficients are found to increase with CO_2 concentration for both ions and CO_2. It can be seen from the figure that the cation diffuses faster than the anion in

Table 8.3: Diffusion coefficients of anion, cation and CO_2 in the [bmim][PF_6] - CO_2 mixture obtained from simulations at different concentration of CO_2.

CO_2 mol %	D_- ($\times 10^{-12}$ m^2s^{-1})	D_+ ($\times 10^{-12}$ m^2s^{-1})	D_{CO_2} ($\times 10^{-12}$ m^2s^{-1})
0	4.7	6.7	
10	8.8	12.4	201.0
30	19.1	22.5	386.9
50	54.8	64.3	678.5
70	146.2	158.3	1453.8

[bmim][PF_6] - CO_2 mixtures which is also seen in experiments [13] as well as in simulations [6, 14] of pure ionic liquids. The values of diffusion coefficients at various concentrations of CO_2 are presented in Table 8.3. The cation diffuses faster than the anion at all concentrations of CO_2 in the mixture.

The variation of diffusion coefficients with concentration of CO_2 along with the best fit for anions and cations is presented in figure 8.5. The increase in diffusion of ions is slow at low CO_2 concentrations but becomes steeper as one proceeds towards higher concentration of CO_2. The diffusion coefficients were fitted to a cubic equation of the form,

$$D_{\pm} = a_0 + a_1 x + a_2 x^2 + a_3 x^3 \tag{8.1}$$

where a_0, a_1, a_2, a_3 are constants. The best fit values to curves that can be used to obtain diffusion coefficients values of ions and CO_2 at intermediate concentrations of CO_2 in the mixture are provided in Table 8.4.

8.4 Conclusion

Molecular dynamics simulation studies have been carried out on [bmim][PF_6] - CO_2 mixtures at varying concentration of CO_2 in the mixture. The volume expansion obtained

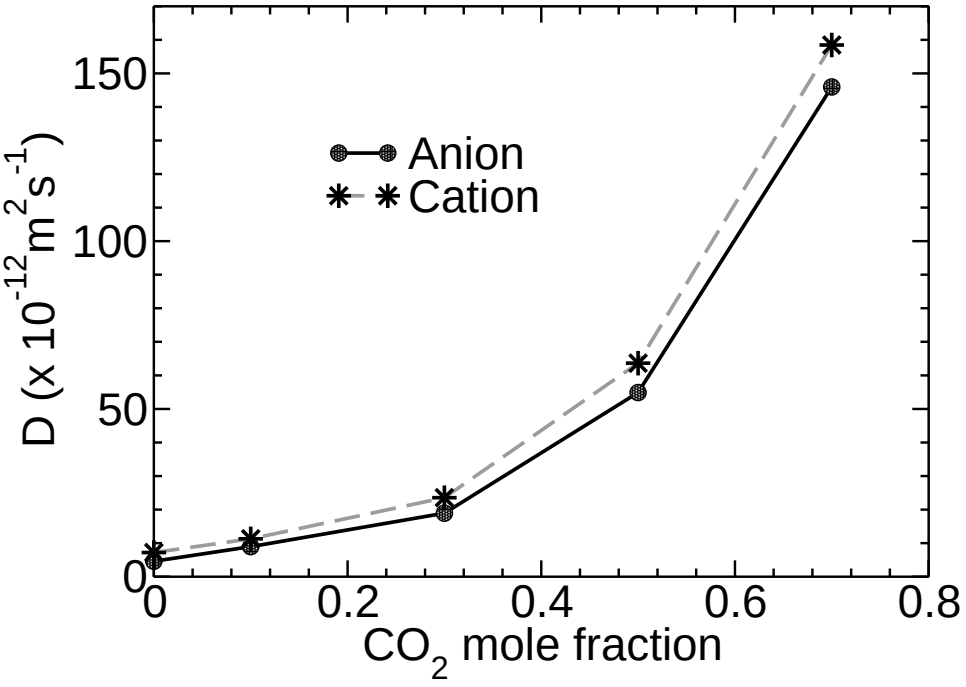

Figure 8.5: Variation of diffusion coefficients of ions with the concentration of CO_2.

Table 8.4: Values from the best fit to equation 8.1 for diffusion coefficients of anion, cation and CO_2.

Ion/Molecule	a_0	a_1	a_2	a_3
Anion	4.608	59. 509	-221.299	606.834
Cation	7.198	50.773	-155.533	559.556
CO_2	29.56	2212.25	-5766.25	78875.00

from simulations agree well with experimental data. The negligible volume expansion at low concentration of CO_2 suggests that CO_2 occupies pre-existing voids in the ionic liquid as reported in previous studies [3]. Trends in the radial distribution of anions around an anion as well as anions around cation indirectly suggests that there is anion - CO_2 specific interaction. This has also been seen in the anion-CO_2 radial distribution function. The diffusion coefficient of the ions and of CO_2 increases with increase in CO_2 concentration. This non-linear increase has been fitted to a cubic equation, the best fit of which provides diffusion coefficients at intermediate values of CO_2 concentrations that have not been studied.

Bibliography

[1] C. Cadena, J.L. Anthony, J.K. Shah, T.I. Morrow, J.F. Brennecke, E.J. Maginn, *J. Am. Chem. Soc.*, **126**, 5300 (2004).

[2] S.G. Kazarian, B.J. Briscoe, T. Welton, T. *Chem. Commun.*, 2047 (2000).

[3] X. Huang, C.J. Margulis, Y. Li, B.J. Berne, *J. Am. Chem. Soc.*, **127**, 17842 (2005).

[4] M. Kanakubo, T. Umecky, Y. Hiejima, T. Aizawa, H. Nanjo, Y. Kameda, *J. Phys. Chem. B*, **109**, 13847 (2005).

[5] M.E. Tuckerman, D.A. Yarne, S.O. Samuelson, A.L. Hughes, G.J. Martyna, *Comput. Phys. Commun.*, **128**, 333 (2000).

[6] B.L. Bhargava, S. Balasubramanian, *J. Chem. Phys.*, **127**, 114510 (2007).

[7] B.L. Bhargava, S. Balasubramanian, *J. Phys. Chem. B*, **111**, 4477 (2007).

[8] O. Borodin, G.D. Smith, R.L. Jaffe, *J. Comput. Chem.*, **22**, 641 (2001).

[9] S.N.V.K. Aki, B.R. Mellein, E.M. Saurer, J.F. Brennecke, *J. Phys. Chem. B*, **108**, 20355 (2004).

[10] G.J. Martyna, M.L. Klein, M.E. Tuckerman, *J. Chem. Phys.*, **97**, 2635 (1992).

[11] M.E. Tuckerman, B.J. Berne, G.J. Martyna, *J. Chem. Phys.*, **97**, 1990 (1992).

[12] L.A. Blanchard, D. Hancu, E.J. Beckman, J.F. Brennecke, *Nature*, **399**, 28 (1999).

[13] H. Tokuda, K. Hayamizu, K. Ishii, A.B.H. Susan, M. Watanabe, *J. Phys.Chem. B*, **108**, 16593 (2004).

[14] B.L. Bhargava, S. Balasubramanian, *J. Chem. Phys.*, **123**, 144505 (2005); **125**, 219901 (2006).

Chapter 9

Ab Initio Molecular Dynamics Study of 1-ethyl-3-methylimidazolium fluoride - hydrogen fluoride mixture

9.1 Introduction

Acidic 1-ethyl-3-methylimidazolium fluoride (EMIF.2.3HF) is a room temperature ionic liquid (RTIL) mixture with potential applications in electrochemistry. The mixture melts at 183K and has a electrochemical window of around 3 V. It exhibits a high electrical conductivity of 100 mScm^{-1} at 298K [1, 2].

Despite the large number of experimental investigations [1–5] of this electrolyte, theoretical or computational studies on this system are limited [6]. Turq and coworkers [6] have carried out empirical potential molecular dynamics simulations of EMIF.2.3HF and have looked at the geometries and properties of several anion clusters. In an earlier study of a related solution, Rosenvinge et al [7] have reported results of ab initio MD simulation of KF.2HF. Apart from changes in the structure of the liquid that could arise from the molecular nature of the cation in EMIF.2.3HF (compared to KF.2HF), another crucial

difference exists between these two systems. The formation of a hydrogen bond between the cation and the anion is a feature of imidazolium based ionic liquids that is absent in the latter compound. Thus, the properties of the EMIF.2.3HF liquid is expected to be determined not only by charge-charge interactions but also by hydrogen bonding between oppositely charged ions. The importance of hydrogen bond in room temperature ionic liquids has been recognized and discussed in detail in earlier works [8–13]. Density functional theory based MD simulations are able to accurately reproduce the cation-anion hydrogen bond. With this backdrop, we report here a Car-Parrinello MD simulation study of EMIF.2.3HF. Anticipating our results, we find evidence for the existence of polyfluoride species, for a cation-anion hydrogen bond, stacking of ring planes of neighboring cations. Interesting results on the geometry and vibrational properties of the polyfluorides are presented.

9.2 Methodology and Simulation Details

Ab initio MD (AIMD) simulations [14] of EMIF.2.3HF was carried out using the CPMD code [15]. With 16 units each of ion pairs ([emim] and fluoride) along with 37 HF molecules, the simulated system consisted of 394 atoms. The simulation was performed at the experimental density of 1.135 g/cc [2] at 298K with a cubic box of edge length 16.044Å under constant NVT conditions. The initial configuration for this CPMD run was generated by equilibrating the system for 8 ns within an all atom fully flexible, classical force field [16]. Potential parameters for the HF molecules were taken from the work of Cournoyer and Jorgensen [17], and cross interactions during this run were treated using Lorentz-Berthelot combination rules.

Norm conserving pseudopotentials of the Troullier-Martins form [18] were employed to take into account the effect of the core electrons and the nuclei on the valence electrons. Gradient corrected exchange and correlation functionals prescribed by Becke [19] and Lee, Yang, Parr [20] were used. A plane wave basis set with an energy cutoff of 90 Ry was

used to expand the electronic orbitals. This cutoff value was chosen after checking the convergence of the forces on the ions as a function of energy cutoff. Three dimensional periodic boundary conditions were applied to obtain bulk behavior. All the hydrogens in the system were substituted by deuterium, in order to enable the use of a larger time step of integration. Prior to the CPMD run, the electronic degrees of freedom were quenched to the Born-Oppenheimer surface. During the CPMD simulations, a fictitious electron mass of 700 a.u. was employed. The kinetic energy of the ions was controlled using a Nosé-Hoover chain thermostat [21]. The equations of motion were integrated with a time step of 5 a.u. (around 0.12 fs) over a duration of 13 ps out of which the last 10 ps data was used for analysis. The conservation in total energy was found to be 3 parts in 10^9 over a duration of 1 ps.

9.3 Results and Discussions

A schematic of [emim][F] is given in Figure 9.1, to aid the discussion, and the various polyfluoride anions studied in the simulation are shown in Figure 9.2.

9.3.1 Gas phase calculations

The [emim] cation was structure optimized under isolated conditions within DFT. The geometry of the optimized structure has been compared with the crystal structure of [emim][F].HF [24] in Table 9.1 and found to agree well. Most of the bond lengths and angles are reproduced with 1.5% of the experiment. The planarity of the imidazolium ring has also been reproduced in these gas phase calculations.

Structure optimizations in the gas phase were also carried out for the following complexes: [emim][F], [emim][F]-HF and [emim][F]-2HF. In the first complex, the fluoride ion was found to abstract the hydrogen atom H(C3) of the cation to form a HF molecule. The energy change for this reaction was found to be 940 kJ.mol^{-1}. The addition of one or

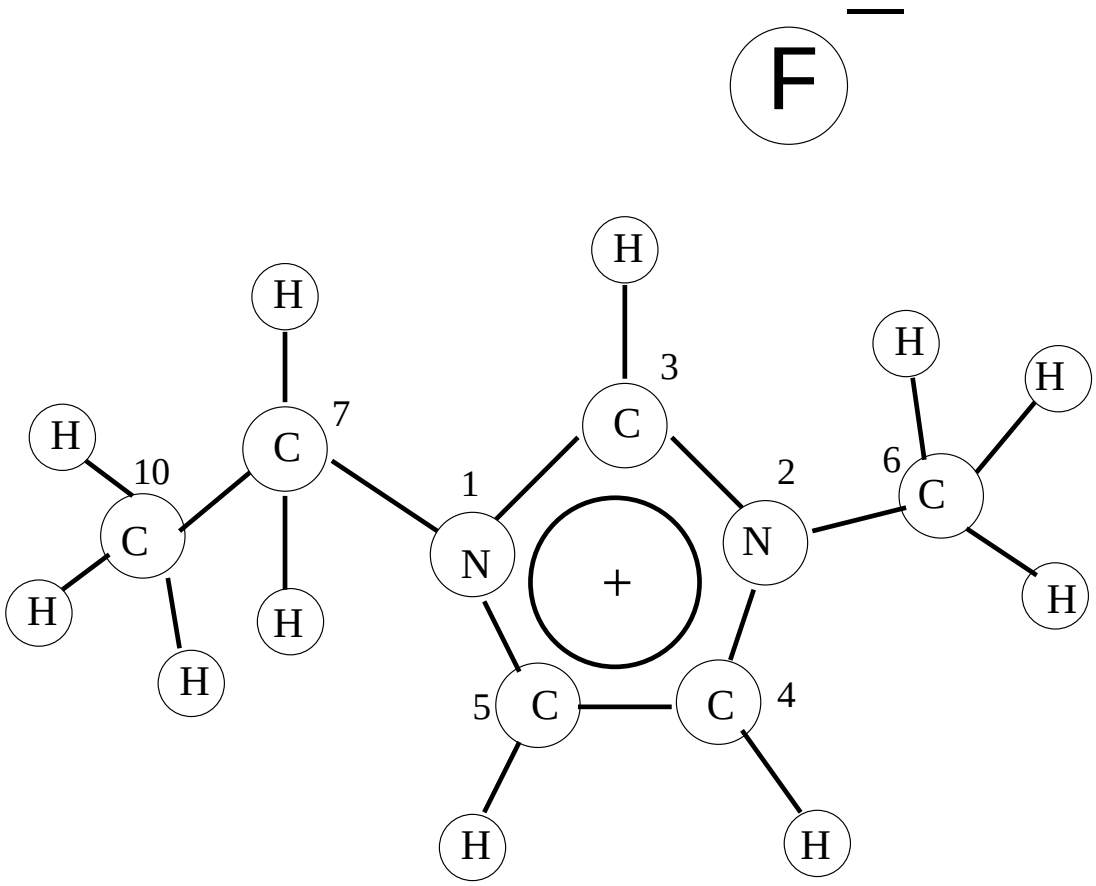

Figure 9.1: Schematic of [emim][F] along with atom numbering scheme.

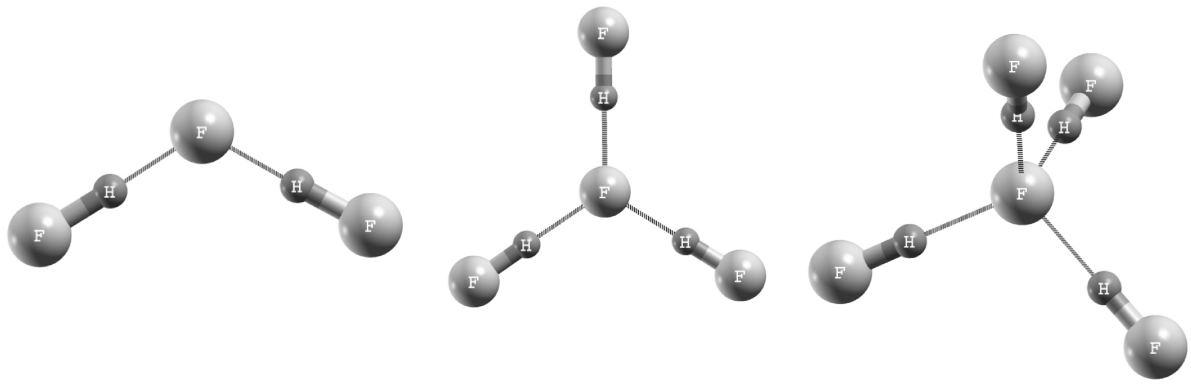

Figure 9.2: Various polyfluoride anions observed during the simulations.

two HF molecules to the cation-anion complex reduces the basicity of the anion. Under such conditions, the fluoride-cation reaction was substituted by the formation of anion

Table 9.1: Comparison between the geometry of 1-methyl,3-ethylimidazolium cation determined from x-ray crystal structure of [emim][F].HF [24] and that from a CPMD optimized configuration in isolated (gas) phase.

Type	Bond Length [Å]	
	Experiment	CPMD
N1-C3	1.33	1.35
N1-C5	1.38	1.39
N2-C2	1.34	1.35
C4-C5	1.34	1.36
N2-C6	1.47	1.48
Type	Angle [degree]	
	Experiment	CPMD
N1-C3-N2	107.5	108.9
C4-C5-N1	107.6	107.5
N1-C7-C8	113.4	113.7

species such as FHF^- and $F(HF)_2^-$. The fluoride ion that is part of these anionic entities was found to interact favorably with the acidic hydrogen of the cation through a hydrogen bond.

The bond length calculated for a free HF molecule was 0.935Å, compared to the experimental value of 0.917Å [22]. Most HF molecules were found to organize around the fluoride ions resulting in the formation of polyfluoride species. Polyfluorides of the form, $F(HF)_n^-$ for values of n between 1 and 4 were observed. Neither free fluoride ions nor free HF molecules were seen. Clusters of the form $(HF)_2$ existed in the liquid, but the percentage of these species was negligible. On an average, only 2% of all the HF molecules were part of the $(HF)_2$ clusters. Polyfluoride anions formed the biggest species type present in the liquid and we naturally focus our attention on them in further discussions.

In the backdrop of the knowledge gained from zero temperature gas phase calculations, we found that that during the entire trajectory of the CPMD simulation of the bulk liquid,

the H(C3) atom of the cation was found not to break its covalent bond with C3. However, we have observed the dissociation of the covalent bond within a few HF molecules during the course of the CPMD run. Thus, for the analyses reported here, we do not make any distinction between fluorine atoms that were part of a HF molecule and those that were present as anions in the initial configuration.

9.3.2 Structure factor

Partial structure factors were calculated for all distinct pairs of atom types using the relation,

$$S_{\alpha\beta}(q) = \delta_{\alpha\beta} + 4\pi\sqrt{\rho_\alpha \rho_\beta}\int_0^\infty r^2[g_{\alpha\beta} - 1]\frac{\sin(qr)}{qr}dr \tag{9.1}$$

where $\rho_\alpha = \frac{N_\alpha}{V}$, N_α being number of atoms of type α, and V is the volume of the system. The upper limit in the integral has to be limited to half the box length due to the finite size of the system. The total X-ray structure factor is given by

$$S(q) = \sum_\alpha \sum_\beta c_\alpha c_\beta \frac{f_\alpha(q) f_\beta(q)}{\langle f(q)\rangle^2} S_{\alpha\beta}(q) \tag{9.2}$$

where c_α is the concentration of atom type α, f_α is the atomic form factor and $\langle f(q)\rangle = \sum_\alpha c_\alpha f_\alpha(q)$. Wavevector dependent atomic form factors were used to obtain the total structure factor for the liquid, calculated with a resolution of 0.39 Å^{-1}.

The total X-ray structure factor obtained from the simulation [23] is compared with the experimental result in Figure 9.3. Three prominent peaks found in the structure factor within 10Å^{-1} are reproduced well. From an analysis of the partial structure factors (not shown) weighted with the number concentration and the atomic form factor, it was found that the peak at 1.78Å^{-1} has a predominant contribution from fluorine-fluorine correlations. The other partials which contribute significantly to this peak include C-C (C6 and C7 in the schematic), N - N and C_W - C_W (C4 and C5 in the schematic). The organization of HF molecules around the fluoride anion results in the formation

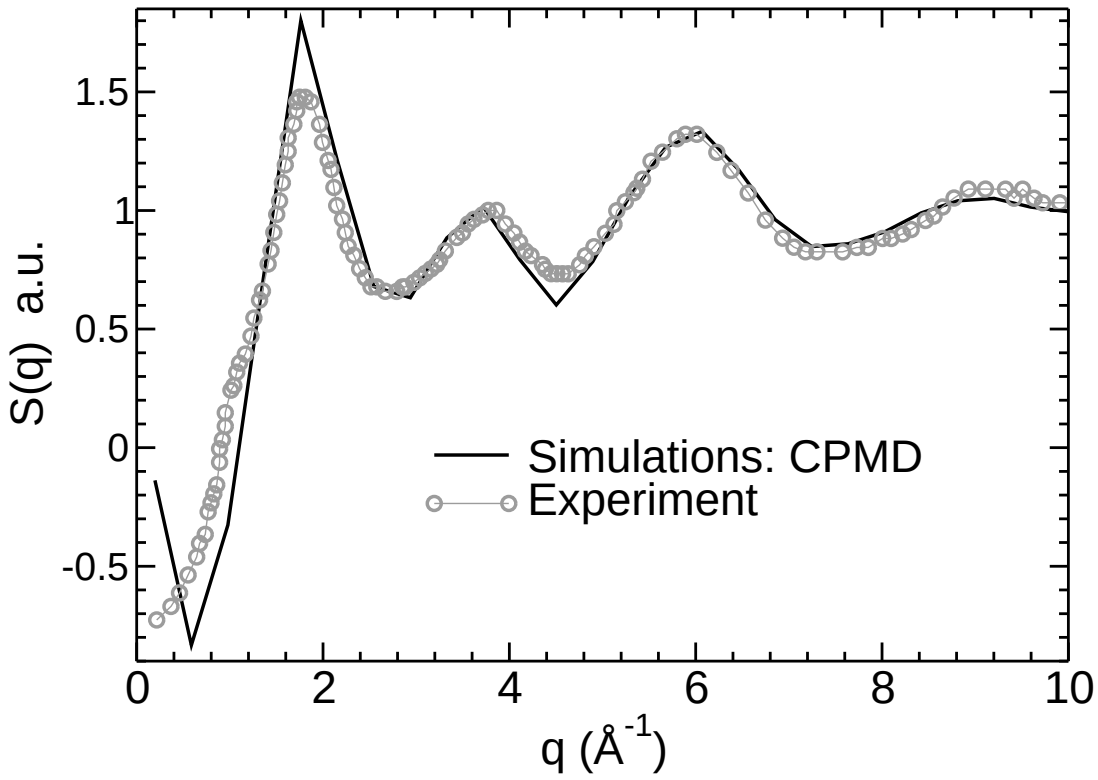

Figure 9.3: Structure factor obtained from simulation compared to experiment [3].

of polyfluoride species in which the hydrogen bond length is around 1.5ÅṪhis leads to a correlation length of 3.5Å between the fluoride ions. It is thus evident that the polyfluoride ions are mainly responsible for the peak at 1.78Å^{-1} in the total structure factor. The 3.8Å^{-1} peak is coming from the intramolecular correlations. The shoulder at around 1Å^{-1} in the experimental data is absent in our simulation, possibly due to limited system size.

9.3.3 Polyfluoride species

In order to identify various polyfluoride species, one needs to develop criteria to define intermolecular neighbors. Here, we use a distance cutoff of 2.1Å for a H-F pair, below which these are assumed to be hydrogen bonded. This cutoff was chosen from an examination of the corresponding pair correlation function (see later).

Table 9.2: Covalent and H-bond distances between hydrogen and fluorines of polyfluoride anions in liquid and gas phases. The distance in the liquid is the most probable value.

Type	Covalent bond length [Å]		Hydrogen bond length [Å]	
	Liquid	Gas phase	Liquid	Gas phase
$F(HF)^-$	1.04	1.17	1.24	1.17
$F(HF)_2^-$	1.02	1.03	1.36	1.35
$F(HF)_3^-$	0.98	0.99	1.48	1.46
$F(HF)_4^-$	0.96	0.97	1.54	1.56

Polyfluoride species of the form $F(HF)_n^-$ (n=1-4) were observed in the simulation. The percentage of fluoride ions forming polyfluoride species were 6.8, 41.5, 37.4 and 6.2 for values of n 1, 2, 3 and 4 respectively. Some of the fluoride ions (around 8%) were not part of any polyfluoride species. These were found to form hydrogen bond only with the cationic ring hydrogen. Polyfluoride species of the type $F(HF)_2^-$ and $F(HF)_3^-$ exist in larger proportion compared to $F(HF)^-$ and $F(HF)_4^-$. A snapshot of a part of the system containing only the fluoride ions and HF molecules is shown as Figure 9.4. It can be observed from the figure that most of the anions exist as $F(HF)_2^-$ and $F(HF)_3^-$. Very few F(HF)− are seen and in the region that is shown in the figure, there are no $F(HF)_4^-$ species. The fluoride ions and HF molecule which appear to be free in the figure are actually H-bonded to the cation ring hydrogen.

The distributions of covalent and hydrogen bond lengths between hydrogen and fluorine atoms of the polyfluoride species are presented in Figure 9.5. The H-bond distance increases in the higher polyfluorides. As a fluoride ion makes many hydrogen bonds, the strength of individual h-bonds should decrease leading to a larger h-bond length. Consequently, the length of the covalent bond between H and F (within a HF molecule) will decrease as seen in the figure. The effect of these changes on the vibrational properties will be discussed later. The geometry of the polyfluorides in the liquid state are quite similar to their structures obtained under isolated conditions, as can be seen from Table 9.2

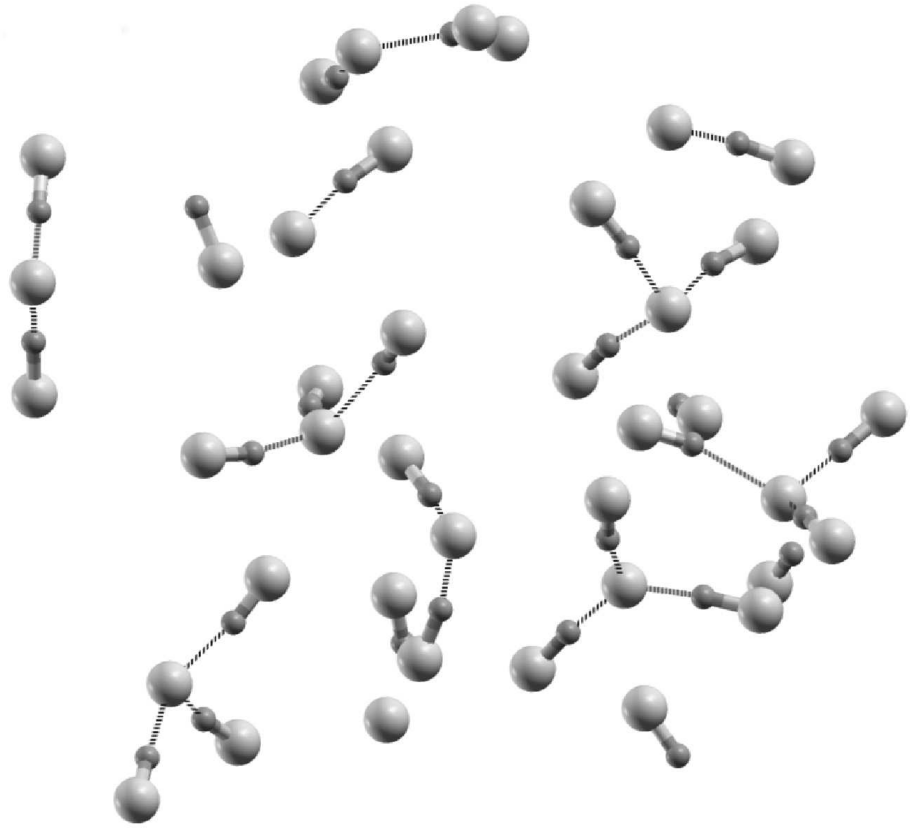

Figure 9.4: Snapshot of part of the system showing only the fluoride ions and the HF molecule. Hydrogen bonds are shown as the dotted lines that connects the fluorine and hydrogen atoms. Cations are not shown for clarity. Free fluoride ions seen in the figure are hydrogen bonded to the cation, in reality.

Under isolated conditions, the hydrogen atom in the $F(HF)^-$ ion is present exactly in between the two fluorine atoms. However in the [emim][F].2.3HF liquid, the covalent bond and the hydrogen bond distances in this species are distinct, although their distributions overlap significantly. Among the polyfluoride species, the hydrogen bond in the $F(HF)^-$ ion is the strongest, but its occurrence is rare in the liquid phase.

The distribution of FFF angle in different polyfluoride anion species shown in in Figure 9.6 illuminates their geometry further. The distribution for the $F(HF)_2^-$ ion shows a most probable value at 123°, whereas that for $F(HF)_3^-$ and $F(HF)_4^-$, show peaks at 114° and 104° respectively. As the number of HF associated with the fluorine approaches four, the angle shifts towards the value for a tetrahedron. In the gas phase for n equal to 2, 3

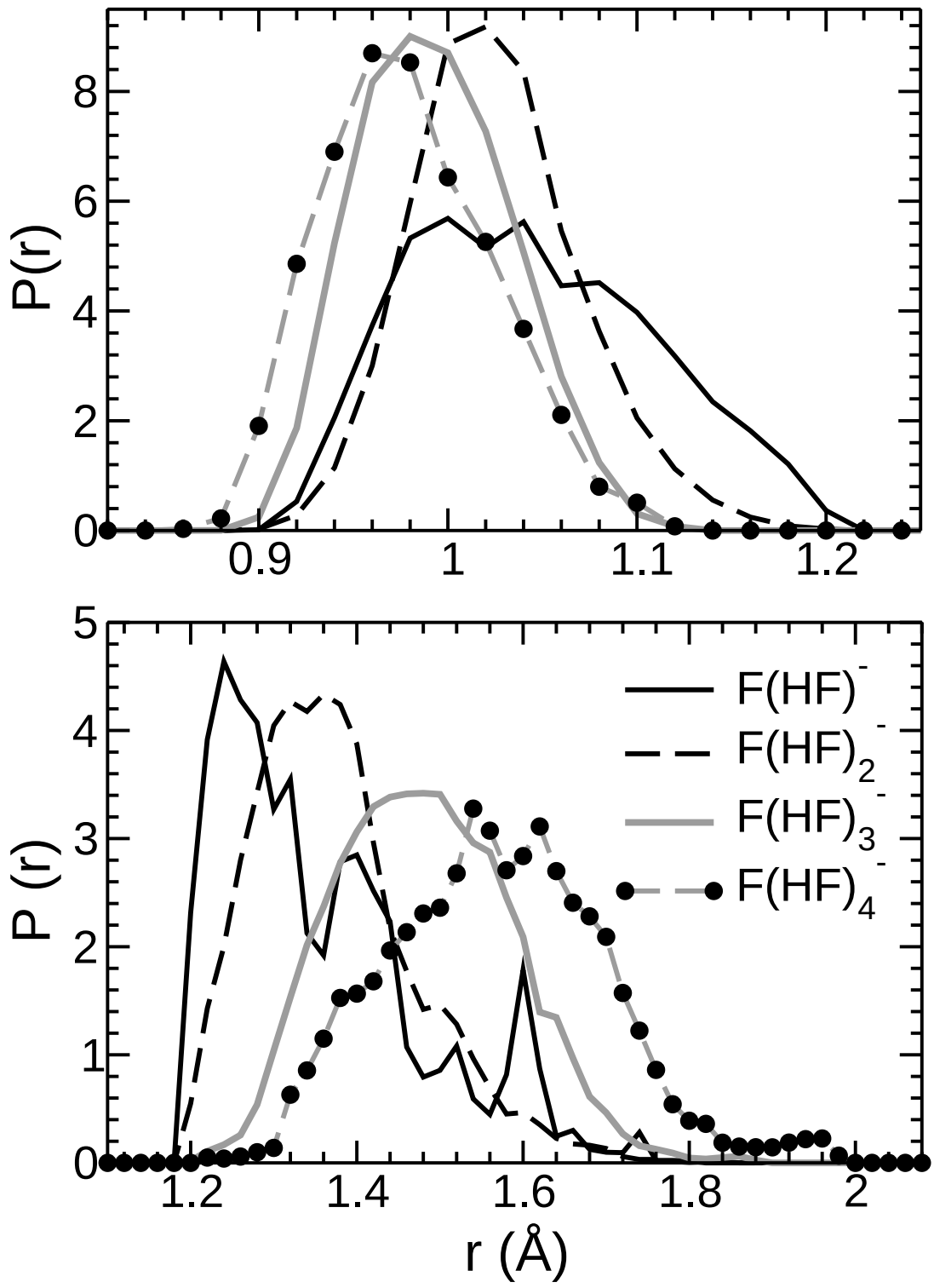

Figure 9.5: Probability distributions of covalent and hydrogen bond distances between hydrogen and fluorine atoms in various polyfluoride species.

and 4, the optimized structures showed angles of 118.5, 120 and 109.4° respectively. The geometry of polyfluorides in the liquid exhibits some features of the species in the gas phase; however the distance and angle distributions are quite broad.

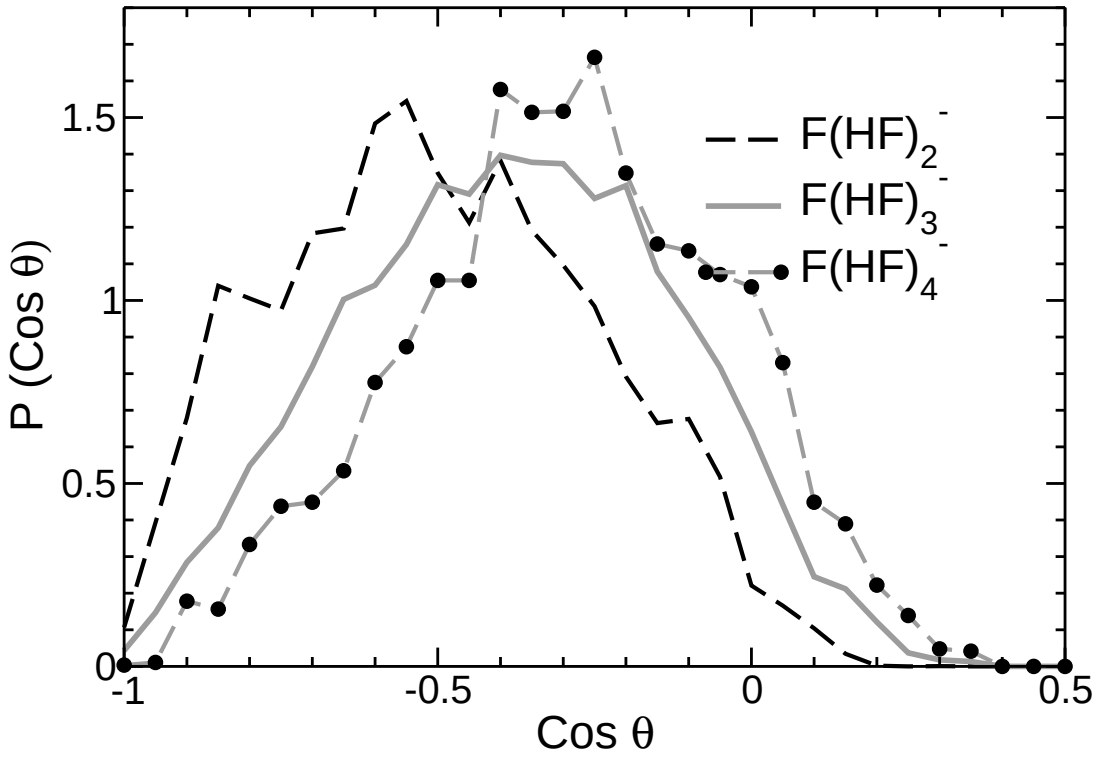

Figure 9.6: Distribution of FFF angle in various polyfluoride anions. θ is the angle formed by the vectors connecting the fluorine atom of the HF molecule with that of the central fluoride ion.

9.3.4 Radial and spatial distribution functions

The site - site partial radial distribution functions between the fluorines and the cation are presented in Figure 9.7. The cation position is taken as the geometric center of the imidazolium ring. The main figure shows the RDFs above a distance of 2.5ÅṪhe fluorine - fluorine RDF that exhibits a peak below this distance is shown in full in the inset. The fluorine - fluorine RDF peaks at 2.35Å and has a coordination number of 1.4 up to the first minimum of 2.85Å. This distance corresponds to two fluorine atoms separated by a covalent and a hydrogen bond within a polyfluoride. A second clear peak is observed

at 4.15Å with a minimum at 4.85 Å. This feature points to correlation between fluorine atoms of HF molecules belonging to the same polyfluoride species. The third, broad feature at 6.55Å arises from fluorine atoms present in different polyfluoride species.

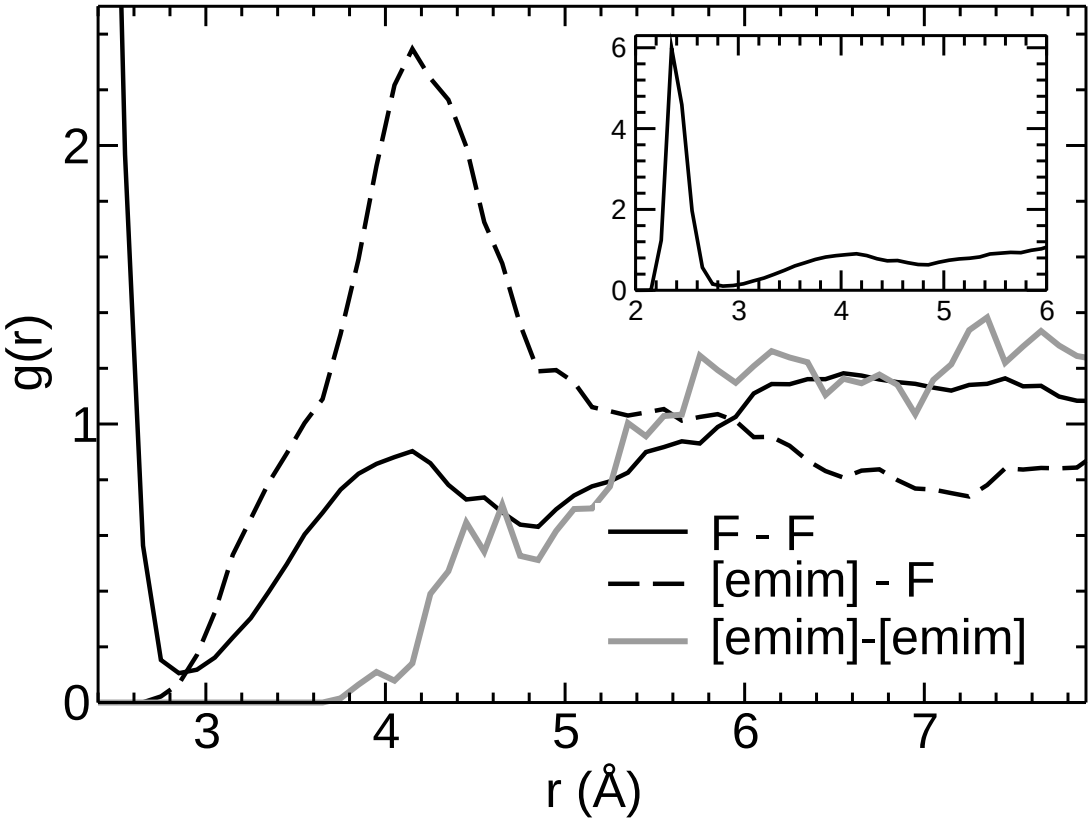

Figure 9.7: Fluorine - fluorine, cation - fluorine and cation - cation radial distribution functions between 2.5Å and 8Å. Inset shows the complete anion - anion RDF.

The cation - fluorine RDF peaks at 4.15Å with a coordination number of 6.6 up to the first minimum at 7.25Å. This RDF also shows a small hump at 5.85Å. The ordering of the anions around the cations is evident from the clear peak in the RDF. A hump is also seen at 3.15Å and the number of fluorine atoms surrounding the cation ring up to 3.65Å is slightly greater than one. The main peak is present at 4.15Å with a broad shoulder at 5.85Å. To examine the origin of these features, we have calculated the spatial distribution of fluorine atoms around the cation ring center. The spatial distribution function (SDF) of fluorine atoms that are within 3.65Å from the center of the ring is

shown in Figure 9.8. The feature at 3.15Å is seen to arise from fluorines that are present above and below the imidazolium ring. The SDF of the fluorine atoms that are between 3.65 and 4.85Å, i.e., the region of the main peak in the RDF is presented in Figure 9.9. The highest density of the fluorines is found near the three ring hydrogen atoms. By increasing the isosurface value, it was found that the maximum density is along the C-H bond vectors, supporting the argument that these fluorines form a hydrogen bond with the cation. The SDF of fluorines present between 4.85 to 7.25Åaround the cation exhibits a rather diffuse distribution mainly around the methyl and ethyl groups of the cation (Figure not shown). This feature was also observed as a hump in the anion - cation RDF in liquid [mmim][Cl] [11], that was attributed to anions present near the methyl groups of the cation.

The cation - cation RDFs peaks at 7.3Å and shows a small hump around 4.6Å. Despite the paucity of statistics, this feature is clear enough to be further investigated (see later).

Shown in Figure 9.10 are the RDFs of fluorine atoms around the hydrogen atoms of the imidazolium ring, H(C3), H(C4) and H(C5) respectively. The RDF curves corresponding to H(C3), H(C4) and H(C5) exhibit peaks at 2.15, 2.25 and 2.35Å respectively. The functions for H(C4) and H(C5) are almost identical, as expected on the basis of the structure of the imidazolium ring. We observe a shift of about 0.2Åin the H(C3) - F RDF relative to the other two functions, due to the acidic character of H(C3). This enables H(C3) to form a relatively stronger hydrogen bond with the fluorines of the liquid. Such a cation-anion hydrogen bond has been observed in ab initio MD simulations of other ionic liquids such as [mmim][Cl] [9–11] and [bmim][PF_6] [12]. Interionic hydrogen bonding is discussed in detail in the following sections. Since the fluoride ions form polyfluoride species, features in these RDFs found at distances greater than 3Å relate to correlations of the cationic hydrogen with atoms present in the polyfluoride species.

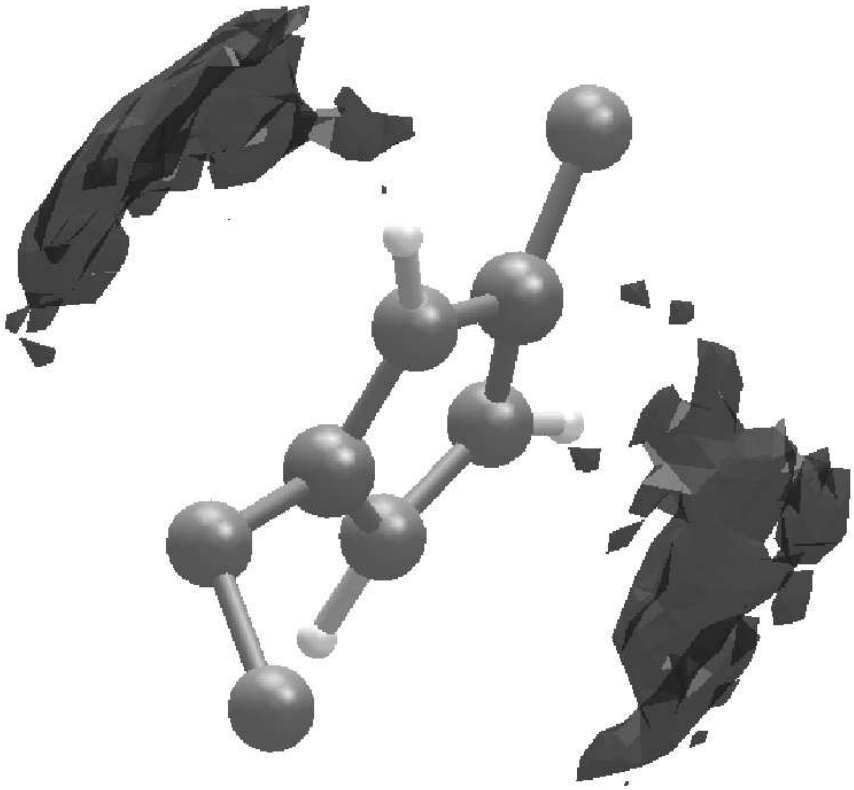

Figure 9.8: The spatial distribution function of fluorine atoms that are present within 3.65Å from the center of the imidazolium ring of the cation. The density of the isosurface shown is 0.044 $Å^{-3}$ i.e., 3.5 times the average number density of fluorine atoms in the system. Hydrogen atoms on the methyl and ethyl groups are not shown for clarity.

9.3.5 Hydrogen bonds

The classical MD simulations of [emim][F]-2.3HF by Salanne *et al* [6] report the absence of hydrogen bonds between the fluoride ions and the ring hydrogen atoms based on criteria of distance between the pair of atoms and the directionality of the bond. We have analyzed our CPMD simulation trajectory for the presence of such hydrogen bonds. In this effort, we employ two conditions to determine the existence of a hydrogen bond between the fluorine and the ring hydrogen: first, the distance between the hydrogen and the fluorine should be less than 2.5Å, and second, the angle C_α - H(C_α) - F be greater than 160°. Based on these criteria, we have found that around 14% of fluorine atoms form a hydrogen bond with the ring hydrogens. By adopting a liberal criteria, i.e., with an angle cutoff

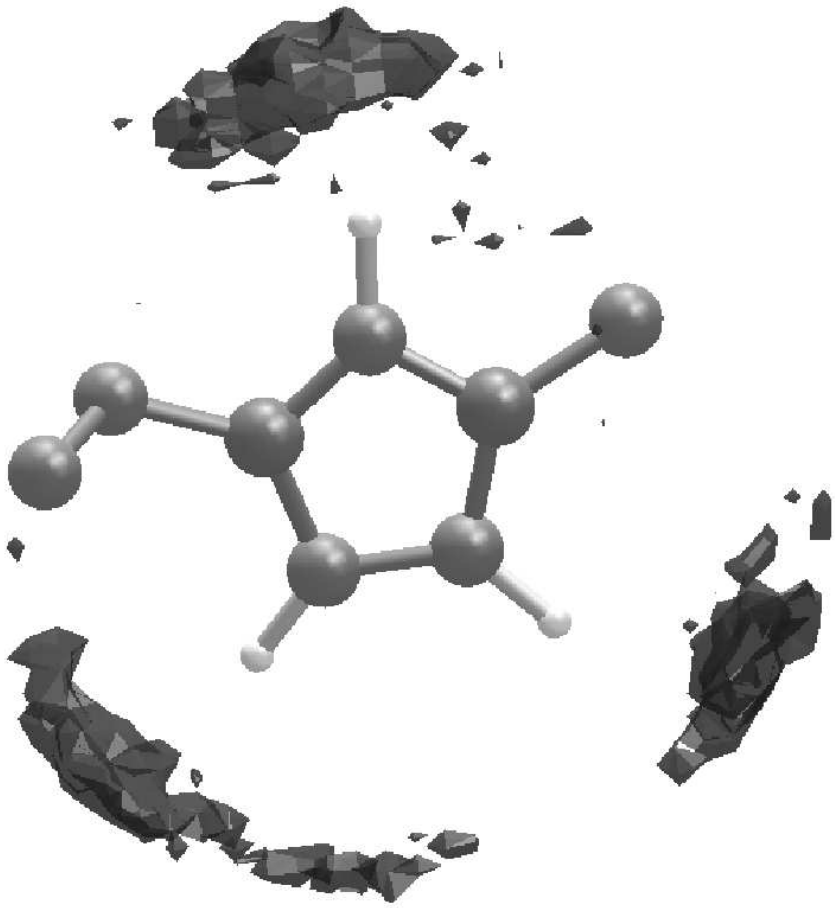

Figure 9.9: The spatial distribution function of fluorine atoms that are present between 3.65Å and 4.85Å from the center of the imidazolium ring of the cation. The density of the isosurface shown is 0.088 $Å^{-3}$ that is about 7 times the average number density of fluorines in the system. Hydrogen atoms on the methyl and ethyl groups are not shown for clarity.

of 140°, the percentage of such fluorines increases to 39. With reference to the cation, using the stricter angle cutoff, one among every two cations was hydrogen bonded with fluorines, while the liberal cutoff yielded more than one hydrogen bond per cation.

The distribution of C_α-H(C_α)-F angle is presented in Figure 9.11. From the figure, it is evident that most of the fluorines which are within 2.5Å from the hydrogen prefer to approach the imidazolium cation along the direction of the C-H vector.

Matsumoto *et al* [24] have observed the presence of three fluorine-ring hydrogen bonds

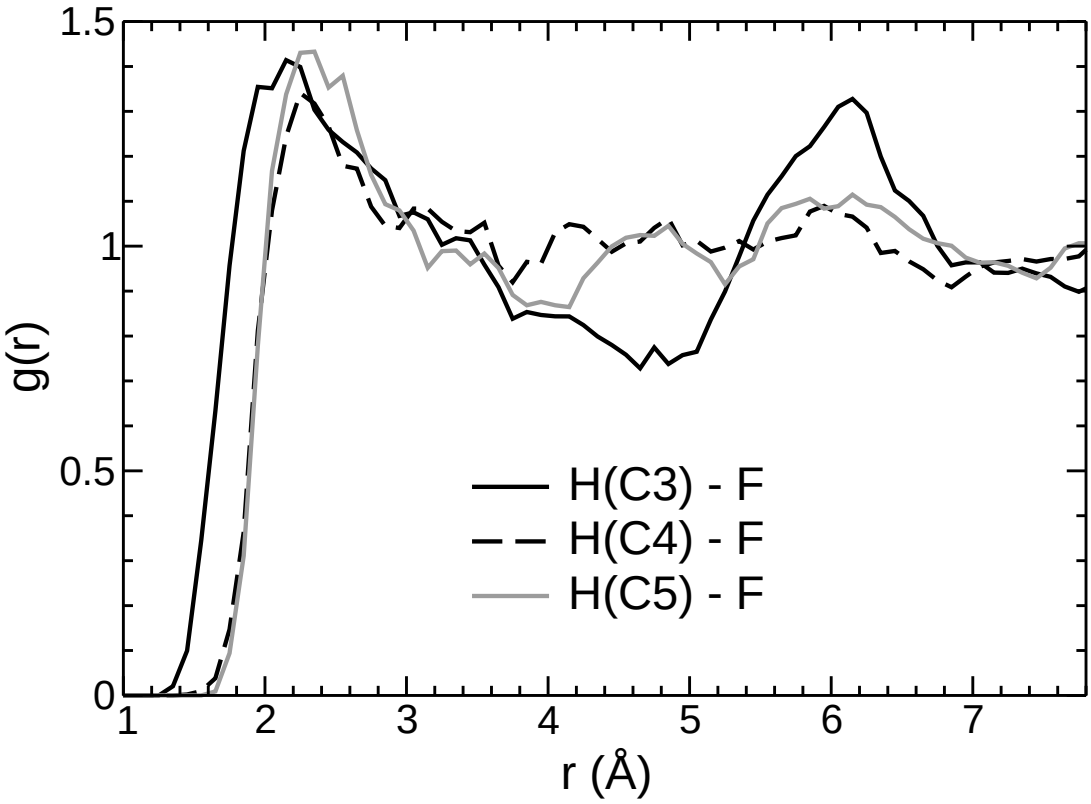

Figure 9.10: Radial distribution functions of the fluorines around different hydrogen atoms of imidazolium ring.

in crystalline [emim][F].HF. While one fluorine is bonded to H(C5), the other is bonded to H(C3) and H(C4) through two hydrogen bonds. The hydrogen bonding distances were 1.951, 2.166 and 2.226Å respectively H(C3), H(C4) and H(C5). Based on infrared spectroscopic studies, they concluded that the addition of HF would weaken the hydrogen bonding between the cations and anions. In our CPMD simulations, the peak positions in the RDFs of ring hydrogen and fluorine (Figure 9.10) are 2.15, 2.25 and 2.35Å respectively for H(C3), H(C4) and H(C5). This signifies a weakening of the hydrogen bond compared to the experimental values for the [emim][F].HF crystal, in accordance with experiments [24]. We wish to point out that although the H-bonds are weaker in liquid [emim][F].2.3HF compared to that in crystalline [emim][F].HF, they are reasonably stronger since the distance between them is still smaller than the sum of the van der Waals radii of hydrogen (1.20Å) and fluorine (1.50Å). The number of hydrogen bonds per

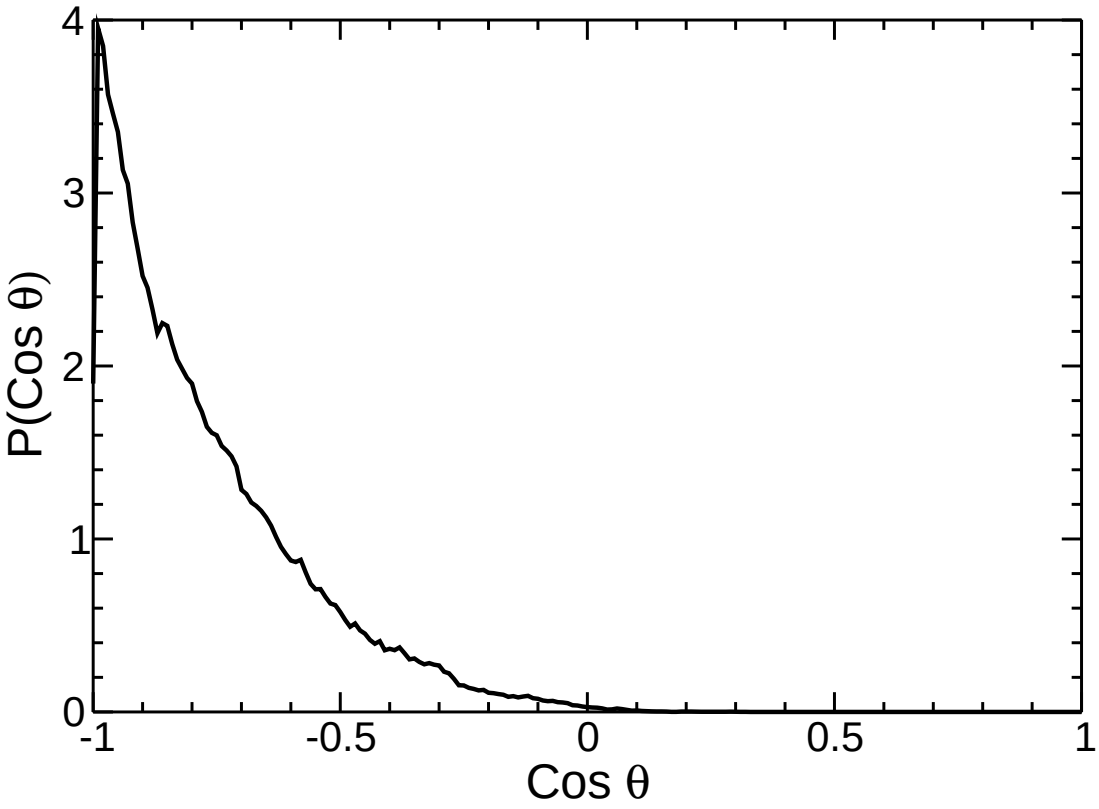

Figure 9.11: Distribution of C_α-H(C_α)-F angle for the fluorine atoms that are within 2.5Å from the hydrogen atom. C_α refers to one of the carbon atom belonging to the imidazolium ring.

cation is also reduced from three in the crystal structure of [emim][F].HF to around one in liquid [emim][F].2.3HF. This can be rationalized as due to the decrease in the basicity of the anion upon addition of HF. Some of the fluoride ions that are H-bonded to the ring hydrogens are also hydrogen bonded to one or more HF molecules, while others are not bound to any HF molecule through hydrogen bonding. Such fluoride ions constitute 5.2% of the total when strict hydrogen bond criteria is imposed and 9.5% of the total with the liberal criteria.

Fluoride anions are mostly H-bonded to the acidic hydrogen of the ring. Analyses of the trajectory showed that the probability for the fluoride ion to form H-bond with the acidic hydrogen is 62.9% compared to values of 16.9% and 20.2% with H(C4) and H(C5) respectively. The neutral fluorine atom of the HF molecule forms H-bond with

H(C3), H(C4) and H(C5) with the probabilities of 38.2, 29.8 and 32.0% respectively. The closeness of these values indicates that while the anion prefers the acidic hydrogen for hydrogen bonding over the other ring hydrogens, the neutral fluorines do not exhibit any such preference. 47% of all the H-bonds formed with the ring hydrogens are with the acidic hydrogen (H(C3), whereas the other two ring hydrogen accounts of a total of 53%. A similar behavior was observed by us in the *ab initio* studies of [mmim][Cl] [11], where the chloride anion was primarily hydrogen bonded to the acidic hydrogen. It is thus clear that although all the three ring hydrogens are capable of forming H-bonds, the strength and the number of such bonds formed is greater for the acidic hydrogen of the cation ring.

To summarize, we believe that the propensity for hydrogen bond formation between the ring hydrogen of the cation and the anion is decreased in liquid [emim][F].2.3HF compared to that in crystalline [emim][F].HF. However, such hydrogen bonds are not absent in the liquid modeled within DFT.

9.3.6 Cation - cation orientation

The cation - cation RDF shows a prepeak at around 4.65Å. In order to find the origin of this shoulder, the probability distribution of the angle between ring normals of two cation neighbors (within 4.8Å) is shown in Figure 9.12. Proximal cations exhibit a preference to be aligned parallel. The parallel alignment is seen only for closely spaced cation rings and not for those separated far apart – hence there is no stacking of the ring planes as is the case in the crystal. Such a preferential cation orientation has also been observed previously in the case of [mmim][Cl] studied using *ab initio* simulations [10, 11] and also through empirical potential MD in the case of [emim][F].2.3HF [6]. The parallel ring orientation could contribute to the 1.8$Å^{-1}$ peak observed in the structure factor. Experimentally, the stacking of layers has been observed in the [emim][F].HF crystal [24] at 324K. It was found that all atoms except the hydrogen atoms on the alkyl chains are coplanar and that the interlayer separation is 3.38Å. Hagiwara *et al* from their X-ray diffraction

studies on alkylimidazolium fluorohydrogenate molten salts, have concluded that the first sharp diffraction peak at 1.8Å^{-1} corresponds to the layer separation of the flat cations formed by ordering of ions [3]. Our results on the liquid add considerable support to this observation.

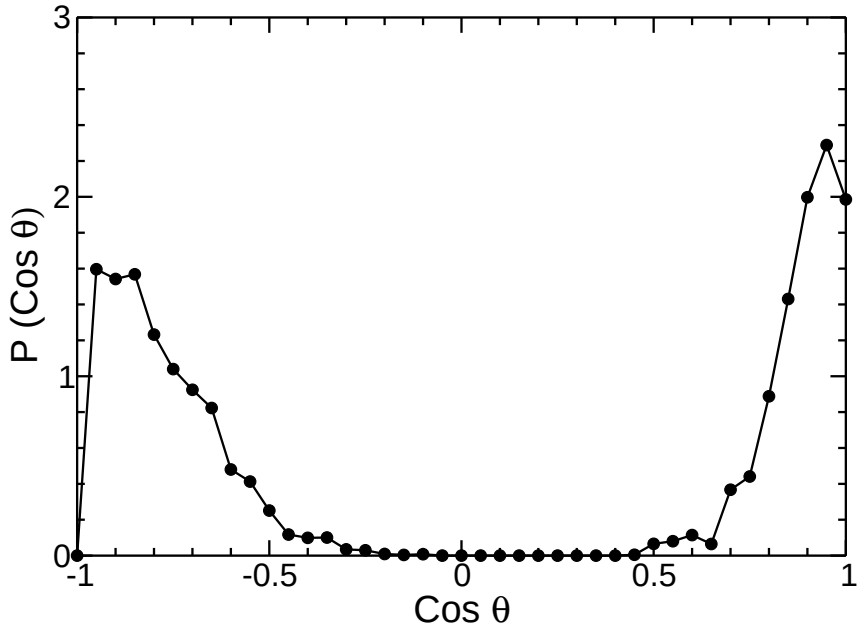

Figure 9.12: The distribution of angle between the normals of the cation ring when the ring centers are within 4.8Å.

9.3.7 Vibrational analysis

The change in the covalent bond length between hydrogen and fluorine in the HF molecule in different polyfluoride anionic species should affect the H-F stretching frequency. Figure 9.13 shows the vibrational density of states for different polyfluoride species in the system. The data is presented for the polyfluorides, $F(HF)_2^-$, $F(HF)_3^-$ and $F(HF)_4^-$. In the region between 400 to 1000 cm^{-1} that corresponds to the stretching of the hydrogen bond the spectrum of higher polyfluoride species exhibit a red shift, signifying a weakening of the hydrogen bond. These observations are consistent with our discussion on the hydrogen bond lengths earlier, as well as with vibrational density of states data of Rosenvinge

et al [7] on liquid KF.2HF. In the region 1500 to 2500 cm^{-1}, that corresponds to the F - D stretching mode, there is a clear blue shift of the spectrum for the larger polyfluoride anions. This can be reasoned as due to the stiffening of the covalent bond of the HF molecule when it is H-bonded to a fluoride ion that is H-bonded to more number of HF molecules. In this case, the H-bond becomes weaker and the electron cloud of hydrogen is pulled more towards the fluorine atom that is covalently bonded resulting in a stronger and more rigid H-F covalent bond. However, it should be noted that DFT is found to under-estimate the frequencies.

9.4 Conclusions

We have carried out an *ab initio* molecular dynamics simulation of the room temperature ionic liquid electrolyte [emim][F].2.3HF. Intramolecular structural parameters obtained from our simulation as well as from gas phase calculations agree well with such data obtained from experimentally determined crystal structures. The intermolecular structure in the liquid has been characterized through the calculation of the X-ray structure factor, and compared to the scattering results of Hagiwara and coworkers [3]. The origin of several features in that quantity has been analyzed using partial structure factors of distinct pairs of atoms. The feature at $1.8 Å^{-1}$ arises from fluorine-fluorine and cation-cation correlations and the intramolecular correlations lead to the one at $3.8 Å^{-1}$.

The predominant moieties present in this liquid are the polyfluoride species of the form $F(HF)_n^-$. Species with values of n equal to 2 or 3 are present in significant quantities, while those with n equal to 1 or 4 are rare. About 10% of the total amount of fluorine atoms are not part of any polyfluoride species, but are associated with the [emim] cation through a hydrogen bond with its acidic (and to some extent, non-acidic) ring hydrogens. Interestingly, the length of the covalent H-F bond in the polyfluoride species is found to decrease with an increase in the number of HF molecules in the species, implying its strengthening. In contrast, the hydrogen bond between H and F is found to weaken with

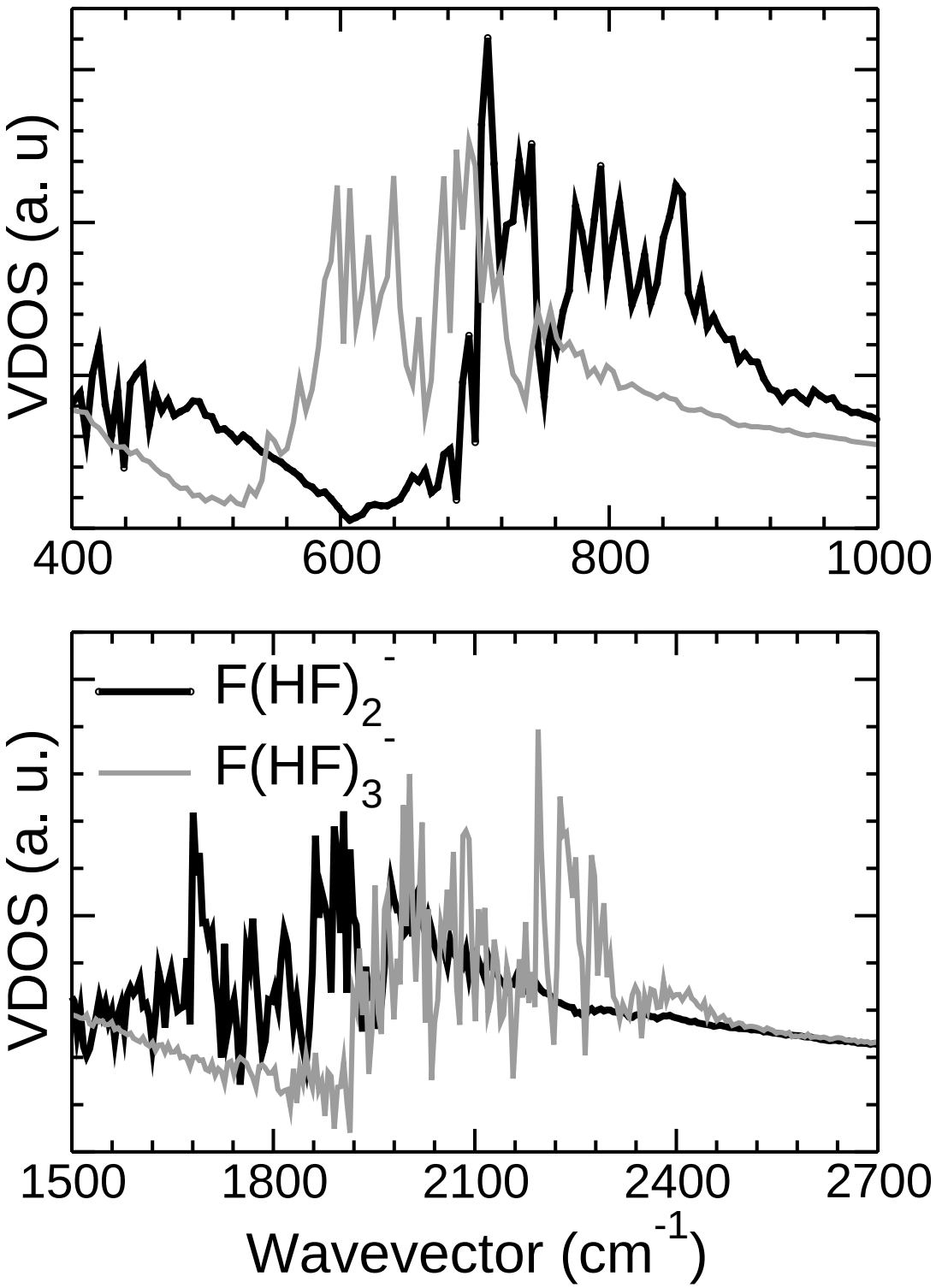

Figure 9.13: Vibrational density of states for the different polyfluoride anions present in the system.

an increase of HF molecules in the polyfluorides. These observations are consistent with the fact of a decreased basicity of the anion with increasing values of n. The changes in the covalent and hydrogen bond lengths impact the vibrational spectra as well. The H-F stretching mode related to the covalent bond exhibits a blue shift while that corresponding to the hydrogen bond shows a red shift with increasing n. We have also characterized the geometry of the polyfluorides – while species with smaller n tend to be planar, $F(HF)_4^-$ is nearly tetrahedral. In these analyses on the polyfluoride species, our results are in full agreement with that of Rosenvinge et al [7].

One of the key differences in our work, as compared to the earlier MD simulation using empirical potentials [6] is in the existence of a cation-anion hydrogen bond. Our results show the presence of a hydrogen bond between the acidic hydrogen and the fluoride ion, while such a hydrogen bond was absent in the classical MD simulations. In the latter, although the pairs of atoms were present within the cutoff distance usually employed in defining a hydrogen bond, the anion was found not to approach the acidic hydrogen atom along the C3-H(C3) bond. Our CPMD simulation demonstrates the presence of a hydrogen bond, that is well characterized using both distance and orientation criteria. The observed cation-anion hydrogen bond is however, weaker than that seen in crystalline [emim][F].HF [24], as expected.

Our work is limited by the size of the system considered. Yet, CPMD simulations of a liquid containing close to 400 atoms, 1128 valence electrons in a cubic box of edge length around 16Å are demanding. However, system size effects cannot be discounted. One could actually notice it in the comparison of the structure factor presented in Figure 9.3, where the low angle peak at 1Å $^{-1}$ is not well reproduced in the simulation. The reduced duration of the trajectory (few tens of picoseconds) is less of a problem, as the ions are fairly mobile. At the least, intermolecular structure obtained from our simulations up to the first coordination shell can be guaranteed to be realistic. Future efforts will be made to study larger sizes of this system and similar ionic liquids.

Bibliography

[1] R. Hagiwara, T. Hirashige, T. Tsuda, Y. Ito, *J. Fluorine Chem.*, **99**, 1 (1999).

[2] R. Hagiwara, T. Hirashige, T. Tsuda, Y. Ito, *J. Electrochem. Soc.*, **149**, D1 (2002).

[3] R. Hagiwara, K. Matsumoto, T. Tsuda, Y. Ito, S. Kohara, K. Suzuya, H. Matsumoto, Y. Miyazaki, *J. Non-Crystalline Solids*, **312-314**, 414 (2002).

[4] R. Hagiwara, K. Matsumoto, Y. Nakamori, T. Tsuda, Y. Ito, H. Matsumoto, K. Momota, *J. Electrochem. Soc.*, **150**, D195 (2003).

[5] R. Hagiwara, Y. Nakamori, K. Matsumoto, Y. Ito, *J. Phys. Chem. B*, **109**, 5445 (2005).

[6] M. Salanne, C. Simon, P. Turq, *J. Phys. Chem. B*, **110**, 3504 (2006).

[7] T. von Rosenvinge, M. Parrinello, M.L. Klein, *J. Chem. Phys.*, **107**, 8012 (1997).

[8] C. Hardacre, J.D. Holbrey, S.E.J. McMath, D.T. Bowron, A.K. Soper, *J. Chem. Phys.*, **118**, 273 (2003).

[9] M.G. Del Pópolo, R.M. Lynden-Bell, J. Kohanoff, *J. Phys. Chem. B*, **109**, 5895 (2005).

[10] M. Bühl, A. Chaumont, R. Schurhammer, G. Wipff, *J. Phys. Chem. B*, **109**, 18591 (2005).

[11] B.L. Bhargava, S. Balasubramanian, *Chem. Phys. Lett.*, **417**, 486 (2006).

[12] B.L. Bhargava, S. Balasubramanian, *J. Phys. Chem. B*, **111**, 4477 (2007).

[13] R.M. Lynden-Bell, M.G. Del Popolo, T.G.A. Youngs, J. Kohanoff, C.G. Hanke, J.B. Harper, C.C. Pinilla, *Acc. Chem. Res.*, (2007). (In Press). DOI: 10.1021/ar700065s

[14] R. Car, M. Parrinello, *Phys. Rev. Lett.*, **55**, 2471 (1985).

[15] J. Hutter, P. Ballone, M. Bernasconi, P. Focher, E. Fois, S. Goedecker, D. Marx, M. Parrinello, M.E. Tuckerman, CPMD Version 3.11.1, Max Planck Institut fuer Festkoerperforschung, Stuttgart, and IBM Zurich Research Laboratory, 1990-2006.

[16] J.N.C. Lopes, J. Deschamps, A.A.H. Pádua, *J. Phys. Chem. B*, **108**, 2038 (2004). **108**, 11250 (2004).

[17] M.E. Cournoyer, W.L. Jorgensen, *Mol. Phys.*, **51**, 119 (1984).

[18] N. Troullier, J.L. Martins, *Phys. Rev. B*, **43**, 1993 (1991).

[19] A.D. Becke, *Phys. Rev. A*, **38**, 3098 (1988).

[20] C. Lee, W. Yang, R.G. Parr, *Phys. Rev. B*, **37**, 785 (1988).

[21] G.J. Martyna, M.L. Klein, M.E. Tuckerman, *J. Chem. Phys.*, **97**, 2635 (1992).

[22] *CRC Handbook of Chemistry and Physics*, 81st ed. Lide, D. R., Ed.; (CRC Press, Boca Raton, FL, 2000), Chapter 9, p 20.

[23] The simulation data was scaled to match the experimental intensity at long wavevector region.

[24] K. Matsumoto, T. Tsuda, R. Hagiwara, Y. Ito, O. Tamada, *Solid State Sciences*, **4**, 23 (2002).

List of Publications

- Dynamics in a Room Temperature Ionic Liquid: A Computer Simulation Study of 1,3-dimethylimidazolium chloride.
  B.L. Bhargava and S. Balasubramanian
  J. Chem. Phys. **2005**, *123*, 144505.
  J. Chem. Phys. **2006**, *125*, 219901.(Erratum)

- Intermolecular structure and dynamics in an ionic liquid: A Car-Parrinello molecular dynamics simulation study of 1,3-dimethylimidazolium chloride.
  B.L. Bhargava and S. Balasubramanian
  Chem. Phys. Lett. **2006**, *417*, 486.

- Layering at an Ionic Liquid-Vapor Interface: A Molecular Dynamics Simulation Study of [bmim][PF_6].
  B.L. Bhargava and S. Balasubramanian
  J. Am. Chem. Soc. **2006**, *128*, 10073.

- Insights into the Structure and Dynamics of a Room Temperature Ionic Liquid: *Ab initio* Molecular Dynamics Simulation Studies of [bmim][PF_6] and the [bmim][PF_6] - CO_2 Mixture.
  B.L. Bhargava and S. Balasubramanian
  J. Phys. Chem. B **2007**, *111*, 4477.

- Probing Anion-Carbon dioxide Interactions in Room Temperature Ionic Liquids.

B.L. Bhargava and S. Balasubramanian
Chem. Phys. Lett. **2007**, *444*, 242.

- A refined potential model for atomistic simulations of an ionic liquid, [bmim][PF_6].
  B.L. Bhargava and S. Balasubramanian
  J. Chem. Phys. **2007**, *127*, 114510.

- Nanoscale Organization in Room Temperature Ionic Liquids: A Coarse Grained Molecular Dynamics Simulation Study.
  B.L. Bhargava, R. Devane, M.L. Klein and S. Balasubramanian
  Soft Matter **2007**, *3*, 1395.

- *Ab initio* studies on [bmim][PF_6] - CO_2 mixture and CO_2 clusters.
  B.L. Bhargava, M. Saharay and S. Balasubramanian
  Bulletin of Material Science **2007** (Communicated).

- Structural Correlations and Charge Ordering in a Room Temperature Ionic Liquid: The case of [bmim][PF_6].
  B.L. Bhargava, M.L. Klein, S. Balasubramanian
  ChemPhysChem **2007** (Communicated).

- Molecular Dynamics Study of [bmim][PF_6] - CO_2 mixture: Variation of CO_2.
  B.L. Bhargava and S. Balasubramanian (Manuscript in Preparation)

- *Ab initio* Molecular Dynamics Studies of liquid [emim][F] - 2.3 HF mixture.
  B.L. Bhargava and S. Balasubramanian (Manuscript in Preparation).